



# Power laws behavior and nonlinearity mechanisms in mesoscopic elastic materials

Sonia Idjmarene

## ► To cite this version:

Sonia Idjmarene. Power laws behavior and nonlinearity mechanisms in mesoscopic elastic materials. Other [cond-mat.other]. Université du Maine, 2013. English. NNT : 2013LEMA1033 . tel-01037944

**HAL Id: tel-01037944**

**<https://theses.hal.science/tel-01037944>**

Submitted on 23 Jul 2014

**HAL** is a multi-disciplinary open access archive for the deposit and dissemination of scientific research documents, whether they are published or not. The documents may come from teaching and research institutions in France or abroad, or from public or private research centers.

L'archive ouverte pluridisciplinaire **HAL**, est destinée au dépôt et à la diffusion de documents scientifiques de niveau recherche, publiés ou non, émanant des établissements d'enseignement et de recherche français ou étrangers, des laboratoires publics ou privés.

## PHD THESIS

**Sonia IDJIMARENE**

Dissertation presented to obtain

**grade de Docteur de l'Université du Maine**

sous le label de L'Université Nantes Angers Le Mans

**École doctorale : SPIGA**

**Spécialité : Acoustique**

**Unité de recherche : Laboratoire d'Acoustique de l'Université du Maine — UMR CNRS 6613**

**titolo di Dottore di Ricerca del Politecnico di Torino**

**Scuola di Dottorato : SCUDO**

**Dottorato in Fisica**

**Dipartimento di Scienza Applicata e Tecnologia**

**Defended on 7<sup>th</sup> February 2014**

**Thesis N° :**

# **POWER LAWS BEHAVIOR AND NONLINEARITY MECHANISMS IN MESOSCOPIC ELASTIC MATERIALS.**

## **JURY**

Rapporteurs : **Koen VAN DEN ABEELE**, Professor, Catholic University of Leuven, Belgium

**Michele GRIFFA**, Senior Research Scientist and Team Leader at EMPA, Swiss Federal Laboratories for Materials Science and Technology, Switzerland

Examiners : **Vitalyi GUSEV**, Professor, Université du Maine, France

**Antonio GLIOZZI**, Assistant Professor, Politecnico di torino, Italy

**Giovanni BARBERO**, Professor, Politecnico di torino, Italy

Promotor : **Rachid EL GUERJOUMA**, Professor, Université du Maine, France

Co-Promotor : **Marco SCALERANDI**, Professor, Politecnico di torino, Italy

**Mourad BENTAHAR**, HDR, Université du Maine, France



## Résumé

Depuis que leur particularité a été mise en évidence, les matériaux non-linéaires mésoscopiques tels que le béton, les roches, les composites, les tissus biologiques, etc. suscitent un intérêt de plus en plus croissant. L'étude du comportement dynamique de ces matériaux à l'aide de la théorie classique de Landau s'est révélée incapable d'expliquer les différentes observations expérimentales effectuées sur cette "nouvelle classe" de matériaux. En effet, ces derniers présentent des singularités (microfissures, contacts, joints de grains, dislocations, etc.) distribuées de manière hétérogène à l'échelle mésoscopique. Par conséquent, différents mécanismes physiques associés au comportement desdites singularités peuvent être à l'origine des non-linéarités observées. Ce travail de thèse s'intéresse à la réponse macroscopique de différents matériaux mésoscopiques et ce dans le but d'extraire des indicateurs non-linéaires  $y$  dont la dépendance en fonction de l'amplitude d'excitation  $x$  est une loi de puissance  $y = ax^b$  indépendamment de la méthode expérimentale adoptée. En général, l'exposant  $b$  connu pour être lié au mécanisme physique responsable de la non-linéarité varie de 1 à 3. Dans un premier temps, le lien existant entre les propriétés de la microstructure de chacun des matériaux étudiés et la valeur de l'exposant  $b$  nous a permis de définir différentes classes de matériaux. Par ailleurs, ce travail de thèse est également destiné à étudier la relation entre la valeur mesurée de l'exposant  $b$  et les mécanismes physiques microscopiques générés par la perturbation acoustique. A cet effet, le formalisme de Preisach-Mayergoyz a été généralisé pour définir des modèles multi-états. Cela s'est effectué en discrétisant les différentes équations continues qui décrivent différents mécanismes physiques microscopiques tels que l'adhésion ou le clapping entre les deux surfaces d'une microfissure, les forces capillaires dues à la présence de fluides ou le mouvement des dislocations au sein d'un polycristal. Dans chaque modèle, on définit un ensemble statistique d'éléments microscopiques où chaque élément est caractérisé par ses constantes élastiques décrivant son état mécanique et ses paramètres de transition inter-états. La prise en compte de tous les éléments microscopiques permet de décrire le comportement global mésoscopique. Moyennant cette démarche, il nous a ainsi été possible de remonter aux résultats expérimentaux par simple résolution de l'équation de propagation dans un milieu composé de plusieurs éléments mésoscopiques. L'un des résultats importants de cette thèse est que la valeur de l'exposant  $b$  peut être théoriquement prédite connaissant le nombre de paramètres de transition dans le modèle, les contraintes géométriques ainsi que leur distribution statistique. De plus, l'application de cette étude dans le cas du béton de génie civil graduellement microfissuré a permis de montrer que la prise en compte d'un seul mécanisme de non-linéarité n'était pas suffisante pour expliquer les observations expérimentales. En effet, l'étude théorique a montré que l'évolution de la microfissuration entraîne celle des mécanismes non-linéaires mis en jeu où la combinaison "hystérésis-clapping", par exemple, a permis d'expliquer l'évolution du comportement non-linéaire du béton de génie civil à l'échelle microscopique.

## Abstract

Nonlinear mesoscopic elastic (NME) materials present an anomalous nonlinear elastic behavior, which could not be explained by classical theories. New physical mechanisms should be individuated to explain NMEs response. Dislocations in damaged metals, fluids in rocks and adhesion (in composites) could be plausible. In this thesis I have searched for differences in the macroscopic elastic response of materials which could be ascribed to different physical processes. I have found that the nonlinear indicators follow a power law behavior as a function of the excitation energy, with exponent ranging from 1 to 3 (this is not completely new). This allowed to classify materials into well-defined classes, each characterized by a value of the exponent and specific microstructural properties. To link the measured power law exponent to plausible physical mechanisms, I have extended the Preisach-Mayergoyz formalism for hysteresis to multi-state models. Specific multi-state discrete models have been derived from continuous microscopic physical processes, such as adhesion-clapping, adhesion-capillary forces, dislocations motion and hysteresis. In each model, the microscopic behavior is described by a multistate equation of state, with parameters which are statistically distributed. Averaging over many microscopic elements the so-called mesoscopic equation of state is derived and, from wave propagation simulations in a sample composed by many mesoscopic elements, the experimental results could be reproduced. In the work of the thesis, I have shown that model predictions of the exponent  $b$  (the exponent  $b$  has not been introduced before) are linked in a 'a priori' predictable way to the number of states and the properties of the statistical distribution adopted. We have classified models into classes defined by a different exponent  $b$  and comparing with experimental results we have suggested plausible mechanisms for the nonlinearity generation.

**Mots clés**

Non linéarité, modèles multi-états, loi de puissance, micro-structure, Scaling Subtraction Method (SSM). Fast Fourier Transform (FFT)

**Key Words**

Nonlinearity, multi-scale models, power law, micro-structure, Scaling Subtraction Method (SSM). Fast Fourier Transform (FFT)



---

To my parents and family

To my second family in Le Mans

To my S.H.I.Z

---

# Acknowledgements

The present PhD thesis has been one of the most significant challenges I have ever had to face. It would not have been completed without the support, patience and guidance of many people. I owe my deepest gratitude to

- My supervisors Professors Marco Scalerandi, Mourad Bentahar and Rachid El Guerjouma, for providing me with an excellent atmosphere for doing research. They let me experience different research aspects between Physics and acoustics, Modeling and experiments. Working with you was a pleasure, thank you for every thing.
- I would also like to thank Professor K. Van Den Abeele from university of Leuven and Dr. Michele Griffa, senior research scientist at EMPA, for the time and interest they provided reading and reviewing this thesis. I am grateful to Professor Vitaly Gushev, Dr. Antonio Gliozzi and Professor Giovanni Barbero who accepted to be examiners in my final oral defense.
- All the persons I had the good fortune to meet over the three years I spent between Laboratoire d'Acoustique de L'université du Maine and Politecnico di Torino, I think especially to Charefedine, Paola and Antonio.
- I gratefully acknowledge the funding sources that made my Ph.D. work possible. I was funded by both Algerian and French Higher Education Ministries for 3 years. My work was also supported by Université Franco-Italienne, in the framework of Vinci project, who always covered my travel and accomodation expenses in Torino.



---

# Contents

	<b>i</b>
<b>Acknowledgements</b>	<b>ii</b>
<b>List of Figures</b>	<b>vii</b>
<b>Introduction</b>	<b>xv</b>
<b>References</b>	<b>xx</b>
<b>I Elasticity and acoustic wave propagation in solids: from classical theory to Nonlinear Mesoscopic Elasticity (NME)</b>	<b>1</b>
1 Introduction . . . . .	1
2 Classical theory of wave propagation in solids . . . . .	2
2.1 Classical linear theory . . . . .	2
2.2 Classical nonlinear theory . . . . .	4
2.3 Effects of nonlinear terms in the wave equation . . . . .	6
2.3.1 Harmonics and sidebands generation . . . . .	7
2.3.2 Resonance frequency shift . . . . .	8
3 Non classical nonlinear wave propagation in solids . . . . .	10
3.1 Quasi-static behavior . . . . .	10
3.2 Dynamic behavior . . . . .	12
3.2.1 Fast dynamic experiments . . . . .	12
3.2.2 Slow dynamic effects . . . . .	14
4 Conclusions . . . . .	17
<b>References</b>	<b>19</b>

<b>II</b>	<b>Models for Nonlinear Mesoscopic Elasticity</b>	<b>21</b>
1	Introduction . . . . .	21
2	Physical models . . . . .	21
2.1	Internal friction . . . . .	22
2.1.1	Granato-Lucke model of dislocations . . . . .	22
2.1.2	Stick-slip motion . . . . .	23
2.2	Clapping mechanism . . . . .	24
2.3	Adhesion mechanism . . . . .	25
3	Preisach-Mayergoyz models of nonlinear elasticity . . . . .	26
3.1	Equation of state of the microscopic elements . . . . .	26
3.2	PM formalism . . . . .	28
4	Phenomenological multistate models . . . . .	31
4.1	General considerations . . . . .	31
4.2	Hysteretic model . . . . .	32
4.2.1	Equation Of State . . . . .	32
4.2.2	PM formalism and mesoscopic EOS . . . . .	34
4.2.3	Macroscopic scale calculations . . . . .	35
4.3	Clapping model . . . . .	37
4.3.1	Microscopic equation of state . . . . .	37
4.3.2	Mesososcopic equation of state . . . . .	39
4.4	Adhesion model . . . . .	40
4.4.1	Microscopic equation of state . . . . .	40
4.4.2	Mesososcopic equation of state . . . . .	41
5	Conclusions . . . . .	42
	<b>References</b>	<b>43</b>
<b>III</b>	<b>Power laws behavior in nonlinear acoustic experiments</b>	<b>45</b>
1	Introduction . . . . .	45
2	Nonlinear measurements set-up and data analysis . . . . .	46
2.1	Experimental set-up . . . . .	46
2.2	Numerical set-up . . . . .	47
2.3	Data analysis and definition of the nonlinear indicator . . . . .	48
2.3.1	Scaling Subtraction Method (SSM) . . . . .	49
2.3.2	Nonlinear Elastic Wave Spectroscopy(NEWS) method . . . . .	50
3	Power law evolution of nonlinear indicators . . . . .	51
3.1	Definition . . . . .	51
3.2	Experimental problems and motivation . . . . .	54
3.2.1	Noise and saturation effects . . . . .	54
3.2.2	Dependence on the experimental configuration . . . . .	56
4	Amplitude threshold for nonlinearity detection . . . . .	56
4.1	Equipment noise . . . . .	57
4.1.1	Noise quantification . . . . .	57

4.1.2	Equipment noise effects on SSM and FFT analysis . . . . .	58
4.2	Ambient noise . . . . .	60
4.2.1	Ambient noise effects on SSM analysis . . . . .	60
4.2.2	Ambient noise effects on FFT analysis . . . . .	61
4.3	Discussion . . . . .	62
4.4	Experimental results . . . . .	64
4.5	Implications for the experimental analysis . . . . .	65
5	Effects of the experimental configuration and data analysis parameters . . . . .	68
5.1	Numerical analysis . . . . .	69
5.2	Effects due to the experimental set-up . . . . .	70
5.2.1	Continuous waves . . . . .	71
5.2.2	Pulses . . . . .	73
5.3	Effects of the data analysis parameters . . . . .	74
6	Conclusions . . . . .	77
<b>References</b>		<b>79</b>
<b>IV Power laws exponent based classification of nonlinearity mechanisms</b>		<b>82</b>
1	Introduction . . . . .	82
2	Universality classes of materials . . . . .	83
2.1	Data analysis . . . . .	83
2.1.1	Materials classification . . . . .	83
2.1.2	Evolution of damage . . . . .	85
3	Nonlinearity in multi-state multi-scale models . . . . .	86
3.1	General definition . . . . .	87
3.2	Hysteresis, memory and conditioning . . . . .	88
3.3	Nonlinearity in the macroscopic response . . . . .	89
3.3.1	Uniform distribution . . . . .	90
3.3.2	Non uniform distribution . . . . .	91
4	Constitutive equation based classification of multi state multi scale models . . . . .	91
4.1	Numerical simulation . . . . .	92
4.2	Hysteretic model with conditioning . . . . .	92
4.2.1	Microscopic equation of state . . . . .	92
4.2.2	PM space and theoretical predictions of $b$ . . . . .	93
4.2.3	Model parameters and numerical results . . . . .	95
4.3	Adhesion model with and without hysteresis . . . . .	96
4.3.1	Microscopic equation of state . . . . .	96
4.3.2	PM space and theoretical predictions for $b$ . . . . .	98
4.3.3	Model parameters and numerical results . . . . .	98
4.4	Clapping model . . . . .	99
4.4.1	Microscopic equation of state . . . . .	99
4.4.2	PM space and theoretical predictions for $b$ . . . . .	99
4.4.3	Model parameters and numerical results . . . . .	100

4.5	Results and discussion . . . . .	101
5	Geometrical constraints based classification . . . . .	102
5.1	The geometrical constraints . . . . .	102
5.2	Results and discussion . . . . .	104
6	Distribution based classification . . . . .	107
6.1	The distribution functions . . . . .	107
6.2	Results and discussion . . . . .	107
7	Application of the classification to experimental damage characterisation . . . .	109
7.1	Experimental data for the characterisation of damage evolution . . . . .	109
7.1.1	Experimental set up . . . . .	109
7.1.2	Previous results . . . . .	109
7.2	Characterisation of damage evolution . . . . .	110
7.2.1	Mixed multi-state models . . . . .	110
7.2.2	Results and discussion . . . . .	111
7.2.3	Fitting the experimental data . . . . .	111
8	Conclusions . . . . .	113
<b>References</b>		<b>115</b>
<b>V Conditioning effects on the power law behavior of NME materials</b>		<b>118</b>
1	Introduction . . . . .	118
2	Experimental results . . . . .	119
3	Multi scale multi state models with conditioning . . . . .	120
4	Hysteretic model . . . . .	121
4.1	Theory . . . . .	121
4.2	Simulation and results . . . . .	124
5	Adhesion hysteretic model with conditioning . . . . .	125
5.1	The model . . . . .	126
5.1.1	Theory . . . . .	127
5.2	Simulation and results . . . . .	129
5.2.1	Simulation . . . . .	129
5.2.2	Results . . . . .	130
6	Conclusions . . . . .	132
<b>References</b>		<b>134</b>
<b>Conclusion and Perspectives</b>		<b>135</b>

---

## List of Figures

I.1	(a) Axial stress protocol for the quasi-static stress-strain experiment; (b) Stress-strain experimental result corresponding to the protocol shown in (a) for a sandstone [13]. . . . .	10
I.2	Plot of the wave velocity vs. applied pressure for dry Berea sandstone and Berea with a bond system (flat pores) filled with epoxy. Open circles represent the second upward cycle [20]. . . . .	11
I.3	Second and third harmonic amplitudes as a function of measured strain amplitude in Berea sandstone. The harmonic amplitudes were obtained from Fourier analysis of the recorded time signals. [13] . . . . .	13
I.4	Right: resonance curves for a Fontainebleau sandstone cylindrical sample at increasing drive: the resonance peak shifts to the left and the Q-factor increases. Left: normed frequency shift $\frac{ \omega-\omega_0 }{\omega_0}$ , where $\omega_0$ is the linear resonance frequency, plotted as a function of strain amplitude for various rocks. The slope of the curves is approximately one, indicating that non classical nonlinearity is responsible for the peak shift [13] . . . . .	15
I.5	Conditioning in a damaged concrete sample. As conditioning time increases, the wave velocity diminishes (blue circle), while the nonlinearity of the sample (indicator $\theta$ ) increases (red circles and black squares for the Scaling Subtraction Method and harmonics indicators, respectively) . . . . .	16
I.6	Slow dynamics in a concrete sample. Left: Conditioning at constant amplitude; Right: Relaxation process in time [23]. . . . .	17
II.1	(a) The successive drawings indicate schematically the bowing out of a pinned dislocation line by an increasing applied stress; (b) Stress-strain equation in the Granato-Lucke model. The equation for a single dislocation line is reported as a solid line, while averaging over dislocations lines with different lengths give the macroscopic stress-strain equation reported as a dashed line [8] . . . . .	23
II.2	Stick- slip processes as consequence of frictional sliding between two surfaces in contact under shearing applied stress . . . . .	24

II.3	(a) The Lennard-Jones potential between two molecules as a function of the distance $r$ separating them; (b) Lennard-Jones-like interaction between two surfaces in contact separated by a distance $\Delta x$ as described in the Clapping model, the Lennard-Jones potential is approximated by 4 segment-like intervals. [10] . . . . .	25
II.4	(a) The short-scale intermolecular Lennard-Jones potential; (b) An effective potential $\Phi_{ad} \propto \Phi + \Phi_H + \Phi_0$ ; (c) a piece-wise linear approximation for the effective potential. [11] . . . . .	26
II.5	Behavior of one microscopic element in an elastic PM model . . . . .	27
II.6	(a) Macroscopic equation of state derived from a pressure protocol using the hysteretic PM model; (b) The pressure variation causes a redistribution of elements between open and closed states; (c) The stress-strain relation could be derived counting the number of elements in the closed state at each pressure value. The stress-strain equation is only qualitatively depicted; (d) The modulus derived as a function of time deriving the stress-strain equation. . . .	29
II.7	Diagram explaining the different steps in the multi-scale multi-state approach used to model nonlinear phenomena in NME materials. The material (macroscopic) is discretized into cells (mesoscopic). Each mesoscopic level is discretized into a set of microscopic elements, each of them represented as a spring with elastic constant depending on a control variable $z$ which defines transitions from one elastic state to another. The equation of motion at the macroscopic level describes the second time derivative of the nodes displacements ( $u_i$ ) as a function of the stresses due to the surrounding MEs, as reported in the figure. . . . .	32
II.8	Equation Of State of (a) One microscopic hysteretic element; (b) A mesoscopic element ME, using the hysteretic model; (c) P-M space distribution of $N = 100$ elements . . . . .	33
II.9	Dynamic pressure cycle. The letters ( $A, B, C, D$ ) are attributed to the four phases within one period of the signal. . . . .	34
II.10	The P-M space evolution during a pressure excitation of amplitude $A_0$ starting from a relaxed configuration. $R$ indicate areas where all elements are in the rigid state and $E$ the areas with elements in the elastic state. . . . .	34
II.11	Spring system representation of (a) One microscopic element in the clapping model; (b) The mesoscopic element built from a parallel arrangement of microscopic elements . . . . .	37
II.12	Equation Of State for (a) One clapping microscopic element; (b) A mesoscopic cell, in the clapping model . . . . .	39
II.13	Spring system representation of (a) One microscopic element in the adhesion model; (b) The mesoscopic element built from a parallel arrangement of microscopic elements . . . . .	40
II.14	Spring system representation of (a) One microscopic element in the adhesion model; (b) The mesoscopic element built from a parallel arrangement of microscopic elements . . . . .	41

III.1	Nonlinearity evaluation using the Scaling Subtraction Method - SSM. (a) Time signals calculated at a large amplitude excitation (solid red line) and reference signal (blue dotted line); (b) SSM signal; (c) Plot of the nonlinear indicator $y_{SSM}$ vs. driving amplitude $x_u$ . . . . .	50
III.2	Nonlinearity evaluation using the analysis in the frequency domain (Fast Fourier Transform - FFT). The time signal analyzed is the same as that used for the SSM analysis (see Fig. III.1. (a) frequency spectrum of the time signal, the filtering bandwidth is indicated; (b) filtered signal in the bandwidth of subplot(a): $10KHz$ around the third harmonic; (c) plot of the nonlinear signature $y_{FFT}$ vs. driving amplitude $x_u$ . . . . .	52
III.3	Nonlinear indicator $y$ as a function of driving amplitude $x_u$ for different nonlinearity strengths $\lambda$ : (a) SSM analysis; (b) FFT analysis. . . . .	53
III.4	Results from an experiment performed on a cracked steel disk excited with a CW at frequency $100KHz$ . (a) Picture of the sample we used to perform the experiment; (b) $y_{SSM}$ plotted as a function of the driving $x_u$ . Data start to be meaningful at the amplitude threshold $x_u^{th}$ and fit a power law only in the intermediate amplitude range. . . . .	55
III.5	Results from an experiment performed on a long concrete bar with receivers located in different positions. In all cases the dependence of the nonlinear indicator on the excitation is a power law function, but the measured nonlinearity strongly depends on the relative distance separating the source and the receiver. . . . .	56
III.6	Nonlinear indicator $y$ as a function of driving amplitude $x_u$ for nonlinearity strength $\lambda = 1.6 \cdot 10^{-4}$ and different equipment noise levels $n_e$ : (a) SSM analysis; (b) FFT analysis. . . . .	59
III.7	Nonlinear indicator $y$ as a function of driving amplitude $x_u$ for nonlinearity strength $\lambda = 1.6 \times 10^{-4}$ and different noise choices: (a) SSM analysis; (b) FFT analysis. . . . .	61
III.8	Nonlinear-to-linear signals ratio at the threshold level vs. strength of the noise contribution to the nonlinear signal. The solid line indicate when the two are identical. (a) SSM analysis; (b) FFT analysis. . . . .	63
III.9	Nonlinear indicators measured experimentally on a concrete prism (with a joint) under load. (a) $y_{SSM}$ vs. $x_u$ ; (b) $y_{FFT}$ vs. $x_u$ . The detection threshold is larger for lower nonlinearity and it is always much larger when the analysis is performed in the frequency domain. Compare results with Fig. III.6. . . . .	65
III.10	SSM nonlinear indicator measured experimentally on a reinforced concrete prism at different levels of corrosion. The detection threshold decreases when increasing damage (i.e. increasing nonlinearity). In all cases nonlinearity is detectable when $y_{SSM}$ is larger than 0.03, thus confirming the presencs of the same equipment noise in the three experiments. . . . .	66
III.11	SSM nonlinear indicator measured experimentally on a reinforced concrete prism at an intermediate corrosion level. Data were analyzed by increasing the amplitude of the low driving $u_0$ used to generate the reference signal. As expected, the threshold increases with increasing $u_0$ . See also Eq. III.20. . . . .	67

III.12	Determination of the power law exponent from numerical results obtained simulating a sample with both a hysteretic and a clapping scatterer (described using models reported in the previous Chapter). Without noise the exponent $b$ is found to be 1.5 (squares), but when noise is added, without considering a threshold for amplitude detection the exponent is found to be 1.1 (circles and blue fitting curve) as for purely hysteretic scatterers. Thus the presence of the clapping scatterer is undetected. . . . .	68
III.13	Determination of the threshold for detection using SSM (same case as in Fig.III.6). Here the threshold for detection is calculated when different mechanisms producing the SSM signal are considered: nonlinear attenuation (green), phase shift (blue) and transfer of energy into harmonics (magenta). Red symbols refer to the complete SSM signals, while squares denote results in the presence of noise. . . . .	69
III.14	SSM indicator $y_{SSM}$ vs. output signal energy $x_u$ without noise and for different positions of the receiver $x_{rcv}$ . The sample is excited using a CW signal. . . . .	71
III.15	(a) SSM indicator $y_{SSM}$ vs. output signal energy $x_u$ with noise and for different positions of the receiver $x_{rcv}$ . The sample is excited using a CW signal; (b) SSM indicator $y_{SSM}$ vs. input signal energy $x_s$ . In both plots, the dashed lines represent a power law fitting in the amplitude range where specimen nonlinearity is detectable. . . . .	72
III.16	(a) SSM indicator $y_{SSM}$ vs. output signal energy $x_u$ with and without noise for different positions of the receiver $x_{rcv}$ . The sample is excited using a pulse; (b) SSM indicator $y_{SSM}$ vs. input signal energy $x_s$ . In both plots, dashed lines represent a power law fitting in the amplitude range where specimen nonlinearity is detectable. . . . .	74
III.17	(a) FFT indicator $y_{FFT}$ vs. output signal energy $x_u$ without noise for different positions of the receiver $x_{rcv}$ . The sample is excited using a pulse; (b) FFT indicator $y_{FFT}$ vs. input signal energy $x_s$ . In both plots, dashed lines represent a power law fitting in the amplitude range where specimen nonlinearity is detectable. . . . .	75
III.18	Nonlinear indicator $y_{SSM}$ as a function of the output energy $x_u$ for different reference signal amplitudes and in the absence of noise. . . . .	75
III.19	SSM indicator $y_{SSM}$ vs. output signal energy $x_u$ for different choices of the amplitude of the reference signal $A_{ref}$ . The sample is excited using a pulse. In both plots, dashed lines represent a power law fitting in the amplitude range where specimen nonlinearity is detectable. (a) Equipment noise proportional to the amplitude of the signal; (b) Environmental noise at constant amplitude. . . . .	76



IV.1	Power law exponent $b$ measured using the third harmonic amplitude or the Scaling Subtraction Method for various samples. <b>A: classical nonlinear samples</b> with exponent $b \approx 2$ : CLi = Duraluminum [11], steel [12] and teflon [13]. <b>B hysteretic nonlinear samples</b> with exponent $b \approx 1$ : DUF = fatigued duraluminum [11]; CFf = carbon fiber reinforced composite with delaminations [14]; STf: fatigued 4340 steel bar [15]; BOi = bones [6, 16]; SAI = Sandstones [17, 18], SLf = microcracked slate beam [19]; COi = Intact concrete samples [12, 13]; COa = Portland cement damaged by Alkali Silica Reactions at different stages [10]; COc = Corroded concrete samples at different stages of corrosion [9]. <b>C: macroscopically damaged nonlinear samples</b> with exponent $b \approx 3$ : COD = concrete with strong mechanical damage [13]; COT = concrete after strong thermal damage [20]; COD = mechanically damaged granite (unpublished). <b>D: nonlinear samples measured at increasing levels of damage</b> with exponent $b$ between 1 and 3: COD = concrete damaged in quasi static compression tests at increasing load (unpublished); COD = concrete damaged by successive thermal loadings at increasing temperature [20]; STD = steel disk with a partially open crack [21]; SLd = slate beam damaged with successive impacts [22]; SLf = Slate beam damaged at increasing number of fatigue cycles [22]. . . . .	84
IV.2	Exponent $b$ of the power law fitting function as a function of load. The increase of the exponent may be related to transitions to different damage conditions (progression of damage)[? ]. . . . .	86
IV.3	Typical microscopic stress-strain equation for a microscopic element in a multi-state formalism. Here for simplicity the driving variable is assumed to be the strain: $z = \epsilon$ . (a) nonlinear microscopic element; (b) hysteretic microscopic element; c) hysteretic microscopic element with memory . . . . .	87
IV.4	Typical distribution of $M = 1800$ microscopic elements in the PM space for a three state system without hysteresis ( $z_{ij} = z_{ji}$ ). . . . .	89
IV.5	Hypercube spanned by an excitation with $z_{min} \leq z(t) \leq z_{max}$ in the case of a PM space bounded by the condition $ z_{i,j}  \leq \Lambda$ . The coordinates of two selected points in the graph (blue circles) are given in the plot. . . . .	91
IV.6	Microscopic EOS for the hysteretic model. Transitions points are shown with dashed red lines and their values $\vec{Z} = (P_o, P_c)$ are reported. . . . .	93
IV.7	Hysteretic PM model for nonlinearity with conditioning effects. (a) The distribution $\rho_0$ of microscopic elements in the PM space. The amplitude of the excitation is $A$ and the activated area of the PM space corresponds to the triangle denoted by $T$ ; (b) Macroscopic EOS derived from averaging. . . . .	93
IV.8	Hysteretic PM model for nonlinearity without conditioning. (a) Macroscopic EOS derived from averaging over many elemnts; (b) The distribution $\rho_0$ of microscopic elements in the PM space. The activated area of the PM space for an amplitude $A$ of the excitation are the triangle in the center (denoted by $T$ ) and the rectangle $R$ . . . . .	95

IV.9	SSM nonlinear indicator vs. driving for the hysteretic model with conditioning. The curves refer to different values of the parameter $\lambda$ . Solid lines are a power law fit, as expected $b = 1$ . . . . .	96
IV.10	Adhesion model. (a) Microscopic EOS, transition thresholds $\vec{Z} = (x_1, x_2)$ are reported; (b) Macroscopic EOS derived from averaging; (c) The distribution $\rho_0$ of elements in the PM space. . . . .	97
IV.11	Adhesion model with hysteresis. (a) Microscopic EOS, transition thresholds $\vec{Z} = (x_0, x_1)$ are reported; (b) Macroscopic EOS derived from averaging; (c) The distribution $\rho_0$ of elements in the PM space. . . . .	97
IV.12	SSM nonlinear indicator vs. driving for the adhesion model with hysteresis. The curves refer to different values of the parameters. Solid lines are a power law fit. As expected $b = 2$ . . . . .	99
IV.13	Clapping model. (a) Plot of the microscopic EOS, where transitions between different states are shown as dashed red lines and the transition thresholds $\vec{Z} = (x_0, x_1, x_2)$ are reported; (b) Macroscopic EOS derived from averaging; (c) The distribution $\rho_0$ of elements in the PM space. . . . .	100
IV.14	SSM nonlinear indicator vs. driving for the clapping model. The curves refer to different values of the parameters. Solid lines are a power law fit. As expected $b = 3$ . . . . .	101
IV.15	Power law exponent $b$ predicted from simulations implementing numerically the SSM method for various models. <i>A</i> : hysteretic model with conditioning ( $b \approx 1$ ); <i>B</i> : adhesion and hysteretic without conditioning models, with $b \approx 2$ ; <i>C</i> : clapping mode, $b \approx 3$ . . . . .	102
IV.16	Distribution of the microscopic adhesion elements in the generalised PM space. The three cases correspond to the following constraints: (a) Type I: see Eq. IV.15; (b) Type II: see Eq. IV.16; (c) Type III: see Eq. IV.17. . . . .	103
IV.17	$y_{SSM}$ and $y_{FFT}$ vs. $x_u$ for the three types of constraints discussed in Fig. IV.16. Green squares: type I; Red diamonds: type II; Blue circles: type III. . . . .	104
IV.18	$y_{SSM}$ and $y_{FFT}$ vs. $x_u$ for constraints of type I (shown in the inset). The various curves correspond to increasing values of the ratio $k_2/k_1$ . . . . .	105
IV.19	$y_{SSM}$ and $y_{FFT}$ vs. $x_u$ for constraints of type II. The various curves correspond to increasing values of the parameter $\alpha$ . . . . .	105
IV.20	$y_{SSM}$ and $y_{FFT}$ vs. $x_u$ for constraints of type III. The various curves correspond to increasing values of the parameter $\gamma$ . . . . .	106
IV.21	Exponent $b$ and coefficient $a$ for the SSM and FFT nonlinear indicators vs. the ratio $k_2/k_1$ for the three types of constraints discussed in Fig. IV.17 Green diamonds: type I; Red squares: type II; Blue circles: type III. . . . .	106
IV.22	Exponent $b$ and coefficient $a$ for the SSM nonlinear indicator vs. the ratio $k_3/k_1$ for the three types of constraints discussed in Fig. IV.17. Green diamonds: type I; Red squares: type II; Blue circles: type III. . . . .	107
IV.23	$y_{SSM}$ and $y_{FFT}$ vs. $x_u$ for the adhesion model and constraints on the values of the transition parameters of type II. We used different nonuniform distributions in the PM space. . . . .	108

IV.24	Exponent $b$ and coefficient $a$ for the SSM nonlinear indicator vs. the exponent $\beta_0$ describing a non uniform power law distribution in the PM space for the adhesion model and constraints on the values of the transition parameters of type II. . . . .	108
IV.25	SSM indicator $\theta_{SSM}$ plotted as a function of the output signal for a concrete sample under different loading levels.[25] . . . . .	110
IV.26	$y_{SSM}$ vs. $x_u$ for (a) The hysteretic; (b) Clapping; (c) Mixed models. The curves in in (a) and (b) refer to different values of the model parameters. . . .	112
IV.27	(a) $y_{SSM}$ vs. $x_u$ experimentally measured (solid symbols) and numerically calculated (empty symbols) for a concrete sample subject to increasing mechanical load; (b) Power law exponent determined from experimental and numerical data of subplot (a) (blue circles and green squares) and ratio $\Delta$ (red triangles) used in the mixed model to fit the experimental data of subplot (a). . . . .	112
V.1	Experimental results obtained exciting: (a) A fatigue damaged metal based composite sample(stainless steel matrix reinforced with TiC particles) with a sweep source at frequencies close to the third flexural mode of the sample; (b) A concrete bar using a sinusoidal wave. $y_{FFT}$ is plotted as function of the driving $x$ before (blue) and after (red) conditioning in both experiments and at the beginning of relaxation (green) for the first experiment. . . . .	120
V.2	The dynamic excitation protocol used to simulate conditioning effect. The letters ( $A, B, C, D$ ) are attributed to the four phases within one period of the signal: increasing tension( $A$ ), decreasing tension( $B$ ), increasing compression( $C$ ) and decreasing compression( $D$ ). The exponential decay of the source amplitude at late times ensure a correct simulation of attenuation effects in real experiments. . . . .	122
V.3	Hysteretic PM model for nonlinearity with conditioning effects. (a) Microscopic stress-strain equation; (b) Macroscopic equation of state derived from averaging; (c) Distribution $\rho_0$ of microscopic elements in the PM space . . . .	122
V.4	The distribution $\rho_0$ of microscopic elements in the PM space. The state evolution for each element in the PM space is shown during a strain excitation of amplitude $A_0$ starting from a relaxed configuration. $R$ indicate areas where all elements are in the rigid state and $E$ the areas with elements in the elastic state. . . . .	123
V.5	The distribution $\rho_0$ of microscopic elements in the PM space. The state evolution for each element in the PM space is shown during a strain excitation of amplitude $A_0$ starting from a conditioned configuration. The letter $R$ indicates areas occupied by elements in the rigid state, while the letter $E$ to areas occupied by elastic elements. . . . .	124
V.6	SSM nonlinear indicator plotted as a function of the output energy before and after conditioning. The plot shows a decrease of nonlinearity after conditioning and an increase of the exponent $b$ at the same time. . . . .	125

V.7	Constitutive equation for the adhesion model with conditioning : (a) Microscopic equation where the transition parameters $\vec{Z} = (x_0, x_1, x_2)$ and the elastic constants $E = (k_1, k_2, k_3)$ are reported; (b) Macroscopic stress-strain relation.	126
V.8	The distribution $\rho_0$ of microscopic elements in the PM space. The amplitude of the excitation is $A_0$ shown by red lines. In the first cycle of excitation, during tension no element is changing state, while some elements contribute to nonlinearity and conditioning as a consequence of the compressive part of the excitation. . . . .	128
V.9	The distribution $\rho_0$ of microscopic elements in the PM space for an excitation applied after conditioning. The amplitude of the excitation is $A_0$ shown by red lines. In the first cycle of excitation, both during tension and compression more elements contribute to nonlinearity with respect to the same case for the relaxed sample. . . . .	129
V.10	Time Evolution of the number $N_i$ of elements in each of the three states ( $i = 1, 2, 3$ ) for an excitation amplitude $A = 0.35 \cdot 10^{-9}$ : (a) Before conditioning; (b) After conditioning. . . . .	130
V.11	Nonlinear indicator plotted as a function of the output energy before and after conditioning. The plot shows an increase of nonlinearity after conditioning while the exponent $b$ does not change: (a) SSM indicator; (b) FFT indicator. .	131
V.12	The mesoscopic stress-strain equation at (a) small strain amplitude $A = 0.15 \cdot 10^{-9}$ ; (b) at an intermediate strain amplitude $A = 0.3 \cdot 10^{-9}$ . The curves are plotted for the relaxed(blue) and conditioned(red) samples . . . . .	132

---

# Introduction

Recent experimental observations have shown that micro inhomogeneous media manifest a nonlinear elastic behavior which can not be explained by the classical theory of nonlinear elasticity proposed by Landau and applicable to homogeneous and crystalline media. The term Nonlinear Mesoscopic Elasticity (NME) was introduced to describe the properties of such materials, which include most types of rocks, concrete, bones, some damaged metals and composites, etc. They all share the characteristic of being complex structures or of presenting micro defects like cracks, grain boundaries, dislocations, etc. [1].

The heterogeneity manifests itself through nonlinear effects in both quasi static and dynamic acoustic experiments. For what concerns quasi static testing, the dependence of strain on stress (or the opposite) is a multivalued function and the constitutive equation shows a hysteresis loop with memory properties [2]. Under a dynamic excitation (propagation mode), the proportionality between input and output is no longer valid. The effect which is most commonly observed is wave distortion, which takes place as a consequence of the interaction of propagating waves with such media [3]. In such case, Wave propagation is accompanied by generation of amplitude dependent higher harmonics and sidebands. In addition, a dynamic perturbation creates a decrease in the elastic modulus of the medium. Thus in resonance frequency experiments, increasing the excitation amplitude makes the resonance frequency shift to lower values [4].

Furthermore, it is experimentally observed that, for relatively large amplitudes of dynamic excitations (still within the reversible limit), the softening of the elastic properties persists even when the excitation is switched off [5]. This effect is termed conditioning and it takes seconds to minutes for an excitation at a given amplitude to fully perturb the elastic properties of the sample and lead it into a new elastic (equilibrium) state. When the excitation is switched off, it takes minutes to days to the medium to go back to its original elastic state. This process is termed relaxation and often occurs logarithmically in time [6].

These effects, which appear as the signature of nonlinearity sources, may be quantified and differ from one media to another. Nevertheless, so far in the literature the different responses of NME materials have not been clearly investigated and they were all grouped into one class in contrast with the class of classical (described by Landau's theory) nonlinear media.

Both from the experimental and theoretical point of view, a link between the material micro-structure and the nonlinear response has been postulated [7]. Studies with neutron scattering have confirmed that the nonlinear behavior is localized in small regions close to discontinuities

---

of the specimen [8]. Despite the nonlinear behavior looks similar, such small regions have different properties and the microscopic constitutive equation could be due to different physical mechanisms. It follows that relating different microscopic features, which are at the origin of the nonlinear behavior, to different macroscopic observations might open up new horizons in the field of basic research and for applications in diagnostics, imaging and Non Destructive Testing (NDT).

From the experimental point of view, the signature of nonlinearity is detected using different techniques based on the determination of the amplitude dependence of the material response to an external ultrasonic excitation. Among others, the Nonlinear Elastic Wave Spectroscopy (NEWS), proposed by K. Van Den Abeele [9], and the Scaling Subtraction Method (SSM), introduced by M. Scalerandi [10], are most commonly used. In both cases a nonlinear indicator  $y$  could be defined and its dependence on the energy of the excitation  $x$  is generally studied.

Regardless of the adopted method, the dependence of  $y$  on  $x$  is a power law  $y = ax^b$ . Several experiments are reported in the literature confirming such a dependence in several systems. Indeed, NME materials share the characteristic of a power law exponent  $b \neq 2$ , being  $b = 2$  the exponent predicted in the Landau theory.

Experiments at low strain levels (in the range from  $10^{-8}$  to  $10^{-6}$ ) show that the exponent  $b$  assumes different values for different NME materials. Thus, as we will discuss here, the exponent of the power law dependence could be the macroscopic parameter linked to the physical properties at the micro- structural level. We will show in this thesis that  $b$  is ranging from  $b = 1$  in intact consolidated granular media or samples with closed micro cracks [11] to  $b = 3$  for highly damaged media [12]. Furthermore, the exponent  $b$  generally increases when increasing damage within the investigated samples, assuming intermediate (not necessary integer) values, always in the interval  $1 \leq b \leq 3$  [13].

From the theoretical point of view, the physical origin of mesoscopic nonlinearity is still unclear. Since it is manifested by materials with very different properties, it is difficult to link its origin to a single mechanism. In damaged metals, dislocations are generating nonlinearity [14]. However, no dislocations are shown in rocks, where adhesion mechanisms are present at the interface between grains [15]. Also, the presence of fluids could be relevant [16]. In the case of open cracks, clapping often occurs [17].

As a consequence, phenomenological models are usually introduced. They are discrete models and have the advantage to allow the implementation of non analytical features, such as hysteresis or threshold activated mechanisms. As we will show here, a link exists between the microscopic equation of state (EOS), related to any of the mechanisms discussed above, and the exponent  $b$  describing the behavior of the macroscopic nonlinear indicator [18].

In this thesis, we take advantage of both experimental observations and theoretical predictions, to propose an approach for tracing the microscopic features which might be behind the value of the exponent  $b$  determined from macroscopic measurements. To this purpose, we propose a multi scale multi state modeling approach based on the Preisach-Mayergoyz statistical distribution. This approach allows the description of the behavior of heterogeneities at different scales which afterward could be used to build the macroscopic measurements.

---

The thesis is organized as follows.

In the **first Chapter**, we discuss the transition from linear to nonlinear elasticity and we show the theoretical and experimental background which are the basis for the development of a theory of Nonlinear Mesoscopic Elastic materials. We briefly give an overview of the classical linear theory of Landau. Several applications of linear elasticity in NDT, be it in materials characterization or in structures inspection, have been developed. However, the linear approximation of the wave equation is not sufficient to detect microscopic imperfections because of their small size in comparison to the acoustic wavelengths, which makes linear methods insensitive to early damage in materials. As an alternative, the classical nonlinear theory considers higher order terms in approximating the Taylor expansion of stress as a function of strain. This results in a nonlinear term in the equation of propagation, leading to some amplitude dependent nonlinear features like generation of harmonics and resonance frequency shift. Nonlinear NDT exploits the amplitude dependence of such phenomena to evaluate the amount of nonlinearity in materials presenting geometrical nonlinearity at the atomistic scale level.

Besides the classical nonlinear theory which finds its origin in the geometrical anharmonicity of the atomic lattice, we include a section on an emergent type of nonlinearity which have been first observed in rocks, and later in all micro inhomogeneous materials like concrete, composites and micro-damaged elastic materials. We present some experimental observations on their nonlinear behavior which should be described by a non classical multivalued nonlinear EOS as required by the hysteretic dependence in the quasi static stress-strain relation. Nonlinearity, conditioning and relaxation should also be taken into account as reported in literature for such materials.

It is difficult, to find a general analytical formulation which takes into account the multivalued character of the EOS. Therefore, usually discrete models are used to understand nonlinear mesoscopic elasticity. In **Chapter II**, we briefly recall some of the theoretical descriptions proposed in the literature. Models based on physical mechanisms are first introduced and then we describe the Preisach-Mayergoyz (PM) formalism introduced in elasticity by R.A.Guyer and coworkers.

In the same chapter, we also propose the generalization of the PM space formalism to a multi-scale statistical description which, considering the possibility of implementation of different mechanisms at the microscopic level, seems to be the best approach to model the nonlinear elasticity specific to materials containing structural features like cracks, grain boundaries, and contacts of typical size of some micrometers. In the last Section of Chapter II, we describe in details the microscopic EOS corresponding to hysteresis, adhesion and clapping. The three models are at the basis of the numerical analysis reported in the thesis [19].

In **Chapter III**, we introduce the definition of the nonlinear indicators usually measured in experiments reported in the literature. We also present some experimental data making in evidence some major problems usually met in experiments. In particular, we show how the power law behavior is valid only in a limited range of excitation amplitudes. Effects of noise and saturation might indeed affect the estimation of the power law coefficient  $a$  and exponent  $b$ . Using numerical data we show how noise effects could be estimated and we propose a



---

methodology to define a threshold for the correct determination of acoustic nonlinearity. Both equipment and environmental noises are considered in the analysis [20].

Furthermore, the experimental data collected in the framework of the thesis, indicate that the measured nonlinearity is not independent from the experimental configuration adopted. A numerical analysis show how it is possible to correct part of the dependency of the nonlinear indicator on the configuration considering the resonance structure of the specimen. However, this is not always feasible. Nevertheless, we also show that the exponent  $b$  of the power law analysis does not depend on the experimental set-up, thus providing an absolute information about the nature of the nonlinearity [21].

Furthermore, signal processing issues might affect the correct determination of the power law behavior. For a given method of analysis, a not accurate choice of the signal processing parameters can lead to a wrong estimation of nonlinearity. In the last part of the Chapter III, we analyze the importance of the choice of the low amplitude signal used to build the SSM signal.

The power law exponent  $b$  was thus proved to be an absolute indicator of nonlinearity. In **Chapter IV** we first show how nonlinear mesoscopic materials could be classified in classes according to the value of the power law exponent in their elastic response. Depending on the presence of open cracks in the sample, the exponent ranges from 1 to 3, as shown by classifying data present in the literature.

The main work of the thesis concerns the use of the multi-state models we have developed and described in Chapter II to define classes of models characterized by the same exponent  $b$ . In particular, we start by considering that, in the approach proposed here, models differ in the number of possible states for the microscopic elements upon which the model is built. Furthermore, the statistical distribution of the properties of the microscopic elements could be characterized by different choices and constraints for the values of the control variable at which transitions between states occur. On this basis, we show that the classification of models could be done considering different features: the properties of the microscopic equation of state, described by the number of states used in the model [19]; the properties of the statistical distribution of the properties of the microscopic features; the constraints on the values of the transition parameters between different states [22]. We show that, for a given model, the exponent  $b$  can be predicted a priori without any knowledge about the model parameters (e.g. the values of the elastic constants for each state).

We finally propose an application to analyze some experimental results obtained on a concrete sample subject to quasi-static loading at increasing levels of the load. The exponent  $b$  measured from the experiment increases continuously from 1 to 3 as a function of damage progression. The changes in the exponent could be related to the eventual evolution of its micro structure from that of a consolidated granular medium to that of a micro cracked (with closed cracks) and later of a macro cracked (with open cracks) medium. To fit experimental data, we propose a model mixing clapping and hysteretic mechanisms.

Finally, in **Chapter V** we investigate the effect of nonlinearity activation due to conditioning, which is manifested by strongly damaged media. Preliminary results seem to indicate the possibility to describe the effect using the same approaches developed in the previous Chapter.



---

In particular, it will be shown how a purely hysteretic model predicts a decrease of nonlinearity after conditioning (possibly in agreement with observations in rocks), while adhesion and dislocations model might predict an increase of the nonlinear response in a conditioned sample. Numerical results are compared with experimental observations. Results reported in the Chapter are preliminary for a more complete study [\[23\]](#).

---

## References

- [1] R. A. Guyer and P. A. Johnson. Nonlinear mesoscopic elasticity: Evidence for a new class of materials. *Phys. Today*, 52:3, 1999. [xv](#)
- [2] B. Zinszner, P. A. Johnson, and P. N. J. Rasolofosaon. Influence of change in physical state on elastic nonlinear response in rock: Significance of effective pressure and water saturation. *J. Geoph. Res.*, 102:8105–8120, 1997. [xv](#)
- [3] K. Van Den Abeele, J. Carmeliet, J. Tencate, and P. A. Johnson. Nonlinear elastic wave spectroscopy (NEWS) techniques to discern material damage, part II: Single-mode nonlinear resonance acoustic spectroscopy. *Res. Nondestr. Eval.*, 12:31–42, 2000. [xv](#)
- [4] M. Bentahar, H. El. Agra, R. El Guerjouma, M. Griffa, and M. Scalerandi. Hysteretic elasticity in damaged concrete: quantitative analysis of slow and fast dynamics. *Phy. Rev. B*, 73:014116, 2006. [xv](#)
- [5] J. Tencate et al. Nonlinear and nonequilibrium dynamics in geomaterials. *Phys.Rev.Lett.*, 93:065501, 2004. [xv](#)
- [6] P. A. Johnson and A. Sutin. Slow dynamics and anomalous nonlinear fast dynamics in diverse solids. *J. Acoust. Soc. Am.*, 117:124–130, 2005. [xv](#)
- [7] V. Aleshin and K. Van Den Abeele. Microcontact-based theory for acoustics in microdamaged materials. *J. Mech. Phys. Solids*, 55:765–787, 2007. [xv](#)
- [8] T. W. Darling, J. A. Tencate, and S. Sven et al. Localizing nonclassical nonlinearity in geological materials with neutron scattering experiments. volume 838, pages 12–19, 2006. [xvi](#)
- [9] K. Van Den Abeele, P. A. Johnson, and A. Sutin. Nonlinear elastic wave spectroscopy (NEWS) techniques to discern material damage, part I: Nonlinear wave modulation spectroscopy(NWMS). *Res.Nondestruct. Eval.*, 12:17, 2000. [xvi](#)

- 
- [10] C. L. E. Bruno, A. S. Gliozzi, M. Scalerandi, and P. Antonaci. Analysis of elastic nonlinearity using the scaling subtraction method. *Phys. Rev. B*, 79:064108, 2009. [xvi](#)
  - [11] G. Renaud, P. Y. Le Bas, and P. A. Johnson. Revealing highly complex elastic nonlinear (anelastic) behavior of earth materials applying a new probe: dynamic acoustoelastic testing. *J. Geoph. Res.-Solid Earth.*, 117:B06202, 2012. [xvi](#)
  - [12] P. Antonaci, C. L. E. Bruno, P. G. Bocca, M. Scalerandi, and A. S. Gliozzi. Nonlinear ultrasonic evaluation of load effects on discontinuities in concrete. *Cement and Concrete Research.*, 40:340–346, 2010. [xvi](#)
  - [13] M. Scalerandi, M. Griffa, P. Antonaci, M. Wyrzykowski, and P. Lura. Nonlinear elastic response of thermally damaged consolidated granular media. *J. Appl. Phys.*, 113:154902, 2013. [xvi](#)
  - [14] A. Granato and K. Lucke. Theory of mechanical damping due to dislocations. *J. Appl. Phys.*, 27:583, 1956. [xvi](#)
  - [15] V. Gusev and N. Chigarev. Nonlinear elastic response of thermally damaged consolidated granular media. *J. Appl. Phys.*, 107:124905, 2010. [xvi](#)
  - [16] B. Capogrosso and R. A. Guyer. Dynamic model of hysteretic elastic systems. *Phys. Rev. B*, 66:224101, 2002. [xvi](#)
  - [17] S. Delrue and K. Van Den Abeele. Three-dimensional finite element simulation of closed delaminations in composite materials. *Ultrasonics*, 52:315–324, 2012. [xvi](#)
  - [18] K. R. McCall and R. A. Guyer. Equation of state and wave propagation in hysteretic nonlinear elastic material. *J. Geoph. Res. Solid Earth*, 94:23887–23897, 1994. [xvi](#)
  - [19] M. Scalerandi, S. Idjmarene, M. Bentahar, and R. El Guerjouma. Evidence of evolution of microstructure in solid elastic media based on a power law analysis. *submitted to Physical Review E*, 2013. [xvii](#), [xviii](#)
  - [20] M. Bentahar, R. El Guerjouma, S. Idjmarene, and M. Scalerandi. Influence of noise on the threshold for detection of elastic nonlinearity. *Journal of Applied Physics*, 113:043516, 2013. [xviii](#)
  - [21] S. Idjmarene, M. Bentahar, R. El Guerjouma, and M. Scalerandi. Effects of experimental configuration on the detection threshold of hysteretic elastic non linearity. *Ultrasonics*, In press. [xviii](#)
  - [22] M. Scalerandi, A. S. Gliozzi, and S. Idjmarene. Power laws behavior in multi-state elastic models with different constraints in the statistical distribution of elements. *submitted to Communications in Nonlinear Science and Numerical Modelling*, October 2013. [xviii](#)
  - [23] S. Idjmarene, M. Scalerandi, M. Bentahar, and R. El Guerjouma. Modelling nonlinearity activation due to conditioning induced by dislocation dynamics. *Ultrasonics*, to be submitted. [xix](#)

---

---

# Chapter I

---

## Elasticity and acoustic wave propagation in solids: from classical theory to Nonlinear Mesoscopic Elasticity (NME)

### 1 Introduction

Acoustic Non Destructive Testing (NDT), whose goal is to evaluate the 'health state' of materials, is based on the interaction between an acoustic propagating wave and defects which might be present in the structure to inspect.

Being the first approaches developed and based on the classical linear theory of Landau, linear NDT methods exploit this interaction in terms of impedance contrast at the interface between the propagation medium and the defected zone. Such methods generally use either transmitted or reflected waves to evaluate the attenuation or the velocity of an acoustic propagating wave. This makes it possible to trace eventual defects in the medium like flaws, cracks and void. However, sensitivity of this kind of characterization depends on the size of imperfections which are detectable only if their dimensions are comparable to the acoustic wavelengths normally used in NDT.

Actually, microscopic imperfections are by far the most frequent source of fracture process in materials but since their size is considerably shorter than the acoustic wavelengths, linear acoustic characterization seems to be unable to detect any microscopic degradation of the material's integrity.

To avoid the limits of linear methods, nonlinear acoustic NDT has been introduced, based on the classical nonlinear theory of Landau. The resulting approaches work well when applied to materials presenting geometrical imperfections at the atomistic scale level, such as crystalline solids. These materials display, as described in literature, a nonlinear behavior manifested by the amplitude dependence of some of their parameters, such as the elastic modulus and wave velocity. Classical nonlinear methods based on the amplitude dependence of material parameters like the Nonlinear Elastic Wave Spectroscopy NEWS[1] and the Scaling subtraction Method SSM [2] have been developed to quantify the amount of classical nonlinearity, considered as intrinsic to the material.

Recent experiments on rocks, concrete, composites and micro-damaged elastic materials have proved the evidence for a new class of materials with a specific interest in NDT [3]. These

media are characterized by the brick-mortar structure: they are often composed of an assembly of mesoscopic sized grains of microscopically uniform material (the bricks) which are separated from each other by an elastically different system (the mortar). We speak about materials that are inhomogeneous on a scale which is small compared to the sample size and large compared to the microscopic length scale ( $l_{meso} = 10\mu m - 100\mu m$ ). Thus they are simply termed Nonlinear Mesoscopic Elastic (NME) materials.

Besides the classical nonlinear theory which finds its origin in the geometrical anharmonicity of the atomic lattice, NME materials exhibit unusual nonlinear behavior. They are extremely nonlinear at modest quasi-static stress, show hysteresis and memory in quasi static stress-strain protocols [4], have resonance frequency shift [5–7], nonlinear attenuation and harmonics generation [8] properties in dynamic measurements that are beyond the possible explanations using the classical model of nonlinear elasticity and recover from transient disturbances logarithmically in time [9].

In this chapter, we provide a brief overview of the theory of linear elasticity and wave propagation in solids. We will also discuss the main experimental observations which render necessary the introduction of non classical elastic models, which are discussed in the next Chapter

## 2 Classical theory of wave propagation in solids

Let us consider, for simplicity, an isotropic body on which we apply a small mechanical perturbation leading the particles to move from their equilibrium position. Internal elastic forces  $\sigma_{ij}$  are consequently generated to bring back the particles to the equilibrium position. As a result, particles oscillate with displacement  $u(t)$  around their equilibrium position. The classical Landau theory allows to derive the propagation equation and the expression of the elastic modulus.

In the approximation of small deformations, the free energy of an elastic system can be expanded as a power series with respect to the strain tensor. The general expression for the free energy of an isotropic body in the third approximation can be reduced by the convention of Eistein notation to

$$F = f_0 + C_{ijkl}\epsilon_{ij}\epsilon_{kl} + C_{ijklmn}\epsilon_{ij}\epsilon_{kl}\epsilon_{mn}. \quad (I.1)$$

Where  $f_0$  is constant and  $C_{ijkl}$ ,  $C_{ijklmn}$  are respectively the second and third order elastic tensors.

### 2.1 Classical linear theory

For very small strain amplitudes, the cubic term in the elastic energy (see Eq. I.1) can be neglected and the free energy expression reduces to

$$F = f_0 + C_{ijkl}\epsilon_{ij}\epsilon_{kl}. \quad (I.2)$$

## I.2 Classical theory of wave propagation in solids

---

In the specific case of isotropic materials, the expression could be further reduced as

$$F = f_0 + \mu \epsilon_{ij}^2 + \frac{1}{2} \lambda \epsilon_{ii}^2 \quad (\text{I.3})$$

where  $\lambda$  and  $\mu$  are the Lamé coefficients.

For infinitesimal deformations of a continuum body, in which the displacements gradient is small compared to unity, it is possible to perform a geometric linearisation of the Eulerian finite strain tensor where second-order terms of the finite strain tensor are neglected [10]. Thus

$$\epsilon_{ij} = \frac{1}{2} \left( \frac{\partial u_i}{\partial x_j} + \frac{\partial u_j}{\partial x_i} \right) \quad (\text{I.4})$$

is the  $ij$  component of the infinitesimal strain tensor and  $u_i$  is the  $i^{th}$  component of the displacement vector.

Components of the stress tensor  $\sigma_{ij}$  are defined as the first derivative of the free energy with respect to the corresponding strain component whereas the second order derivative provides the expression of the elastic moduli  $K_{ijkl}$ .

$$\sigma_{ij} = \frac{\partial F}{\partial \epsilon_{ij}} = 2\mu \epsilon_{ij} + \lambda \epsilon_{ii} \delta_{ij} \quad (\text{I.5})$$

The elastic constants of the medium are consequently given as

$$\begin{aligned} K_{ijij} &= \frac{\partial \sigma_{ij}}{\partial \epsilon_{ij}} = 2\mu + \lambda \delta_{ij} \\ K_{ijkl} &= \frac{\partial \sigma_{ij}}{\partial \epsilon_{kl}} = 2\mu \end{aligned} \quad (\text{I.6})$$

The equation of motion for the displacement field is

$$\rho \frac{\partial^2 u_i}{\partial t^2} = \frac{\partial \sigma_{ij}}{\partial x_j} \quad (\text{I.7})$$

Substituting in the free energy the strain expressed as a function of the displacement field (Eq. I.4), we find the expression for  $\sigma_{ij}$

$$\sigma_{ij} = \mu \left( \frac{\partial u_i}{\partial x_j} + \frac{\partial u_j}{\partial x_i} \right) + \lambda \frac{\partial u_i}{\partial x_j} \delta_{ij} \quad (\text{I.8})$$

Substituting into the equation of motion I.7, we obtain a partial differential equation for the displacement field:

$$\rho \frac{\partial^2 u_i}{\partial t^2} = \mu \frac{\partial^2 u_i}{\partial x_j^2} + \mu \frac{\partial^2 u_j}{\partial x_i \partial x_j} + \lambda \frac{\partial^2 u_i}{\partial x_j^2} \delta_{ij} \quad (\text{I.9})$$

## I.2 Classical theory of wave propagation in solids

---

In the case of plane waves, we have two limit cases.

If  $\frac{\partial u_i}{\partial x_j} = 0$  when  $i \neq j$ , we have the wave equation for longitudinal waves

$$\rho \frac{\partial^2 u_i}{\partial t^2} = (2\mu + \lambda) \frac{\partial^2 u_i}{\partial x_i^2} \quad (\text{I.10})$$

$$\frac{\partial^2 u_i}{\partial x_i^2} - \frac{1}{C_l^2} \frac{\partial^2 u_i}{\partial t^2} = 0 \quad (\text{I.11})$$

Here  $C_l^2 = \frac{\lambda+2\mu}{\rho}$  is the longitudinal wave velocity.

If  $\frac{\partial u_i}{\partial x_j} = 0$  when  $i = j$ , we have the wave equation for shear waves

$$\rho \frac{\partial^2 u_i}{\partial t^2} = \mu \frac{\partial^2 u_i}{\partial x_j^2} + \mu \frac{\partial^2 u_j}{\partial x_i \partial x_j} \quad (\text{I.12})$$

In the following of the thesis we will be mostly interested in the 1-D approximation, in which

$$\frac{\partial u_j}{\partial x_i} = 0 \quad i = 2, 3; j \neq i$$

As a result we obtain a propagation velocity  $C_l^2 = \frac{K}{\rho}$ , where  $K = \lambda + 2\mu$  and

$$\frac{\partial^2 u}{\partial x^2} - \frac{1}{C_l^2} \frac{\partial^2 u}{\partial t^2} = 0 \quad (\text{I.13})$$

In the case of wave propagation in a finite medium of length  $L$ , the following considerations could be drawn:

- Depending on the boundary conditions, the resonance frequencies  $\omega_r$  of the sample could be calculated. They correspond to the frequencies of the forcing disturbance applied to the sample generating a maximum displacement;
- If a monochromatic forcing is assumed, i.e. the mechanical disturbance is at frequency  $\omega$ , the response generated in the sample is a displacement with the same frequency as the forcing, plus the frequencies corresponding to the resonance structure of the sample. In other words, no multiple harmonics of the forcing are generated;
- Attenuation could be introduced in the model. Several approaches could be followed, depending whether the attenuation coefficient is or not frequency dependent. In most cases, an attenuative term proportional to the particles velocity ( $\partial u / \partial t$ ) is sufficient.

## 2.2 Classical nonlinear theory

At larger but still infinitesimal strains, the contribution of the third order elastic term in the free energy expansion of Eq. 1.1 can no more be neglected. Thus the general expression for an isotropic medium is the following

$$F = f_0 + \mu \epsilon_{ij}^2 + \frac{1}{2} \lambda \epsilon_{ii}^2 + \frac{1}{3} A \epsilon_{ij} \epsilon_{ik} \epsilon_{kl} + B \epsilon_{ij}^2 \epsilon_{ii} + \frac{1}{3} C \epsilon_{ii}^3 \quad (\text{I.14})$$

## I.2 Classical theory of wave propagation in solids

---

where  $A, B$  and  $C$  are the components of the second order elastic tensor for isotropic bodies.

Consequently, the components of the stress tensor, obtained deriving the free energy with respect to strain, are given by

$$\sigma_{ij} = \frac{\partial F}{\partial \epsilon_{ij}} = 2\mu\epsilon_{ij} + \lambda\epsilon_{ii}\delta_{ij} + \frac{1}{3}A\epsilon_{jk}\epsilon_{kl} + 2B\epsilon_{ij}\epsilon_{ii} + B\epsilon_{ii}^2\delta_{ij} + C\epsilon_{ii}^2\delta_{ij} \quad (\text{I.15})$$

Since strains are still infinitesimal, the corresponding elastic constants of the medium are given by

$$K_{ijkl} = \frac{\partial \sigma_{ij}}{\partial \epsilon_{kl}}. \quad (\text{I.16})$$

In the 1-D case, only one component is not zero. Thus this equation reduces to the compressional stress  $\sigma$

$$\sigma = (2\mu + \lambda)\epsilon + \left(\frac{1}{3}A + 3B + C\right)\epsilon^2. \quad (\text{I.17})$$

The elastic modulus reduces to

$$K = \frac{\partial \sigma}{\partial \epsilon} = (2\mu + \lambda) + \left(\frac{1}{3}A + 3B + C\right)\epsilon = K_0(1 + \beta\epsilon) \quad (\text{I.18})$$

where  $K_0$  is, in this case, the young modulus and  $\beta = \frac{\frac{1}{3}A + 3B + C}{2\mu + \lambda}$  is the quadratic nonlinear coefficient for longitudinal waves in isotropic media.

Notice that, if we further develop to the fourth order the expansion of the free energy, we obtain higher order terms of the elastic modulus expressed as a function of the strain field:

$$K = K_0(1 + \beta\epsilon + \delta\epsilon^2 + \dots) \quad (\text{I.19})$$

where

$$\delta = \frac{3l + 2m}{2\lambda + 2\mu} \quad (\text{I.20})$$

is the cubic nonlinear coefficient expressed as a function of the components of the first and third order elastic tensors ( $l$  and  $m$  are constants of Murnaghan).

In the 3-D case, the equation of motion for the displacement field is

$$\rho \frac{\partial^2 u_i}{\partial t^2} = \frac{\partial \sigma_{ij}}{\partial x_j} \quad (\text{I.21})$$

Using the strain expression previously derived, we obtain the expression of  $\sigma_{ij}$  as



$$\begin{aligned}
\sigma_{ij} = & \mu \left( \frac{\partial u_i}{\partial x_j} + \frac{\partial u_j}{\partial x_i} \right) + \lambda \frac{\partial u_i}{\partial x_i} \delta_{ij} + \frac{1}{4} A \frac{\partial u_k}{\partial x_i} \frac{\partial u_k}{\partial x_j} + \\
& + \frac{1}{2} B \left[ 2 \frac{\partial u_i}{\partial x_i} \frac{\partial u_i}{\partial x_j} + \left( \frac{\partial u_i}{\partial x_j} \right)^2 \delta_{ij} \right] + \frac{1}{12} A \frac{\partial u_j}{\partial x_k} \frac{\partial u_k}{\partial x_i} + \\
& + \frac{1}{2} B \left[ \frac{\partial u_j}{\partial x_i} \frac{\partial u_i}{\partial x_i} + 2 \left( \frac{\partial u_i}{\partial x_j} \right) \delta_{ij} \right] + C \left( \frac{\partial u_i}{\partial x_i} \right)^2.
\end{aligned} \tag{I.22}$$

We finally write the equation of motion in the nonlinear case

$$\rho \frac{\partial^2 u_i}{\partial t^2} = \mu \frac{\partial^2 u_i}{\partial x_j^2} + \mu \frac{\partial u_j}{\partial x_i} \frac{\partial u_i}{\partial x_j} + \lambda \frac{\partial^2 u_i}{\partial x_i \partial x_j} \delta_{ij} + f_i \tag{I.23}$$

where  $f_i$  contains all second order terms of the gradient displacement field.

$$\mu \frac{\partial^2 u_i}{\partial x_j^2} + \mu \frac{\partial u_j}{\partial x_i} \frac{\partial u_i}{\partial x_j} + \lambda \frac{\partial^2 u_i}{\partial x_i \partial x_j} \delta_{ij} - \rho \frac{\partial^2 u_i}{\partial t^2} = -f_i \tag{I.24}$$

When we have a longitudinal plane wave (i.e.  $\partial u_i / \partial x_j = 0$  when  $i \neq j$ ), we end up with

$$(2\mu + \lambda) \frac{\partial^2 u_i}{\partial x^2} - \rho \frac{\partial^2 u_i}{\partial t^2} = -f_i \tag{I.25}$$

In the 1-D case, the equation of motion becomes

$$\frac{\partial^2 u}{\partial x^2} - \frac{1}{C_l^2} \frac{\partial^2 u}{\partial t^2} = -2\beta \frac{\partial^2 u}{\partial x^2} \frac{\partial u}{\partial x} \tag{I.26}$$

## 2.3 Effects of nonlinear terms in the wave equation

In materials exhibiting classical nonlinearity, two main effects are usually observed in the literature. The first is the generation of higher order harmonics (or sidebands), i.e. for a given frequency of the source function, the response of the system is a time function which contains other frequencies as well. The second effect is a shift of the sample's resonance frequency, which always corresponds to softening. As we will show here, the indications from classical nonlinear elasticity are that third harmonics are generated with amplitude proportional to the cube of the amplitude of the fundamental and that the shift of the resonance frequency is proportional to the square of the strain amplitude.

### 2.3.1 Harmonics and sidebands generation

The cubic terms in the free energy give quadratic terms in the stress field and in the equation of motion as well. We limit our study here to the 1-D case, using Eq. 1.26

Solving the equation by the method of successive approximations, we first omit the quadratic terms:

$$\frac{\partial^2 u}{\partial x^2} - \frac{1}{C_l^2} \frac{\partial^2 u}{\partial t^2} = 0 \quad (\text{I.27})$$

This is the ordinary linear equation, whose solution  $u_0(x, t)$  could be put in the form of a superposition of monochromatic traveling waves of frequencies  $w_n$  and amplitudes  $C_n$ :

$$u_0 = \sum_n C_n e^{i(w_n t - k_n x)} + \sum_n C_n e^{i(w_n t + k_n x)} \quad (\text{I.28})$$

Going to the second order approximation, we look for a solution in the form

$$u(x, t) = u_0(x, t) + u_1(x, t)$$

Substituting in Eq. 1.26 and omitting higher order terms in  $u_1(t)$  we obtain

$$\frac{\partial^2 u_0}{\partial x^2} + \frac{\partial^2 u_1}{\partial x^2} - \frac{1}{C_l^2} \frac{\partial^2 u_0}{\partial t^2} - \frac{1}{C_l^2} \frac{\partial^2 u_1}{\partial t^2} = -2\beta \frac{\partial^2 u_0}{\partial x^2} \frac{\partial u_0}{\partial x} \quad (\text{I.29})$$

Linear terms in  $u_0$  will disappear since  $u_0$ , by definition, satisfies the homogeneous linear equation. The result is an inhomogeneous linear equation for the first order correction  $u_1(x, t)$ , where the right-hand side contains only known functions.

In the particular case in which the source function is the superposition of two monochromatic waves, i.e. two sine functions, with frequencies  $w_1$  and  $w_2$ , we have  $u_0(x, t) = C_1 e^{i(w_1 t - k_1 x)} + C_1 e^{i(w_1 t + k_1 x)} + C_2 e^{i(w_2 t - k_2 x)} + C_2 e^{i(w_2 t + k_2 x)}$ . To determine the first order correction, we have to solve the equation

$$\frac{\partial^2 u_1}{\partial x^2} - \frac{1}{C_l^2} \frac{\partial^2 u_1}{\partial t^2} = -2\beta \frac{\partial^2 u_0}{\partial x^2} \frac{\partial u_0}{\partial x} \quad (\text{I.30})$$

Substituting the first order solution  $u_0$  we obtain:

$$\begin{aligned} \frac{\partial^2 u_1}{\partial x^2} - \frac{1}{C_l^2} \left( \frac{\partial^2 u_1}{\partial t^2} \right) = -2\beta \left[ -ik_1^3 C_1^2 e^{-i(2w_1 t - 2k_1 x)} + ik_1^3 C_1^2 e^{-i(2w_1 t + 2k_1 x)} - ik_2^3 C_2^2 e^{-i(2w_2 t - 2k_2 x)} \right. \\ \left. + ik_2^3 C_2^2 e^{-i(2w_2 t + 2k_2 x)} + iC_1 C_2 (k_2 k_1^2 + k_1 k_2^2) e^{-i(w_2 + w_1)t - (k_1 + k_2)x} + iC_1 C_2 (k_2 k_1^2 + k_1 k_2^2) e^{-i(w_2 - w_1)t - (k_1 - k_2)x} \right] \end{aligned}$$

A particular integral of a linear equation of this type is a sum of terms containing similar exponential factors to those in the free term (the right-hand side) of the equations. Each of them correspond to a traveling wave of frequencies  $w_1 \pm w_2$ ,  $2w_1$  and  $2w_2$  with amplitudes proportional to the distance of propagation and to the square of the injected frequencies amplitudes. In particular, it can be easily verified that the general solution is in the form

## I.2 Classical theory of wave propagation in solids

---

$$\begin{aligned}
 u(x, t) &= u_0(x, t) + u_1(x, t) \\
 &= C_1 e^{i(w_1 t - k_1 x)} + C_2 e^{i(w_2 t - k_2 x)} + \beta \frac{x}{2} \left[ k_1^2 C_1^2 e^{i(2w_1 t - 2k_1 x)} \right. \\
 &\quad \left. + k_2^2 C_2^2 e^{i(2w_2 t - 2k_2 x)} - 2ik_2 k_1 C_1 C_2 e^{i(2(w_1 + w_2)t - 2(k_1 + k_2)x)} - 2ik_2 k_1 C_1 C_2 e^{i(2(w_1 - w_2)t - 2(k_1 - k_2)x)} \right]
 \end{aligned} \tag{I.32}$$

Terms in the solution have a specific meaning. The waves with double frequencies, i.e. with  $2w_1$  and  $2w_2$  are termed second harmonics. They are both proportional to the square of the amplitude of the corresponding frequency, being  $\beta$  the proportionality coefficient. Terms with frequency  $w_1 \pm w_2$  are termed sidebands and their amplitude is proportional to the product of the amplitudes of the corresponding frequencies.

It is to be noted that, when the source function is a pure monochromatic wave with frequency  $w$  ( $C_1 = C_I$  and  $C_2 = 0$ ), the solution contains only two terms:

$$u(x, t) = C_I e^{i(wt - kx)} + C_{II} e^{i(2wt - 2kx)} \tag{I.33}$$

It follows that the nonlinear coefficient  $\beta$  could be measured in experiments by measuring the ratio between the second harmonic amplitude and the square of the fundamental amplitude, using

$$C_{II} = \beta \frac{x}{2} k^2 C_I^2 \tag{I.34}$$

where  $x$  is the propagation distance.

Before concluding the argument, we remark that this method of solution is valid as long as the energy transferred from frequencies  $w_1$  and  $w_2$  to their harmonics and sidebands is a small fraction of the total energy. Eventually, the equation should be solved to higher order terms  $u(x, t) = u_0(x, t) + u_1(x, t) + u_2(x, t) + u_3(x, t) + \dots$ , leading to the appearance of third order harmonics and other terms in the solution, which are proportional to the cube of the amplitude of injected frequencies.

Of course, a complete analysis would require also to consider higher order terms in the expansion of the free energy, i.e. introducing the nonlinear coefficient  $\delta$ . In this case, the solution could be extremely complex. In any case, it will be possible to derive  $\delta$  from the proportionality between the amplitude of the third order harmonics and the cube of the amplitude of the fundamental, similar to Eq. I.34.

### 2.3.2 Resonance frequency shift

The same nonlinear equation of motion established in the case of longitudinal waves can be written in the following manner

$$\frac{\partial^2 u}{\partial t^2} = C_l^2 \left[ \frac{\partial^2 u}{\partial x^2} + 2\beta \frac{\partial^2 u}{\partial x^2} \frac{\partial u}{\partial x} \right] = C_l^2 \frac{\partial^2 u}{\partial x^2} \left[ 1 + 2\beta \frac{\partial u}{\partial x} \right] = C^2 \frac{\partial^2 u}{\partial x^2} \tag{I.35}$$

## I.2 Classical theory of wave propagation in solids

---

where

$$C^2 = C_l^2 \left[ 1 + \beta \frac{\partial u}{\partial x} \right] \quad (\text{I.36})$$

Here  $C_l$  is the linear longitudinal wave speed and  $C$  the wave speed in the nonlinear medium.

If we consider higher order terms in the free energy expansion

$$C^2 = C_l^2 \left[ 1 + 2\beta \frac{\partial u}{\partial x} + 3\delta \left( \frac{\partial u}{\partial x} \right)^2 + \dots \right] \quad (\text{I.37})$$

In both cases, the wave velocity  $C$  is strain amplitude dependent. Thus any change in the strain amplitude in time will affect the propagation velocity in the medium, as a consequence of the change in the elastic modulus.

The same dependence on strain could be observed and measured for the resonance frequency  $\omega_r$  which is proportional to the velocity (in the hypothesis of non dispersive medium of course). We can thus say that, defining  $\omega_l$  the resonance frequency in the linear limit, we have

$$C^2 - C_l^2 = C_l^2 \left[ \beta \frac{\partial u}{\partial x} + 3\delta \left( \frac{\partial u}{\partial x} \right)^2 + \dots \right] \quad (\text{I.38})$$

$$\frac{C^2 - C_l^2}{C_l^2} = \beta \epsilon + \delta \epsilon^2 \quad (\text{I.39})$$

$$\frac{C^2 - C_l^2}{C_l^2} \propto \frac{\omega_r^2 - \omega_l^2}{\omega_l^2} \propto \left( \frac{\omega_r + \omega_l}{\omega_l} \right) \left( \frac{\omega_r - \omega_l}{\omega_l} \right) \propto 2 \frac{\omega_r - \omega_l}{\omega_l} \quad (\text{I.40})$$

The strain dependence of velocity is resulting in a shift of the resonance frequency when strain amplitude (consequently applied stress) increases.

As a result of the calculation, the relation between the resonance frequency shift and the strain amplitude is

$$\left\langle \frac{\omega_r - \omega_l}{\omega_l} \right\rangle \propto \beta \langle \epsilon(t) \rangle + \delta \langle \epsilon^2(t) \rangle \quad (\text{I.41})$$

Being the strain average (considered as a sinusoidal function) over one period of excitation equal to zero, the term proportional to  $\beta$  doesn't contribute to the shift of the resonance peak. This shift is due to only the higher order expansion term  $\delta \langle \epsilon^2(t) \rangle = \delta \frac{1}{2} \epsilon_{max}^2$ . Here  $\epsilon_{max}^2$  is the maximum strain amplitude.

It follows that we can write the resonance frequency shift as a function of strain in the form

$$\frac{\omega_r - \omega_l}{\omega_l} \propto \frac{1}{2} \delta \epsilon_{max}^2 \quad (\text{I.42})$$

As already mentioned, this result is the second consequence of the presence of classical non-linearity in the medium and it is in agreement with what have been experimentally observed in resonance experiments for several materials (with a negative coefficient  $\delta$ ) : *theresonancepeakshiftstolow* with  $b = 2$ .

### 3 Non classical nonlinear wave propagation in solids

The theory discussed in the previous Section is adequate to describe nonlinearity only in a given class of materials, mostly intact metals. On the contrary, it is not sufficient to describe the nonlinear behavior observed in rocks, concrete, cracked metals or composites etc., which belong to the class of Nonlinear Mesoscopic Elastic materials. In this cases, several experimental observations reported in the literature are contradicting the expectations from the Landau theory, as it will be discussed in the following.

#### 3.1 Quasi-static behavior

First observations of nonclassical nonlinearity in solids come from quasi static stress-strain experiments [11, 12]. A typical result is shown in Fig. I.1 in the case of a sandstone sample [13]. The curve presents the dependence of stress on strain (subplot (b)) when a given axial stress protocol (subplot(a)) is applied to the sample. The applied stress is varied very slowly to ensure quasi-static (equilibrium) conditions at each strain and the resulting plot shows that sandstone is nonlinear and presents hysteresis and discrete memory [13].

**Figure I.1** – (a) Axial stress protocol for the quasi-static stress-strain experiment; (b) Stress-strain experimental result corresponding to the protocol shown in (a) for a sandstone [13].

Of course, such a relation between stress and strain could not be predicted within the classical Landau theory. In particular, one needs to include an additional term into the definition of the stress, taking into account the stress dependence on the strain rate and on its sign.

### I.3 Non classical nonlinear wave propagation in solids

---

Introducing hysteresis, Van Den Abeele et al.[14] wrote the following equation of motion:

$$\frac{\partial^2 u}{\partial t^2} = C_0^2 \frac{\partial^2 u}{\partial x^2} \left( 1 + \beta \frac{\partial u}{\partial x} + \delta \left( \frac{\partial u}{\partial x} \right)^2 + \dots \right) + H \left[ \epsilon, \text{sign} \left( \frac{\partial \epsilon}{\partial t} \right) \right] \quad (\text{I.43})$$

Here  $H$  is a function describing hysteretic nonlinearity and  $\partial \epsilon / \partial t$  is the strain rate. It is to be noted that this function should depend not only on the strain rate, but also on the strain history. An analytic expression of the  $H$  function is still missing, but several discrete models [15–18] have been proposed to reproduce and understand experimental observations on NME materials, as it will be discussed in the next Chapter.

To conclude about quasi-static observations, we discuss also some efforts done to trace the origin of this hysteretic behavior in a rock sample. Gist [20] performed a similar quasi-static measurement on a rock sample before and after the elimination of its typical crack-like pores structure. To eliminate the presence of pores, liquid epoxy has been injected into the rock sample to fill, and consequently eliminate, flat pores with size smaller than  $10\mu m$ . As reported in Fig. I.2, it was shown that the pressure dependence of the modulus, indirectly measured from velocity, decreases dramatically and hysteresis disappears after the elimination of small pores.

This observation, together with other measurements, based also on neutron scattering [12], have led researchers to conclude that the origin of hysteresis and discrete memory should be in the interfaces created by the presence of grain boundaries and micro-cracks.

**Figure I.2** – Plot of the wave velocity vs. applied pressure for dry Berea sandstone and Berea with a bond system (flat pores) filled with epoxy. Open circles represent the second upward cycle [20].

### 3.2 Dynamic behavior

In addition to the quasi static behavior described above, other observations suggest that nonlinearity in NME materials should have a different origin from that of atomistic nonlinearity and indeed it should be related to the material structure. Most of these experiments are showing an anomalous dynamic behavior in NME materials, i.e. when a time dependent perturbation is applied.

Results in the literature agree saying that most undamaged materials such as intact aluminum, Plexiglas and mono crystalline solids show only a very small nonlinear response related to deformations at the atomic scale. In this range, their behavior is well described by Landau theory. Evidence of such nonlinearity is only manifested at moderately high strain levels.

However, as soon as damaged, the situation is different. For strain amplitudes up to  $10^{-8}$ , they seem to behave classically and obey the Landau theory. At larger strains, their behavior is more similar to that of Berea sandstone. It is to be noted that even in such strain range classical nonlinearity is still present, being directly related to the material itself and not dependent on its environment. However, for larger strains classical effects are hidden by the stronger effects due to hysteresis.

In this strain range ( $10^{-8}$  to  $10^{-6}$ ) there is evidence of several limits of the classical theory to deal with NME nonlinear behavior. These limits are related to observation of an anomalous scaling of third order harmonics and resonant peak shift with strain amplitude. Furthermore, slow dynamics is an additional effect which cannot be explained within the classical theory framework.

Like it was shown in the classical nonlinear case, dynamic nonlinear response may manifest itself in a variety of ways. Therefore, many indicators of nonlinearity could be defined, linking the detected strain amplitude of the driving frequency to the harmonics amplitude, resonance frequency shift, break of the superposition principle. As mentioned, additional indicators not existing for classical nonlinear materials could be introduced exploiting the properties linked to slow dynamical effects.

Depending on whether the experiment is done in few seconds or in some hours, effects in mesoscopic materials might be very different. In the following we define two categories of experiments. In the first case the experiment time is of the order of the period of the perturbation exciting the system: we speak of fast dynamics. In the second case, the response of the system is tracked on a much longer time scale, to observe conditioning and relaxation effects. We speak of slow dynamics.

#### 3.2.1 Fast dynamic experiments

Fast dynamic effects appear very rapidly. In principle, only few pico seconds of dynamic excitation at increasing strain level are needed to observe the amplitude dependence of the aforementioned nonlinear indicators. A fast dynamic experiment could be realized in different manners: in the time or in the frequency domain, using standing or transient waves, with CWs or pulses excitations, etc. as will be discussed in the following.

#### Harmonics generation

A typical experiment dealing with harmonics generation phenomena is very similar to that described already for classical nonlinear materials. The sample is excited with a source function  $f(t)$ , the signals recorded at the receivers positions after having traveled into the medium are analyzed to measure the harmonics amplitudes via a Fourier analysis. Most experiments have been conducted in Young's mode resonance, however, some torsional measurements have been conducted as well by Bonner and al.[21].

The plot of the second and third harmonic amplitudes as a function of the strain amplitude of the fundamental is a power law  $y = ax^b$ , as for classical nonlinearity. The calculation of the slope  $b$  of the same curve plotted in logarithmic scale, however, provides a significant quantitative information about the nature of the nonlinearity. Indeed, the exponent is found to be the same for the second and third harmonics, in contradiction with what theoretically expected.

As an example, we show here a typical result obtained for Berea sandstone: see Fig. I.3. The slope is  $b = 2$  for both curves. In addition, for the same strain, the third harmonic (hollow circles) has an amplitude larger than the second harmonic (filled circles), denoting a further difference with respect to classical predictions.

**Figure I.3** – Second and third harmonic amplitudes as a function of measured strain amplitude in Berea sandstone. The harmonic amplitudes were obtained from Fourier analysis of the recorded time signals. [13]

#### Nonlinear resonance frequency shift

The amplitude dependence of the resonance frequency, known as the Nonlinear Resonant Ultrasound Spectroscopy technique, can be used for calculation of the average elastic modulus of the medium and wave propagation speed. Due to the amplification that resonance experiment



provides, it is perhaps the most sensitive way to observe nonlinear behavior, even at extremely small dynamic strains, as small as  $\epsilon = 10^{-9}$ .

A typical 1-D resonance experiment consists on sweeping both upward and downward around the fundamental resonance frequency. Many frequency sweeps are repeated at successively increasing drive voltage over the same frequency interval in order to monitor the resonance peak shift. By plotting the frequency shift as a function of the fundamental mode strain amplitude, one can learn about the nature of the nonlinearity. The dependence between the normalized frequency shift and the strain is again a power law relation  $y = ax^b$ . The exponent measured in experiments on NME materials is  $b = 1$ , again different from that predicted in the classical Landau theory.

We show in Fig. 1.4, the results of an experiment performed on Fontainebleau, Berea and Lavoux sandstones. The resonance curves for Fontainebleau sandstone (output amplitude as a function of frequency of excitation) are shown in the right plot. The absolute value of the resonance frequency shift is shown in the left plot. Besides noting a downward shift of the frequency at which maximum response is observed, the plot indicates that different results are obtained when the sweep over frequency is performed in the upward (increasing frequency) or downward directions. This is again an indication of a limit of the classical theory and it is a direct consequence of effects due to conditioning, as discussed in the next paragraph.

#### 3.2.2 Slow dynamic effects

Slow dynamics, by far the most typical characteristic of non classical NME, refers to the logarithmic time dependence recovery of the elastic modulus to its initial value after being softened by a large amplitude strain. It includes two different time scale mechanisms: conditioning which takes place on a time scale of few seconds to minutes and relaxation which occurs on a much longer time scale (of the order of  $10^3$  seconds to days).

At first glance, a creep-like behavior seems to provide the possible explanation about the mechanism responsible of slow dynamic effects. But, this hypothesis fails since creep is observed in quasi static experiments, while in rocks and some damaged metals slow dynamics is induced by a dynamic driving and occurs under dynamic strain levels three orders of magnitude below those of a typical creep experiment. In addition, slow dynamics behavior is always reversible and repeatable.

#### Conditioning

The softening of the material, also termed conditioning, takes place under dynamic strain levels of the order of  $10^{-6}$  and larger. Full conditioning is obtained in a short time (from few seconds to minutes). At a first glance, this time scale seems to be long enough to allow neglecting its effects in fast dynamic experiment (time scale of the order of micro seconds). Nevertheless, experiments indicate most of the conditioning to be occurring almost instantaneously and thus coupling between conditioning and fast dynamics have always to be considered. In other words, the same wave propagating in a dynamic experiment is causing a non negligible self-conditioning effect.

**Figure I.4** – Right: resonance curves for a Fontainebleau sandstone cylindrical sample at increasing drive: the resonance peak shifts to the left and the Q-factor increases. Left: normed frequency shift  $\frac{|\omega - \omega_0|}{\omega_0}$ , where  $\omega_0$  is the linear resonance frequency, plotted as a function of strain amplitude for various rocks. The slope of the curves is approximately one, indicating that non classical nonlinearity is responsible for the peak shift [13]

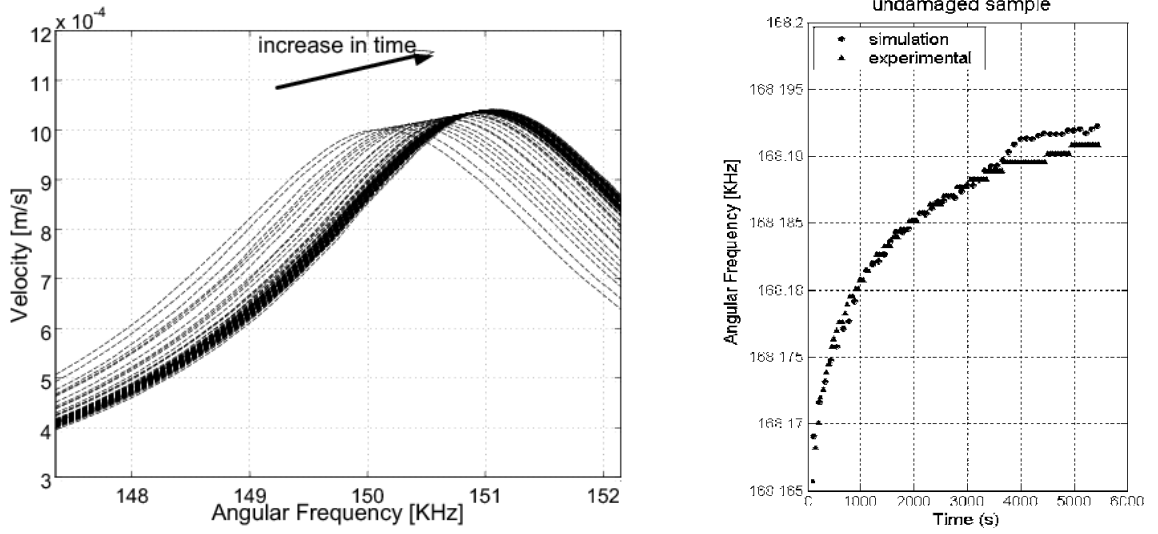
The typical observation of conditioning is the modulus decrease during the application of a dynamic excitation of NME materials. If the excitation persists the modulus decreases continuously for some period of time until the material reaches a new equilibrium state where no more change takes place. Consequently, the amount of conditioning depends on the time duration of the excitation and its amplitude. Experiments show that the total decrease in modulus increases with increasing duration and amplitude of the excitation. As a second example, in Fig. I.5, results for a damaged concrete sample are shown [22]. Here, a large amplitude excitation is applied to a cylindrical concrete sample for a long time. Lower amplitude ultrasonic waves are used to test the sample by measuring the wave velocity at different times during conditioning. The plot of velocity vs. time, shows a decrease up to stationary conditions are reached (blue triangles), that is a typical conditioning observation. At the same time, an indicator of nonlinearity is also measured (red circles - SSM indicator; black squares - harmonics indicator). Albeit we will discuss better the result in the last chapter of this thesis, we anticipate here that an increase of nonlinearity of the sample could be observed, while conditioning is increasing. In the experiments, temperature and humidity were controlled in order to separate conditioning effects from those due to fluctuations in the environmental parameters.

**Figure I.5** – Conditioning in a damaged concrete sample. As conditioning time increases, the wave velocity diminishes (blue circle), while the nonlinearity of the sample (indicator  $\theta$ ) increases (red circles and black squares for the Scaling Subtraction Method and harmonics indicators, respectively)

#### Relaxation

After full conditioning is obtained, relaxation occurs. In experiments, the drive which has conditioned the sample is turned off and the way followed by the sample to return back to its original state is monitored. It takes a relatively large time for the recovery process to take place and it depends on the logarithm of time, over minutes to days depending on the strain amplitude used to condition and its duration.

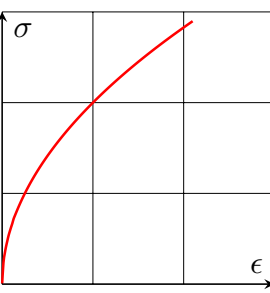
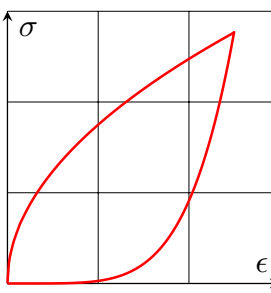
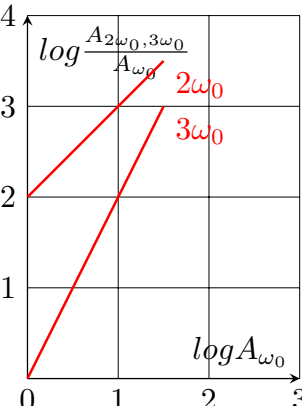
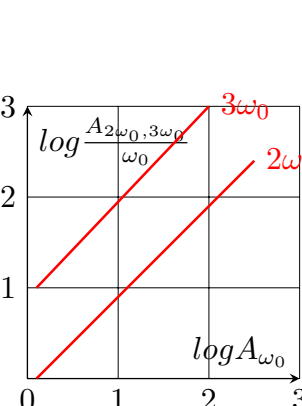
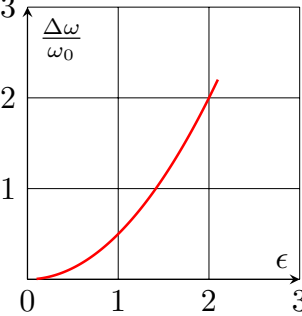
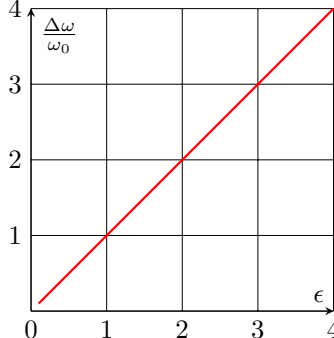
To clearly see the slow dynamic behavior, one can perform the following measurement of the resonance frequency. A first frequency sweep is performed at a small strain amplitude, followed by a second sweep performed at a large strain amplitude and at a very slow rate (about few minutes duration) to ensure full conditioning. Afterward, successive sweeps are repeated at the lowest excitation amplitude and the resonance frequency shift  $\Delta\omega/\omega_0$  is monitored in time. Immediately after conditioning, a significant shift is observed. The negative value of the shift is indication of softening. However, slowly in time,  $\Delta\omega/\omega_0$  diminishes, up to returning to zero, thus indicating the elastic modulus has recovered its original state after a relatively long time. It is noticed that the slow dynamical scaling of the resonance frequency recovery in time is logarithmic. An example of slow dynamics is illustrated in the two plots of Fig. I.6, for a concrete specimen [23].



**Figure I.6** – Slow dynamics in a concrete sample. Left: Conditioning at constant amplitude; Right: Relaxation process in time [23].

## 4 Conclusions

In this first chapter, we have introduced the basic equations for wave propagation in classical nonlinear media and briefly summarized the results expected from the theory. We have shown how experimental observations in a wide class of materials, including rocks, concrete, bones and damaged metals or composites, are indicating the need of more complex models to describe the link between stress and strain. In Table I.1, the main predictions observed in Nonlinear Mesoscopic Elastic materials are summarized and compared with those emerging from classical nonlinear theories. In the next Chapter, some of the models proposed in the literature to explain all these emerging features will be discussed.

Summary		Classical Nonlinear	Nonclassical Nonlinear
Quasi static			
Fast dynamic	Harmonics generation		
	Resonance shift		
Slow dynamics		no	yes

**Table I.1** – Basic similarities and differences in the behavior of classical and nonclassical elastic media.

---

## References

- [1] K. A. Van Den Abeele, P. A. Johnson, and A. Sutin. Nonlinear elastic wave spectroscopy(NEWS) techniques to discern material damage, partI: Nonlinear wave modulation spectroscopy(NWMS). *Res Nondestr Eval*, 12:17–30, 2000. [1](#)
- [2] M. Scalerandi, A. S. Gliozzi, and C. L. E. Bruno. A scaling method to enhance detection of a nonlinear elastic response. *App. Phys. Lett.*, 92:101912, 2008. [1](#)
- [3] R. A. Guyer and P. A. Johnson. Nonlinear mesoscopic elasticity: Evidence for a new class of materials. *Physics Today*, 52:30–35, 1999. [1](#)
- [4] R. A. Guyer and P. A. Johnson. Hysteresis, energy landscapes and slow dynamics: A survey of the elastic properties of rocks. *j. Mater. proces. Manufac. Sci.*, 9, 2000. [2](#)
- [5] A. Novac, M. Bentahar, V. Tournat, R. El Guerjouma, and L. Simon. Nonlinear acoustic characterisation of micro-damaged materials through higher harmonic resonance analysis. *NDT & E International*, 45:1–8, 2012. [2](#)
- [6] P. A. Johnson, B. Zinszner, and P. N. J. Rasolofosaon. Resonance and elastic nonlinear phenomena in rock. *J. Geophys. Res.*, 101:11–553, 1996. [2](#)
- [7] V. E. Nazarov, A. V. Radostin, and I. A. Soustova. Effect of an intense sound wave on the acoustic properties of a sandstone bar resonator. experiment. *Acoust. Phys.*, 48:76–80, 2002. [2](#)
- [8] A. Sutin J. Carmeliet P. A. Johnson K. Van Den Abeele. Micro-damage diagnostics using nonlinear elastic wave spectroscopy (NEWS). *NDT & E International*, 34:239–248, 2001. [2](#)
- [9] J. A. TenCate. Slow dynamics of earth materials: An experimental overview. *Pure. Appl. Geophys*, 168:2211–2219, 2011. [2](#)
- [10] F. D. Murnaghan. Finite deformation of an elastic solid. *American journal of Mathematics*, 59:235–260, 1937. [3](#)

- 
- [11] T. W. Darling et al. Localizing nonclassical nonlinearity in geological materials with neutron scattering experiments. volume 838, pages 19–26. AIP conference Proceedings, 2006. [10](#)
- [12] R.A. Guyer et al. Quantitative implementation of preisach-mayergoyz space to find static and dynamic elastic moduli in rock. *J. Geophys. Res -Solid Earth*, 102:5281–5293, 1997. [10](#), [11](#)
- [13] P. A. Johnson and P. N. J. Rasolofosaon. Manifestation of nonlinear elasticity in rock: convincing evidence over large frequency and strain intervals from laboratory studies. *Nonlin. Proces. Geophys.*, 3:77–88, 1996. [vii](#), [10](#), [13](#), [15](#)
- [14] B. Capogrosso Sansone and R.A. Guyer. Dynamic model of hysteretic elastic systems. *Phys. Rev. B*, 66:224101, 2002. [11](#)
- [15] M. Scalerandi and P.P. Delsanto. Modeling nonclassical nonlinearity, conditioning, and slow dynamics effects in mesoscopic elastic materials. *Phys. Rev. B*, 68:064107, 2003. [11](#)
- [16] G. Shkerdin and C. Glorieux. Nonlinear modulation of lamb modes by clapping delamination. *J. Acoust. Soc. Am.*, 124:3397–3409, 2008. [11](#)
- [17] V. Gusev, B. Castagnède, and M. Moussatov. Hysteresis in response of nonlinear bistable interface to continuously varying acoustic loading. *Ultrasonics*, 41:643–654, 2003. [11](#)
- [18] C. Pecorari. Adhesion and nonlinear scattering by rough surfaces in contact: Beyond the phenomenology of the preisach-mayergoyz framework. *J. Acoust. Soc. Am*, 116:1938–1947, 2003. [11](#)
- [19] I. D. Mayergoyz. Hysteresis models from the mathematical and control theory point of view. *J. Appl. Phys*, 57:3803–3805, 1985.
- [20] G. A. Gist. Fluid effects on velocity and attenuation in sandstones. *J. Acoust. Soc. Am*, 96:1158–1173, 1994. [vii](#), [11](#)
- [21] B. P. Bonner, P. Berge, C. AracneâRuddle, C. Boro, E. Hardy, and C. Trombino. Ultrasonic characterization of synthetic soils for application to near surface geophysics. In *Proceedings of the Symposium on the Application of Geophysics to Engeneering and Environmental problems*, pages 455–463, 1999. [13](#)
- [22] M. Scalerandi, A.S. Gliozzi, C.L.E. Bruno, and P. Antonaci. Nonequilibrium and hysteresis in solids: Disentangling conditioning from nonlinear elasticity. *Phys.Rev.B*, 81:104114, 2010. [15](#)
- [23] M. Bentahar, H. El Aqra, R. El Guerjouma, M. Griffa, and M. Scalerandi. Hysteretic elasticity in damaged concrete: Quantitative analysis of slow and fast dynamics. *Phys.Rev.B*, 73:104114, 2006. [vii](#), [16](#), [17](#)

---

---

# Chapter II

---

## Models for Nonlinear Mesoscopic Elasticity

### 1 Introduction

Several experimental observations pointed out that NME materials could not be described in the framework of the classical nonlinear theory, as stated in the previous Chapter. Therefore they should be described by a non classical nonlinear Equation Of State (EOS) which has the particularity of being multivalued (it presents hysteresis in the quasi static stress-strain relation) and amplitude dependent (due to nonlinearity). Furthermore, memory and relaxation effects have been reported in the literature for such materials.

Several continuous models have been proposed to analytically describe the non classical term in the equation of motion Eq. 1.43 of Chapter I [1–4]. However, in addition to the fact that they do not account for conditioning and relaxation processes, their use is limited to describe very specific experiments, i.e. with a given material and geometry. Thus the continuous approaches misses universality.

As a consequence of the presence of multivalued functions and/or threshold activated mechanisms, the analytical formulation of the EOS is indeed generally not feasible and discrete modeling is required to understand and explain the experimental observations reported in the literature. It was shown that a multi-scale statistical description based on the generalized Preisach-Mayergoyz discrete formalism [5] could be a suitable approach to model the nonlinear elasticity[6] specific to materials containing mesoscopic structural features like cracks, grain boundaries, and contacts of typical size of some micrometers.

The goal of this Chapter is to provide a brief overview of some of the models reported in the literature and to define in details the EOS for the models which will be used in the following of the thesis. In this work, hysteresis, clapping and adhesion models have been reformulated in the framework of a multi-state approach, as discussed in the last Section of the Chapter.

### 2 Physical models

Nonlinearity in NME materials finds its origin in the bond system i.e. the contacts between grains, micro cracks, zones separating different phases, etc. The bond represents the soft part of the material compared to the matrix which is elastically harder. An adequate physical model to deal with this kind of materials must be able to describe the behavior of the soft zone and



the interactions susceptible to be present at the microscopic level. Such interactions might manifest in terms of friction, adhesion and clapping mechanisms.

## 2.1 Internal friction

Since hysteresis in the stress-strain relation describing rocks behavior has been experimentally observed in 1940, a considerable interest has been given to explain the physical mechanisms behind this phenomenon. For more than three decades, it was attributed to internal friction that derives from several dissipation mechanisms acting at the microscopic level. As a consequence some models have been proposed accordingly.

### 2.1.1 Granato-Lucke model of dislocations

It is undoubtedly established that the structure of grain boundaries is crystal-like [7] and this is the case of grain boundaries in many hysteretic materials. On the other hand, a network of dislocations is known to be present in some crystalline systems before deformation. On these basis, it was postulated that in a consolidated granular system the concentration of dislocations is mostly located at the grain boundaries, rather than inside grains. As a consequence, the contribution of the motion of dislocations to the internal friction in nonlinear materials should be great. Based on such ideas, the theory of dislocations as sources of mechanical damping has been developed by Granato and Lucke in 1956 [8].

For large enough concentrations of impurity atoms, the length of the network loop is determined by intersection of the dislocation segments which are pinned down by every two successive impurity particles. The Granato-Lucke model assumes the vibration of a dislocation line segment pinned to impurity atoms under an alternating stress equivalent to the problem of the forced damped vibration of a string.

There are two characteristic lengths in the model: the network length  $l_n$  and the length  $l_d$  of dislocation segments between two successive impurity atoms, as long as an external shear stress is applied. As we can see in Fig. II.1.(a), the dislocation segment, initially undeformed (A), begins bending (B) after the application of an external stress up to forming dislocation loops (C). Finally the maximum deformation of  $l_d$  corresponds to a critical value of stress, termed breakaway stress, at which the dislocation segments are disconnected from impurity atoms (D). At this point, a sudden large increase in the dislocation strain occurs without the corresponding increase in the applied stress causing the material to become softer. When the stress is reduced, the strain decreases along the same softer line, i.e. during the unloading part of the stress cycle, from (D) to (A), the network loop is pulled until the segment loop has completely collapsed with those in the initial situation (A). Here, dislocations are again pinned by the impurity particles and returns to the initial situation before inducing the dislocations to react.

The process leads to an irreversible dislocation strain which is shown in Fig. II.1.(b) and could be described by an EOS represented by the solid line. Assuming that the impurity atoms are randomly distributed in the crystal, a distribution of segment lengths  $l_d$  can be used to describe the different dislocation loops. By averaging over all the elements, the dislocation

stress-strain curve becomes smoother as shown by the dashed curve.

The energy losses in the model are thus of two different natures. The first loss is due to the fact that the motion which is forced by the external stress is opposed by some damping mechanism. The second type of loss is due to the asymmetry of the loading/unloading processes. This loss is proportional to the area enclosed by the stress-strain loop very similar to the hysteretic loop in the PM space based hysteretic model described in the following.

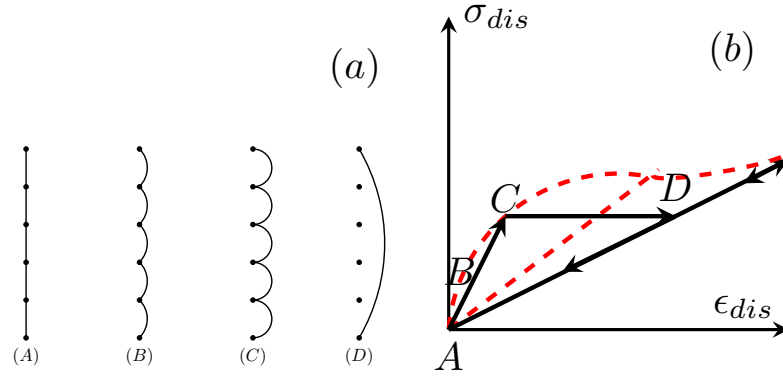


**Figure II.1** – (a) The successive drawings indicate schematically the bowing out of a pinned dislocation line by an increasing applied stress; (b) Stress-strain equation in the Granato-Lücke model. The equation for a single dislocation line is reported as a solid line, while averaging over dislocations lines with different lengths give the macroscopic stress-strain equation reported as a dashed line [8]

### 2.1.2 Stick-slip motion

A typical stick-slip experiment is illustrated in Fig. II.2, where a mass  $m$ , which is initially at rest, is pulled over a block by a spring of elastic constant  $k$  which is deformed at constant velocity  $v$  during loading. The spring is progressively elongated, being the elongation denoted as  $x$ , until the applied force is sufficient to overcome the static frictional force. At that point, the mass is not in equilibrium and suddenly it is displaced with respect to the block.

During the unloading phase, the spring is compressed i.e. the pulling force decreases and the mass eventually stops after a certain time. Again, static friction is important and the mass could perhaps remain stationary until the loading force in the spring (of opposite direction with respect to the loading phase) reaches once more a value sufficient to overcome the friction force. The process is repeated, creating a periodic motion consisting of phases where the mass sticks and slips.

The classical explanation for this jerky type of motion in brittle rocks can be derived assuming sudden fractures of locked regions on surfaces which are in contact. This phenomenon brings the two surfaces out of equilibrium and a relative motion is established. It follows that the friction force falls suddenly to a lower value equal to the dynamic friction. The force in the

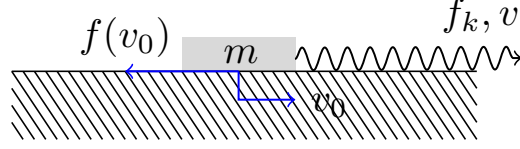


**Figure II.2** – Stick- slip processes as consequence of frictional sliding between two surfaces in contact under shearing applied stress

spring is now greater than the force required to maintain sliding of both surfaces at constant velocity  $v$ , so that the system is not in equilibrium and one surface accelerates with respect to the other [9].

The differential equation for the motion of the mass on the flat can be derived by adding all the forces acting on the mass during its motion and equating this sum to the acceleration:

$$\begin{aligned} m\ddot{x}_m &= k(x - x_m) - f \\ \dot{x} &= v - v_m \end{aligned} \quad (\text{II.1})$$

where  $x$  and  $x_m$  denote the loading position and the mass coordinate respectively. Here the friction force  $f$  at the shearing surfaces is generally a function of  $x_m$ ,  $v_m$  and  $t$ . Such a function could be written to provide hysteretic effects.

The models reported in the literature generally assume a particular functional form for the friction as a function of velocity:  $f(v_m)$ . To describe such functional form, a large number of mechanically coupled elements forming the contact is postulated and statistical averaging performed.

## 2.2 Clapping mechanism

When two contacting surfaces are subject to an applied stress cycle, the separation distance between the centers of grains belonging to these surfaces corresponds to a strain varying in time with the same period of the forcing stress, at least in a first approximation. When two asperities composing the two surfaces of the grains approach each others, without yet being in contact, the separation distance becomes of the order of inter-atomic distances. At such length scales, chemical interactions take place between the asperities. This interaction could be well described in terms of a Lennard Jones potential, i.e. a potential which is derived from the balance between attractive forces (describing van der Waals attraction at long ranges) and repulsive forces (describing Pauli repulsion at short ranges due to overlapping electron orbitals).

As a consequence of such interaction, the behavior at the interface might become very complex and hysteretic. Let us consider a simple system in which two surfaces in contact, representing for example the two lips of a crack, are subject to an external pressure cycle. Under tension, no force is exerted by one surface over the other (open contact), while when compression occurs the surfaces approaches. Once their separation distance is of the order of

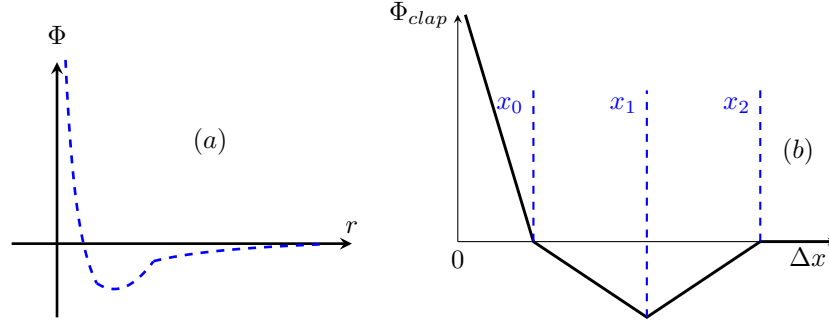


**Figure II.3** – (a) The Lennard-Jones potential between two molecules as a function of the distance  $r$  separating them; (b) Lennard-Jones-like interaction between two surfaces in contact separated by a distance  $\Delta x$  as described in the Clapping model, the Lennard-Jones potential is approximated by 4 segment-like intervals. [10]

inter atomic distances, as a consequence of the Lennard-Jones potential, a force starts being generated, upon the time in which full contact is achieved and a full force is generated at the interface.

We will discuss better this model in the following. We mention here that to model this system and describe the behavior of the contact regions between the two surfaces, a clapping microscopic element is introduced, with EOS reported in Fig. II.3. In other words, the Lennard Jones potential is approximated by four linear segments (three elastic states with different elastic constants ( $k_1, k_2, k_3$ ) and one state supporting zero force  $k_4 = 0$ ) [10]. In the Figure, the variable  $\Delta x$  denotes the separation distance between the surfaces in contact.

## 2.3 Adhesion mechanism

It is a more complex form of the interaction between two surfaces in contact. Besides the intermolecular potential  $\Phi$  (see Fig. V.7. (a)), described in clapping model and considered as the only contribution, the potential in adhesion model proposed by Vitalyi Gussev [11] contains additional terms, like potential of capillary forces due to the presence of liquids at the interface, potential of external preloading  $\Phi_0$  and of Hertzian contact stress  $\Phi_H$  in rough surfaces, which interact during deformation and results in an effective potential  $\Phi_{ad}$  (see Fig. V.7. (b)). This interaction is often so complex that it is difficult to predict its form. This can be done in several ways, here the piece-wise linear approximation is considered as shown in Fig. V.7. (c).

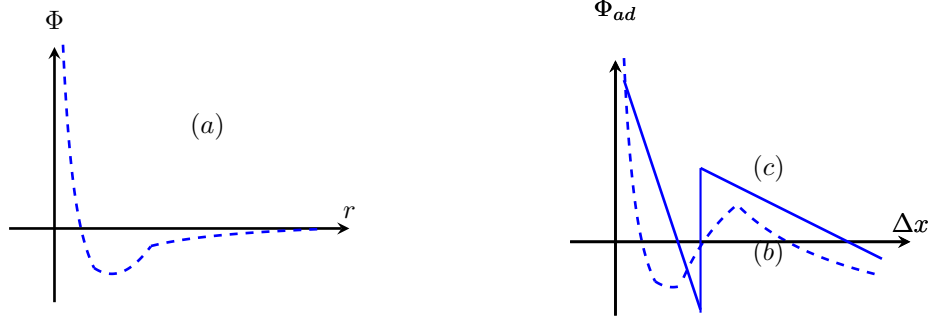


**Figure II.4** – (a) The short-scale intermolecular Lennard-Jones potential; (b) An effective potential  $\Phi_{ad} \propto \Phi + \Phi_H + \Phi_0$ ; (c) a piece-wise linear approximation for the effective potential. [11]

## 3 Preisach-Mayergoyz models of nonlinear elasticity

The main paradigm of hysteretic phenomena is the one observed in ferromagnetic systems, for which the Preisach-Mayergoyz (PM) formalism was initially proposed. This approach was later generalized to any hysteretic phenomenon independently from its origin [5] and it was translated by Guyer et al. [12] to the field of NME materials to model the hysteresis and dynamic nonlinear effects shown in experiments.

In the PM formalism, some mesoscopic elements (ME) are defined with a particular simple equation of state (EOS). The macroscopic stress-strain relation is obtained averaging over a large number of MEs with different microscopic properties as it will be detailed in the following.

### 3.1 Equation of state of the microscopic elements

Each microscopic unit is defined as a two states (open and closed) element with different properties. Also a pair of characteristic pressure parameters ( $P_o$  and  $P_c$ ) is defined, termed opening and closing pressure respectively. The applied pressure  $P$  is in fact chosen as the external variable controlling the transition between the two states.

The behavior of the microscopic element is shown in Fig. II.5. Increasing the applied pressure (loading), each element being initially open will switch suddenly to the closed state when the driving variable  $P$  exceeds the characteristic value  $P_c$  of the element ( $P > P_c$ ); the unloading process leads initially closed elements to go back to the open state when the applied pressure falls below the opening pressure of the element:  $P < P_o$ . We observe the element is always in the closed (open) state for  $P > P_c$  ( $P < P_o$ ) while in the intermediate region  $P_o < P < P_c$ , it may be in each one of the two states depending on the last state that has been imposed by the pressure previously applied to the sample, i.e. depending whether  $\frac{\partial P}{\partial t} < 0$  or  $\frac{\partial P}{\partial t} > 0$ .

In the original model proposed by McCall and Guyer [12, 13], the open and closed states are both rigid states and a pair of element lengths ( $l_o$  and  $l_c$ ) are associated to the two states.

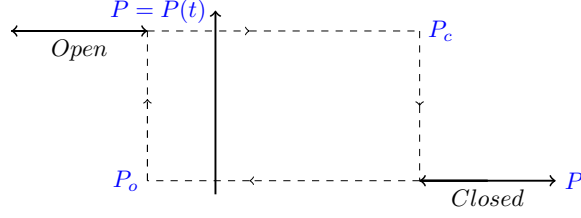


**Figure II.5** – Behavior of one microscopic element in an elastic PM model

In other words, the element which are open (closed) have a length  $l_o$  ( $l_c$ ). When the pressure increases, the element keeps the same length and behaves rigidly up to the value  $P = P_c$  where the element instantaneously closes and assume the length  $l_c < l_o$ . For further increase in pressure the element continue to behave rigidly with length  $l_c$ . When decreasing the pressure the length of the element remains the same until the opening pressure value is reached. At that pressure level the element switches instantaneously to the open state and its length becomes  $l_o$  again and remains unchanged even if the pressure is further decreased.

The pairs  $(l_c, l_o)$  could be connected in a deterministic or statistical way to the pairs of  $(P_c, P_o)$ . We consider here a simple model with the same two values of equilibrium lengths for all the hysteretic elements and define  $l_c = (1 - \alpha)l_o$ , where  $0 \leq \alpha < 1$ . This system could be treated using the effective medium theory, as done in ref.[13]. In this approach, the inhomogeneous system is replaced by a uniform system using springs with an equilibrium length equal to the average value of the system.

The total length at pressure  $P$  is therefore

$$l[P] = N \left[ l_o N_o[P] + l_c N_c[P] \right] \quad (\text{II.2})$$

where  $N_o[P]$  and  $N_c[P]$  are the fraction of open and closed elastic units at pressure  $P$ , respectively.  $N$  is the total number of elements.

The averaged length is obtained dividing by  $N$ :

$$\bar{l}[P] = l_o N_o[P] + l_c N_c[P] = l_o + (l_c - l_o) N_c[P] \quad (\text{II.3})$$

which could be rewritten as

$$\bar{l}[P] = l_o (1 - \alpha N_c[P]) \quad (\text{II.4})$$

As a result, the applied strain on the ME can be defined as

$$\epsilon[P] = \frac{\bar{l}[P] - l_o}{l_o} = -\alpha N_c[P]. \quad (\text{II.5})$$

where it is assumed all elements to be in the open state at  $P = 0$  (rest length is  $l_o$ ). Therefore the equation of state is completely determined by the fraction  $N_c[P]$  of closed elements during the pressure protocol. To estimate such a fraction and plot the stress-strain equation, the PM formalism is then introduced.

### 3.2 PM formalism

To scale up the EOS from microscopic to mesoscopic level, a statistical averaging is performed over all the hysteretic elements. In other words, the number of elements in the closed state  $N_c$  should be calculated. To provide statistical averaging, the pair of parameters  $(P_o, P_c)$  should be randomly assigned to each element and their position with respect to the applied pressure should be checked at every time to determine the equation of state.

A suitable way to do so, is to take advantage of a PM representation. Indeed, each hysteretic element could be represented, in a closing pressure - opening pressure space, commonly called PM space, by a point having as coordinates its characteristic parameters  $(P_c, P_o)$ .

The PM space is only partly filled, since the condition  $P_c \geq P_o$  should be verified. It follows that only the space region below the bisecting line is filled (lower triangle of the PM space). The hysteresis in the stress-strain relation is related to the fact that each element can be in two different states, so in two different energy levels, under the same loading. It follows that the contribution of a microscopic element to macroscopic hysteresis is a function of the difference between its two characteristic values  $P_c - P_o$ . Elements situated on the diagonal  $P_c = P_o$  are consequently not hysteretic. On the other hand, the further the element is from the diagonal, the more it is hysteretic.

Fig. II.6 shows how the stress-strain equation could be derived applying a pressure protocol  $P(t)$  shown in subplot(a). The different PM space configurations corresponding to some time instances during this protocol are shown in subplot (b). In each configuration, the state of the elements is represented using a color code: open elements are represented in white, while the black is reserved to closed elements.

Both hysteretic and non hysteretic (i.e. with  $P_o = P_c$ ) elements contribute in the PM space with densities  $\rho_B$  and  $\rho_D$  respectively. Notice that the choice of the density distribution is very important. Often both densities could be assumed constant (i.e. not pressure dependent), at least as far as a very small portion only of the PM space is spanned by the applied pressure. In the case discussed here the PM density of the nonhysteretic elastic units on the diagonal is defined as a pressure dependent function

$$\rho_D(P_c, P_o) = D(P)\delta(P_c - P_o) \quad (\text{II.6})$$

Where  $\delta(P_c - P_o)$  is the delta function. These elements are found to be the major percentage of the PM space density determined empirically from stress- strain measurements. The PM density of the hysteretic elements, situated off the diagonal, is

$$\rho_B(P_c, P_o) = B(P_c, P_o) \quad (\text{II.7})$$

In the pressure protocol considered, at the initial state  $P(t) = P(0) = 0$  and all elements characterized by  $P_o > 0$  and a small portion of those with  $P_c > 0$  are open. Increasing the pressure in time (displacement in subplot (a) of the red vertical line from the configuration ① to ③) all open elements with  $P(t) > P_c$  switch to the closed state. The number of closed elements  $N_c$  during one protocol cycle could be easily calculated and the changes in the fraction  $N_c$  evaluated at each pressure  $P(t)$ .

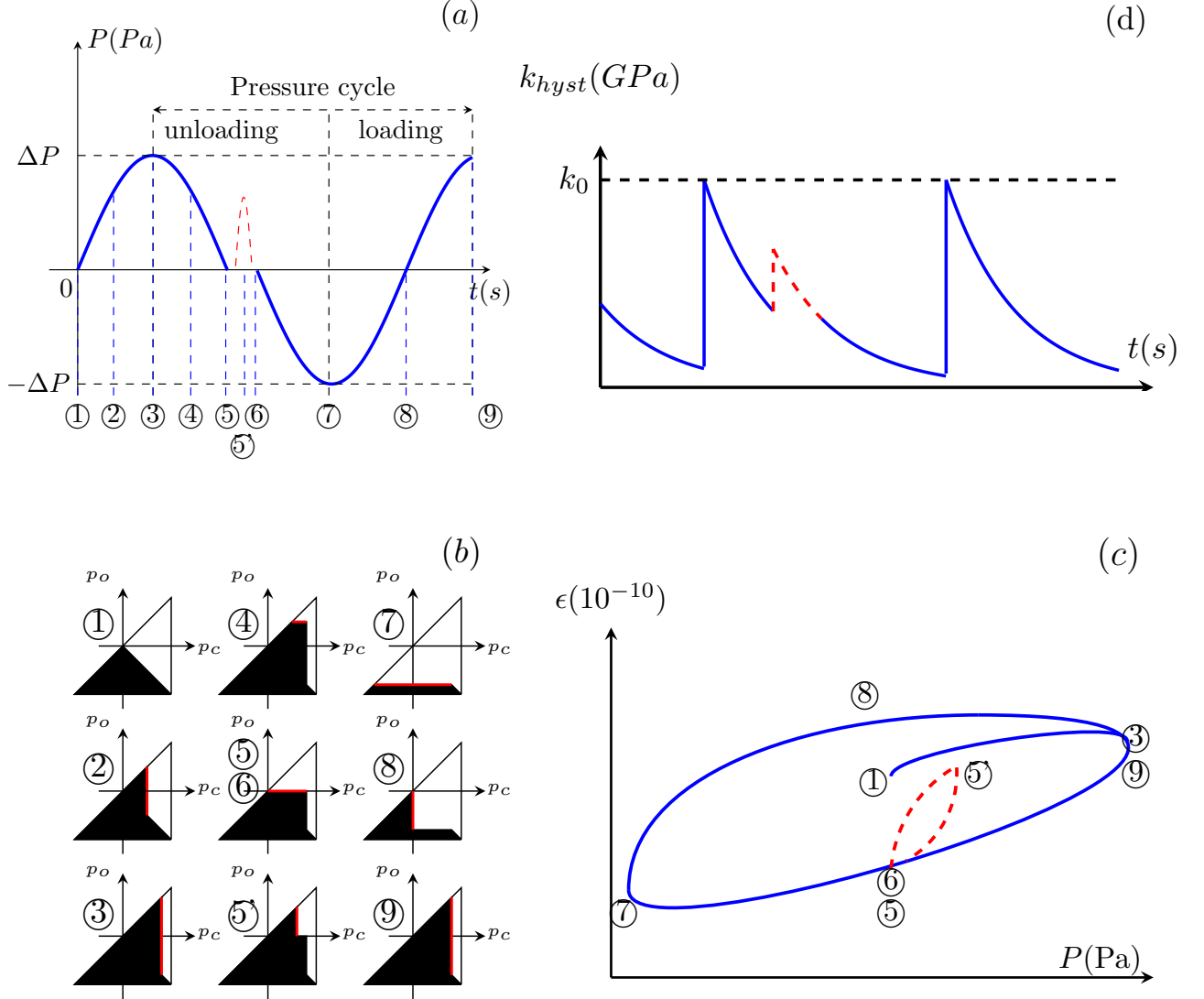


**Figure II.6** – (a) Macroscopic equation of state derived from a pressure protocol using the hysteretic PM model; (b) The pressure variation causes a redistribution of elements between open and closed states; (c) The stress-strain relation could be derived counting the number of elements in the closed state at each pressure value. The stress-strain equation is only qualitatively depicted; (d) The modulus derived as a function of time deriving the stress-strain equation.

During the unloading process (displacement of the red horizontal line from the configuration ③ to the number ⑤), all the elements satisfying the condition  $P < P_o$  go back to the open state. Starting from the configuration ⑤, the pressure decreases again and initially closed elements progressively switch to the open state until the configuration ⑦ where the minimum



### II.3 Preisach-Mayergoyz models of nonlinear elasticity

applied pressure is reached. The change in the fraction  $N_c$  during the unloading process is

$$\Delta N_c(\downarrow) = \rho_D(P_{max} - \Delta P) - \frac{1}{2}\rho_B(P_{max} - \Delta P)^2 \quad (\text{II.8})$$

where  $P_{max}$  is the maximum value of  $P_o$  and  $P_c$ . The corresponding strain is

$$\epsilon(\downarrow) = \epsilon(\Delta P) - \alpha N_c(\downarrow) \quad (\text{II.9})$$

The modulus is given by

$$K(\downarrow) = \frac{\partial \epsilon}{\partial P} = \alpha \frac{\partial N_c(\downarrow)}{\partial P} \quad (\text{II.10})$$

The pressure protocol is reversed at  $P = -\Delta P$ , as the pressure increases in time (displacement of the red vertical line from the configuration ⑦ to ⑨), more and more elements are concerned by the condition  $P(t) > P_c$  and switch again to the closed state. The evolution of the fraction  $N_c$  during the loading process is

$$\Delta N_c(\uparrow) = \rho_D(P_{max} + \Delta P) + \frac{1}{2}\rho_B(P + \Delta P)^2 \quad (\text{II.11})$$

The corresponding strain is

$$\epsilon(\uparrow) = \epsilon(-\Delta P) - \alpha N_c(\uparrow) \quad (\text{II.12})$$

and the modulus is given by

$$K(\uparrow) = \frac{\partial \epsilon}{\partial P} = \alpha \frac{\partial N_c(\uparrow)}{\partial P} \quad (\text{II.13})$$

In Fig. II.6.(c), we show the stress as a function of the strain resulting from the calculations reported above. The curve is a hysteresis loop which could be explained by the behavior of the off diagonal elements in the PM space. We can clearly see that in the PM space configurations ⑥ and ⑧, both corresponding to the same pressure-coordinate, the strain-coordinate is different. In fact, the configuration of the elements in the PM space is different, being higher the number of elements in the closed state when time corresponds to the point ⑧ than to ⑥. It follows that, applying the same pressure we could have two different possible values of strain depending on its history.

Finally, it is important to note that each change in the pressure variations sign involves a discontinuity in the elastic modulus, which is plotted as a function of the applied pressure in Fig. II.6.(d). Also, we stress that the model predicts end-point memory: Indeed, when the pressure protocol is interrupted at any point and a smaller loop pressure cycle is applied, as shown by the dashed line in Fig. II.6(a), an interior small loop is created inside the hysteretic stress-strain curve (as shown by the dashed line in subplot(d)), which is however always a closed loop. Right after, this loop follows again the same path as if the inner loop was not done.

## 4 Phenomenological multistate models

The approach described in the last Section could be easily generalized to more complex conditions, as it will be discussed here. In this case, we talk about statistical multi state models in the framework of a generalized PM space approach.

### 4.1 General considerations

A multi-scale multi state approach could schematically be introduced as shown in Fig. II.7. From the length-scales perspectives, the macroscopic sample is considered as composed of a finite number  $m$  of mesoscopic elements termed ME and labeled by an index ( $i = 1, \dots, m$ ). The typical length scale is of  $10^{-1}$  to 10 m, at the macroscopic level, and of the order of the mm for the ME length.

Each ME might contain inhomogeneities, grain boundaries or cracks with typical length of 0.1 to 100 micrometers. Thus, it is described by a statistical ensemble of micro-scale units of index ( $j = 1, \dots, M$ ), each of them characterized by a microscopic multi-state EOS. Depending on the involved mechanism, the microscopic element is allowed to be in a given number  $N$  of states. The state of a given element at time  $t$  is determined by a control variable which is in general the applied pressure  $P(t)$  (it could also be the strain). Transition from state  $n$  to state  $n + 1$  occurs when the driving variable exceeds a given value  $Z_{n,n+1}$ , characteristic to the element and called 'transition point'. Note that, if the mesoscopic zone is homogeneous, its behavior is classical, i.e. described by Hook's elasticity. In this case, the MEs are defined with only one elastic state and no transition.

It follows that each microscopic element is completely defined once two vectors are given:  $E = (k_1, k_2, \dots, k_N)$  is the  $N$ -dimensional elastic vector;  $Z = (z_{1,2}, z_{2,3}, \dots, z_{n-1,n})$  is the transition points vector. The latter is in general  $(N - 1)$ -dimensional. In hysteretic systems, some of the transition points from a state  $j$  to its nearest neighbor state  $j + 1$  is different from the transition point from  $j + 1$  to  $j$ . In such cases, the vector  $Z$  could have higher dimensionality.

In each state, the  $j^{th}$  microscopic element of the  $i^{th}$  ME, supports a stress  $\sigma_{ij}$  which is defined as a function of  $Z$ , or of the strain upon which  $z$  is dependent. By averaging over all the microscopic units, the global (mesoscopic) stress-strain relation could be established. Such averaging process should be performed introducing a large enough statistical ensemble of elements. As mentioned in the previous chapter, this condition could be achieved introducing a generalized Preisach-Mayergoyz (PM) representation. Each ME is characterized by a vector  $Z$  containing the values of all transition points, thus could be considered as a point in a multidimensional PM space. The values of the transition points are assigned randomly, with a given statistical distribution and with some constraints on the values assumed.

To implement such approach, various numerical and analytical methods are possible. Our approach is based on the Finite Differences method, using a first order forward scheme for both time and space derivatives. More details will be given for the models analyzed in the following. In principle, physical or phenomenological models found in the literature could be mapped onto a multi- state approach of the kind described here. In the following, three models used in this thesis will be described in details.

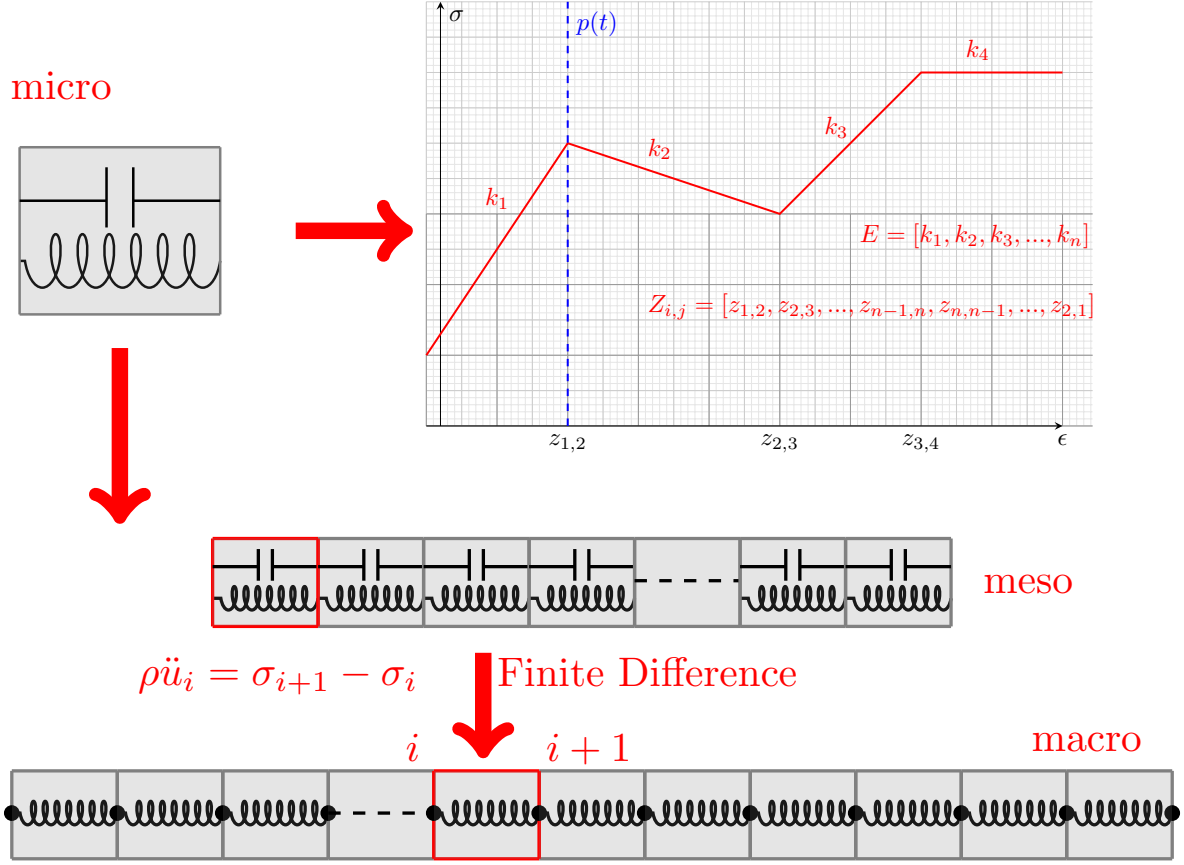


**Figure II.7** – Diagram explaining the different steps in the multi-scale multi-state approach used to model nonlinear phenomena in NME materials. The material (macroscopic) is discretized into cells (mesoscopic). Each mesoscopic level is discretized into a set of microscopic elements, each of them represented as a spring with elastic constant depending on a control variable  $z$  which defines transitions from one elastic state to another. The equation of motion at the macroscopic level describes the second time derivative of the nodes displacements ( $u_i$ ) as a function of the stresses due to the surrounding MEs, as reported in the figure.

## 4.2 Hysteretic model

### 4.2.1 Equation Of State

A spring model, which is very similar to the description proposed by McCall and Guyer, was proposed in the literature [12]. Instead of using elements with two rigid states and different element lengths, elements assuming two states which are elastically different are considered.

## II.4 Phenomenological multistate models

The open state corresponds to an elastic spring supporting an elastic stress  $\sigma_{i,j}$  given as:

$$\sigma_{i,j} = K_i \epsilon_{i,j} \quad (\text{II.14})$$

The element behaves linearly elastic up to the pressure  $P_c$ , when the element becomes rigid (infinite modulus). Increasing further the pressure applied, the strain  $\epsilon_{ij}$  remains constant and equal to the limit value corresponding to an applied pressure  $P = P_c$  while a third state is implicitly defined due to hysteresis. Using this definition, we could state that each microscopic element is a linear elastic spring in parallel with a rigid contact and it is described by the equation of state of a damped sticky spring:

$$\begin{aligned} \sigma &= k\epsilon & \text{if } P \leq P_o \\ \sigma &= P, \epsilon = P_c/k & \text{if } P \geq P_c \\ \sigma &= \begin{cases} k\epsilon \\ P \end{cases} & \text{if } P_o < P < P_c \end{aligned} \quad (\text{II.15})$$

where  $P(t)$  is the applied driving pressure and  $K = \{k, \infty\}$  and  $Z = \{z_{12} = P_o, z_{21} = P_c\}$ .

Assuming both stress and strain to be positive in tension, the EOS is plotted for one single element in Fig. II.8.(a).

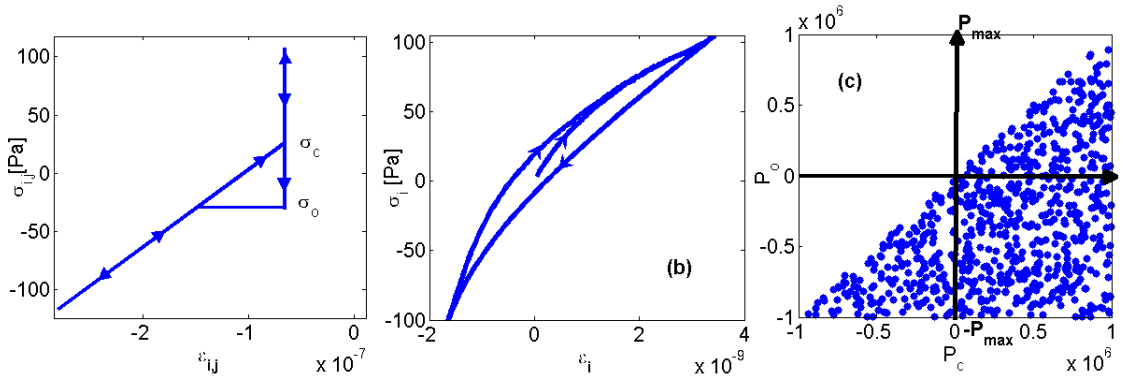


**Figure II.8** – Equation Of State of (a) One microscopic hysteretic element; (b) A mesoscopic element ME, using the hysteretic model; (c) P-M space distribution of  $N = 100$  elements

The behavior of one mesoscopic element could be predicted following the evolution of the P-M space of Fig. II.8. (c) when a dynamic pressure cycle (see Fig. II.9) is applied. When comparing the initial and last configurations, one can see that elements in the triangle delimited by dashed red lines are continuously switching between elastic and rigid states, they are at the origin of nonlinearity in the model. Inside the dashed yellow rectangle, each element made only one transition from elastic to rigid state and remain rigid at the end of the pressure cycle, they are responsible of conditioning effects.

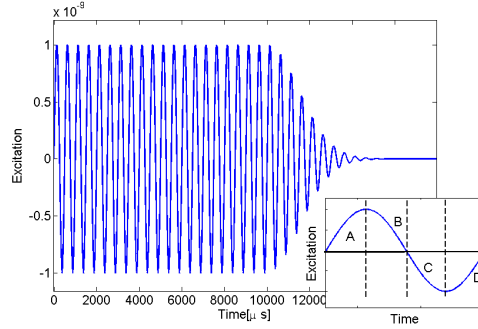


**Figure II.9** – Dynamic pressure cycle. The letters ( $A, B, C, D$ ) are attributed to the four phases within one period of the signal.

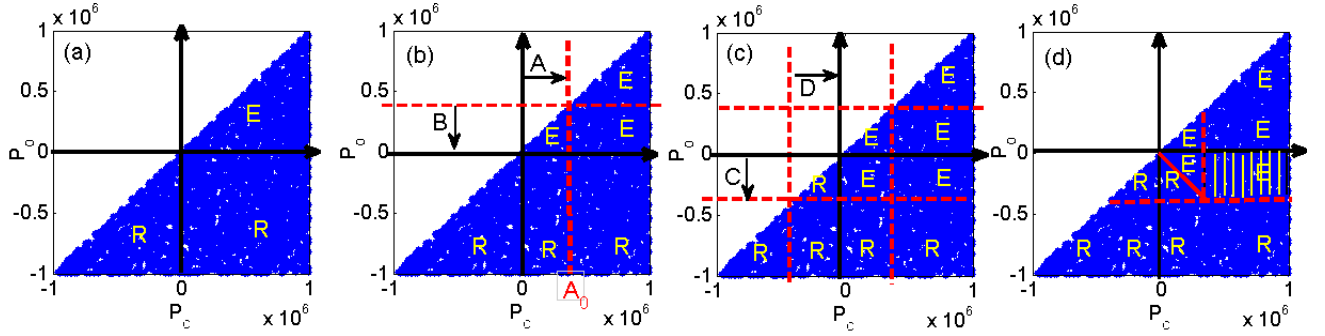


**Figure II.10** – The P-M space evolution during a pressure excitation of amplitude  $A_0$  starting from a relaxed configuration.  $R$  indicate areas where all elements are in the rigid state and  $E$  the areas with elements in the elastic state.

#### 4.2.2 PM formalism and mesoscopic EOS

Let us consider a cell  $I$ , whose tips are labeled as  $i$  and  $i + 1$  (see Fig. II.7). The global elongation  $l_i$  of the mesoscopic cell is given by the sum of elongations  $l_{i,j}$  of its constitutive microscopic elements ( $j = 1 \dots M$ ), which have an initial rest length  $l_o$ :

$$l_i = \sum_j l_{i,j} = \sum_{elastic} l_{i,j} + \sum_{rigid} l_{i,j} = \sum_j (u_{i,j+1} - u_{i,j}) = u_{i+1} - u_i \quad (\text{II.16})$$

where  $u_i$  is the displacement of the  $i^{th}$  node and  $u_{ij}$  is the displacement of the tip of the  $j^{th}$  microscopic element. Assuming the elastic constant  $K_i$  to be identical for all microscopic elements belonging to the same mesoscopic cell, Eq. II.16 can be written as a function of the microscopic stress  $\sigma_{ij}$  and of the rigid deformations  $\delta_{i,j}$  of the microscopic elements:

$$l_o \left[ \sum_{elastic} \frac{\sigma_{i,j}}{K_i} + \sum_{rigid} \delta_{i,j} \right] = u_{i+1} - u_i \quad (\text{II.17})$$

Assuming that the stress equilibrium within each mesoscopic cell is reached very rapidly so

that each ME belonging to the same cell supports the same stress, which is also equal to the stress applied to the cell, we obtain:

$$\sigma_i \sum_{elastic} \frac{1}{K_i} + \sum_{rigid} \delta_{ij} = \frac{du_i}{l_o} \quad (\text{II.18})$$

Here  $du = u_{i+1} - u_i$  is the global elongation of the mesoscopic cell of index  $i$ . Therefore  $du_i/l_o$  is the cell strain.

It follows that the mesoscopic stress  $\sigma_i$  could be derived as a function of the mesoscopic strain  $\epsilon_i$  as

$$\sigma_i = \frac{K_i}{N_{elastic}^i} \left( \epsilon_i - \sum_{rigid} \delta_{i,j} \right) \quad (\text{II.19})$$

Given the total deformation  $du_i$  of the cell  $i$ , the number  $N_{elastic}^i$  of elements in the elastic state and the total deformation of rigid elements at each time, the applied stress on the cell could be calculated from equation II.19. It follows from the same equation that the equivalent elastic modulus  $E_i$  of the mesoscopic cell is stress dependent and its expression is given by

$$E_i = \frac{K_i}{N_{elastic}^i} \quad (\text{II.20})$$

We show in Fig. II.8.(b) the microscopic EOS scaled to the mesoscopic level averaging over all elements.

To do that, one need to represent each microscopic element coordinates  $(P_o, P_c)$  in the PM space. Thus, knowing the state of each microscopic element at every time, we can learn about the global behavior. The PM space is shown in Fig. II.8. (c), where elements are uniformly distributed according to a constant density  $\lambda = \frac{M}{S_{PM}} = \frac{M}{2P_{max}^2}$  where  $S_{PM}$  is the area of the PM space.

The amount of nonlinearity in the model is related to the number of occurring transitions during the dynamic excitation. Thus, the density of the P-M space could be used as a free parameter to control the amount of generated nonlinearity in the model.

### 4.2.3 Macroscopic scale calculations

Given the EOS describing the different mesoscopic cells composing the macroscopic sample, the equation of motion of the particles, represented by the nodes at the interface between cells, can be easily derived from the Newton's second law knowing that the initial cell length is  $\varepsilon = Nl_o$  (rest length):

$$\rho \ddot{u}_i = \frac{\partial \sigma_i}{\partial x} = \frac{\sigma_{i+1} - \sigma_i}{\varepsilon} \quad (\text{II.21})$$

where  $\rho$  is the material density.

Substituting Eq. II.19, the equation of motion becomes

$$\rho \ddot{u}_i = \frac{k_i}{\varepsilon} \left[ \frac{u_{i+1} - u_i - \sum_{rigid} \delta_{i+1,j}}{N_{elastic}^i} - \frac{u_i - u_{i-1} - \sum_{rigid} \delta_{i,j}}{N_{elastic}^{i+1}} \right] \quad (II.22)$$

There exist several computer simulation techniques known in the literature which could be used to solve this kind of equations. For the sake of simplicity, in this simple one dimensional configuration we opt in for a Finite Difference method. A first order forward scheme is sufficient to ensure good convergence of the solution and satisfactory results. Furthermore, it is a fast and simple approach to implement.

From the Taylor expansion of the displacement in time, assuming a time step  $\tau$  for time discretization, one can obtain the finite difference scheme for the temporal derivatives:

$$\ddot{u}_i = \frac{u_i^{t+1} + u_i^{t-1} - 2u_i^t}{\tau^2} \quad (II.23)$$

Equation II.23 is substituted in Eq. II.22:

$$\frac{u_i^{t+1} + u_i^{t-1} - 2u_i^t}{\tau^2} = \frac{1}{\rho} \frac{k_i}{\varepsilon} \left[ \frac{u_{i+1}^t - u_i^t - \sum_{rigid} \delta_{i+1,j}^t}{N_{elastic}^i} - \frac{u_{i+2}^t - u_{i+1}^t - \sum_{rigid} \delta_{i,j}^t}{N_{elastic}^{i+1}} \right] \quad (II.24)$$

Finally we obtain

$$u_i^{t+1} = 2u_i^t - u_i^{t-1} + c \left[ \frac{u_{i+1}^t - u_i^t - \sum_{rigid} \delta_{i+1,j}^t}{N_{elastic}^i} - \frac{u_{i+2}^t - u_{i+1}^t - \sum_{rigid} \delta_{i,j}^t}{N_{elastic}^{i+1}} \right] \quad (II.25)$$

which is the iteration equation.

Here  $C = \frac{\tau^2 k_i}{\rho \varepsilon}$ . Normally  $C$ , which is called the Courant's number, is very important in defining the stability conditions for the FD approach. In a linear limit, it is shown that a choice of  $\tau$  such that  $c = 1$  ensures optimal stability and convergence. However, in a nonlinear case, being the velocity smaller than the corresponding linear velocity at least for some values of the strain level, we should choose the time step so that  $c < 1$  is ensured, even though convergence of the method might be slightly poorer.

Given the displacement vectors at times  $t_0$  and  $t_1$  from the initial conditions ( $u_i(t = t_0), u_i(t = t_1)$ ) and knowing the number of HEs in the elastic state  $N_{elastic}^i$  in each mesoscopic cell and the total length of rigid elements  $\sum_{rigid} \delta_{i,j}$  at time  $t$  (i.e. the applied force at each mesoscopic cell), the iteration equation enables the displacement to be calculated for each node at every time  $t + 1$  as a function of the displacements at the previous times. Of course, the number of elastic microscopic elements should be updated at any time considering the pressure applied on the mesoscopic element and the transition parameters of each cell. Although this purely phenomenological approach doesn't consider a physical interpretation for the origin of hysteresis and it is not introducing explicitly the micro mechanical mechanisms of nonlinearity, it allowed to describe well several complicated engineering systems. In particular, using this approach, it is possible to reproduce conditioning effects (see Chapter 1), which are

not predicted in the classical hysteretic PM model described in the previous Section . In addition, physically based models could be used to justify a rigid to elastic transition, based on micro-contact mechanics [14].

### 4.3 Clapping model

The microscopic system in the clapping model is the parallel of two springs, as shown in Fig. II.11: one spring is purely linear, while the second is nonlinear with clapping properties as detailed in the following. When an external force is applied to the mesoscopic element, each of its microscopic constituents oscillates with a strain  $\Delta x_i$ , which varies with time and, due to the parallel arrangement of the elements, is the same for each of them.

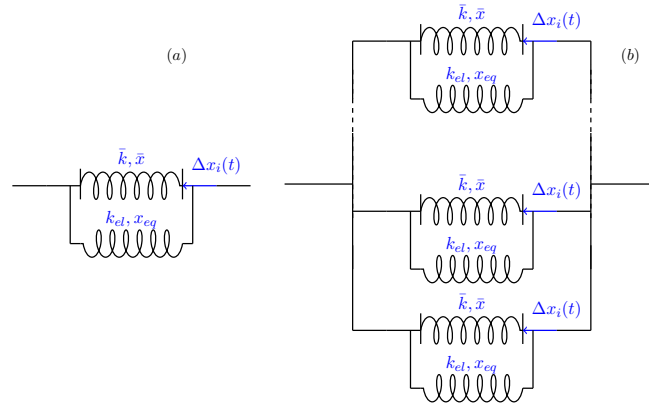


**Figure II.11** – Spring system representation of (a) One microscopic element in the clapping model; (b) The mesoscopic element built from a parallel arrangement of microscopic elements

#### 4.3.1 Microscopic equation of state

The total stress  $\sigma_{i,j}$  of the microscopic element of index  $j$  is linked to the strain  $\Delta x_i$  and it is the sum of contributions of both the elastic and clapping springs,  $\sigma_{el}$  and  $\sigma_{cl}$  respectively (see Fig. II.12).

$$\sigma_{i,j} = \sigma_{cl} + \sigma_{el}$$

The clapping element is a four state system, with elastic constants  $E = (k_1, k_2, -k_3, 0)$  and three transition points  $Z = (x_0, x_1, x_2)$ , which correspond to strain values. The microscopic stress is given by the following set of equations



$$\begin{aligned}
\sigma_{cl} &= k_1(\Delta x_i - x_0) && \text{if } \Delta x_i \leq x_o \\
\sigma_{cl} &= k_2(\Delta x_i - x_0) && \text{if } x_o < \Delta x_i \leq x_1 \\
\sigma_{cl} &= -k_3(\Delta x_i - x_2) && \text{if } x_1 < \Delta x_i \leq x_2 \\
\sigma_{cl} &= 0 && \text{if } \Delta x_i > x_2
\end{aligned} \tag{II.26}$$

The continuity of stress at the transition point between state 2 and 3, i.e. at  $\Delta x_i = x_1$ , implies a relation between  $k_2$  and  $k_3$

$$\begin{aligned}
k_2(x_1 - x_0) &= k_3(x_1 - x_2) \\
k_3 &= k_2 \frac{x_1 - x_2}{x_1 - x_0}
\end{aligned} \tag{II.27}$$

The stress due to the elastic spring is

$$\sigma_{el} = k_{el}(\Delta x_i - x_{eq}) \tag{II.28}$$

where  $x_{eq}$  corresponds to equilibrium length of the elastic spring and it can be calculated from the equilibrium condition applied to the clapping surface:

$$\begin{aligned}
\Delta x_i = 0 &\Rightarrow \sigma_{i,j} = \sigma_{cl} + \sigma_{el} = 0 \\
k_{el}(\Delta x_i - x_{eq}) + \bar{k}(\Delta x - \bar{x}) &= 0
\end{aligned} \tag{II.29}$$

with

$$\begin{aligned}
\bar{x} &= x_0, \bar{k} = k_1 && \text{if } \Delta x_i < x_o \\
\bar{x} &= x_0, \bar{k} = k_2 && \text{if } x_o < \Delta x_i < x_1 \\
\bar{x} &= x_2, \bar{k} = k_3 && \text{if } \Delta x_i < x_2 \\
\bar{x} &= 0, \bar{k} = 0 && \text{if } \Delta x_i > x_2
\end{aligned} \tag{II.30}$$

Consequently

$$x_{eq} = -\frac{\bar{k}}{k_{el}}\bar{x} \tag{II.31}$$

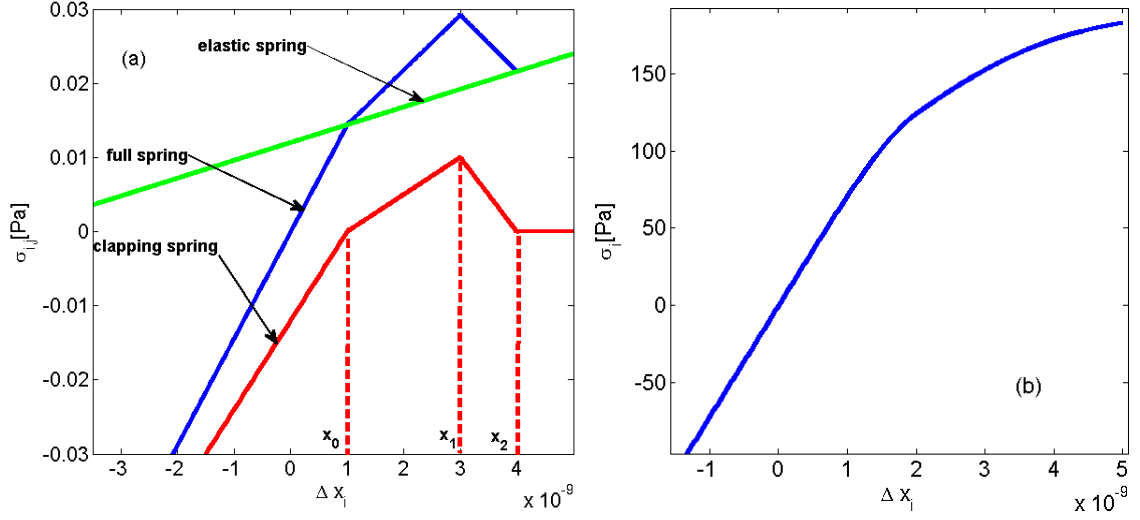


**Figure II.12** – Equation Of State for (a) One clapping microscopic element; (b) A mesoscopic cell, in the clapping model

The equation of state of a clapping element is finally defined by the following

$$\begin{aligned}
 \sigma_{i,j} &= k_{el} \left( \Delta x_i + \frac{k_1}{k_{el}} x_0 \right) + k_1 (\Delta x_i - x_0) & \text{if } \Delta x_i < x_0 \\
 \sigma_{i,j} &= k_{el} \left( \Delta x_i + \frac{k_2}{k_{el}} x_0 \right) + k_2 (\Delta x_i - x_0) & \text{if } x_0 < \Delta x_i < x_1 \\
 \sigma_{i,j} &= k_{el} \left( \Delta x_i + \frac{k_3}{k_{el}} x_2 \right) - k_3 (\Delta x_i - x_2) & \text{if } x_1 < \Delta x_i < x_2 \\
 \sigma_{i,j} &= k_{el} \Delta x_i & \text{if } \Delta x_i > x_2
 \end{aligned} \tag{II.32}$$

The driving variable in this model is the strain  $\Delta x_i$  at the clapping surface. As the physical mechanism of clapping is an atomic scale feature, i.e. due to interactions between atoms and molecules at the interface between two surfaces in contact,  $\Delta x_i$  is taken to be of order of inter-atomic distance. The microscopic equation of state of one single element is shown in Fig. II.12.(a).

#### 4.3.2 Mesoscopic equation of state

The average behavior of all the contact zones of the two surfaces of a crack can be obtained by defining a statistical ensemble of microscopic elements, which, as stated before, are arranged in parallel. The parallel arrangement is more practical in comparison with an arrangement in series which is leading to a broken system if even only one microscopic element is in state four. The statistical ensemble is defined by random attribution of transition points vector

$Z = \{z_{1,2} = x_0, z_{2,3} = x_1, z_{3,4} = x_2\}$  to each clapping element. Thus, when an external time dependent perturbation  $\Delta x_i(t)$  is applied to the system, each microscopic element supports the same strain  $\Delta x_i$ , but reacts with a different stress  $\sigma_{i,j}$  depending on its transition points and on the drive.

The total stress  $\sigma_i$  of the mesoscopic element could be calculated and depends on the number of microscopic elements in each of the states considered. The resulting mesoscopic equation of state is plotted as a function of the strain  $\Delta x_i$  in Fig.II.12.(b). This curve is obtained assuming the condition  $x_0 > 0$ .

The actual state of each element could be calculated at any time (i.e. any value of the strain) as in the previous case, being the only difference is that the PM space is a three dimensional space. Also, the approach to derive the macroscopic equations of motion is exactly the same as before and will not be repeated here.

#### 4.4 Adhesion model

The driving variable is again the separating distance  $\Delta x_i$  between the two surfaces of the element with two transition points ( $z_{12} = x_0, z_{23} = x_1$ ). Each microscopic element is defined, in addition to its transition points, by three equilibrium strains  $\Delta x_0 = 0, x_{01}, x_{02}$  and three elastic constants ( $k_1, k_2, k_3$ ).

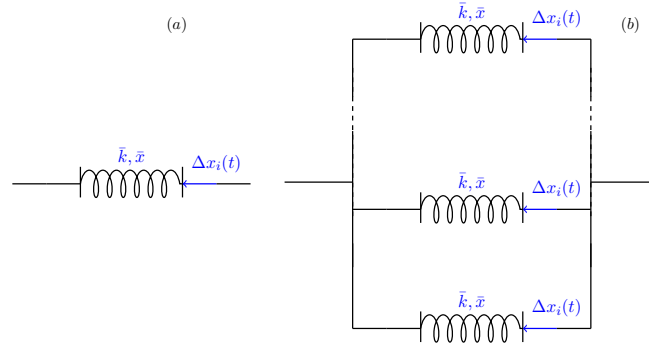


**Figure II.13** – Spring system representation of (a) One microscopic element in the adhesion model; (b) The mesoscopic element built from a parallel arrangement of microscopic elements

##### 4.4.1 Microscopic equation of state

We introduce here hysteresis in the adhesion model we discussed above. Therefore, one additional state appears in the microscopic stress-strain defined by the following set of equations.

$$\begin{aligned}
 \sigma_{i,j} &= k_1 \Delta x_i && \text{if } \Delta x_i < x_0 \\
 \sigma_{i,j} &= \begin{cases} k_2 \left( \Delta x_i - x_{01} \right) \\ k_3 \left( \Delta x_i - x_{02} \right) \end{cases} && \text{if } x_0 < \Delta x_i < x_1 \\
 \sigma_{i,j} &= k_3 \left( \Delta x_i - x_{02} \right) && \text{if } \Delta x_i > x_1
 \end{aligned} \tag{II.33}$$

and is presented in Fig. II.14.(a) The equilibrium strains are calculated from the continuity

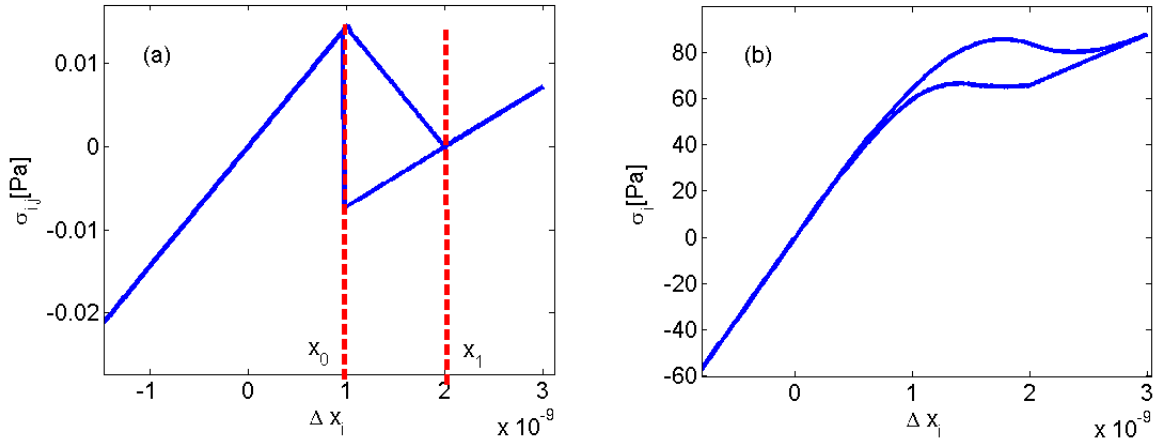


**Figure II.14** – Spring system representation of (a) One microscopic element in the adhesion model; (b) The mesoscopic element built from a parallel arrangement of microscopic elements

condition of the force at the transition points.

#### 4.4.2 Mesoscopic equation of state

An ensemble of MEs is defined (assigning randomly the transition points to each ME). Elements are arranged in parallel and an external time dependent perturbation  $\Delta x_i(t)$  is forced to the system. Each ME, thus, support the same deformation, but reacts with a different force, depending on its state, which is defined by the value of  $\Delta x_i(t)$ . The total force is calculated for each  $t$  and plotted vs.  $\Delta x_i$  providing the macroscopic equation of state plotted in Fig. II.14.(b).

## 5 Conclusions

Along this line, we presented some mechanisms related to the micro structure of different microinhomogeneous materials such as friction, adhesion and clapping, reported in literature to be behind the macroscopic nonlinear observed phenomena. All of these mechanisms, could be defined with microscopic multi state elements, and implemented in the multi scale phenomenological approach using the Preishah-Mayergoyz statistical description. The advantage of this semi-phenomenological procedure lies in one hand on its universality and capability to describe features such as end point memory and conditioning as a result of the use of a P-M distribution. On the other hand, it allows to relate results obtained from macroscopic measurements to some physical origin in the micro structure by introducing elementary units with physical parameters and governing rules. Results based on these physical considerations will be present in the next chapters.

---

## References

- [1] V. E. Nazarov, A. V. Radostin , L. Ostrovsky, and I. A. Soustova. Wave processes in media with hysteretic nonlinearity. part I. *J. Geophys. Res*, 99:23–887–23–897, 1994. [21](#)
- [2] T. Meurer, J. Qu , and L.J. Jacobs. Wave propagation in Nonlinear and Hysteretic media-A numerical study. *Int. J. Sol.Struc*, 39:5585–5614, 2002. [21](#)
- [3] V. Yu. Zaitsev, V. E. Nazarov , and I. Yu. Belyaeva. The equation of state of a microin-homogeneous medium and the frequency dependence of its elastic nonlinearity. *Acoust. Phys.*, 47:178–183, 2001. [21](#)
- [4] K. A. Van Den Abeele et al. On the quasi-analytic treatment of hysteretic nonlinear response in elastic wave propagation. *J. Acoust. Soc. Am.*, 101(4):1885–1898, 1997. [21](#)
- [5] I. D. Mayergoyz. Hysteretic models from the mathematical and control theory point of view. *J. Appl. Phys*, 57:3803–3805, 1985. [21](#), [26](#)
- [6] K. A. Van Den Abeele and S. Vanaverbeke. *Multiscale approach and simulation of wave propagation and resonance in media with localized microdamage*. Springer, 2007. [21](#)
- [7] P. Lejcek. Grain boundary segregation in metals. *Springer Series in Materials Science*, 136:239, 2010. [22](#)
- [8] A. Granato and K. Lucke. Theory of mechanical damping due to dislocations. *J. Appl. Phys*, 27:583, 1956. [vii](#), [22](#), [23](#)
- [9] G. G. Adams. Steady sliding of two elastic half-spaces with friction reduction due to interface stick-slip. *J. Appl. Mech*, 65:470–475, 1998. [24](#)
- [10] S. Delrue and K. Van Den Abeele. Three-dimensional finite element simulation of closed delaminations in composite materials. *Ultrasonics*, 52(2):315–324, 2012. [viii](#), [25](#)

- [11] V. Gusev, B. Castagnède, and M. Moussatov. Hysteresis in the response of a nonlinear bistable interface to continuously varying acoustic loading. *Ultrasonics*, 41:643–654, 2003. [viii](#), [25](#), [26](#)
- [12] R. A. Guyer and P. A. Johnson. Hysteresis, energy landscapes and slow dynamics: A survey of the elastic properties of rocks. *J. mater. proces. Manufac. Sci.*, 9, 2000. [26](#), [32](#)
- [13] K. R. McCall and R. A. Guyer. Equation of state and wave propagation in hysteretic nonlinear elastic materials. *J. Geophy. Res*, 99:23–887–23–897, 1994. [26](#), [27](#)
- [14] V. Aleshin et al. Characterization of hysteretic stress–strain behavior using the integrated preisach density. *Int. J. Nonlin. Mech.*, 43:151–163, 2008. [37](#)

---

---

# Chapter III

---

## Power laws behavior in nonlinear acoustic experiments

### 1 Introduction

The acoustic response of NME materials to an external dynamic excitation contains a signature of their strong characteristic nonlinearity [1]. This signature, used in nonlinear acoustic Non Destructive Testing (NDT) as an indicator of damage [2], can be extracted by quantifying nonlinear features observed in experiments such as higher order harmonics generation [3, 4], resonance frequency shift [5, 6] and loss in proportionality between input and output signals [7]. Different experimental methods have been developed to define a nonlinear indicator corresponding to each of these features[7–10].

Independently from the analysis method, experimental measurements show a power law dependence of nonlinear indicators  $y$  as a function of the excitation amplitude  $x$ :  $y = ax^b$ . The exponent of the power law is often used to distinguish between classical and nonclassical nonlinear behavior. However, as it will be discussed in details in the next Section, we show that a more detailed classification should be done. In any case, the parameters of the power law provide a physical interpretation of the nonlinear response. The exponent  $b$  is linked to the mechanisms responsible of the observed nonlinear response and thus allows to distinguish between different sources of nonlinearity. The coefficient  $a$  quantifies the nonlinearity strength.

It is however observed, in experimental data, that the power law behavior is valid only in a limited amplitudes range, thus a correct estimation and understanding of materials nonlinear responses can not be obtained before the validity range is well determined. In other words, a correct prediction is possible when measurements contain only effects connected to the sample nonlinearity, while all other effects due to saturation or noise have to be eliminated. Indeed, contributions of nonlinear features to the response of a propagation medium are often very small and the Nonlinear-to-Linear Ratio (NLR), defined as the ratio of the nonlinear over the linear signal, is often smaller than the Signal-to- Noise Ratio (SNR). Consequently, nonlinear effects could be submerged within the noise level, even though the recorded signals used to extract them might be well above noise. Since nonlinear effects increase as a power law of the driving amplitude:  $y \propto x^b$ , with  $b > 0$ , the noise issue can be easily overcome, in principle, by arbitrarily increasing the excitation amplitude  $x$ . However, experimental limitations related to amplification, frequency, transducers bandwidth, etc. always make it not practicable.



Therefore, noise should always be considered to define the performance of a given experimental method.

In addition to issues related with noise, all nonlinear indicators defined so far in the literature present the problem of being strongly dependent on the experimental set-up used. As an example, it is sufficient to move the receiver from one detecting point to another location to get a different value of the considered nonlinear indicator. Often, models do not exist to provide a solution as a function of the set-up, thus allowing for the reconstruction of the real nonlinearity of the specimen. It follows that nonlinearities could be compared only if the same experimental configuration is adopted, which is not always feasible. We will show in this chapter how to define a property of the nonlinear indicator which is set-up independent and thus provide a sort of "absolute" quantification of the nonlinearity.

Furthermore, signal processing issues might affect the correct determination of the power law behavior. For a given method of analysis, a not accurate choice of the signal processing parameters can lead to a wrong estimation of nonlinearity.

The three issues discussed indicate that the quantity which is directly measured in an experiment as the nonlinear signature could be far from being an absolute value of the nonlinearity present in the sample. Thus corrections are needed. In the present chapter, numerical and experimental results will be shown, in order to:

- define the threshold for nonlinearity detection, i.e. the minimum amplitude of excitation above which nonlinear measurements start to be meaningful. Different kind of noises which might be present in experiments are analyzed and discussed;
- discuss the effects of the experimental configuration on the definition of absolute nonlinearity indicators, give alternatives to reduce them and show that the power law exponent is indeed configuration independent;
- study the influence of signal processing parameters on the nonlinearity detection. We will focus on the effects of the choice of the reference signal on the nonlinearity measured when data are analyzed in the time domain using the Scaling Subtraction Method (SSM) [7].

## 2 Nonlinear measurements set-up and data analysis

### 2.1 Experimental set-up

Ultrasonic experiments are usually performed injecting in the sample through a proper ultrasonic transducer a propagating wave with arbitrary waveform. The source position is of course located on one of the accessible surfaces of the sample analyzed. A signal is detected in another position and the time signal could be decomposed into a linear and a nonlinear part.

In the experimental set-up adopted in this thesis, both in this and the following chapters, the source signal was generated with an arbitrary waveform generator connected to a linear 20x amplifier, with bandwidth from 1KHz to 500KHz. The resulting voltage signal was converted into strain using Piezoelectric Transducers (PZT). The PZTs were glued onto the sample using

either plasticine or PhenylSalicilate, after having tested their linear behavior in the strain ranges considered.

Receivers were also glued to the sample investigated. Again, PZT transducers were used, identical to the source transducer in order to guarantee the same response bandwidth. The strain waveform received, was converted into a voltage without pre-amplification and sent to an oscilloscope for data acquisition. Sampling rate was chosen to be very high (usually  $10\text{MSa/S}$ ) to allow a better data analysis. Signals were also averaged over multiple realizations to reduce the noise level.

In each experiment reported in the following, the linearity of the acquisition system was carefully tested. Experiments on linear reference samples with the same (or similar) geometries have been performed in the frequency and amplitude ranges adopted to characterize the nonlinear samples. In all cases, the nonlinear indicator was found to be amplitude independent and with a negligible value, i.e. within the noise level.

For each of the experiments performed during this thesis, details of the experimental parameters will be specified in the following.

## 2.2 Numerical set-up

In order to introduce and define the nonlinear indicators, we will show results obtained analyzing numerical data. Samples were simulated as a 1-D bar and their nonlinear properties were described using a Preisach-Mayergoyz based hysteretic model (discussed in chapter II).

We have simulated the response of a  $1 - D$  sample of 10 cm length, with Young modulus  $E = 72\text{GPa}$ , density  $\rho = 2700\text{ kg/m}^3$  and linear  $Q$  factor equal to 2000. A small scatterer of  $l = 0.5\text{mm}$  length was located in the center of the bar, i.e. at the position  $x = 5\text{ cm}$ . The intensity of nonlinearity is varied by changing the nonlinearity density parameter  $\lambda$  (defined in Chapter II). From the numerical point of view, the sample is discretized into  $N=1000$  Mesoscopic Elements. ME behave linearly (one state only), except those located in the damaged zone (i.e. where the nonlinear scatterer is located), which have been described using  $M=1000$  microscopic two states elements. Numerical results proved to be independent from the number of chosen elements.

In simulations, the excitation is assumed to be either a continuous wave (cw) of frequency  $\omega$  and amplitude  $A$  or a pulse. In both cases, the frequency (central frequency in the case of pulses) is chosen close to the first Young resonant mode of the considered sample ( $\omega = 25.9\text{KHz}$ ), in order to optimize excitation of the nonlinear features as done in experiments. Drive amplitudes are calculated to give strain levels within the sample in the range  $6 \cdot 10^{-9}$  to  $7 \cdot 10^{-7}$ , in agreement with experimental conditions. These strain amplitudes are obtained for an amplitude span corresponding to  $40\text{dB}$ .

Simulations provided the strain, displacement and velocity fields across the sample at each time and position. For the analysis, the temporal evolution of the velocity field is recorded at different positions, simulating the signals recorded by a PZT transducer in the sample. The choice to record velocities, rather than strains, was adopted for simplicity. However, velocity and strains have same phases and amplitudes ratio linked to the wave frequency. In the case of a cw forcing, as in experiments the analysis of the signals was performed using a time window

when standing wave conditions are reached. On the contrary, in the case of pulses, a short time window around the time of first arrival has been used in the analysis.

### 2.3 Data analysis and definition of the nonlinear indicator

In both numerical or experimental data, temporal signals  $u(t)$  are collected and analyzed. As mentioned they could always be decomposed into a linear and a nonlinear contributions:

$$u(t) = u_{lin}(t) + u_{nl}(t) \quad (\text{III.1})$$

The goal of such a procedure is to extract the nonlinear components from a temporal signal which is naturally dominated by the linear term. In experiments, the amplitude of  $u_{nl}$  is of the order of at most few percent of the linear signal amplitude.

The choice of the technique used to extract the nonlinear contribution in the recorded signal is extremely important in order to optimize the Nonlinear-to-Linear Ratio. Besides methods which exploit the dependence of the resonance frequency of the sample on the excitation amplitude [11, 12] (which are not discussed in this thesis), we could classify data analysis techniques in two main classes:

- a) an analysis in the time domain can be performed when the break of basic properties of linear elastic media, such as proportionality between input and output signals [13] and reciprocity [14], is used. In the former case, in particular, when the excitation amplitude is amplified by a factor  $k$ , the output response is not simply amplified correspondingly. These features are exploited by the Scaling Subtraction Method (SSM) [15, 16] and Nonlinear Loss of Reciprocity (NLR) based methods [17];
- b) an analysis in the frequency domain is usually based on the detection of higher order harmonics (or sidebands), generated during the propagation of an elastic wave, both continuous waves or pulses. In particular, when exciting the material at frequency  $\omega$ , the Fourier spectrum of the response contains components at integer multiples of the input frequency. Such techniques are termed Nonlinear Elastic Wave Spectroscopy methods (NEWS) [9]. NEWS can be exploited either using single mode experiments [18] or modulation experiments [19]. Note that in some cases subharmonics are also generated during the interaction of a large amplitude propagating wave with a closed crack [20].

For what concerns the experimental (and numerical) set-up required by the present work, the same procedure can be adopted to provide the signals to analyze, although with specific optimization for each method. We could state that one excitation is applied to the sample and one response signal is measured. A proper time windowing is then applied and the resulting signal is analyzed in different ways in order to extract a nonlinear physical quantity ( $y$ ), which is analyzed at increasing driving variable ( $x$ ).

### 2.3.1 Scaling Subtraction Method (SSM)

In the SSM analysis, one takes advantage of the influence of nonlinearity on the superposition principle. In fact, validity of the superposition principle is one requirement for a system to be linear. By considering a linear function  $F$ , if  $v(t) = Av_0(t)$  is the input function, we have

$$u_A = F(Av_0) = AF(v_0) = Au_0 \quad (\text{III.2})$$

Here the variable  $u$  denotes the output signal,  $F$  the transfer function,  $A$  the amplification factor.

The presence of micro-damage in a given medium generates nonlinearity and consequently breaks the superposition property. Therefore, if we excite a nonlinear system at amplitude  $A_0$ , small enough so that nonlinearity is negligible, the system will behave linearly and its response is  $u_0(t)$ . At a larger excitation amplitude  $A$ , the response  $u(t)$  of the same system is no longer equal to

$$u_{ref}(t) = \frac{A}{A_0} \cdot u_0(t) \quad (\text{III.3})$$

which would be the response of that system if it remains linear even at large amplitudes. Calculating the difference between the two responses as an indicator of nonlinearity, the SSM has proved to be very sensitive to damage detection and easy to set [15].

The details of the experimental (and numerical) SSM procedure consists therefore on the following steps. At first, the sample is excited at a very low amplitude (i.e. sufficiently low to provide negligible nonlinear effects) and the reference signal for amplitude  $A$  is defined from the recorded signal  $u_0$ , as in Eq. III.3.

As a second step, the output signal  $u(t)$  is recorded for a larger excitation amplitude  $A$  and the nonlinear scaled subtracted signal  $w$ , termed SSM signal, is introduced:

$$w(t) = u(t) - u_{ref}(t) \quad (\text{III.4})$$

The intensity of  $w(t)$  can be considered as the nonlinear variable to be calculated:

$$\begin{aligned} \theta_{SSM} &= \sqrt{\frac{1}{T} \int_0^T w^2(t_0 + t) dt} \\ x_u &= \sqrt{\frac{1}{T} \int_0^T u^2(t_0 + t) dt} \end{aligned} \quad (\text{III.5})$$

where  $T$  is the time window length and  $t_0$  the window initial time. Here, we have also calculated the intensity of the response signal  $x_u$ . Note that in the case of continuous waves, which are mostly discussed in this chapter, signals are roughly sinusoidal. Thus we have  $x_u \sim \frac{1}{\sqrt{2}} \max(u)$ . In the following the intensities will be often termed energies, as usually done in signal processing.

The normalized SSM nonlinear indicator is finally defined dividing the nonlinear energy with the energy  $x_u$  of the driving

### III.2 Nonlinear measurements set-up and data analysis

$$y_{SSM} = \frac{\theta_{SSM}}{x_u} \quad (\text{III.6})$$

When the procedure is repeated for different amplitude values  $A_i$  of the source function, both the nonlinear indicator  $y_{SSM}$  and the energy  $x_u$  become vectors.

Results of the application of the SSM procedure are illustrated in Fig. III.1, using numerical data obtained from simulations, as discussed in the previous subsection. Given a recorded temporal signal  $u(t)$  at amplitude  $A$ , we select a short time window of the signal (solid red line in Fig. III.1(a)) and compare it with the reference signal (dashed blue line) built for the same sample using a low amplitude signal and using Eq. III.3. The resulting SSM signal (Eq. III.4) is shown in Fig. III.1(b). Its energy  $y_{SSM}(A)$  is plotted as a function of the energy of the recorded signal  $x_u(A)$ , by calculating it at increasing values of the driving amplitude  $A$ : see Fig. III.1(c). The dashed line represents the data fitting using a power law. A better discussion will also be given in the next Section.

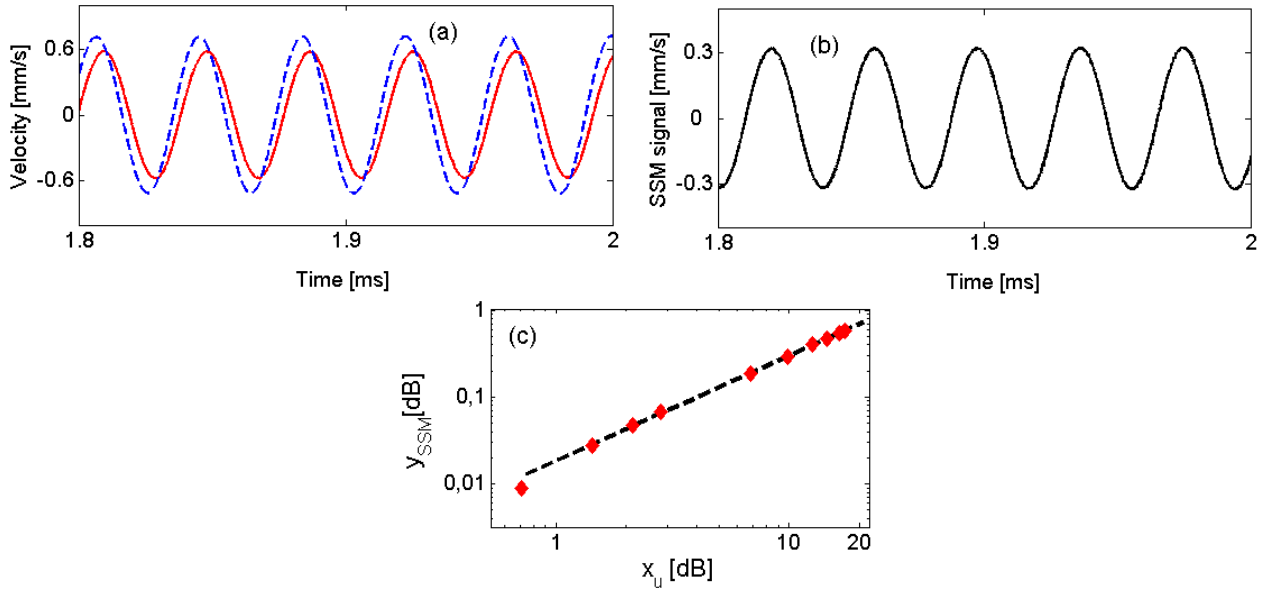


**Figure III.1** – Nonlinearity evaluation using the Scaling Subtraction Method - SSM. (a) Time signals calculated at a large amplitude excitation (solid red line) and reference signal (blue dotted line); (b) SSM signal; (c) Plot of the nonlinear indicator  $y_{SSM}$  vs. driving amplitude  $x_u$ .

#### 2.3.2 Nonlinear Elastic Wave Spectroscopy(NEWS) method

The same data set used for the SSM analysis is analyzed in the frequency domain. In this case, the generation of higher harmonics is exploited as indicator of nonlinearity.

The approach is based here on a standard procedure. First, the Fast Fourier Transform of the signal  $u(t)$  is performed and only the components of the frequency spectrum around the third harmonic, which is the most interesting component of the spectrum, are kept. These separated contributions are brought back to the time domain obtaining a signal  $u_{III}(t)$ .

The intensity of the filtered signal is extracted as a nonlinear variable

$$\theta_{FFT} = \sqrt{\frac{1}{T} \int_0^T u_{III}^2(t_0 + t) dt} \quad (\text{III.7})$$

After rendering it adimensional, the FFT nonlinear indicator is defined as:

$$y_{FFT} = \frac{\theta_{FFT}}{x_u} = \frac{\sqrt{\frac{1}{T} \int_0^T u_{III}^2(t_0 + t) dt}}{x_u} \quad (\text{III.8})$$

where  $T$  is the time window length and  $t_0$  the window initial time. The driving variable  $x_u$  is defined as the energy of the response signal due to the fundamental frequency contribution.

$$x_u = \sqrt{\frac{1}{T} \int_0^T u_I^2(t_0 + t) dt} \quad (\text{III.9})$$

Here  $u_I$  represents the signal obtained by band pass filtering the signal  $u(t)$  around the fundamental frequency. Note that, due to the low amplitude of the nonlinear components,  $u_I(t) \approx u(t)$ .

The implementation of the procedure using numerical data is illustrated in Fig. III.2. As mentioned, the signal is the same as reported in Fig. III.1. (a). The frequency spectrum, obtained performing the FFT analysis of the signal, is shown in Fig. III.2.(a); the band-pass filter range to obtain the  $u_{III}$  signal is highlighted (10KHz around the third harmonic). The resulting filtered signal is shown in Fig. III.2.(b). For each amplitude,  $y_{FFT}$  is calculated and plotted vs.  $x_u$  in Fig. III.2.(c). The solid line represents the fitting function.

Note that, assuming an hysteretic nonlinearity, for a given driving amplitude the ratio between  $y_{SSM}$  and  $y_{FFT}$  is around 40 dB. Therefore the nonlinear signal amplitude is much larger in the SSM analysis, thus a better estimation of the nonlinear indicator is expected. However the advantages of an analysis in the time domain are not the same for any kind of nonlinearity and a comparison between the methods should account also for experimental set up conditions.

## 3 Power law evolution of nonlinear indicators

### 3.1 Definition

Experiments and numerical data show that the dependence of  $y$  on  $x$ , at least in a certain range of excitation amplitudes, is a power law:

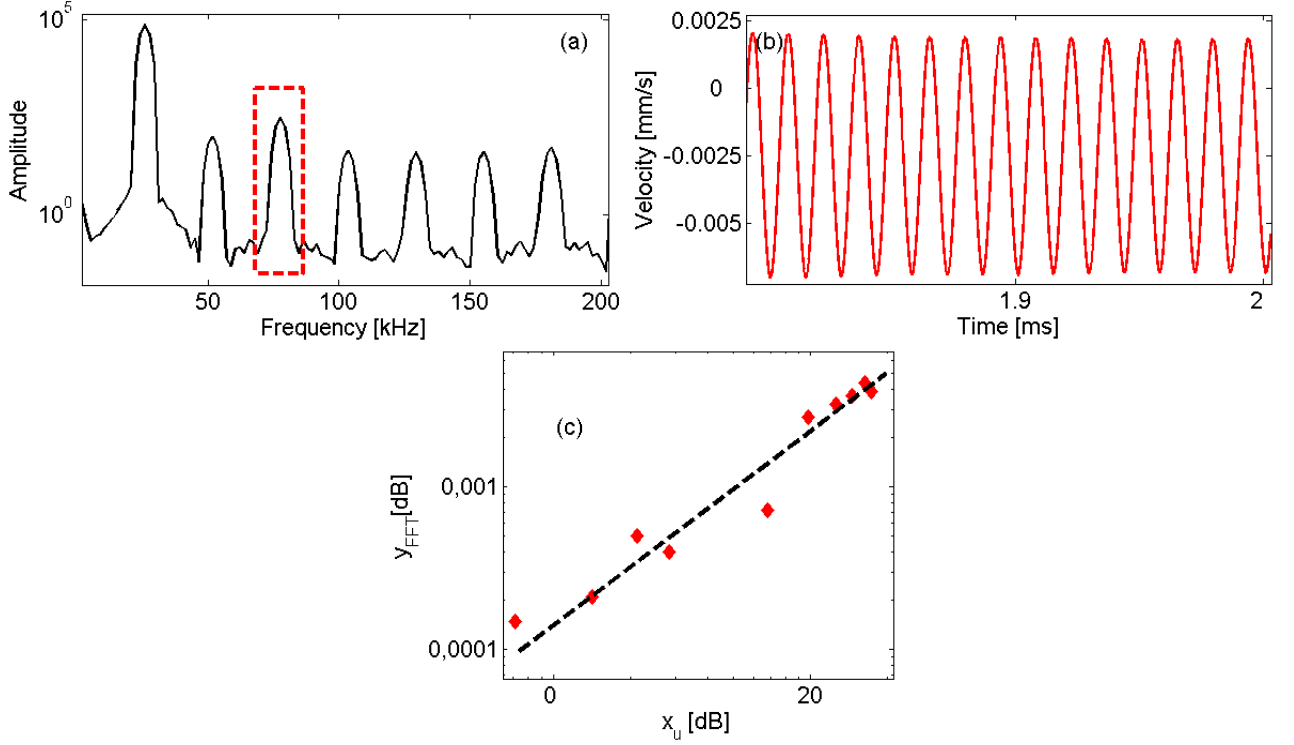


**Figure III.2** – Nonlinearity evaluation using the analysis in the frequency domain (Fast Fourier Transform - FFT). The time signal analyzed is the same as that used for the SSM analysis (see Fig. III.1). (a) frequency spectrum of the time signal, the filtering bandwidth is indicated; (b) filtered signal in the bandwidth of subplot(a): 10KHz around the third harmonic; (c) plot of the nonlinear signature  $y_{FFT}$  vs. driving amplitude  $x_u$ .

$$y = ax^b \quad (\text{III.10})$$

From this relation, the nonlinearity strength could be estimated by measuring the parameter  $a$ . The exponent  $b$  gives information about the kind of nonlinearity, i.e. an indication of the involved physical mechanisms, as discussed in the next Chapter.

The easiest way to verify the existence of a power law and to estimate the two parameters is to plot the dependence in a log-log scale:

$$\log(y) = \log(a) + b \log(x) \quad (\text{III.11})$$

Thus, in the log-log scale which will be always adopted in the following of this thesis, the exponent  $b$  represents the slope of the straight line and the parameter  $a$  could be found from its intersection with the  $y$  - axes.

### III.3 Power law evolution of nonlinear indicators

In Fig. III.3.(a),  $y_{SSM}$  is plotted vs  $x_u$  for different values of the hysteretic parameter  $\lambda$  (the larger  $\lambda$  is, the stronger the nonlinearity). Here and in the following we have used  $\lambda = [4 \times 10^{-5}, 1.6 \times 10^{-4}, 4 \times 10^{-3}] \text{Pa}^{-2}$ . In the log-log scale, data correspond to roughly parallel lines, thus indicating approximately the same exponent  $b$  for each  $\lambda$ . On the contrary, the coefficient  $a$  increases significantly with increasing nonlinearity. It can be noticed that on the full range of excitation amplitudes used in the simulation, data fit a straight line.

Using the same values of  $\lambda$ , Fig III.3.(b) shows  $y_{FFT}$  plotted vs  $x_u$ . In this log-log scale plot, only data for large driving amplitudes are distributed along almost parallel lines (solid lines represent the power law fitting), thus indicating approximately the same exponent  $b$  for each  $\lambda$ . Again, the coefficient  $a$  increases with increasing nonlinearity. However,  $y_{FFT}$  is almost constant for low excitation amplitudes (at least for some values of nonlinearity): the nonlinear signature is too small and effects linked to numerical accuracy in the FFT analysis appear. In the next subsection such an issue will be analyzed and discussed in details.

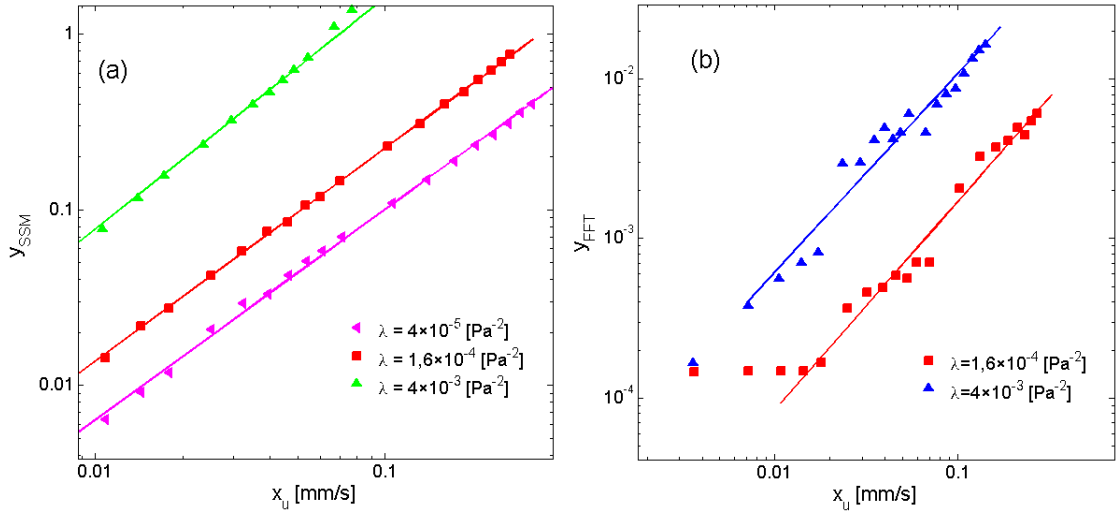


**Figure III.3** – Nonlinear indicator  $y$  as a function of driving amplitude  $x_u$  for different nonlinearity strengths  $\lambda$ : (a) SSM analysis; (b) FFT analysis.

It is important to observe that the exponent  $b$  corresponding to best fit ( $b \approx 1$ ) is the same using both approaches. The better quality of results using the SSM procedure is also to be expected. Indeed, the SSM signal contains nonlinear contributions to all the generated higher harmonics and to the fundamental frequency as well, while FFT based methods filter the fundamental component out and keep only the contributions to some harmonics. It is usually observed in experiments that nonlinear contributions at the fundamental frequency often have a large magnitude, compared to harmonics, mostly due to nonlinear attenuation and conditioning effects. Thus, the nonlinear signal obtained using the SSM has amplitude which could be one order of magnitude larger than harmonics.



## 3.2 Experimental problems and motivation

A huge amount of experimental studies in the literature confirm the power law dependence of nonlinear indicators on the driving amplitude independently from the adopted analysis method. However, in practice, several problems arise when trying to exploit experimental data in order to extract a useful information about nonlinearity.

Such problems are linked to the definition of the correct range of amplitudes in which a fit with a power law function is possible and to the transducers location.

### 3.2.1 Noise and saturation effects

Fitting experimental data using a power law is valid only in a limited region as stated before, this could be due to noise and/or saturation effects.

In this context, the effect of noise upon low amplitude measurements is more of interest. This effect was encountered in an experiment performed to measure the nonlinearity of stainless steel disks with a crack and was found to be characteristic of several measurements reported in the literature.

In the experimental analysis, we have considered a cracked steel disk with radius of 15cm and thickness of less than 1cm (see Fig. III.4.(a)). The linear elastic properties of the sample have been evaluated by the producer, providing longitudinal and shear wave velocities  $c_l \approx 5700m/s$  and  $c_s \approx 3100m/s$ . PZT disks, with working frequency at 100KHz were glued to the lateral surface of the disk, so that the direct source-receiver path was crossing the center of the disk. The crack (about 2mm long and 1  $\mu m$  wide) was approximately in the center of the disk and crossing from the upper to the lower surface.

Using the experimental set up described previously, the SSM indicator was measured at increasing amplitudes of excitation and results are shown in Fig. III.4.(b). Instead of a good power law behavior, three regions could be identified:

- At low amplitudes, experimental noise is generating a non negligible contribution to the nonlinear signal. We noticed that, in this range,  $y_{SSM}$  is constant with increasing amplitude and consequently is not measurable. It is important to determine the threshold at which noise becomes negligible, in order to get a good estimation of the power law exponent  $b$ , which could be in generally underestimated if points in the noise region are considered in the fitting.
- At large amplitude values we observe saturation effects. The plot of the nonlinear indicator  $y_{SSM}$  vs. the driving amplitude  $x_u$  does not fit a power law any more. We observe a bending, which is due here to saturation of the amplitude of the detected signal, but could also be saturation of the amplitude of the nonlinear signal, as shown in other different cases found in the literature. This effect could be due to the experimental set-up saturation, e.g. due to degradation of the contact between transducer and sample, or to physical saturation of nonlinearity. In principle it is very difficult to determine which of the two origins is the most important. Nevertheless, it is again important to avoid using points at the transition between nonlinear and saturated regimes in order to avoid under or overestimation of the nonlinear parameters.

### III.3 Power law evolution of nonlinear indicators

- At intermediate amplitudes, the behavior of the nonlinear indicator is a power law over an amplitude range of about 15dB. It should be mentioned that, in case the power law is restricted to a very narrow amplitude range, the power law analysis loses of course its meaning.

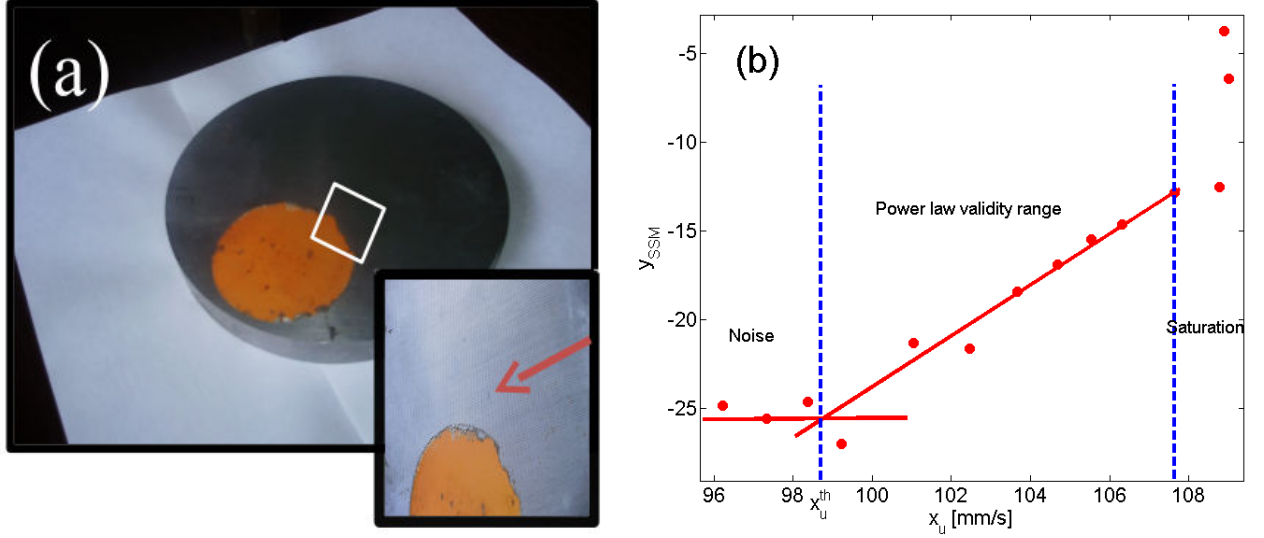


**Figure III.4** – Results from an experiment performed on a cracked steel disk excited with a CW at frequency  $100\text{KHz}$ . (a) Picture of the sample we used to perform the experiment; (b)  $y_{SSM}$  plotted as a function of the driving  $x_u$ . Data start to be meaningful at the amplitude threshold  $x_u^{th}$  and fit a power law only in the intermediate amplitude range.

We also mention that an additional effect has been observed in the literature (as it will be discussed later), linked to the choice of parameters in the data analysis. The SSM analysis applied on a slightly damaged concrete sample excited with a CW at a frequency close to its resonance frequency, shows that at small amplitudes of excitation the SSM indicator does not fit a power law if the lowest excitation amplitude  $A_0$  was not sufficiently small. In that case, the propagating wave already excites slightly the nonlinearity of the sample and  $u_0(t)$  contains a nonlinear contribution. As a consequence, as it will be shown later, the dependence of  $y_{SSM}$  on  $x$  at small amplitudes could predict a higher exponent where  $b$  could be overestimated. Thus, the choice of the reference signal is of great importance in order to optimize the measurement of  $y_{SSM}$ .

All these experimental observations, indicate that the amplitude range validity of the power law dependence should be accurately tested before measurements. In this thesis (and particularly in this chapter) the quantitative definition of a correct amplitude range is, at least partially, addressed.

#### 3.2.2 Dependence on the experimental configuration

As already mentioned, experimental results indicate that the choice of the experimental configuration is not irrelevant for the determination of the nonlinearity.

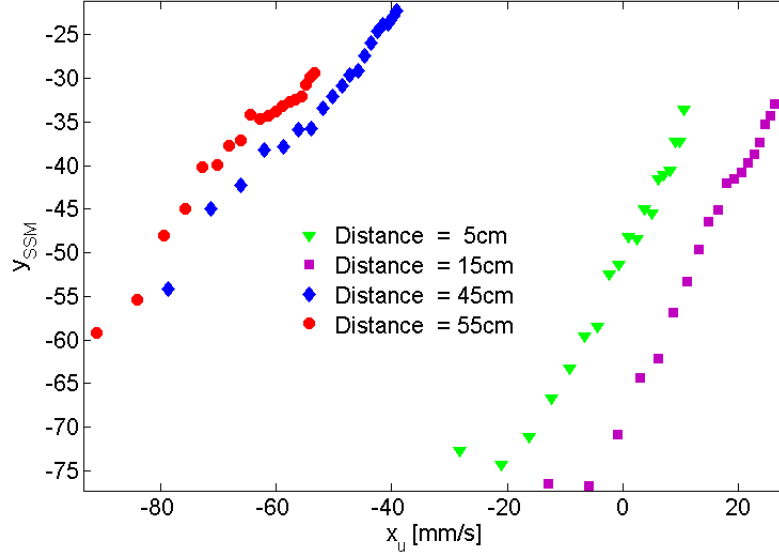


**Figure III.5** – Results from an experiment performed on a long concrete bar with receivers located in different positions. In all cases the dependence of the nonlinear indicator on the excitation is a power law function, but the measured nonlinearity strongly depends on the relative distance separating the source and the receiver.

Here, we limit ourselves to show some experimental data taken from the literature. They refer to a concrete bar (100x10x150 cm long). The SSM measurement was performed by positioning the receiving transducer at different locations from the source. As shown in Fig. III.5, the power law behavior is always valid, but the strength of the nonlinearity depends on the relative distance between source and detector. consequences of such a change in the nonlinear behavior appear when comparing nonlinearity in different samples.

## 4 Amplitude threshold for nonlinearity detection

Within this Section, we numerically study the effects of experimental noise on the nonlinearity detection. As we have seen, depending on the noise level, the nonlinear response could fall within noise at low amplitudes. Here we characterize the effects of noise and define how it is possible to calculate the smallest amplitude (threshold) at which nonlinear features in the detected signal become meaningful.

### III.4 Amplitude threshold for nonlinearity detection

---

To introduce the experimental noise in simulations, we use two approaches to contaminate the results of simulations to obtain effects comparable to noise due to equipment or to the environment. In both cases, a white additive noise is used. Its basic properties are:

- the noise is additive. If the received signal resulting from the simulation without noise is  $u(t)$ , noise is added as a random time signal  $\eta(t)$  which is statistically independent from  $u(t)$ . Thus the signal to be used in the analysis is  $u'(t) = u(t) + \eta(t)$ ;
- the noise is white. Its average value is zero ( $\langle \eta(t) \rangle = 0$ ) and its power spectral density is flat. The autocorrelation of the noise in the time domain is zero for any non-zero time offset:  $\langle \eta(t)\eta(t') \rangle = \mu\delta(t, t')$  where  $\delta$  is the usual delta function.

In practical terms, noise in the signals is generated as an additive stochastic variable with zero average, added to the signal after the simulations are performed. Including noise in the source function or random distributions in the sample properties, i.e. in the simulation process, provides equivalent results when noise is small.

We will consider here the combination of two types of additive white noises. The first is used to simulate ambient noise. We introduce a signal  $\eta_a(t)$  which is at constant amplitude. Its strength  $n_a$  is measured in mm/s when the signal  $\eta_a(t)$  is a velocity. The second is to simulate noise due to equipment, which is proportional to the amplitude of the injected wave. Since the reference signal is proportional to the input, we define the equipment noise  $\eta_e(t)$  with amplitude proportional to the reference signal. Thus, we define it as an adimensional quantity, with strength  $n_e$ .

The numerical analysis is performed on the noisy signal  $u'(t)$  defined as:

$$u'(t) = u(t) + \eta_a(t) + \eta_e(t) \max[u_{ref}(t)] \quad (\text{III.12})$$

The response  $u(t)$  of the propagation medium in absence of noise is obtained using the Preisach-Mayergoyz approach based hysteretic model[21–24].

In this Chapter, we first show the existence of a strain amplitude threshold for nonlinearity detection as a consequence of the presence of noise, which is similar to that observed in experiments and provides the explanation of the indicator behavior at low amplitudes. We also describe the dependence of such threshold on the method adopted for data analysis (SSM or FFT). Finally, we will discuss the sensitivity of both time domain and frequency domain approaches to the two different types of noise and derive a method to calculate a driving amplitude threshold for nonlinearity detection.

## 4.1 Equipment noise

### 4.1.1 Noise quantification

In the absence of ambient noise, the noisy signal in Eq. III.12 contains only the term proportional to the driving, i.e. to the maximum amplitude of the signal:

### III.4 Amplitude threshold for nonlinearity detection

$$\begin{aligned} u'(t) &= u(t) + \eta_e(t) \max[u_{ref}(t)] \\ u'(t) &= u(t) + n_e f(t) \max[u_{ref}(t)] \end{aligned} \quad (\text{III.13})$$

Here  $f$  represents the white noise function with zero average and autocorrelation 1, while  $n_e$  is the noise strength.

The noise level allows estimating the signal-to-noise ratio. However, noise is also propagating in the definition of the nonlinear indicators. In order to understand its effect on the determination of the nonlinearity, the noise level on the SSM and bandpass filtered signals used in the definition of the nonlinear indicators should be properly calculated.

- Noise in the SSM signal  $w(t)$  is a sum of two identical noise contributions  $n_e f(t) \max[u_{ref}(t)]$  due to both the large amplitude and the reference signals  $u(t)$  and  $u_{ref}(t)$  respectively (see Eq. III.4). It follows:

$$w'(t) = w(t) + \eta_e(t) \max[u_{ref}(t)] - \eta_e(t) \max[u_{ref}(t)] \quad (\text{III.14})$$

The strength of the resulting noise should be properly rescaled. In fact, given two identical white noises with autocorrelations  $\Psi$ , the autocorrelation of the noise resulting from the sum of the two is  $\sqrt{2}\Psi$ . That means that the actual equipment noise in the SSM signal will have strength:

$$n_e^{SSM} = \sqrt{2} \cdot n_e \quad (\text{III.15})$$

- The noise strength on the filtered signal  $u_{II}(t)$  is much smaller than the noise strength  $n_e$  on the response signal  $u(t)$ , since the noise is band-pass filtered as well. For the case considered here, the noise on the filtered signal has strength  $n_e^{FFT} \sim 0.04 \cdot n_e$ , where the coefficient 0.04 is obtained filtering an additive white noise variable in a  $10\text{KHz}$  frequency window.

It follows that the effects of noise on the SSM signal are stronger in absolute terms than on the FFT signal. In real experiments, equipment noise is found to be of the order of a few percent of the signal, which corresponds to noise levels in the range -50 to -30 dB. In some cases, we could even expect noise up to -20dB due to the equipment.

#### 4.1.2 Equipment noise effects on SSM and FFT analysis

To show the effects of equipment noise on nonlinear measurements, both SSM and FFT indicators are plotted, in Fig. III.6, for  $\lambda = 1.6 \cdot 10^{-4}$  and considering different equipment noise levels  $n_e$  in the experimental noise range.

The curves do not show a general power law behavior. However, splitting the amplitude range into two regions, it is possible to fit with independent power laws at low and high

### III.4 Amplitude threshold for nonlinearity detection

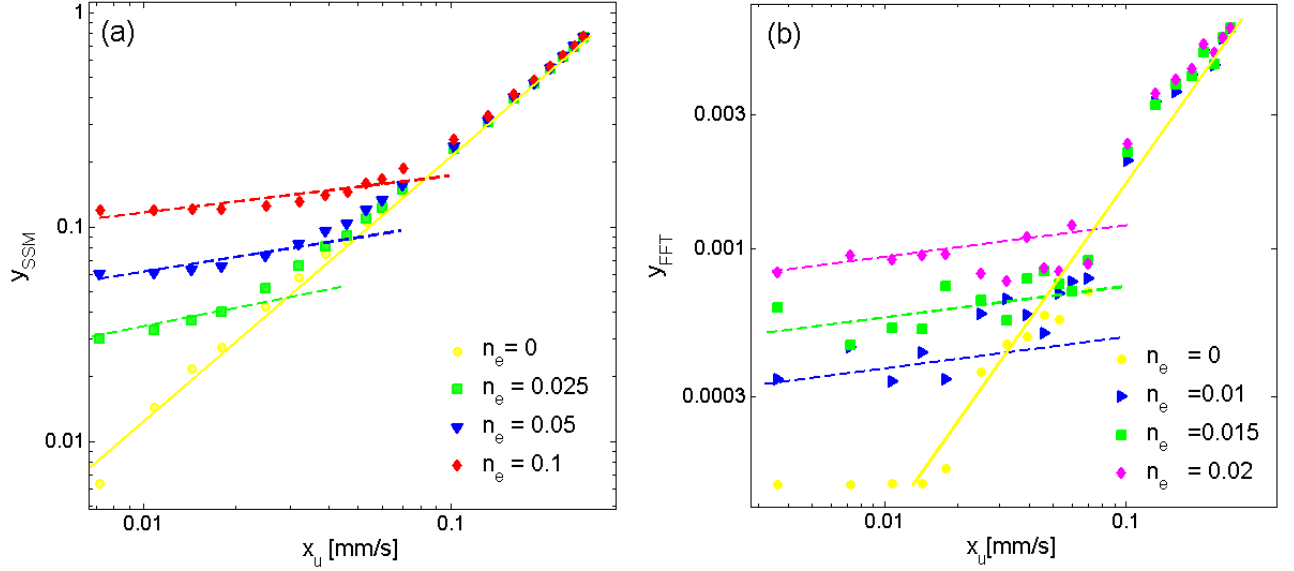


**Figure III.6** – Nonlinear indicator  $y$  as a function of driving amplitude  $x_u$  for nonlinearity strength  $\lambda = 1.6 \cdot 10^{-4}$  and different equipment noise levels  $n_e$ : (a) SSM analysis; (b) FFT analysis.

amplitudes. Fitting functions are reported as dashed/solid lines in Fig. III.6. The detection threshold, defined as the intersection between the solid and dashed fitting lines, moves to higher driving amplitudes, i.e. on the  $x$  axes, when increasing noise.

In the SSM analysis, up to a noise amplitude of order of 10% of the signal amplitude, corresponding to  $-20dB$ , we can still measure the strength of nonlinearity  $a$  and the exponent  $b$ , as shown in III.6(a). Both power law parameters are noise independent:  $a_{SSM} = 0.07$  and  $b_{SSM} = 1.07$  for all curves.

Larger noise effects are noticed when the FFT analysis is performed (Fig. III.6 (b)). The explanation comes from the fact that white noise has a flat spectrum in the frequency domain. Adding the frequency components of the noise to the ones of the response signal, the third harmonic amplitude of  $u(t)$ , which is relatively small, can be easily smaller than the third harmonic amplitude of  $\eta_e(t)$ , thus submerged into noise. Thus, the threshold is already very large at 1% noise, i.e. at  $-40dB$ , as represented as blue triangles in Fig. III.6.(b). However, once the nonlinear signal emerges from noise, the nonlinearity parameters are noise independent:  $a_{FFT} = 0.002$  and  $b_{FFT} = 1.08$ .

Effects observed analyzing numerical data are similar to those experimentally observed (see Fig. III.4).

## 4.2 Ambient noise

Unlike equipment noise, which provides qualitatively similar effects on the detection threshold using FFT and SSM analysis, we will see that ambient noise has to be considered differently depending on the method of analysis used.

### 4.2.1 Ambient noise effects on SSM analysis

For what concerns the time domain analysis, given the responses  $u_0(t)$  and  $u(t)$  at the lowest excitation amplitude  $A_0$  and at large amplitude  $A$  respectively, the ambient noise in the reference signal  $u_{ref}(t)$  defined by equation III.3 is obtained amplifying by a factor  $k = A/A_0$  the ambient noise level  $n_a(t)$  in the lowest excitation amplitude signal  $u_0(t)$ . Thus, in the absence of equipment noise, the noisy SSM signal becomes:

$$w'(t) = w(t) + n_a(t) - kn_a(t) = w(t) + n_a(t) - \frac{A}{A_0}n_a(t) \quad (\text{III.16})$$

In a first approximation, if we assume the system to have a linear transfer function, we can consider the following proportionalities:

$$\begin{aligned} \max(u_{ref}) &\propto A \\ \max(u_0) &\propto A_0 \end{aligned} \quad (\text{III.17})$$

Thus,

$$w'(t) = w(t) + n_a(t) - \frac{n_a(t)}{\max(u_0)} \max(u_{ref}) \quad (\text{III.18})$$

It follows that, neglecting  $n_a(t)$  in equation III.16, which is correct, except for small amplitudes (i.e. when  $\max(u) \gg \max(u_0)$ ), Eq. III.18 is reduced to

$$w'(t) = w(t) - \frac{n_a(t)}{\max(u_0)} \max(u) \quad (\text{III.19})$$

As a result, the ambient noise is equivalent to an equipment noise of intensity

$$n_e = \frac{n_a}{\sqrt{2} \max(u_0)} \quad (\text{III.20})$$

where the factor  $\sqrt{2}$  is due to the additivity of two identical noises in the  $w$  signal when equipment noise is present (as previously discussed).

In Figure III.7(a),  $y_{SSM}$  is plotted as a function of the driving  $x_u$  for  $\lambda = 1.6 \times 10^{-4}$  and different noise choices.

### III.4 Amplitude threshold for nonlinearity detection

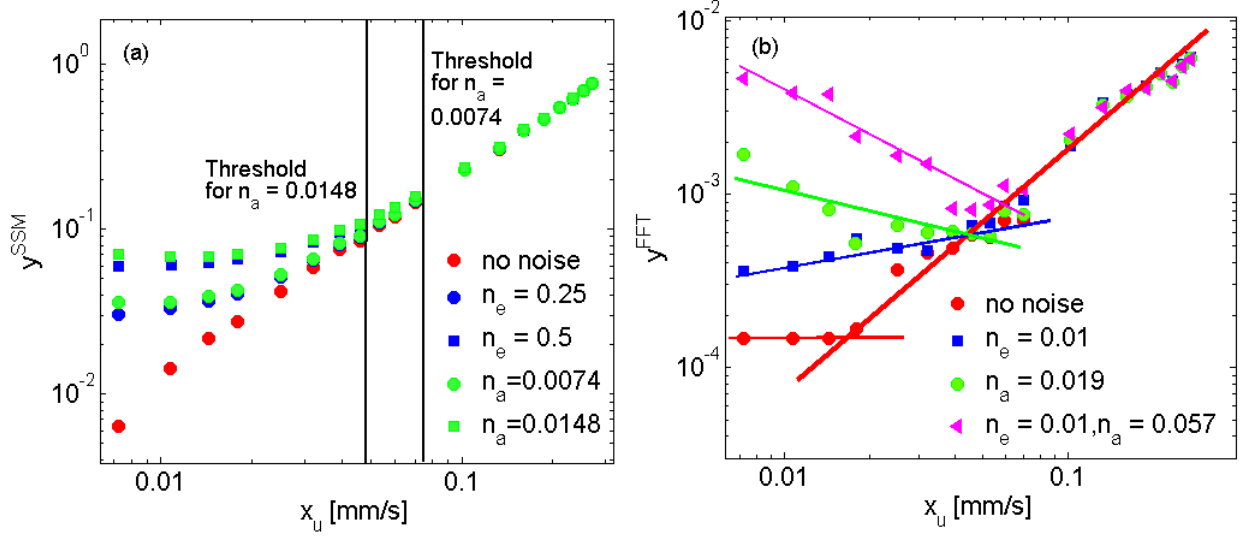


**Figure III.7** – Nonlinear indicator  $y$  as a function of driving amplitude  $x_u$  for nonlinearity strength  $\lambda = 1.6 \times 10^{-4}$  and different noise choices: (a) SSM analysis; (b) FFT analysis.

It can be seen that, both in the case of  $n_a = 0.0074$  mm/s and  $n_a = 0.0148$  mm/s, the ambient noise provides the same results as those obtained with an equipment noise of amplitude given by Eq. III.20, for all amplitudes larger than the threshold amplitude, i.e. on the right of the vertical solid lines.

At low amplitudes discrepancies are evident, given by non negligible effects of the term  $n_a(t)$  in Eq. III.18.

#### 4.2.2 Ambient noise effects on FFT analysis

The ambient noise in the FFT analysis is the same for each excitation amplitude, i.e. with the same strength. Thus the Ambient Noise to Signal Ratio decreases with amplitude  $A$ :

$$ANSR_A = \frac{n_a}{\max[u]} \quad (\text{III.21})$$

In this case, if we consider a nonlinearity detection threshold at amplitude  $x_u = \Gamma$  which is due to equipment noise contribution  $\eta_e(t)$  to the FFT signal, ambient noise is significant only if it gives stronger effects than equipment noise, i.e. produces a new threshold at an amplitude larger than  $\Gamma$ .

Recalling that  $x_u^2$  is the integral of  $u^2(t)$ , and  $u(t)$  is roughly sinusoidal, we obtain

$$x_u^2 = \frac{1}{2}(\max[u(t)])^2 \Rightarrow \max[u(t)] = \sqrt{2}x_u \quad (\text{III.22})$$



### III.4 Amplitude threshold for nonlinearity detection

---

When the driving amplitude is such that  $x_u = \Gamma$ , then the Ambient-Noise to Signal Ratio is given by

$$ANSR_\Gamma \sim n_a / \sqrt{2}\Gamma \quad (\text{III.23})$$

Thus, the condition for having effects on the threshold due to ambient noise is that:

$$ANSR_\Gamma > ENSR_\Gamma \Rightarrow n_a \geq \sqrt{2}\Gamma n_e \quad (\text{III.24})$$

where the Equipment-Noise to Signal Ratio is

$$ENSR_\Gamma = \frac{n_e \cdot \max[u(t)]}{\max[u(t)]} = n_e \quad (\text{III.25})$$

In Figure III.7.(b), we consider  $\lambda = 1.6 \times 10^{-4}$  and effects of different noise combinations on the FFT analysis. In all cases, we notice that the presence of noise causes an increase in threshold (as already discussed).

When each noise is considered separately, if the respective intensities of ambient and equipment noise are such to satisfy Eq.III.24, the two noises are expected to have similar effects, i.e will produce approximately the same threshold for nonlinearity detection. In this figure, an ambient noise of strength  $n_a = 0.019$  (green circles) provides the same threshold  $\Gamma$  as an equipment noise of strength  $n_e = 0.01$  (blue squares). Notice that in experiments the level of ambient noise is generally smaller than one percent, while the equipment noise level of two percent is generally reasonable.

On the other hand, when both noises are present at the same time, the threshold level imposed by equipment noise alone (magenta triangles) is increased with the introduction of an ambient noise only if the latter satisfies the inequality given by Eq. III.24, i.e.,  $n_a$  is much larger (blue squares). Otherwise (not reported), the threshold remains the same.

## 4.3 Discussion

The analysis reported in the previous Subsection indicates that:

- noise can hide the presence of nonlinear features when the excitation amplitude is below a given threshold, which is often much larger for FFT analysis, due to the lower NLR (nonlinear-to-linear signals ratio);
- ambient noise is always negligible in the case of FFT analysis, since its effect decreases with amplitude, thus it becomes soon negligible with respect to equipment noise;
- ambient noise could be very important in the case of SSM analysis, especially when the lowest excitation amplitude is very small. In fact, the ambient noise is equivalent to an equipment noise with amplitude inversely proportional to the lowest excitation amplitude (see Eq. III.20). Thus, a difficulty which is related to the choice of the lowest excitation

### III.4 Amplitude threshold for nonlinearity detection

amplitude  $A_0$  comes to the fore in performing SSM analysis: the lowest excitation level could not be increased arbitrarily, since it should be such that the elastic behavior is roughly linear at that amplitude. Increasing  $A_0$  in order to reduce effects of ambient noise can easily lead to crossing the linear limit in the response of the medium which corresponds to include nonlinear features already in the reference signal, resulting in deficiency of the method (reducing the NLR), as shown in details in the next Section.

Finally, we wish to discuss the relation between the threshold for nonlinearity detection and the SNR (Signal-to-Noise Ratio). Thus, in Fig. III.8, we compare the NLR (Nonlinear-to-Linear Ratio) at the threshold of nonlinearity detection (equivalent to the value of the nonlinear indicator at threshold:  $y_{th} = ax_{th}^b$ ), with the noise strength on the nonlinear signal ( $w$  or  $u_{III}$ , in SSM and FFT, respectively).

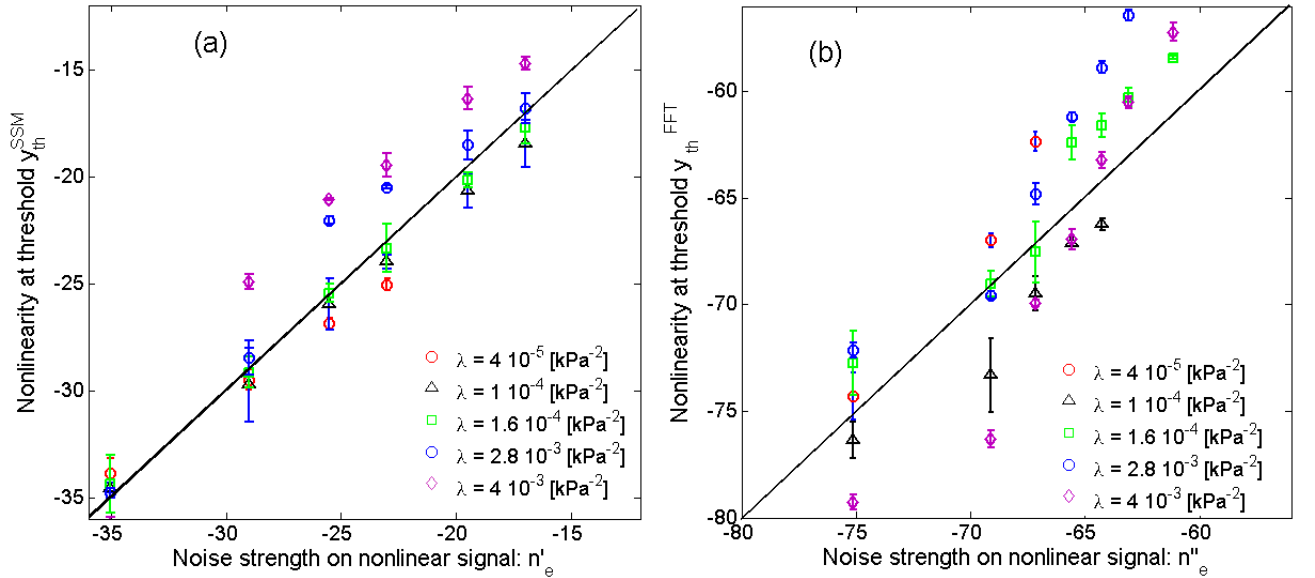


**Figure III.8** – Nonlinear-to-linear signals ratio at the threshold level vs. strength of the noise contribution to the nonlinear signal. The solid line indicate when the two are identical. (a) SSM analysis; (b) FFT analysis.

We have considered an equipment noise of varying strength  $n_e$ ; the corresponding noise strength is  $n_e^{SSM} = \sqrt{2}n_e$  and  $n_e^{FFT} = 0.04n_e$ , for SSM and FFT signals respectively. Data show that for low values of  $\lambda$ , nonlinearity can be detected when  $y_{th} = n_e^{SSM/FFT}$  (corresponding to the diagonal solid line), i.e. as soon as the nonlinear signal is larger than the "nonlinear" noise. However, for larger values of  $\lambda$ , to have detection of the nonlinearity the NLR should be larger than the NonLinear Signal-to-Nonlinear Noise ratio (points are above the diagonal), possibly due to saturation effects in the model used.

#### 4.4 Experimental results

In this Section, dealing with experimental validation of the numerical results previously discussed, we analyze data recorded from two different experiments taken from literature. We wish to prove that:

- In both SSM and FFT measurements, an amplitude threshold for nonlinearity detection is identifiable. Such a threshold diminishes when increasing the nonlinearity of the system for the same experimental set-up, i.e. the same noise level;
- the threshold for nonlinearity detection in SSM is dependent on the amplitude of the excitation used to define the reference signal.

First, we have analyzed data collected in a previously performed experiment [25]. The considered sample was a prism obtained by joining together two identical concrete cubes (20x20x20 cm<sup>3</sup>). The interface between the two cubes was a thin layer of a cement paste (about 4 mm thick). Transducers (emitter and receiver) were glued using PhenylSalicilate both on the same lateral surface on the two opposite sides with respect to the interface. Excitation was chosen as a sinusoidal burst (10 cycles) at 55.5KHz, with amplitudes varying in the range of 10<sup>-8</sup> to 10<sup>-6</sup> strain amplitude. The system was located in a Mechanical Testing Machine to control a quasi static load of the sample (hence inducing damage localized at the interface). Measurements were performed following the same procedure adopted in the numerical analysis. Recorded data were analyzed in a 200  $\mu$ s time window.

The SSM and FFT indicators are reported in Fig. III.9 as a function of the excitation energy  $x_u$  for three levels of the applied load (2, 5 and 10 MPa). Note that early damage starts at a load of 4 MPa, while rupture occurs at about 15MPa [26]. Both  $y_{SSM}$  and  $y_{FFT}$  depend on  $x_u$  as a power law with exponent 1. For what concerns the analysis in the time domain (subplot (a)), nonlinearity is detected for the three cases, even though hardly detectable for the undamaged (lower load) case. The detection threshold is always much larger when data are analyzed in the frequency domain (subplot (b)) and it is not possible to detect the nonlinearity of the undamaged (lower load level) system. Note that measurements were performed under load, thus affected by a significant noise level, responsible of the scattering of data.

A second experiment was conducted on a less noisy system. The system was a fiber reinforced concrete prism (1 m long and 10x10 cm<sup>2</sup> cross section), with different levels of corrosion of the bar induced electrochemically and uniformly distributed. The sample was equipped with two transducers glued on the same face of the prism, at a distance of 40 cm one from the other. Excitation was chosen as a burst composed of 10 sinusoidal cycles at 35KHz. The use of narrow band transducers did not allow us to perform a significant analysis of the results in the frequency domain, thus only SSM data will be presented. Data acquisition and processing was performed as discussed in the previous Sections. Results reported in Fig. III.10 confirm the information given in Fig. III.9: increasing damage increases nonlinearity and the detection threshold moves to lower values of excitation amplitude. The observation that the threshold of detection is in all 3 cases at  $y_{SSM} \approx 0.03$  is to be expected as a consequence of the use of the same experimental set up for all three cases, thus the same experimental noise level.

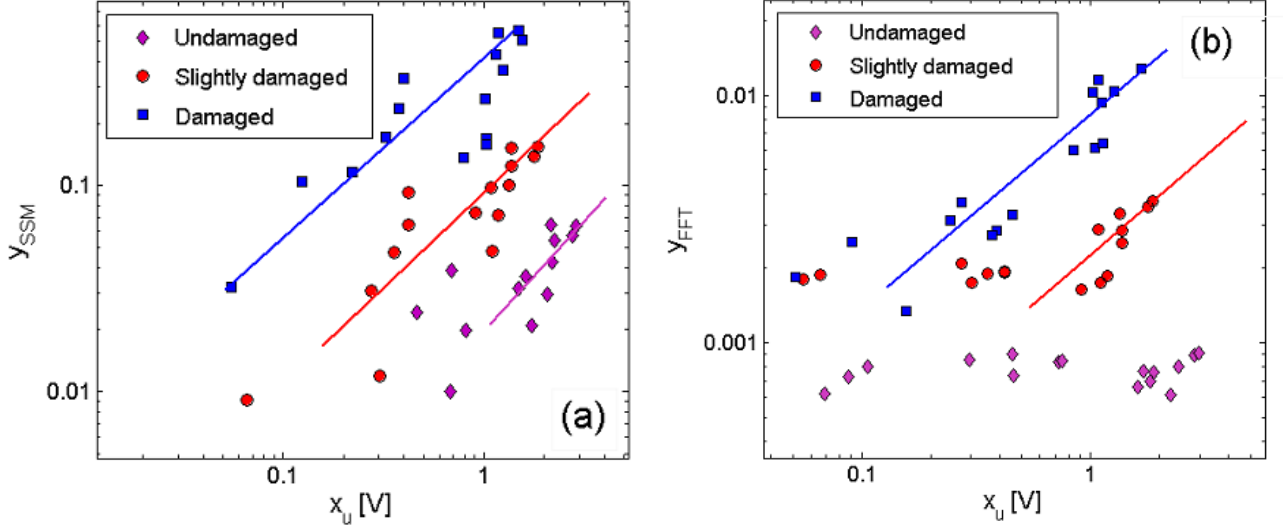


**Figure III.9** – Nonlinear indicators measured experimentally on a concrete prism (with a joint) under load. (a)  $y_{SSM}$  vs.  $x_u$ ; (b)  $y_{FFT}$  vs.  $x_u$ . The detection threshold is larger for lower nonlinearity and it is always much larger when the analysis is performed in the frequency domain. Compare results with Fig. III.6.

The experiment was repeated during the work of this thesis on an identical prism at the intermediate corrosion level to prove the role of environmental noise. To best highlight its effect, we have collected data at 20 different amplitudes, but we have analyzed them using three different values of the excitation amplitude  $u_0$  used to define the reference signal.

Experimental results reported in Fig. III.11 show an increase of the influence of environmental noise with decreasing  $u_0$ . Furthermore, as expected, the detected nonlinearity decreases when increasing  $u_0$ , since part of the nonlinear response is present already in the low amplitude signal, as previously discussed. Results are in agreement with those obtained using numerical data.

## 4.5 Implications for the experimental analysis

The detection of the threshold discussed above is of great importance to correlate properly the experimental observations with the mechanisms responsible of the observed nonlinear behavior. In fact, often the physical nature of the nonlinearity is correlated to the exponent of the power law dependence of the nonlinear indicator. However, as we have shown, it is not always easy to determine the correct power law from experimental (or even synthetic) data. The range of amplitudes at which the nonlinear measurements are significant might be small: for low amplitudes the nonlinear signal is submerged into noise, while for large amplitudes saturation effects and/or set up limits might affect the measurement.

In some cases, like clapping, most of the interesting nonlinear behavior might be localized in a narrow amplitude band, in which local displacements are large enough to open/close cracks

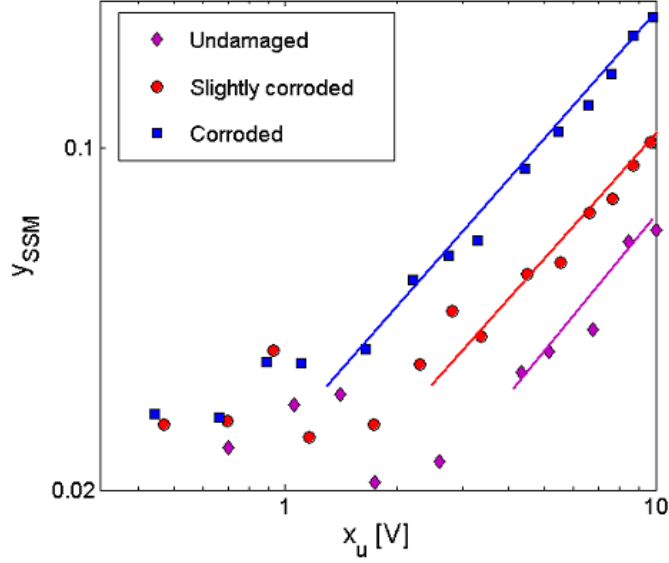


**Figure III.10** – SSM nonlinear indicator measured experimentally on a reinforced concrete prism at different levels of corrosion. The detection threshold decreases when increasing damage (i.e. increasing nonlinearity). In all cases nonlinearity is detectable when  $y_{SSM}$  is larger than 0.03, thus confirming the presences of the same equipment noise in the three experiments.

but small enough so that opening/closing occurs repeatedly. Also, from the computational point of view, numerical accuracy at low amplitudes or model saturation/instability at large amplitudes might easily occur providing, as in experiments, deviations from the expected power law. Not accounting for these effects might easily lead to a wrong determination of the power law exponent  $b$ , thus to a non correct understanding of the physical mechanisms which are at play.

As an example, in Fig. III.12 we show results of a numerical experiment performed introducing an additional nonlinear scatterer in the sample described by a clapping model [27]. As a result of the combination of the effects due to the two scatterers, the exponent is changed from 1 to 1.5, as expected from the theory (see fitting curve of data represented with squares in Fig. III.12). However, when noise is added to the system, a blind analysis of the power law reveals a reasonable fitting of all the amplitude range with an exponent 1.1 (see the blue fitting line of the plot with circles). Thus information about the new physical mechanisms is lost.

Such under-estimation of the exponent is also expected for instance when examining the experimental data of Fig. III.10.

As a final issue to be discussed, we remark that, for the complete analysis of the data, also the coefficient  $a$  is to be carefully accounted for. As we have shown, the nonlinear to linear ratio should be larger than the signal to noise ratio. However, for given physical mechanisms of nonlinearity, the former is linked to the coefficient  $a$ . Analysis methods in the frequency

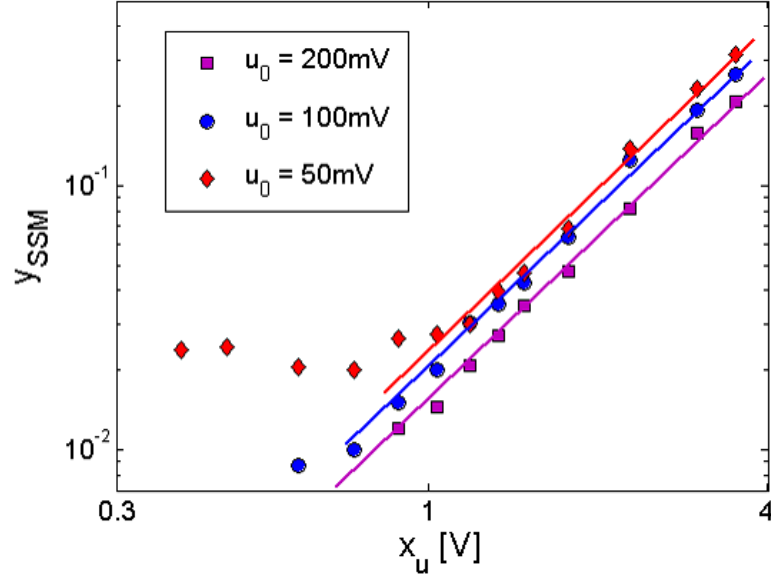


**Figure III.11** – SSM nonlinear indicator measured experimentally on a reinforced concrete prism at an intermediate corrosion level. Data were analyzed by increasing the amplitude of the low driving  $u_0$  used to generate the reference signal. As expected, the threshold increases with increasing  $u_0$ . See also Eq. III.20.

domain (FFT) or time domain (SSM) have been shown here to provide the same estimation of the exponent but a much different coefficient in the power law dependency. It is clear that this difference is linked to the different physical mechanisms exploited by the methods. The effects of a nonlinear scatterer are indeed the transfer of energy from fundamental to higher order harmonics, the reversible change of the elastic properties of the material (conditioning) and an amplitude dependence of attenuation. The former is common to all forms of nonlinearity and it could be best detected using the FFT analysis. On the contrary, the other two mechanisms are mostly inducing effects on the fundamental frequency, which is generally strongest in amplitude than harmonics. In this case SSM could provide the best way to get out of the noise level.

To better analyze this issue, we further analyze the threshold effect on SSM signals. As shown elsewhere [15], effects of nonlinear attenuation, phase shifts and harmonics generation could be separated in the SSM signal by temporal correlating, normalizing or filtering the reference and large amplitude signals before making the analysis. The same data sets used in Fig. III.6 was analyzed separating the three contributions for a given noise level. Results, shown in Figure III.13 clearly highlight the dependence of the minimum amplitude necessary to detect nonlinearity on the physical mechanisms at play.

In the case considered the stronger nonlinear effect comes from phase shifts between reference and large amplitude signals. It is remarkable that all four indicators fit the same slope ( $b = 1$ ).

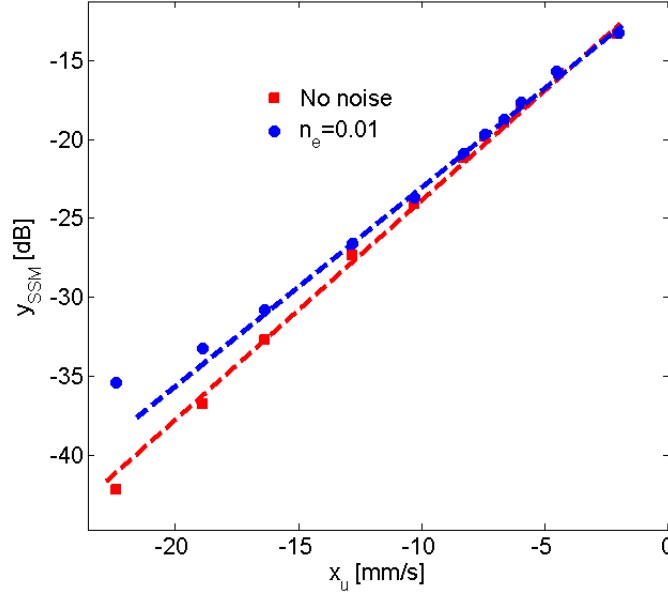


**Figure III.12** – Determination of the power law exponent from numerical results obtained simulating a sample with both a hysteretic and a clapping scatterer (described using models reported in the previous Chapter). Without noise the exponent  $b$  is found to be 1.5 (squares), but when noise is added, without considering a threshold for amplitude detection the exponent is found to be 1.1 (circles and blue fitting curve) as for purely hysteretic scatterers. Thus the presence of the clapping scatterer is undetected.

## 5 Effects of the experimental configuration and data analysis parameters

In this Section, we analyze how the detection threshold of nonlinearity is influenced by some parameters of the experimental configuration, such as the receiver position. Also, we analyze the effects due to the choice of the parameters of the data analysis. We will show here that extracting an absolute value of the nonlinear parameter often requires the a priori knowledge of the resonance structure of the medium. In other words, models are needed to calculate parameters which are independent from the chosen configuration.

As a solution to the problem, we show that the power law exponent  $b$  is the only property which is independent from the experimental configuration and parameters in the data analysis. As a consequence, when normalization with respect to the set up is not possible, the value of the exponent  $b$  could still convey useful information about the nature of the nonlinearity in the material. Nevertheless, its quantification remains a problem.

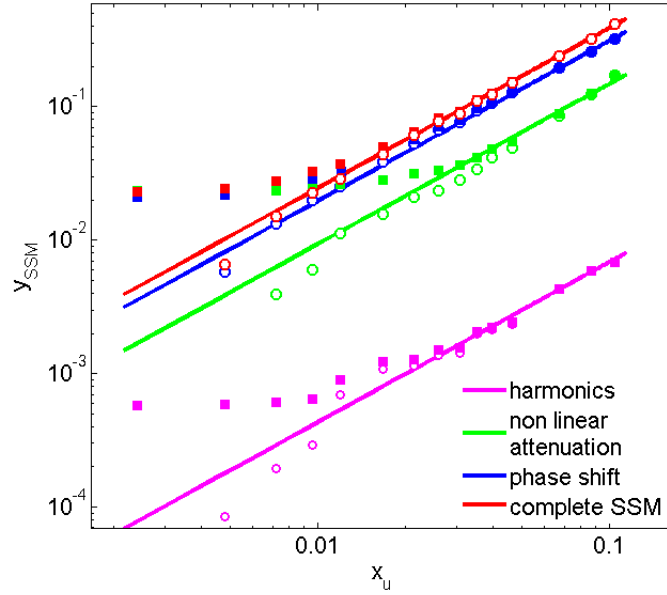


**Figure III.13** – Determination of the threshold for detection using SSM (same case as in Fig.III.6). Here the threshold for detection is calculated when different mechanisms producing the SSM signal are considered: nonlinear attenuation (green), phase shift (blue) and transfer of energy into harmonics (magenta). Red symbols refer to the complete SSM signals, while squares denote results in the presence of noise.

## 5.1 Numerical analysis

In this section, we analyze the effects of the experimental configuration on the detection threshold using numerical data only. It is thus possible to easily control the various parameters and analyze independently their respective influence on the results. However, the results reported here show features that have already been observed in experimental data sets [28, 29].

As in the previous cases, synthetic data are generated using a 1-D code for the propagation of elastic waves in hysteretic media. The model used is based on a Preisach-Mayergoyz approach (PM) [30], i.e. the constitutive equation of the sample emerges from the average of a statistical ensemble of simple hysteretic elements (HE) defined as bistable systems, which switch from an elastic state to a rigid one at a given pressure and return back to the original state at a different (smaller) stress. Given a statistical ensemble of HEs, the two values of pressure at which transition occurs are distributed uniformly in a given interval, much larger than the stress due to the elastic wave. Details can be found in the previous Chapter and in refs. [30, 31].

The sample was considered as a bar  $l = 10$  cm long, with Young modulus  $E = 72$  GPa and Q-factor of 600. A hysteretic nonlinear scatterer (of length  $l_s = 5$  mm) was located in the center of the bar. Elastic waves were injected at  $x = 0$ , i.e. on the left side of the bar and recorded at different positions along the sample.



### III.5 Effects of the experimental configuration and data analysis parameters

---

Both CW excitations  $v_s$  and pulses  $v_p$  were considered in this analysis:

$$v_s = A \sin(\omega_0 t) \quad (\text{III.26})$$

$$v_p = A \sin(\omega_0 t) \exp - \frac{(t - t_0)^2}{2\sigma^2} \quad (\text{III.27})$$

Here the most important parameters are the central frequency  $\omega_0$  and the source amplitude  $A$ . In our simulations, we choose a frequency very close to resonance for CWs ( $\omega_0 = 25.9 \text{ KHz}$ ) and a high frequency for pulses ( $\omega_0 = 400 \text{ KHz}$ ).

For each kind of injection, signals  $u(t)$  were recorded by receivers at increasing excitation amplitudes and analyzed as it has been discussed in the previous Sections to extract the nonlinear indicators. We have considered the effects of noise on the determination of the nonlinear indicator. To this purpose, to each given synthetic data recorded by a receiver ( $u(t)$ ), a white noise has been added to simulate the ambient and equipment noises, as discussed in the previous Section. The noisy signals are thus in the form:

$$\begin{aligned} u'(t) &= u(t) + \eta_a(t) + \eta_e(t) \\ u'(t) &= u(t) + n_a * \beta_a(t) + n_e * \beta_e(t) \end{aligned} \quad (\text{III.28})$$

where  $\beta_a$  and  $\beta_e$  are random variables uniformly distributed between -1 and 1 with zero average. The first noise term  $\eta_a(t)$  has a constant (small) amplitude  $n_a$  and simulates an ambient (environmental) noise. The second parameter  $\eta_e(t)$  has an amplitude  $n_e$  proportional to  $\max(u(t))$ . It describes an equipment noise, which is known to be increasing with increasing amplitude of excitation.

## 5.2 Effects due to the experimental set-up

The detected nonlinearity, or the nonlinear to linear signal ratio, is strongly affected by the propagation from the source of nonlinearity to the detection position. Attenuation of the medium and resonance of the structure might in fact have a different impact on the linear and nonlinear parts of the signal.

As a consequence, the energy of the recorded signal  $x_u$  (see Eq. III.5) and of the SSM signal  $w$  (see Eq. III.14) is strongly dependent on the position where it is recorded, i.e. the position of the receiver. Furthermore,  $x_u$  constitutes only an approximate quantification of the energy which is really exciting the nonlinearity. Indeed, it quantifies the energy at the receiver position, while nonlinearity depends on the energy (eventually averaged) at the location of the nonlinearity. The latter is roughly proportional to  $x_u$ , but for the reasons mentioned before, the proportionality constant depends on the receiver position. As a consequence, quantification of nonlinearity is not feasible, unless the transfer function from the receiver to the zone where nonlinearity is present is known analytically. Even in this case, when nonlinearity is distributed, there are unsolved issues about how averaging should be performed.

In any case, in experiments the problem is present and technical difficulties often are not allowing to estimate the energy at the position of the nonlinearity. Thus, we analyze in this

### III.5 Effects of the experimental configuration and data analysis parameters

Section the effects on the measured nonlinearity by positioning transducers at different distances from the nonlinear scatterer, without taking advantages of the corrections which might be easily introduced in numerical data. We consider first the ideal case without noise and then a similar study is performed after adding an equipment noise to the recorded signals so that the situation is close to experimental conditions.

#### 5.2.1 Continuous waves

We first consider CW injected in the sample and measure the output signals in standing wave conditions. In Figure III.14, the SSM indicator  $y_{SSM}$  is plotted as a function of the output energy  $x_u$  recorded at different positions  $x_{rcv}$  in the absence of noise.

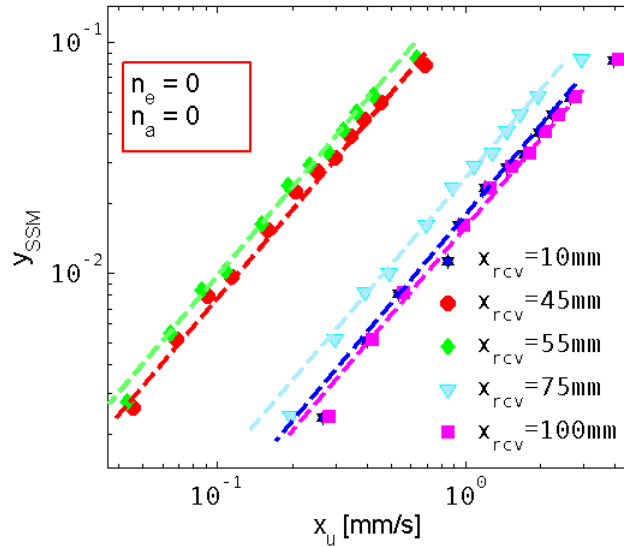


**Figure III.14** – SSM indicator  $y_{SSM}$  vs. output signal energy  $x_u$  without noise and for different positions of the receiver  $x_{rcv}$ . The sample is excited using a CW signal.

Data in log-log scale are fitting parallel straight lines with the same slope for each position of the receiver, i.e. we have a power law  $y = ax^b$  with a constant exponent  $b_{SSM} = 1$ , but different coefficients  $a_{SSM}$ . The numerical results shown here are in good qualitative agreement with typical experimental observations (see Fig. III.5). From the data reported, we can conclude that quantifying the nonlinearity is not possible. However, the power law exponent  $b$  is set-up independent. Therefore, independently from the position of the receiver we still catch the fact that the nonlinearity is of the hysteretic kind.

Furthermore, data reported in Fig. III.14 indicate that, for the same excitation level at the source, we measure the same value of  $y_{SSM}$  for all positions. Indeed, the  $n^{th}$  point of the series of each measurement has the same  $y_{SSM}$  but different  $x_u$ , as a consequence of the resonance structure of the medium. We can also observe that the nonlinear indicator curves are well superimposed for receivers located at equidistant points from the defect which situated at  $x = 50$  mm: see e.g.  $x_{rcv} = 45$  mm (red circles) and  $x_{rcv} = 55$  mm (green losanges). This was

### III.5 Effects of the experimental configuration and data analysis parameters

to be expected, since the fundamental resonance mode (used here) is symmetric with respect to the center of the sample.

Assuming the coefficient  $a_{SSM}$  of the fitting power law to be indicator of the nonlinearity strength, we might conclude that without taking into account the resonance structure of the medium we are introducing an error, since  $x_u$  is not correctly estimating the energy at the scatterer position. Also, we should remark that in the SSM signal  $w(t)$ , contributions at the fundamental frequency are dominant. Therefore, propagating from the scatterer to the receiver, they are affected in the same way by the resonance structure as the complete signal  $u(t)$ . It follows that  $y_{SSM}$ , due to its definition as the ratio between linear and nonlinear components, is independent from where the signal is recorded, provided the amplitude at the source is the same. Indeed, when plotting  $y_{SSM}$  as a function of the energy of the excitation  $x_s$ , all curves collapse into a single one, as expected from Fig. III.14

Figure III.15 is the equivalent of Fig. III.14, but obtained considering noisy data with an equipment noise level  $\eta_e = 0.03$  (i.e. noise is 3 percent of the signal).

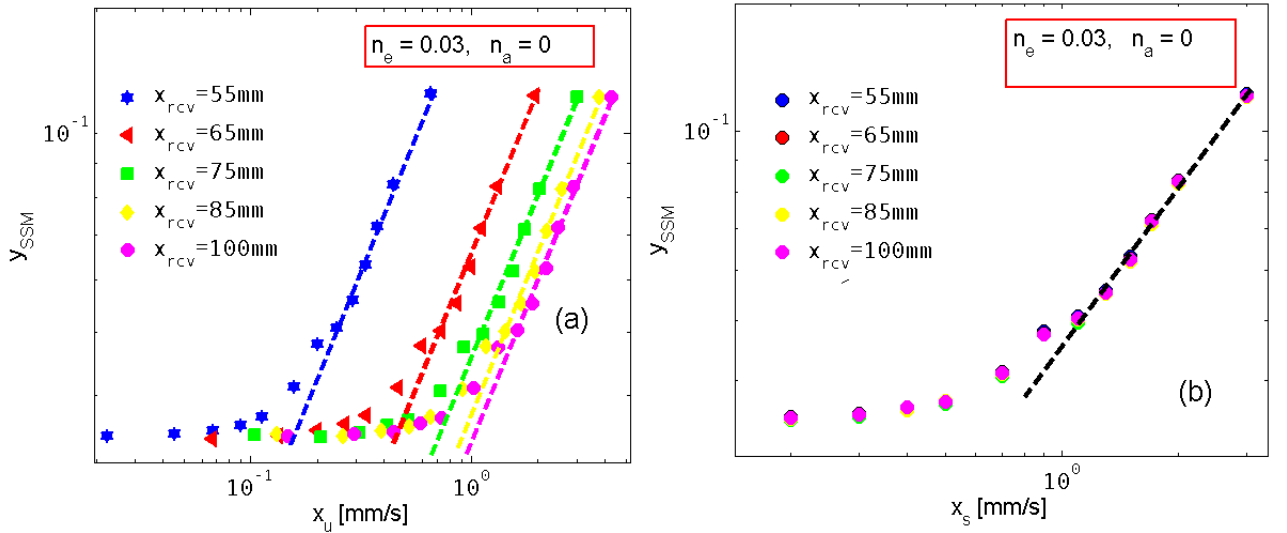


**Figure III.15** – (a) SSM indicator  $y_{SSM}$  vs. output signal energy  $x_u$  with noise and for different positions of the receiver  $x_{rcv}$ . The sample is excited using a CW signal; (b) SSM indicator  $y_{SSM}$  vs. input signal energy  $x_s$ . In both plots, the dashed lines represent a power law fitting in the amplitude range where specimen nonlinearity is detectable.

The receivers were situated at the positions  $x_{rcv} = [55, 65, 75, 85, 100]$  mm. As before, in subplot (a) we observe a parallel shift of the curves toward increased nonlinearity when decreasing the distance between the scatterer and the receiver (we recall that the scatterer is located at  $x = 50$  mm). As mentioned before, all curves collapse when  $y_{SSM}$  is plotted vs. the excitation energy (Fig. III.15.(b)).

When noise is present, we could also define the threshold detection of nonlinearity. As discussed in the previous Section, at low amplitudes, noise is dominating and the nonlinear

### III.5 Effects of the experimental configuration and data analysis parameters

---

contribution, mostly due to nonlinear components of the noise, are proportional to the signal energy:  $y_{SSM}$  is constant. At larger excitation energies, the nonlinear part of the noise becomes negligible and  $y_{SSM}$  follows a power law with  $b \approx 1$ . The intersection between the fitting lines in the two regions defines the detection threshold.

The threshold for the detection of nonlinearity is also dependent on the position of the receiver. Indeed, the onset of the nonlinear behavior shifts to lower values of the output energy  $x_u$  (subplot(a)). However, this information might be misleading. Indeed, the parameter which controls the threshold should be the same, independently from the set-up used for the measurement. In fact, if we consider the threshold as the minimum source amplitude necessary to have a nonlinear signal above the noise level, we note in subplot (b) of Fig. III.15 that the threshold level is the same for each experiment, i.e. for the various detecting positions.

We should note that a similar analysis has also been performed in the frequency domain (FFT). Results are similar when plotting  $y_{FFT}$  as a function of the output energy. However, curves are not collapsing when plotting results as a function of excitation energy. In fact, influence of the resonance structure is different for the fundamental frequency and the higher harmonics. Thus, the nonlinear signal is affected in a different way than the linear one when it is propagating from the nonlinear source to the detection position. Hence,  $y_{FFT}$ , for the same excitation amplitude, varies with the position of the receiver .

#### 5.2.2 Pulses

As we already mentioned, the same effects studied in the previous Subsection are shown when the excitation is a pulse, rather than a CW where first arrivals are considered in the analysis.

In Fig. III.16, we consider results of the data analysis in the time domain. As in Fig. III.15, the SSM indicator as a function of the energy of output (subplot (a)) and of the energy of the input signals (subplot (b)) is shown at different detection positions:  $x_{rcv} = [55, 65, 75, 90, 100]$  mm. When noise effects are not considered (squares in the two plots), data are aligned in parallel straight lines, which can be fitted with a power law with slope  $b \approx 1$ . Again, while the output energy (for the same excitation level) decreases with increasing the distance of the receiver from the defect location due to attenuation, the SSM indicator is independent from the receiver location. When the nonlinear indicator is plotted vs. the source (input) energy, all curves collapse (Fig. III.16. (b)). The introduction of an equipment noise  $\eta_e = 0.03$  (i.e. 3 percent of the signal) produce effects similar to those observed in the case of continuous waves (curves with circle symbols in the plots). In the low amplitude region noise is dominant. The threshold for the detection of nonlinearity (intersection between fitting lines in the nonlinear and in the noise regions) shifts to the right (larger values of the output energy  $x_u$ ) when increasing the distance source-receiver, being, as before, an apparent shift only.

The same set of data has also been analyzed in the frequency domain, in the absence of noise, see Fig. III.17. Here, the amplitude of the nonlinear indicator is much smaller, hence numerical approximations in the FFT analysis are already introducing a threshold for the detection of nonlinearity, even without noise. Indeed, the ratio between  $y_{SSM}$  and  $y_{FFT}$  is almost 100. As before, attenuation in the propagation from nonlinear source to receiver causes

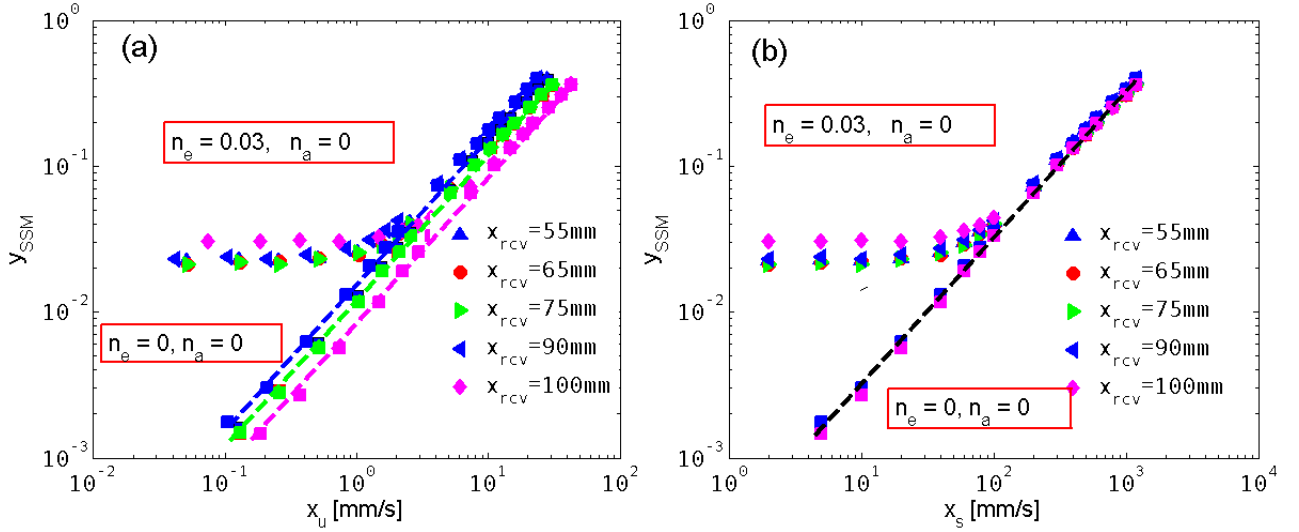


**Figure III.16** – (a) SSM indicator  $y_{SSM}$  vs. output signal energy  $x_u$  with and without noise for different positions of the receiver  $x_{rcv}$ . The sample is excited using a pulse; (b) SSM indicator  $y_{SSM}$  vs. input signal energy  $x_s$ . In both plots, dashed lines represent a power law fitting in the amplitude range where specimen nonlinearity is detectable.

a biased estimation of the power law coefficient  $a_{FFT}$ , thus a correction for attenuation should be considered. However, also in the case of the FFT analysis, all curves collapse into the same curve when  $y_{FFT}$  is plotted vs the input energy (Fig. III.17.(b)), contrary to the case of continuous waves.

The different behavior with respect to the case of continuous waves could be easily explained. In the case of pulses, the difference in the resonance structure for the different harmonics is not important. Moreover, due to the short distance between transducers, all frequency components are attenuated almost uniformly, thus the ratio  $y_{FFT}$  is independent from the propagation distance. Of course this is no longer true when attenuation is highly frequency dependent and/or the propagation distance is large.

### 5.3 Effects of the data analysis parameters

Effects in the choice of the parameters used for the data analysis are particularly important in the SSM analysis, which is based on the definition of a reference (low) amplitude  $A_0 = A_{ref}$  at which the system behaves linearly. This choice could not be predicted a priori for a given system. Hence, in general  $A_{ref}$  is chosen as small as possible, compatibly with the noise level of the system. Since this could be a critical point, as already observed in the previous Section in relation to noise threshold, we further analyze the reference amplitude issue here. The aim is to show that a non appropriate choice of the reference signal can be detected from experimental results and eventually corrected by repeating the experiment with a lower reference amplitude.

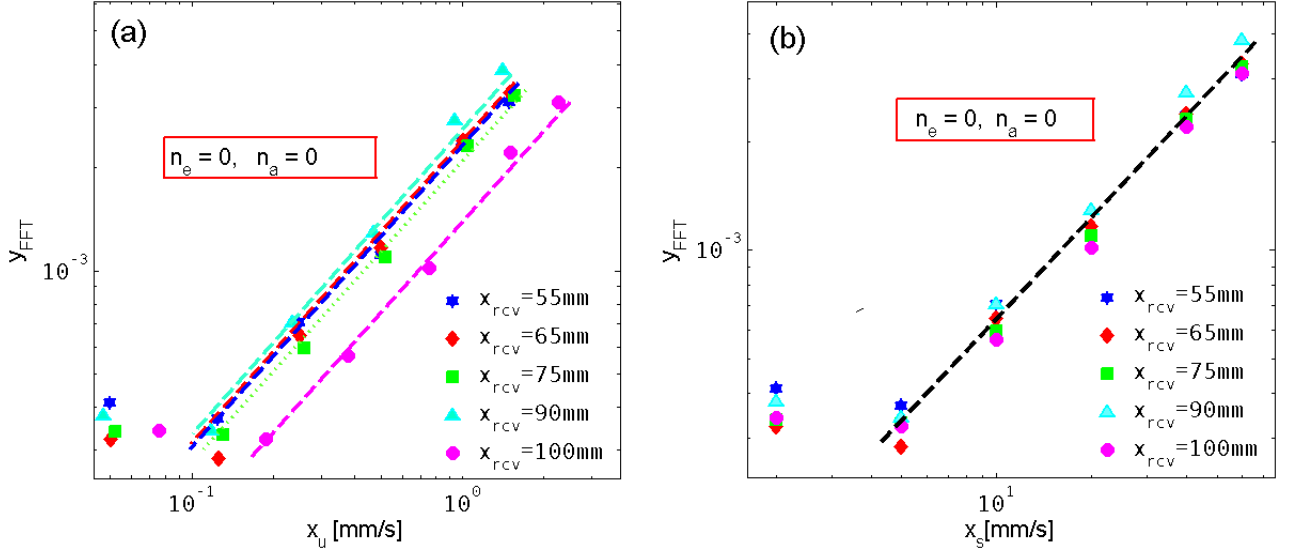


**Figure III.17** – (a) FFT indicator  $y_{FFT}$  vs. output signal energy  $x_u$  without noise for different positions of the receiver  $x_{rcv}$ . The sample is excited using a pulse; (b) FFT indicator  $y_{FFT}$  vs. input signal energy  $x_s$ . In both plots, dashed lines represent a power law fitting in the amplitude range where specimen nonlinearity is detectable.

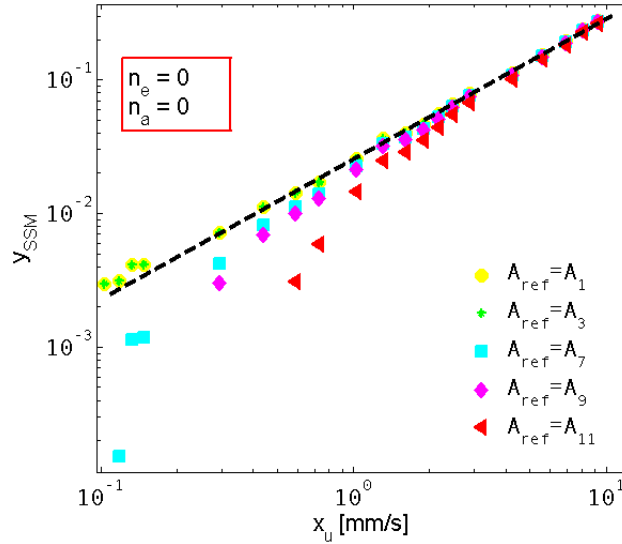


**Figure III.18** – Nonlinear indicator  $y_{SSM}$  as a function of the output energy  $x_u$  for different reference signal amplitudes and in the absence of noise.

First, in Fig. III.18, we consider CW waves and calculate the SSM indicator as a function of the output energy for different choices of the reference amplitude. Here, the reference ampli-

### III.5 Effects of the experimental configuration and data analysis parameters

tudes used are  $A_{ref} = [A_1 = 0.01, A_2 = 0.02, A_3 = 0.03, A_4 = 0.04, A_5 = 0.05, A_6 = 0.06, A_7 = 0.07, A_8 = 0.08, A_9 = 0.09, A_{10} = 0.1, A_{11} = 0.2, A_{12} = 0.3, A_{13} = 0.4] kPa$ .

As we can observe, when  $A_{ref}$  is small enough ( $A_{ref} = [A_1, A_3]$ ), the SSM curves are straight lines which are completely superimposed. When  $A_{ref}$  increases further, it can be observed that the linear dependence of the SSM curves is lost, except in a small region at high amplitudes. Thus, we have a threshold in amplitude, below which nonlinear measurements are not meaningful. Above threshold, the choice of the reference signal doesn't seem to be relevant.

Sensitivity to the reference signal is due to the way  $y_{SSM}$  is defined. Indeed, the SSM signal  $w(t)$  is determined as the difference between the reference signal and the high amplitude signals. If any nonlinear contribution is already present in the low amplitude signal, that would cause a reduction in the amplitude of  $w(t)$ , resulting in a smaller value of the  $y_{SSM}$  indicator, as shown through data at low values of  $x_u$  and large amplitude of the reference signal. However, the residual nonlinearity present in the signal at the excitation amplitude  $A_{ref}$  becomes negligible at higher amplitudes.

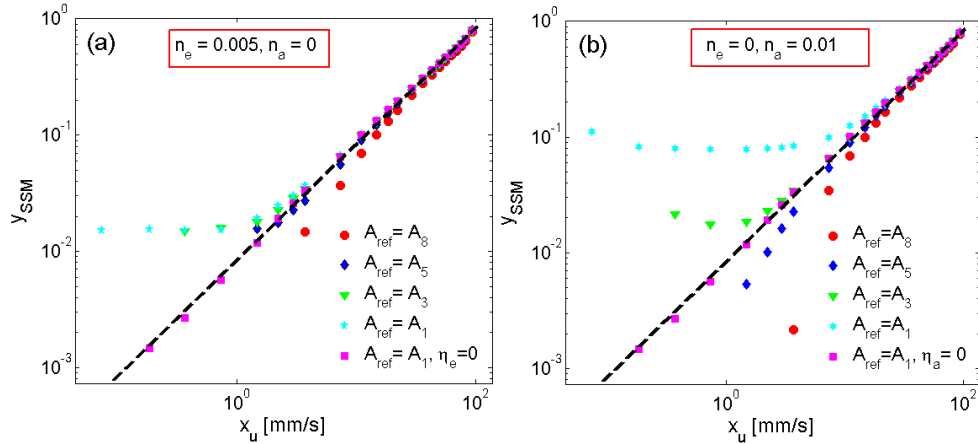


**Figure III.19** – SSM indicator  $y_{SSM}$  vs. output signal energy  $x_u$  for different choices of the amplitude of the reference signal  $A_{ref}$ . The sample is excited using a pulse. In both plots, dashed lines represent a power law fitting in the amplitude range where specimen nonlinearity is detectable. (a) Equipment noise proportional to the amplitude of the signal; (b) Environmental noise at constant amplitude.

Using pulse excitations, we have also considered the behavior in the presence of noise (see Fig. III.19). In the case of equipment noise (subplot (a)), we observe the existence of the usual threshold for detection discussed in the previous section of this Chapter: at low amplitudes, nonlinear effects due to noise are dominant and  $y_{SSM}$  is constant with increasing the energy of excitation  $x_u$ . However this is valid only for low values of the reference amplitude ( $A_{ref} = [A_1, A_3, A_5]$ ), i.e. when noise effects are stronger than nonlinear effects present in the reference signal. In such cases, no effects of the choice of the threshold are visible.

On the contrary, for larger amplitudes of the reference signal ( $A_{ref} = A_8$ , red circles), the opposite occurs. The nonlinear effects in the reference signal are so large that noise is not relevant and the threshold for detection is determined by the choice of  $A_{ref}$  only.

While it might seem possible to conclude that the choice of the lowest possible value for the amplitude of the reference signal is always the best, this is not the case when ambient noise is present. This was already remarked in the previous Section and it is further discussed here.

In Fig. III.19.(b), we analyze the effects of an ambient noise on the measurement, i.e. of a noise with amplitude which does not depend on the amplitude of the source. In this case, the actual noise on the SSM signal at a given amplitude is amplified by a factor  $k = A/A_{ref}$ , as discussed in the previous Section. In these conditions, increasing the amplitude of the reference signal corresponds to:

- decrease the contribution to the SSM signal of the nonlinear components of the noise;
- increase the contribution to the SSM signal of the nonlinear components due to the reference signal.

As a consequence, at low reference signal amplitude values, the first effect is dominant and the detection threshold at first decreases with increasing  $A_{ref}$ : see cyan stars and green triangles in Fig. III.19. Increasing more the amplitude of the reference signal, the second effect becomes more important and the threshold for detection increases again.

## 6 Conclusions

In this Chapter two nonlinear indicators have been introduced to quantify the elastic non-linearity of a material. Their behavior as a function of the elastic energy exciting the material has been shown to be a power law.

However, several issues are to be considered before a reliable analysis of the power law could be conducted as they have been introduced and studied in this Chapter of the thesis. From the experimental point of view, data always show that:

- The power law behavior is valid only in a limited range of excitation amplitudes: at low amplitudes noise effects are hiding the true nonlinear behavior, while at large amplitudes saturation effects might be due to equipment or other uncontrolled sources of nonlinearity. Neglecting this, one could easily under- or over- estimate the power law exponent  $b$ , with drastic consequences on the interpretation of the experimental data and on the discrimination between different physical sources of nonlinearity.
- The quantification of nonlinearity is highly dependent on the set-up of the experiment performed and in particular on the position of source and receivers with respect to the location of the nonlinear scatterer. As a consequence, quantitative measurements and/or comparison of nonlinearity in different systems is often not easy to perform. Unless it is taken extreme care in reproducing equivalent measurement set-ups, the coefficient  $a$  of the power law is usually not providing an information in absolute terms.



- The analysis of nonlinearity is very sensitive to the data processing adopted. In general the SSM analysis is easier to perform and more robust than an FFT analysis, since it accounts for contributions at the fundamental frequency also, while FFT only consider amplitudes of higher order harmonics. Nevertheless, the parameters used, and in particular the choice of the amplitude of the lowest excitation which defines the reference signal, should be carefully evaluated in order to avoid a wrong estimation of the power law exponent  $b$ .

All these issues have been discussed here, using synthetic and experimental data. Most of the observations reported in this Chapter are confirmed also by similar behaviors of data reported in the literature. Given that most of the problems do not have a solution from the experimental point of view, we have suggested how to recognize them when treating data and, in some cases, we have proposed interpretations and/or solutions:

- The amplitude threshold for the detection of the effective nonlinearity has been defined, in the presence of equipment and ambient noises. We have shown how the amplitude range of validity of the power law could be determined for a given set of experimental data where experimental points affected by a significant noise are eliminated. The different effects of the two kind of noises have been compared and suggestions about the optimization of the parameters used for the data analysis have also been given. Ambient noise seems to be easily negligible with respect to effects due to equipment noise, particularly in the FFT analysis.
- In some cases, effects due to attenuation and geometrical dispersion leading to the dependence of the values of the nonlinear indicator on the position of the receiving transducer could be compensated. Whenever attenuation is not frequency dependent, the linear component of the signal and the nonlinear one manifest the same dependence on the position, thus, once the nonlinear indicator is defined as a ratio between linear and nonlinear signal energies they compensate. However, this is not the case if the resonance structure of the system is relevant in the propagation, like in the case of continuous waves. In general, SSM measurements extract the nonlinear signature at the same frequency of the linear components of the signal, thus it is more likely their spatial dependence to be identical and thus canceling in the definition of  $y_{SSM}$ . Nevertheless, at this stage we could not propose any solution for the correct definition of the energy which excites the nonlinearity. It could only be roughly estimated from the input or output energies, both calculated in a point which is not the same as that in which nonlinear features are present.
- We have shown that the exponent  $b$  of the power law dependence is an absolute measurement of the nonlinearity, while the coefficient  $a$  is not. It is very robust both with respect to noise and to experimental configuration, provided some care is taken in measuring it.

The power law dependence of nonlinear indicators has been investigated in this chapter where the exponent  $b$  was found to be independent from the experimental configuration. This parameter will be the basis for the developments proposed in the next two Chapters.

---

## References

- [1] R. A. Guyer and P. A. Johnson. Nonlinear mesoscopic elasticity: Evidence for a new class of materials. *Phys. Today*, 52:3, 1999. [45](#)
- [2] K. Van Den Abeele and J. Carmeliet and J. A. TenCate and P. A. Johnson. Nonlinear elastic wave spectroscopy(NEWS) techniques to discern material damage, partI: Nonlinear wave modulation spectroscopy(NWMS). *Res. Nond. Eval.*, 12:17, 2000. [45](#)
- [3] K. Van Den Abeele, F. Schubert, V. Aleshin, and F. Windels and J. Carmeliet. Resonant bar simulations in media with localized damage. *Ultrasonics*, 42, 2004. [45](#)
- [4] C. Campos-Pozuelo, C. Vanhille, and J. A. Gallego. Comparative study of the nonlinear behavior of fatigued and intact samples of metallic alloys. *IEEE Trans. On Ultras. Ferr. and Freq. Control.*, 5:175, 2006. [45](#)
- [5] C. Payan, V. Garnier, and J. Moysan. Effect of water saturation and porosity on the nonlinear elastic response of concrete. *Cem. Concr. Res.*, 40:473–476, 2010. [45](#)
- [6] M. Bentahar et al. Hysteretic elasticity in damaged concrete: quantitative analysis of slow and fast dynamics. *Phys. Rev. B.*, 73:014116, 2006. [45](#)
- [7] M. Scalerandi, A. S. Gliozzi, C. L. E. Bruno, D. Masera, and P. Bocca. A scaling method to enhance detection of a nonlinear elastic response. *Appl. Phys. Lett.*, 92:101912, 2008. [45](#), [46](#)
- [8] T. J. Ulrich and P. A. Johnson. Application of the bispectrum for detection of small nonlinearities excited sinusoidally. *Phys.Rev.Lett.*, 98:10430, 2007. [45](#)
- [9] I. Solodov and al. al. Nonlinear self-modulation and subharmonic acoustic spectroscopy for damage detection and location. *Appl.Phys.Lett.*, 84:5386, 2004. [45](#), [48](#)
- [10] V. Garnier, C. Payan, and J. Moysan. Effect of water saturation and porosity on the nonlinear elastic response of concrete. *Cem. Concr. Res.*, 40:473, 2010. [45](#)

- 
- [11] K. Van Den Abeele et al. Micro-damage diagnostics using Nonlinear Elastic Wave Spectroscopy (NEWS). *NDT & E International*, 34:239, 2001. [48](#)
  - [12] M. Bentahar, H. El Agra, R. El Guerjouma, M. Griffa, and M. Scalerandi. Hysteretic elasticity in damaged concrete: quantitative analysis of slow and fast dynamics. *Phys. Rev. B*, 73:014116, 2006. [48](#)
  - [13] M. Scalerandi et al. A scaling method to enhance detection of a nonlinear elastic response. *Appl. Phys. Lett.*, 92:101912, 2008. [48](#)
  - [14] J. A. Porto, R. Carminati, and J. J. Greffet. Theory of electromagnetic field imaging and spectroscopy in scanning near-field optical microscopy. *J. Appl. Phys.*, 88:4845, 2000. [48](#)
  - [15] C. L. E. Bruno et al. Analysis of elastic nonlinearity using the scaling subtraction method. *Phys. Rev. B*, 79:064108, 2009. [48](#), [49](#), [67](#)
  - [16] M. Scalerandi, A. S. Gliozzi, C. L. E. Bruno, and K. Van Den Abeele. Nonlinear acoustic time reversal imaging using the scaling subtraction method. *J. Phys. D: Appl. Phys.*, 41:215404, 2008. [48](#)
  - [17] M. Scalerandi, A. S. Gliozzi, and C. L. E. Bruno. Nonequilibrium phenomena in damaged media and their effects on the elastic properties. *J. Acoust. Soc. Am.*, 131:EL81, 2012. [48](#)
  - [18] C. Payan, V. Garnier, and J. Moysan. Effect of water saturation and porosity on the nonlinear elastic response of concrete. *Cem. Concr. Res.*, 40:473, 2010. [48](#)
  - [19] G. Renaud, S. Calle, and M. Defontaine. Remote dynamic acoustoelastic testing: Elastic and dissipative acoustic nonlinearities measured under hydrostatic tension and compression. *Appl. Phys. Lett.*, 94:011905, 2009. [48](#)
  - [20] I. Solodov and G. Busse. Nonlinear air-coupled emission: The signature to reveal and image microdamage in solid materials. *Appl. Phys. Lett.*, 91:251910, 2007. [48](#)
  - [21] J.A. TenCate, E. Smith, and R. A. Guyer. Universal slow dynamics in granular solids. *Phys. Rev. Lett.*, 85:1024, 2000. [57](#)
  - [22] B. Capogrosso Sansone and R. A. Guyer. Dynamic model of hysteretic elastic system. *Phys. Rev. B*, 66:224101, 2002. [57](#)
  - [23] P. P. Delsanto and M. Scalerandi. Modeling nonclassical nonlinearity, conditioning, and slow dynamics effects in mesoscopic elastic materials. *Phys. Rev. B*, 68:064107, 2003. [57](#)
  - [24] M. Scalerandi, A. S. Gliozzi, C. L. E. Bruno, and P. Antonaci. Nonequilibrium and hysteresis in solids: Disentangling conditioning from nonlinear elasticity. *Phys. Rev. B*, 81:104114, 2010. [57](#)
  - [25] P. Antonaci et al. Monitoring evolution of compressive damage in concrete with linear and nonlinear ultrasonic methods. *Cem. Concr. Res.*, 40:340, 2010. [64](#)

- [26] P. Antonaci, C. L. E. Bruno, A. S. Gliozzi, and M. Scalerandi. Evolution of damage-induced nonlinearity in proximity of discontinuities in concrete. *Int. J. Sol. Struct.*, 47:1603, 2010. [64](#)
- [27] S. Delrue and K. Van Den Abeele. Three-dimensional finite element simulation of closed delaminations in composite materials. *Ultrasonics*, 52:315, 2012. [66](#)
- [28] R. El Guerjouma, S. Idijmarene, M. Scalerandi, and M. Bentahar. Influence of noise on the threshold for detection of elastic nonlinearity. *J. Appl. Phys.*, 113:043516, 2013. [69](#)
- [29] C. R. P. Courtney et al. et al. Application of the bispectrum for detection of small nonlinearities excited sinusoidally. *J. of Sound and Vibration*, 329:4279, 2010. [69](#)
- [30] R. A. Guyer and P. A. Johnson. Hysteresis, energy landscapes and slow dynamics: A survey of the elastic properties of rocks. *J. Mater. proces. Manufact. Sci.*, 9, 2000. [69](#)
- [31] I. D. Mayergoyz. Hysteresis models from the mathematical and control theory point of view. *J. Appl. Phys*, 57:3803–3805, 1985. [69](#)

---

---

# Chapter IV

---

## Power laws exponent based classification of nonlinearity mechanisms

### 1 Introduction

Power laws in the form  $y = ax^b$  are a rarer phenomenon in the real world compared to the exponential and the Gaussian functions for instance, which are commonly observed in physics. There are however many situations in which power laws are important. In the analysis of complex systems, in particular, power law dependencies are usually found and their study is of great importance in order to define classes of systems sharing common features, which are usually termed universality classes [1]. As a consequence, in the last decades the values of the power law exponent in various systems have been widely investigated, leading to many hypothesis about what might be the cause for the different values of  $b$ . In particular, changes in the value of the exponent are often associated to phase transitions [2].

One classic example is related to phase transition involving the condensation of a gas into a liquid. In this case, the transition is governed by continuously varying the external conditions, for instance the temperature. The point at which the transition occurs is called critical point. Around this point, the system shows a power law behaviour of its heat capacity as a function of temperature. When the critical point is crossed, a transition from the gas state to the liquid is accompanied by a change in the power law exponent [3].

This kind of power law based analysis and classification into classes has never been extensively applied to nonlinear acoustics, except for describing the difference between classical and nonclassical nonlinearity. We have indeed already seen that several experiments allow to define a nonlinear indicator. The power law dependence when the nonlinear indicators  $y$  are plotted as a function of the driving variable  $x$  is  $y = ax^b$  [4]. Such a dependence is confirmed by a huge amount of data reported in the literature. It is well recognised that the power law exponent  $b$  allows to distinguish between classical nonlinear elasticity characterised by  $b = 2$ , common to all materials [5], and non classical elasticity (also termed Nonlinear Mesoscopic Elasticity - NME), typical of consolidated granular (rocks, concrete, etc.) or damaged media (metals, composites, ceramics), presenting an exponent  $b \approx 1$ .

However, such a classification is not sufficient to account for all experimental data available in the literature, as we will discuss in the first Section. Experiments show, indeed, a wide range of variability of the exponent  $b$  depending on the nature and intensity of damage in the

material. In metals, where atomistic nonlinearity is dominant,  $b = 2$  is observed [6]; in intact consolidated granular media or samples with closed micro cracks, the exponent is  $b = 1$  [7–10]. However, larger values of  $b$ , up to  $b = 3$ , have also been measured. Furthermore, in several cases the exponent  $b$  assumes not integer values and/or evolves (generally increases) when increasing the damage state of the investigated sample.

As a result, it is of interest to explore the information which could be extracted from the value of the power law exponent. In particular, two main issues will be investigated in this Chapter:

- Is it possible, besides the classical and non classical classes of nonlinearity already known in literature, to define new classes of behaviours of nonlinear elastic materials? Is it possible to classify theoretical multi-state multi-scale models, introduced in Chapter 2, on the basis of the exponent  $b$ ?
- If yes, is there any relation between the changes in  $b$  and the evolution of the sample micro structure? What kind of experiments might be suggested to apply theoretical results to perform or optimise the nonlinear acoustic characterisation of nonlinearity in NME materials?

To address these two issues, we will show how classes of materials could be defined depending on the exponent  $b$  and we will discuss the physical characteristics shared by elements belonging to the same class. Also, we will show how different physical mechanisms introduced as multi-state models could account for the observed values of the exponent and we propose an interpretation of a phase transition from hysteretic elasticity to clapping observed in concrete at increasing damage levels.

## 2 Universality classes of materials

As mentioned in the Introduction, different classes of materials manifest a nonlinear elastic behaviour which can not be described in terms of the classical Landau theory (simple Taylor expansion of stress as a function of strain). In general, these materials are termed as nonclassical and are characterised by an exponent  $b = 1$  in contrast with  $b = 2$  observed in classical media. In experiments however different configurations show that other values of the exponent  $b$  are possible, thus suggesting an extension of the characterisation of materials based on their nonlinear response to ultrasonic excitations.

### 2.1 Data analysis

#### 2.1.1 Materials classification

We have analysed an ensemble of experimental data reported in the literature and calculated the exponent  $b$  for all of them. Results are shown in Fig. IV.1. Data refer to experiments on very different materials and using different nonlinear indicators.

As a consequence of the analysis, we have been able to group the results in four classes:

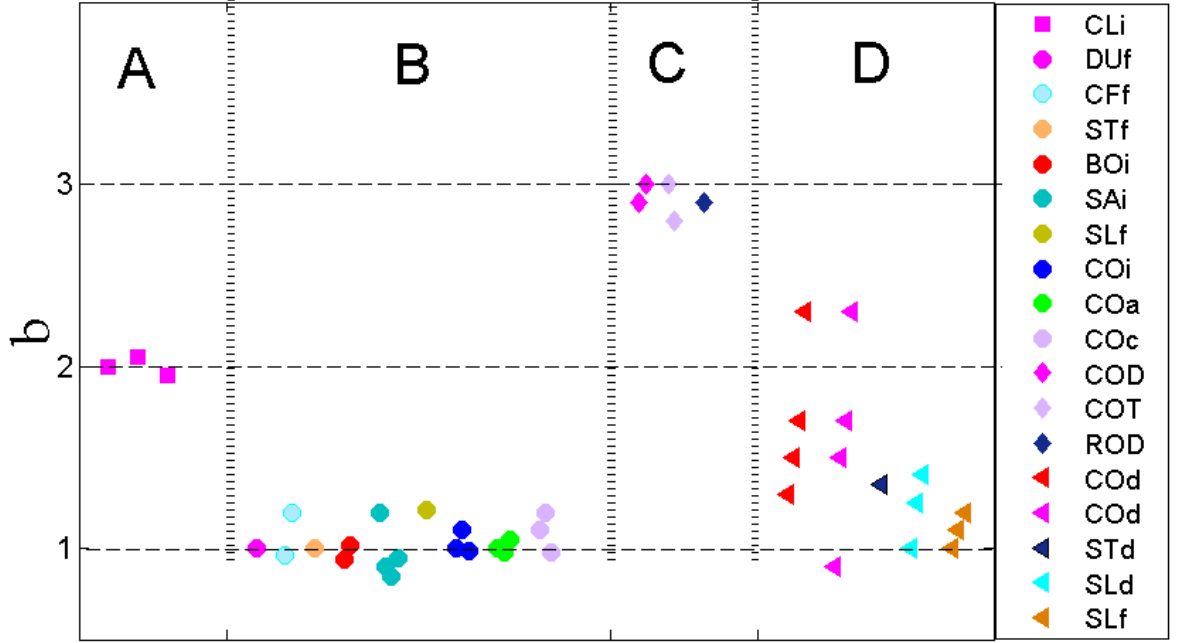


**Figure IV.1** – Power law exponent  $b$  measured using the third harmonic amplitude or the Scaling Subtraction Method for various samples. **A: classical nonlinear samples** with exponent  $b \approx 2$ : CLi = Duraluminum [11], steel [12] and teflon [13]. **B hysteretic nonlinear samples** with exponent  $b \approx 1$ : DUf = fatigued duraluminum [11]; CFf = carbon fiber reinforced composite with delaminations [14]; STf: fatigued 4340 steel bar [15]; BOi = bones [6, 16]; SAI = Sandstones [17, 18], SLf = microcracked slate beam [19]; COi = Intact concrete samples [12, 13]; COa = Portland cement damaged by Alkali Silica Reactions at different stages [10]; COc = Corroded concrete samples at different stages of corrosion [9]. **C: macroscopically damaged nonlinear samples** with exponent  $b \approx 3$ : COD = concrete with strong mechanical damage [13]; COT = concrete after strong thermal damage [20]; COD = mechanically damaged granite (unpublished). **D: nonlinear samples measured at increasing levels of damage** with exponent  $b$  between 1 and 3: COd = concrete damaged in quasi static compression tests at increasing load (unpublished); COd = concrete damaged by successive thermal loadings at increasing temperature [20]; STd = steel disk with a partially open crack [21]; SLd = slate beam damaged with successive impacts [22]; SLf = Slate beam damaged at increasing number of fatigue cycles [22].

- A - classical nonlinear media: the exponent is 2, as already mentioned above. To this class belong mostly metals and solid media in the intact state. It is to be noted that nonlinearity for these samples is very small (the coefficient  $a$  in the power law is small). Furthermore, strain excitation amplitudes larger than those used for the other 3 classes have been used in the reported experiments.;
- B - hysteretic nonlinear media: the exponent is  $b = 1$  for consolidated granular media (rocks and concrete), bones or slightly damaged metals and composites. All these samples share the characteristic of presenting interfaces between grain boundaries and/or small closed microcracks. Particularly significant is the case of concrete damaged by alkali-silica-reaction (ASR) or corrosion of the reinforcing bar, points labelled as COa and COc, respectively. For both cases, we have reported measurements of the exponent  $b$  at successive levels of damage for the same sample. No change in the exponent is observed when damage increases, while  $a$  increases with damage;
- C - open cracks in highly nonlinear media: when the sample is macroscopically damaged, mostly open cracks are present and phenomena such as clapping might occur. Such damage state could be easily achieved in the case of granular media and an exponent  $b = 3$  is found, thus denoting a huge nonlinearity;
- D - evolving nonlinear media: in the last class, we have collected data from experiments performed to monitor the evolution of damage in one sample. Here it is shown how both mechanically induced damage [23] and thermal damage [20] cause a change in the microstructure, revealed by an increase of the exponent  $b$ , corresponding to transition from small closed microcracks (class B) to larger and partially open cracks (class C). Notice that the increase in  $b$  with damage is very small in the case of fatigue damage (curve denoted with SLf), but even in this case a growing trend is observable. In other cases, such as chemical or corrosion damage [9, 24], increasing damage do not correspond to a variation of the exponent.

It should be remarked that the different samples studied present very different strengths of nonlinearity, i.e. the coefficient  $a$  in the power law equation is very different in experiments on materials belonging to the same class. Thus  $a$  seems to be the proper indicator to quantify the nonlinearity, while the exponent  $b$  seems to be mostly connected to the physical origin of nonlinearity.

### 2.1.2 Evolution of damage

Experimental observations on materials subject to mechanical loading such as thermal damage, fatigue tests or quasi static loadings, show that the exponent  $b$  increases from 1 up to 3 with increasing the number and extension of open cracks [20, 25, 26]. Some of the corresponding results have already been presented as belonging to class D in the previous classification.

In this paragraph we show in more details some results taken from literature [13]. SSM measurements were performed on a cubic concrete sample under quasistatic mechanical loading. The sample was excited using a CW at frequency  $\omega_0 = 55.5 KHz$  and the exponent  $b$  was



calculated from the power law dependence of the nonlinear indicator  $y_{SSM}$  on the excitation energy at different damage levels. Mechanical loading induces damage in the sample which failed at a rupture load of about  $13\text{MPa}$ .

In Fig. IV.2, we show the exponent  $b$  increasing from 1, for an intact sample, up to 3 as a function of the applied loading. The variation of  $b$  could be explained assuming that different physical mechanisms, are at play at the microscopic level in different conditions during loading. In fact, it is expected a transition from one situation where distributed closed microcracks are the only present features to another corresponding to coalescence of microcracks into larger cracks, which finally result in visible macrocracks just before failure.

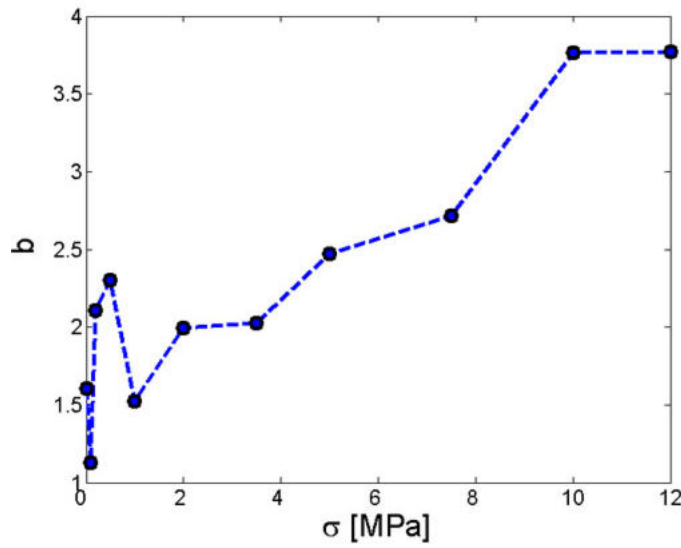


**Figure IV.2** – Exponent  $b$  of the power law fitting function as a function of load. The increase of the exponent may be related to transitions to different damage conditions (progression of damage)[? ].

## 3 Nonlinearity in multi-state multi-scale models

Multi-state models introduced in Chapter II present the advantage of being easy to implement and versatile. Different physical mechanisms could be described using different microscopic equations of state. Furthermore, different sources of nonlinearity could correspond to similar (or the same) equation of state for the microscopic elements, thus resulting in a non unique solution of the problem: see for instance the equations in the Granato-Lücke model for dislocations induced friction and the adhesion model in Chapter II.

Nevertheless, these models still constitute an excellent tool for supporting the interpretation of data and optimization of experiments. Also, their predictions could be easily qualitatively extracted from simple considerations, as we will discuss here.

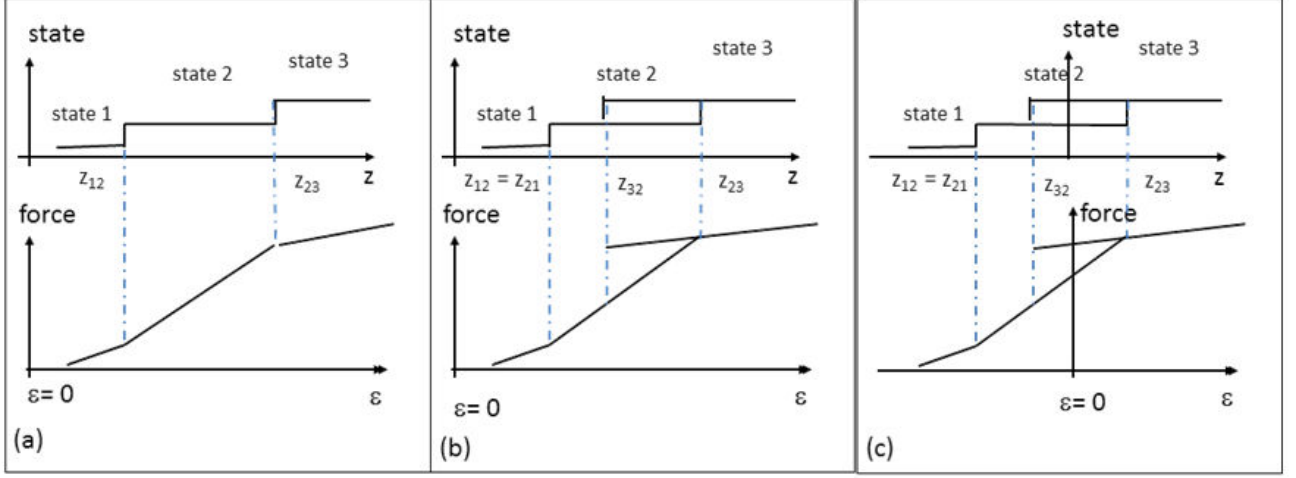


**Figure IV.3** – Typical microscopic stress-strain equation for a microscopic element in a multi-state formalism. Here for simplicity the driving variable is assumed to be the strain:  $z = \epsilon$ . (a) nonlinear microscopic element; (b) hysteretic microscopic element; c) hysteretic microscopic element with memory

### 3.1 General definition

Taking advantage of the generalized multi-scale multi-state approach, described in details in Chapter II, we could define several microscopic equations of state, which are the basis for modeling the macroscopic stress-strain relations.

As mentioned, these microscopic elements might be inhomogeneities, grain boundaries or cracks, with typical length of 0.1 to 100 micrometers. Each microscopic element is allowed to be in a given number  $N$  of elastic states (i.e. with stress proportional to strain). The state of a given element at time  $t$  is determined by a control variable  $z(t)$ , which is in general the applied pressure  $P(t)$  (it could also be the strain). Transition from state  $j$  to state  $j + 1$  occurs when the driving variable exceeds a given value  $z_{j,j+1}$ , characteristic to the element and called transition point. Thus, the microscopic model is fully defined by the number of states  $N$ , the corresponding values of the elastic constants  $\vec{K} = (k_1, k_2, \dots, k_n)$  and the number  $M$  of transition points: see e.g. Fig. IV.3. (a). The transition points define a vector  $\vec{Z}$ .

Once the mechanisms (i.e. the equation of state of the microscopic element) are defined, the model is scaled up to the mesoscopic level using a statistical ensemble of microscopic elements different from each others by their vectors  $\vec{Z}$ . The distribution of values of the driving variables define the generalised Presaich-Mayergoyz distribution  $\rho(\vec{Z})$ . In this context, each microscopic element corresponds to a point in a multidimensional space of coordinates given by the vector  $\vec{Z}$ .

Statistical averaging is performed over a proper distribution to derive the EOS in a scale of the order of 10 to 100  $\mu\text{m}$ , typical of Mesoscopic Elements. From that, it is easy to obtain the macroscopic equation of state, e.g. using the equation of motion and Finite Differences methods. The macroscopic  $\sigma(\epsilon)$  relation is the measurable one and thus constitutes the macroscopic

model.

From what has been stated above, it follows that:

- the microscopic equation of state is related to physical processes. From modelling point of view, the relevant information is contained in the state diagram as a function of the control variable  $z$  (see Fig. IV.3.(a);
- the mesoscopic equation of state depends of course on the microscopic equation of state. However, it is also influenced by the choice of the statistical distribution of elements in the PM space;
- the macroscopic equation of state depends on the mesoscopic one. However, it also depends on the eventually non spatially uniform distribution within the sample under investigation.

### 3.2 Hysteresis, memory and conditioning

One of the main features in a generalised multistate PM approach is the possibility to easily include in the model features such as hysteresis and memory, which can not be easily dealt with in an analytical approach. Thus, multistate models could be classified into hysteretic or non hysteretic models, with or without memory.

Let us refer to Fig. IV.3, the following typical microscopic equations of state are shown:

- Nonlinear element: in subplot(a) a purely nonlinear element is shown. The equation of state is the same when the control variable  $z$  is increasing or decreasing. The element contributes to nonlinearity in the global mesoscopic stress-strain equation only when switching from one state to another, i.e. at  $z(t) = z_{ij}$ .
- Nonlinear hysteretic element: as shown in subplot(b), hysteresis is present when at least one of the transition values of the control variable assumes different values when  $z(t)$  is increasing or decreasing:  $z_{ij} \neq z_{ji}$ . Thus for a given range of the control variable two (or eventually more) states are possible, depending on the conditions at previous times. To determine the actual state of the element at a given time  $t_1$ , it is sufficient to track the transitions occurring in the lapse of time  $[t = 0, t = t_1]$  according to the variations of  $z(t)$  (assuming  $z(t = 0) = 0$ ). Nevertheless, in the considered case, once the 'experiment' is finished, the control variable is zero again and the microscopic element returns to its initial state: no conditioning is observed.
- Nonlinear hysteretic element exhibiting conditioning: as shown in subplot(c), conditioning is an emerging property when the transition values of the control variable are such that for  $z = 0$ , i.e. equilibrium (initial) condition, more than one state are allowed for the microscopic element. In mathematical terms, the condition  $z_{ij} \times z_{ji} < 0$  should be satisfied for at least one couple  $ij$ . In this case, the state at time  $t = 0$ , i.e. when  $z(t) = 0$  is not uniquely defined. It should be calculated tracking the transitions in the interval  $-\infty < t < 0$  and it depends on the values of  $z(t)$  in the same time interval.

Before proceeding to the next Subsection, we remark here that relaxation processes are also involved in multistate models with conditioning, although not discussed here because they occur on a much longer time scale and thus are not relevant for the definition of the nonlinearity of the system. Nevertheless, their definition allows to define in a unique way the state at time  $t = 0$  for a system which was kept at rest for a long time.

### 3.3 Nonlinearity in the macroscopic response

To predict the macroscopic response, statistical averaging should be introduced and thus considerations about the statistical distribution of the values of the transition parameters are necessary. Each microscopic element is represented as a point with components of the vector  $\vec{Z}$  as coordinates in a multidimensional space with a given shape defined by the geometrical constraints imposed in the model, including an upper limit and/or threshold values for each parameter (see Fig. IV.4).

Here, we consider for simplicity a three states system without hysteresis. Geometrical constraints in the PM space correspond to the physical constraint  $z_{1,2} \leq z_{2,3}$ . Also an upper limit for the transition values is assumed and the distribution is uniform within the allowed space.

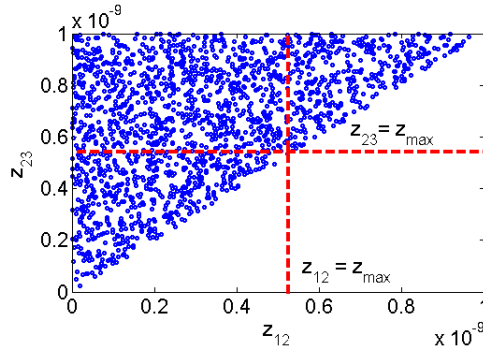


**Figure IV.4** – Typical distribution of  $M = 1800$  microscopic elements in the PM space for a three state system without hysteresis ( $z_{ij} = z_{ji}$ ).

A multi-state element contributes to nonlinearity in the global mesoscopic stress-strain equation only when switching from one state to another. If a perturbation  $z(t)$  ranging from  $z_{min}$  to  $z_{max}$  is applied, only microscopic elements with at least one transition point  $z_{i,j}$  belonging to the proper interval  $z_{min} \leq z_{i,j} \leq z_{max}$  are subject to transitions from one state to another, and consequently contribute to the nonlinear response of the system. In Fig. IV.4 only elements within the triangle in the lower left corner of the figure and in the rectangle (i.e. individuated by the two dashed lines corresponding to the maximum value assumed by the driving variables) are activated.

If we define  $\rho(\vec{Z})$  as the statistical probability to have an element with transition points defined by the vector  $\vec{Z} = (z_{12}, z_{23}, \dots, z_{(n-1)n})$ , the number of active nonlinear elements is therefore

$$N_{act} = \int_{z_{min}}^{z_{max}} \rho(\vec{Z}) dz_{12} dz_{23} \dots dz_{(n-1)n} \quad (\text{IV.1})$$

In the approximation of the same generated nonlinearity for each switching element in the PM space, which turns out to be realistic as verified in the following, the nonlinear response  $y$  is expected to be proportional to  $N_{act}$ .

For some simple density functions  $\rho$ , we could further develop the general equation Eq. IV.1 giving the nonlinear response  $y$  of multi-state multi scale models in order to find a relation between the exponent  $b$  predicted in such a response and the geometrical properties of the statistical distribution.

#### 3.3.1 Uniform distribution

Assuming a uniform distribution  $\rho(\vec{Z}) = \rho_0$ , Eq. IV.1 becomes:

$$\begin{aligned} N_{act} &= \rho_0 \int_{z_{min}}^{z_{max}} dz_{12} dz_{23} \dots dz_{(n-1)n} \\ &= \rho_0 S \end{aligned} \quad (\text{IV.2})$$

From the mathematical point of view, several parameters are important to calculate the value  $S$  of the integral of Eq. IV.2:

- the dimensionality of the PM space, that is to say, the number of transition parameters required by the model. This number is given by the number of allowed states  $N$  and it is defining the microscopic properties of the system;
- the shape of the allowed portion in the PM space, ie. the constraints imposed on the choice of the parameters. For instance, in Fig. IV.4 we have  $0 \leq z_{1,2} \leq z_{2,3} \leq 10^{-9}$ .

In any case,  $S$  can be calculated as the multidimensional volume resulting from the intersection between the PM space filled with density  $\rho_0$  and a sort of hypercube of size  $d = z_{max} - z_{min}$ . In Fig. IV.5 an example is reported, considering a three dimensional PM space bounded by  $|z_{i,j}| < \Lambda$ .

Thus, we end up with a total nonlinearity which is roughly proportional to the multidimensional volume  $S$  spanned by the applied perturbation  $z(t)$  in the PM space. Such a volume is proportional to some power  $b$  of  $d$  depending not only on the number of independent transition points  $z_{i,j}$  but also on the geometrical constraints imposed by the model.

In the following we will apply this approach to calculate the power law exponent for different multi-state multi-scale models, involving different microscopic equations of state. We use the models which have been already described in Chapter II: hysteresis, adhesion, and clapping.

**Figure IV.5** – Hypercube spanned by an excitation with  $z_{min} \leq z(t) \leq z_{max}$  in the case of a PM space bounded by the condition  $|z_{i,j}| \leq \Lambda$ . The coordinates of two selected points in the graph (blue circles) are given in the plot.

### 3.3.2 Non uniform distribution

Within the shape of PM space defined by a given microscopic equation of state and some given geometrical constraints, the transition parameters could be distributed according to any random distribution  $\rho(z_{1,2}, z_{2,3}, \dots, z_{(n-1),n})$ , which might be not uniform. In this case the solution of Eq. IV.1 is more complex and a general solution does not exist. It is clear however than even in this case the volume spanned by the perturbation in the PM space is still important.

In the following we will solve the problem for a particular case of non uniform distributions with a power law dependence. Nevertheless, we should mention that in dynamic experiments a uniform distribution is often the most reasonable choice. In fact, when a sample is dynamically excited, the strain levels are very small, compared to strains involved in quasi-static experiments. Thus, while in the latter the full PM space is explored, only a small portion is spanned by dynamic perturbations. It follows that a uniform approximation is of course reasonable.

In some cases however a non uniform distribution might be needed. This is the case of microscopic features with spatial or temporal correlations. As a second example, we can consider also threshold activated mechanisms, which might be well localised in a narrow strain (or stress) range. These cases are not however objective of the discussion reported in this thesis.

## 4 Constitutive equation based classification of multi state multi scale models

In this Section we will show how the predictions of the exponent  $b$  from Eqs. IV.1 and IV.2 allow to classify models into classes. The analysis is performed numerically and few details

## IV.4 Constitutive equation based classification of multi state multi scale models

---

about the implementation (see also Chapter III) are briefly recalled.

### 4.1 Numerical simulation

We performed 1-D numerical experiments on a bar of length  $l = 16$  cm. The sample is excited using a sinusoidal forcing  $\xi_i(t) = A_i \sin(\omega_0 t)$ , where  $\xi$  is a force or a displacement, at frequency  $\omega_0 = 10$  kHz. The total duration of the excitation is of about 3.14 ms (i.e. 5 cycles). The index  $i$  stands for the repetition of the experiment at different values of the amplitude  $A_i$ .

Drive amplitudes are calculated to give strain levels in the range  $6 \cdot 10^{-9}$  to  $7 \cdot 10^{-7}$ , in agreement with experimental conditions. These amplitudes correspond to stresses of the order of tens of *KPa*. All quantities assume reasonable values as in experiments and thus the elastic constants should be in the range of few *GPa*.

Calculations are performed using the multi-state multi-scale PM based approach described previously. The sample is discretised into mesoscopic zones. If a given zone presents some nonlinearity (micro cracks, dislocations, grain quandaries,...etc), it is further divided into microscopic elements. Depending on the kind of nonlinearity we wish to simulate, the microscopic element is described by a multi-state equation of state which allows a given number  $N$  of elastic states defined by an elastic constants vector  $\vec{K} = (k_1, k_2, \dots, k_N)$ .

We simulate here the response of  $M = 4000$  microscopic elements arranged either in parallel or in series, disposed according to a given distribution  $\rho$  in a PM space with some geometrical constraints on the transition parameters imposed by the model.

Time is discretised using a regular step  $\tau = 3.14 \mu s$ . For each time  $t = n\tau$ , the response  $F_i(t)$  is calculated and the new state for each microscopic element is determined, before proceeding to the following time step. Thus simulations, for each amplitude of excitation, provides two temporal signals:  $\xi(t)$  and  $F(t)$ .

The nonlinearity is extracted using the SSM or FFT indicators.

### 4.2 Hysteretic model with conditioning

#### 4.2.1 Microscopic equation of state

Microscopic elements are defined as two states systems with two transition pressures, called opening ( $z_{1,2} = P_o$ ) and closing ( $z_{2,1} = P_c$ ) pressures, each one is defined as a random variable in the range  $[-P_{c,o}^{max}, P_{c,o}^{max}]$ . The transition values satisfy the condition  $P_o \leq P_c$ , thus the transition to rigid state occurs in compression and the pressure is assumed to be positive. The equation of state is reported in Fig. IV.6 and the stress-strain equation of one hysteretic element is given by Eq. II.15

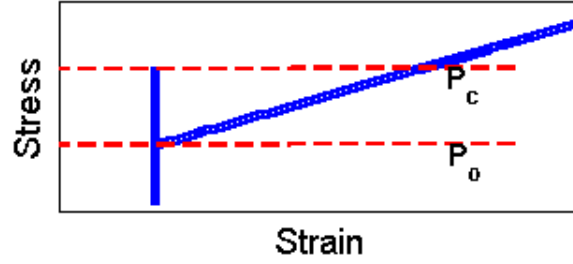


**Figure IV.6** – Microscopic EOS for the hysteretic model. Transitions points are shown with dashed red lines and their values  $\vec{Z} = (P_o, P_c)$  are reported.

#### 4.2.2 PM space and theoretical predictions of b

Hysteretic elements are distributed in a 2-D PM space whose shape is defined by the only geometrical constraint:

$$P_c \geq P_o \quad (\text{IV.3})$$

##### (a) Nonlinearity without conditioning:

As mentioned before, hysteresis without conditioning is obtained when  $P_c \geq P_o \geq 0$  where  $P_c^{min} = P_o^{min} = 0$ . The resulting PM space is shown in Fig. IV.7.

Let us consider a sample at rest:  $P(t = 0) = 0$ . For all elements, the inequality  $P_o > P(t = 0) = 0$  is satisfied, thus all elements are in the elastic state. When a dynamic excitation of amplitude  $A$  is applied (i.e.  $-A \leq P(t) \leq A$ ), all elements belonging to the lower triangle in the PM space (namely  $P_c < A$ ) switch to the rigid and then back to the elastic state repeatedly. Thus they contribute to nonlinearity.

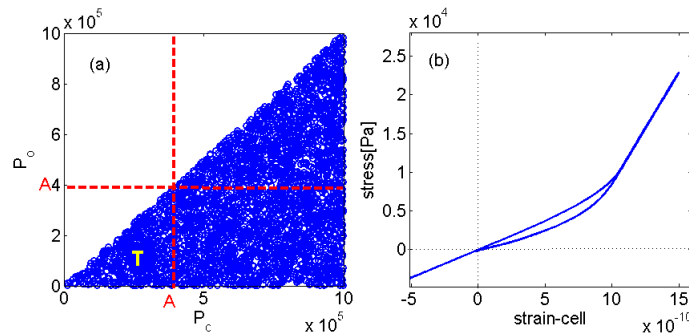


**Figure IV.7** – Hysteretic PM model for nonlinearity with conditioning effects. (a) The distribution  $\rho_0$  of microscopic elements in the PM space. The amplitude of the excitation is  $A$  and the activated area of the PM space corresponds to the triangle denoted by  $T$ ; (b) Macroscopic EOS derived from averaging.



#### IV.4 Constitutive equation based classification of multi state multi scale models

The area of the triangle is  $T = \frac{1}{2}A^2$  and the number of activated elements is

$$\begin{aligned} N_{act} &= \rho_0 \int_{-A}^A dP_c dP_o \\ &= \rho_0 T \\ &= \rho_0 \frac{1}{2} A^2 \end{aligned} \tag{IV.4}$$

From comparaisn of Eq. IV.5 to the power law dependance of the nonlinear indicator on the excitation amplitude  $x$  ( $y = ax^b$ ), it follows that  $b = 2$ .

##### (b) Conditioning effects:

When conditioning is present ( $P_o^{min} = P_c^{min} \leq 0$  and  $P_o^{max} = P_c^{max} \geq 0$ ), at time  $t = 0$  for some elements  $P_o \leq P(t = 0) \leq P_c$ . It follows that they could in principle be in either the rigid or the elastic state. For reasons not discussed here, however, it is assumed that relaxation processes lead all these elements to the rigid state, if the system was at rest for a long time to allow full relaxation.

In the PM space represented in Fig. IV.8.(a), for a given amplitude  $A$  of excitation, elements in the triangle denoted with the letter  $T$  are switching continuously from elastic to rigid state and back thus contributing to nonlinearity. The area  $T$  of this triangle is proportional to  $A^2$  as in the previous case:

$$T = \frac{1}{2} A^2. \tag{IV.5}$$

At the same time, elements in the rectangle  $R$  are switching only once, from rigid to elastic, such elements are known to be responsible of conditioning effects. The region  $R$  has an area:

$$R = A |P_c^{max} - A| = P_c^{max} |A - \frac{A^2}{P_c^{max}}|$$

Since  $A \ll |P_c^{max}|$ , the area becomes

$$R = A P_c^{max}$$

Again, since  $A \ll |P_c^{max}|$  the area  $R$  is larger then  $T$ . Note that the plot in Fig. IV.8(a) is not on scale.

It follows that, when hysteresis is present, conditioning contributions to the nonlinear response are dominant. The total number of elements in the area spanned by the dynamic oscillations is therefore:

$$\begin{aligned} N_{act} &= \rho_0 \int_{-A}^A dP_c dP_o \\ &\approx \rho_0 R \\ &\approx \rho_0 A \cdot P_c^{max} \end{aligned} \tag{IV.6}$$

#### IV.4 Constitutive equation based classification of multi state multi scale models

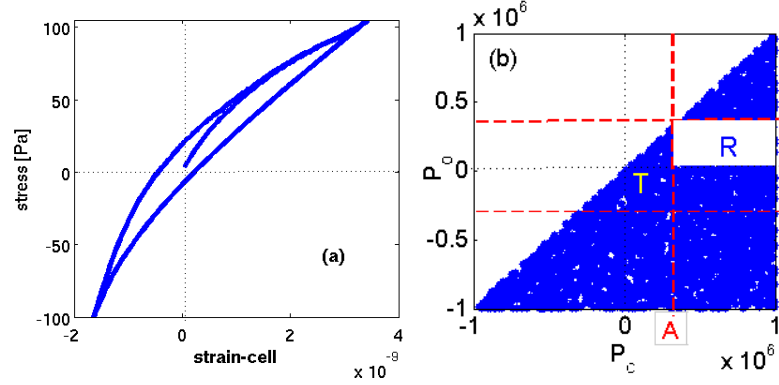


**Figure IV.8** – Hysteretic PM model for nonlinearity without conditioning. (a) Macroscopic EOS derived from averaging over many elements; (b) The distribution  $\rho_0$  of microscopic elements in the PM space. The activated area of the PM space for an amplitude  $A$  of the excitation are the triangle in the center (denoted by  $T$ ) and the rectangle  $R$ .

The exponent in this case is expected to be  $b = 1$ . The same value is expected when the constraint  $P_o = P_c$  is imposed, i.e. elements are on the diagonal (at least mostly) and hysteresis is negligible.

##### 4.2.3 Model parameters and numerical results

Numerical simulations have been performed to confirm the theory proposed. We have used the model with conditioning and  $N = 1000$  hysteretic elements. The chosen parameters of the model are an elastic constant  $E = 72$  GPa and a density  $\rho = 2700$  kg/m<sup>3</sup>.

The driving amplitudes under consideration in the present study are calculated to give typical stress values of the order of tens of  $KPa$ .

Care should be taken to ensure that such amplitudes do not saturate the PM space and we choose the maximum values of  $P_o$  and  $P_c$  to be  $P_o^{max} = P_c^{max}$ . Furthermore,  $P_{o,c}^{min} = -P_{o,c}^{max}$ .

Simulations varying the hysteresis parameters (density of the PM space  $\lambda$ , elastic parameter  $k$ ) have been performed. In all cases, we have found  $b = 1$ . Some typical results are shown in Fig. IV.9. Of course the coefficient  $a$  of the power law is dependent on the parameters: it increases when increasing  $\lambda$ . Similar considerations are valid also for the FFT indicator.

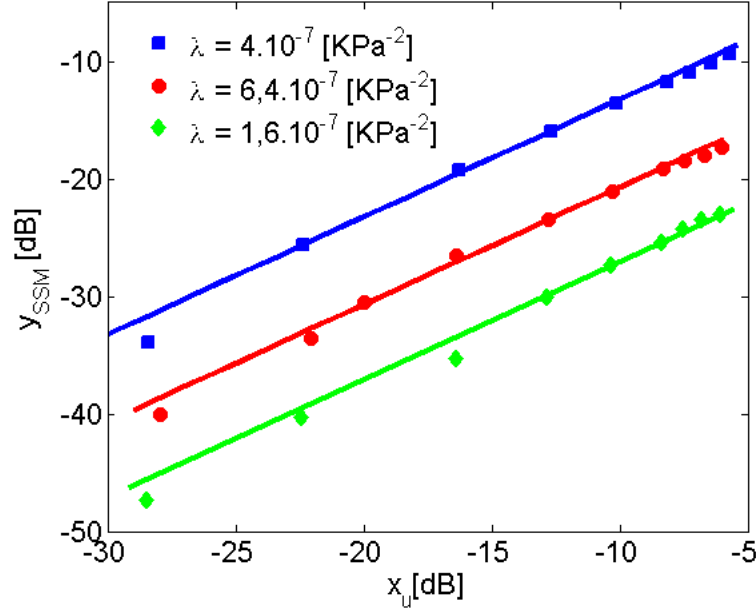


**Figure IV.9** – SSM nonlinear indicator vs. driving for the hysteretic model with conditioning. The curves refer to different values of the parameter  $\lambda$ . Solid lines are a power law fit, as expected  $b = 1$

### 4.3 Adhesion model with and without hysteresis

#### 4.3.1 Microscopic equation of state

In this model, the driving variable is the applied strain  $\epsilon$  on the element and two transition points ( $x_0 = z_{1,2}, x_1 = z_{2,3}$ ) allow each element to switch between three different elastic states characterised by the elastic constants ( $k_1, k_2, k_3$ ). The equation of state in the case without hysteresis is Eq. IV.8 and is shown in Fig. IV.10(a).

$$\begin{aligned}
 \sigma_{i,j} &= k_1 \Delta x_i && \text{if } \Delta x_i < x_0 \\
 \sigma_{i,j} &= k_2 \left( \Delta x_i - x_{01} \right) && \text{if } x_0 < \Delta x_i < x_1 \\
 \sigma_{i,j} &= k_3 \left( \Delta x_i - x_{02} \right) && \text{if } \Delta x_i > x_1
 \end{aligned} \tag{IV.7}$$

#### IV.4 Constitutive equation based classification of multi state multi scale models

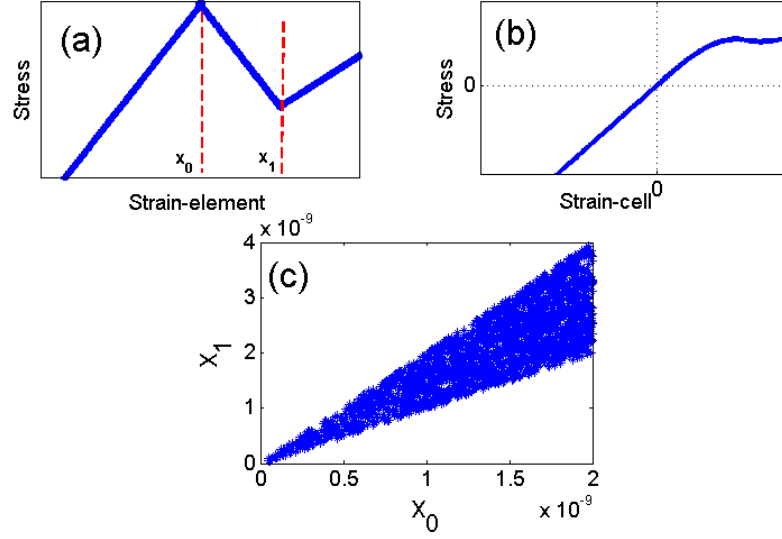


**Figure IV.10** – Adhesion model. (a) Microscopic EOS, transition thresholds  $\vec{Z} = (x_1, x_2)$  are reported; (b) Macroscopic EOS derived from averaging; (c) The distribution  $\rho_0$  of elements in the PM space.

We could introduce hysteresis in the model with an additional fictitious state. For simplicity, we assume a new transition point  $z_{3,1} = z_{1,2} = x_0$ , as shown by the plots of the corresponding equations of state in Fig. IV.11(a).

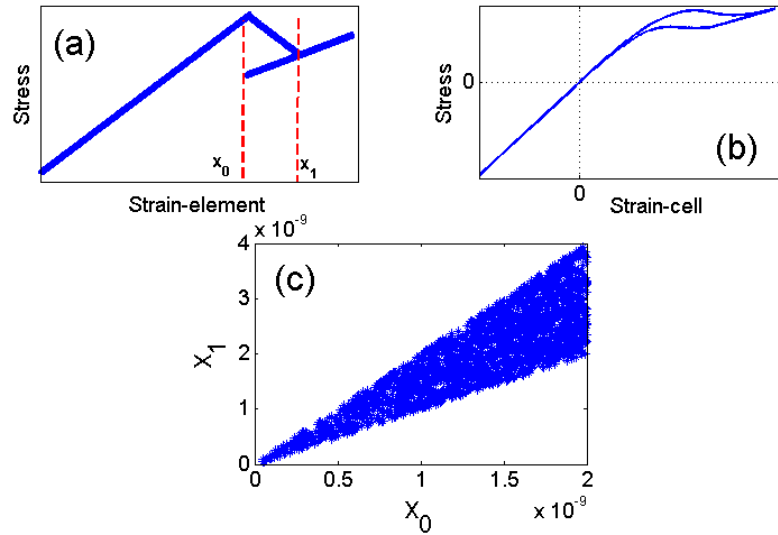


**Figure IV.11** – Adhesion model with hysteresis. (a) Microscopic EOS, transition thresholds  $\vec{Z} = (x_0, x_1)$  are reported; (b) Macroscopic EOS derived from averaging; (c) The distribution  $\rho_0$  of elements in the PM space.

## IV.4 Constitutive equation based classification of multi state multi scale models

### 4.3.2 PM space and theoretical predictions for $b$

The adhesion PM space is a 2-D one. Being derived from an analogy with the Lennard- Jones potential, the following physical constraints to the transition parameters values are introduced:

$$0 \leq x_0 \leq x_0^{max} \quad (\text{IV.8})$$

and

$$x_0 \leq x_1 \leq x_0(1 + \alpha) \quad (\text{IV.9})$$

The resulting PM space is shown in Figs. IV.10. (c) and IV.11. (c). For a given excitation of amplitude  $A$ , elements with transition parameters satisfying the condition  $x_0 < A$  and/or  $x_1 < A$ , make at least one transition and the area  $S$  spanned by this excitation is a triangle with base  $A$  and height  $(\alpha - 1)A$ .

We expect the area to be:

$$S = \frac{1}{2}(\alpha - 1)A^2 \quad (\text{IV.10})$$

The number of elements in this area is consequently

$$\begin{aligned} N_{act} &= \rho_0 \int_{-A}^A dx_0 dx_1 \\ &= \rho_0 S \\ &= \rho_0 \frac{1}{2}(\alpha - 1)A^2 \end{aligned} \quad (\text{IV.11})$$

Thus, both in the case with and without hysteresis, since the distribution in the PM space is the same, we expect an exponent  $b = 2$ .

### 4.3.3 Model parameters and numerical results

For what concerns the material properties, we use the same material density as before  $\rho = 2700 \text{ kg/m}^3$  and the same number  $N$  of microscopic elements ( $N = 1000$ ). The elastic constant for the different states are chosen to give an equivalent elastic modulus  $E = 72 \text{ GPa}$ . In addition, for the same reasons as in the hysteretic model, the maximum value of the deformation  $x_1$  is chosen to be  $x_0^{max} = 10^{-8}$ .

Simulations varying the model parameters (elastic parameters  $k_i$  and maximum of the transition parameters  $x_1^{max}$ ) have been performed. In all cases, we have found  $b = 2$ . Some typical results are shown in Fig. IV.12. Of course the coefficient  $a$  of the power law is dependent on the parameters: it increases when increasing the ratio  $k_2/k_1$  or decreasing  $x_0^{max}$ . Similar considerations are valid also for the FFT indicator.

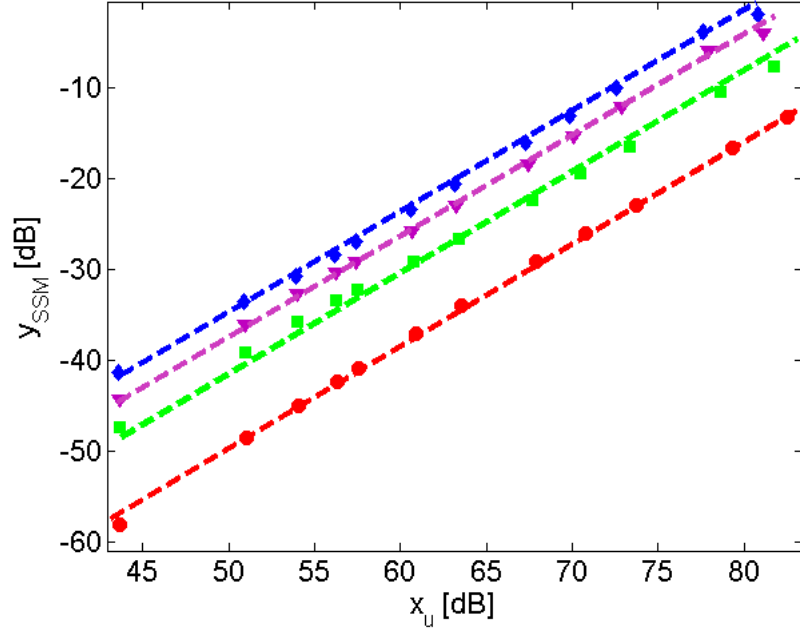


**Figure IV.12** – SSM nonlinear indicator vs. driving for the adhesion model with hysteresis. The curves refer to different values of the parameters. Solid lines are a power law fit. As expected  $b = 2$

## 4.4 Clapping model

### 4.4.1 Microscopic equation of state

The equation of state of a clapping element is defined summing the two equations of state of two springs in parallel. The first spring is linear elastic with elastic constant  $k_e$ ; the second spring is defined as a four state system, i.e. three elastic states with different elastic constants  $k_1, k_2, k_3$  and an open state supporting no force. Therefore we have three transition points and no hysteresis as described by Eq. II.26.

The equation of state is shown in Fig. IV.13. (a), the driving variable is the strain  $\epsilon$  at separating surface. Thus,  $K = \{k_e + k_1, k_e + k_2, k_e + k_3, k_e\}$  and the transition parameters  $Z = \{z_{1,2} = x_0, z_{1,2} = x_1, z_{2,3} = x_2\}$  are generated as random variables.

### 4.4.2 PM space and theoretical predictions for b

The clapping model is another form of analogy to a like-Lennard Jones potential. The same geometrical constraints as in the adhesion model are applied to both  $x_1$  and  $x_2$ . Thus, we have:

$$0 \leq x_0 \leq x_0^{max} \quad (\text{IV.12})$$

$$x_0 \leq x_1 \leq x_0(1 + \alpha_1) \quad (\text{IV.13})$$

#### IV.4 Constitutive equation based classification of multi state multi scale models

$$x_1 \leq x_2 \leq x_1(1 + \alpha_2) \quad (\text{IV.14})$$

The statistical distribution  $\rho_0$  in the PM space is shown in Fig. IV.13(c). Again, for a given excitation amplitude  $A$ , the volume of activated elements could be calculated taking into account the geometrical constraints imposed by the model. The activated volume, in this case, is a pyramid with volume proportional to  $A^3$  (as a consequence we expect an exponent  $b = 3$ ). The number of elements in the volume spanned by the excitation is:

$$N_{act} = \frac{\rho_0 \int_{-A}^A dx_0 dx_1 dx_2}{\rho_0 \alpha_1 \alpha_2 A^3} =$$

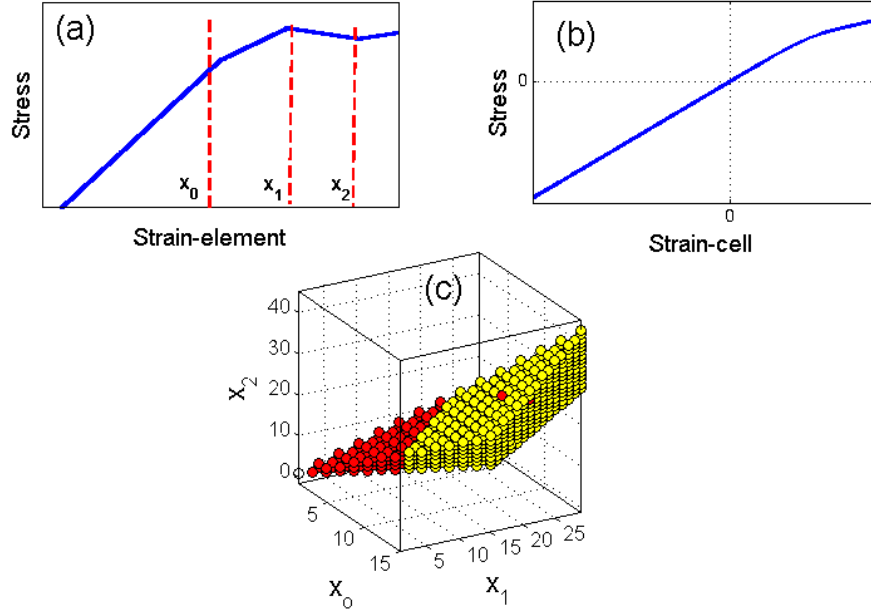


**Figure IV.13** – Clapping model. (a) Plot of the microscopic EOS, where transitions between different states are shown as dashed red lines and the transition thresholds  $\vec{Z} = (x_0, x_1, x_2)$  are reported; (b) Macroscopic EOS derived from averaging; (c) The distribution  $\rho_0$  of elements in the PM space.

##### 4.4.3 Model parameters and numerical results

The elastic constants are fixed such that the equivalent elastic modulus of the medium is  $E = 72$  GPa (property of Aluminium). Thus, Since in the initial state all of  $N = 1000$  elements are in state 1, the elastic spring has a constant  $k_e = \frac{E}{N} - k_1$ . The same material density as for the other models  $\rho_0 = 2700$  kg/m<sup>3</sup> is considered. The maximum value of the deformation  $x_0$  is chosen to be  $x_0^{max} = 10^{-8}$  and  $\alpha_1 = \alpha_2 = \alpha$  is used.

## IV.4 Constitutive equation based classification of multi state multi scale models

We performed some simulations for different choices of the clapping parameters. Results are shown in Fig. IV.14. The exponent  $b$  is independent from the model parameters while the coefficient  $a$  increases when the parameters  $x_o^{max}$  and/or  $\alpha$  decrease. Increasing the elastic constant  $k_1$ , we see that more nonlinearity is generated (corresponding to an increase of  $a$ ).

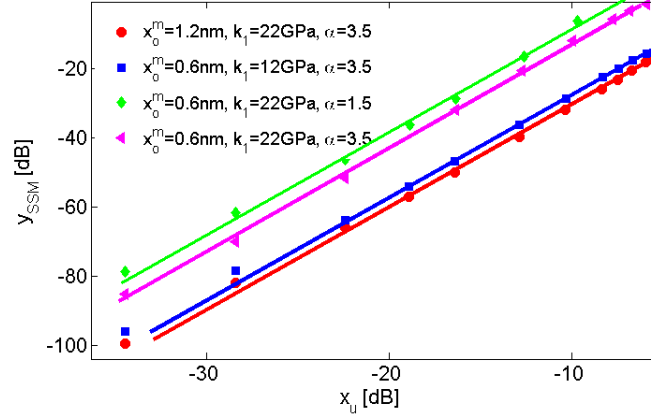


**Figure IV.14** – SSM nonlinear indicator vs. driving for the clapping model. The curves refer to different values of the parameters. Solid lines are a power law fit. As expected  $b = 3$

## 4.5 Results and discussion

As shown in the previous Subsection, the exponent  $b$  can be calculated for various models and depends only on the number  $N$  of allowed states and on the geometrical constraints imposed to the distribution (considered uniform) of elements in the PM space.

To summarise, the exponent  $b$  has been calculated for each one of the multi-state multi-scale models we previously discussed for different choices of the model parameters. In particular simulations have been performed for different values of the elastic constants vector  $K$ , of the PM density  $\rho_0$  and of the values of the upper boundaries in the PM space. Results are reported in Fig. IV.15.

The latter figure shows, for each model, many points corresponding to simulations which have been performed varying the model parameters. As we have already stated in the third Section of this chapter, a slight dependence of the exponent  $b$  on the choice of the vector  $\vec{K}$  could have been expected, since the nonlinearity generated during the transition from one state to another might not be the same for each microscopic element in the PM space. This consideration would make the proportionality between the nonlinear response  $y$  and the number  $N_{act}$  of elements participating to nonlinearity only approximate. Nevertheless, as shown in Fig. IV.15, such effects are negligible since in all cases, the exponent  $b$  is roughly independent from the choice of the parameters. This result confirms the possibility to define classes of multi-state multi-scale models based on their number of transition parameters and constraints only. This



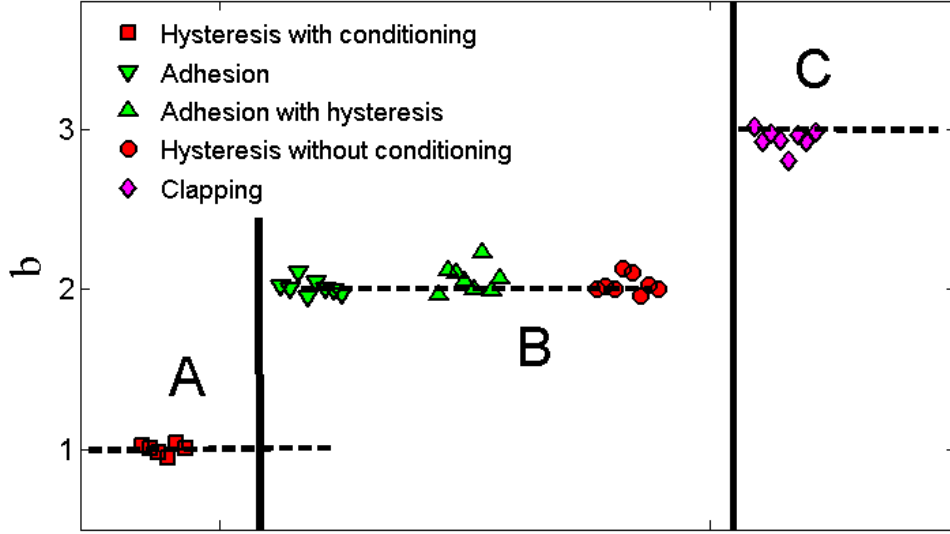


**Figure IV.15** – Power law exponent  $b$  predicted from simulations implementing numerically the SSM method for various models. *A*: hysteretic model with conditioning ( $b \approx 1$ ); *B*: adhesion and hysteretic without conditioning models, with  $b \approx 2$ ; *C*: clapping mode,  $b \approx 3$ .

classification may enable us to predict the mechanisms which are behind the nonlinear behaviour of a given medium by measuring experimentally the exponent  $b$ .

Note that the numerical classifications correspond well to those obtained using experimental data: see Fig. IV.1. Experimental results referring to the experimental class D will be discussed in the last Section of this Chapter when mixed models are introduced.

## 5 Geometrical constraints based classification

Given a uniform distribution  $\rho_0$  of microscopic elements in the PM space, we aim within this Section to prove that keeping the same microscopic equation of state, the only change in geometrical constraints provides a different macroscopic equation of state and may lead to variations of the exponent  $b$ . We propose here to study the variations of  $b$  in the response of multi state multi scale model which is based on the adhesion microscopic equation of state: see Fig. II.14 and Eq. II.33.

### 5.1 The geometrical constraints

We will consider three different cases of geometrical constraints on  $x_2$ , in addition to the condition  $x_2 \geq x_1 \geq 0$  which we have already stated. They are the following:

- Type I : both  $x_0$  and  $x_1$  are bounded by a maximum (constant) value:

## IV.5 Geometrical constraints based classification

---

$$\begin{aligned} 0 &\leq x_0 \leq \Phi \\ x_0 &\leq x_1 \leq \Psi \end{aligned} \tag{IV.15}$$

- Type II :  $x_0$  is bounded by a maximum (constant) value, while  $x_1 - x_0$  is bounded by a maximum value:

$$\begin{aligned} 0 &\leq x_0 \leq \Phi \\ x_0 &\leq x_1 \leq x_0 + \alpha \end{aligned} \tag{IV.16}$$

- Type III :  $x_0$  is bounded by a maximum (constant) value, while  $x_1 - x_0$  is bounded by a maximum value which increases linearly with  $x_0$ :

$$\begin{aligned} 0 &\leq x_0 < \Phi \\ x_0 &\leq x_1 \leq x_0 + \gamma x_0 \end{aligned} \tag{IV.17}$$

In Fig. IV.16, we represent the generalised PM spaces corresponding to a uniform distribution of adhesion microscopic elements with the three different boundaries introduced separately.

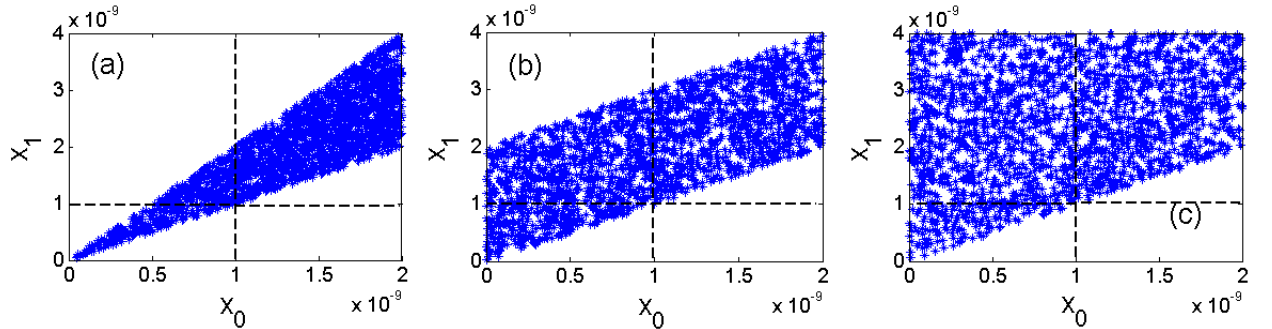


**Figure IV.16** – Distribution of the microscopic adhesion elements in the generalised PM space. The three cases correspond to the following constraints: (a) Type I: see Eq. IV.15; (b) Type II: see Eq. IV.16; (c) Type III: see Eq. IV.17.

In the three cases considered, the PM area activated by a perturbation  $z(t)$  of amplitude  $A$  is different. For types I and II we have a trapezoid (with area given as  $S = \frac{A}{2}(2\Psi - A) \approx A\Psi$ ) and a parallelogram (with area given as  $S = A\alpha$ ). In both cases, theoretically  $b$  is expected to be equal to 1. For type III, the area is a triangle with area  $S = 0.5\gamma A^2$  and thus the exponent is expected to be  $b = 2$ .

## 5.2 Results and discussion

Using the same approach described in the previous Chapter, we can simulate the response of the system for the three different distributions described above. The parameters of the simulations reported in this Chapter, unless otherwise specified, are the same as those reported in the previous Section for the adhesion model. Furthermore here we have used  $\alpha = 2$ .

In Fig. IV.17 the SSM and FFT nonlinear indicators defined above are plotted vs.  $x$  for each of the three choices of PM space distributions bounded as in Fig. IV.16. First, we notice that for all cases the behaviour is qualitatively similar for the two indicators even though the nonlinear to linear signal ratio is much larger when the analysis is performed in the time domain using the SSM indicator. We also see, from Fig. IV.17. (b), that noise effects are dominant at the lowest amplitudes in the case of boundaries of Type III (PM space of Fig. IV.16. (c)), as indicated from the proportionality between  $\theta$  and  $x$ , typical of noise effects [27], as it was discussed in the previous Chapter.

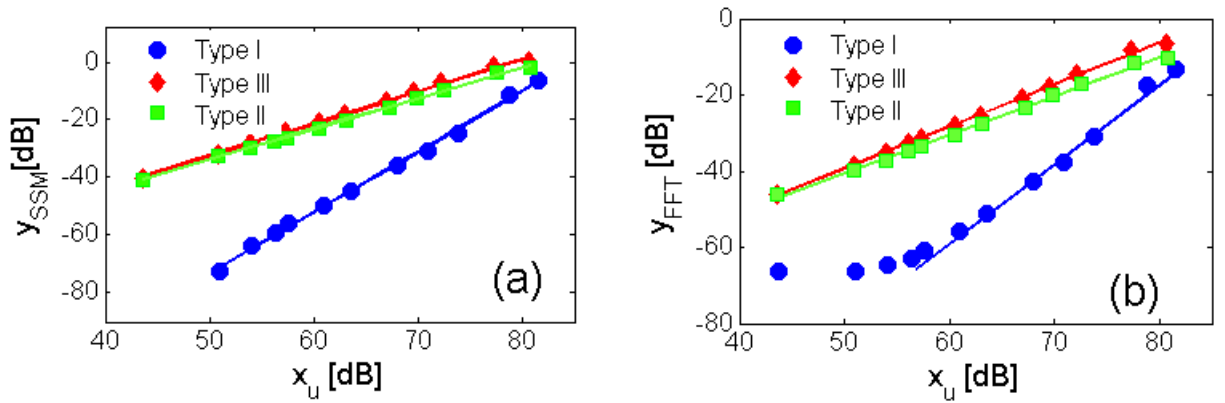


**Figure IV.17** –  $y_{SSM}$  and  $y_{FFT}$  vs.  $x_u$  for the three types of constraints discussed in Fig. IV.16. Green squares: type I; Red diamonds: type II; Blue circles: type III.

It turns out from the same figure that, as expected, the choice of the PM space boundaries is relevant for the determination of the power law exponent  $b$  (slope of the curve in log-log scale): the exponent is  $b = 1$  for Type I (blue circles) and II (green squares), while it is  $b = 2$  for the Type III (red diamonds), as predicted above.

In Figs. IV.18 and IV.19, we prove the exponent to be independent from the choice of the parameters of the model.

In Fig. IV.18, Type I is considered (the corresponding PM space being reported as an inset for reference) and the ratio  $k_2/k_1$  is increasing from  $k_2/k_1 = -1$  to  $k_2/k_1 = 1$  (blue to black). Results confirm that the slope is  $b = 1$  for all curves, independently from  $k_2$ , except for the case  $k_2/k_1 = 1$ . Here the slope is 2, since such limit case corresponds to the disappearance of one of the three states (state 1 is identical to state 2). For both indicators we note a decrease of nonlinearity with increasing the ratio  $k_2/k_1$ .

## IV.5 Geometrical constraints based classification

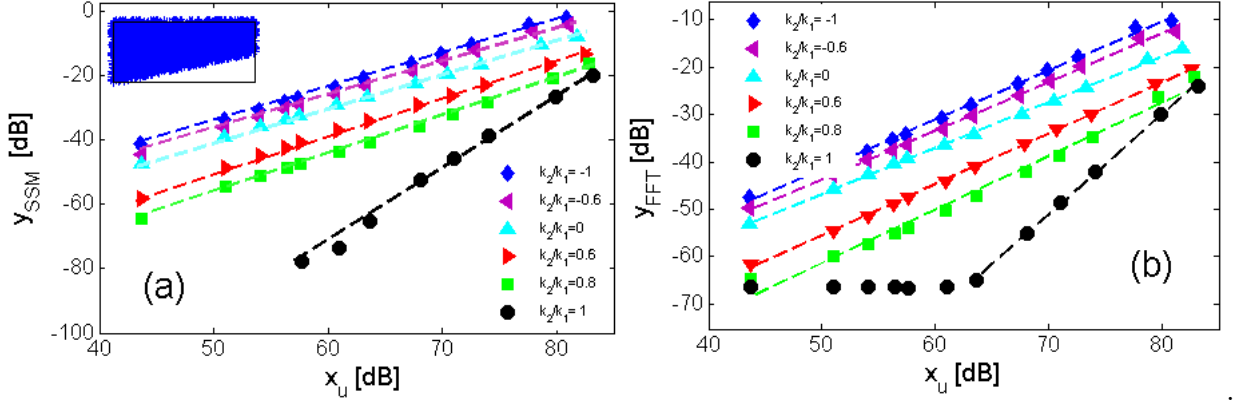


**Figure IV.18** –  $y_{SSM}$  and  $y_{FFT}$  vs.  $x_u$  for constraints of type I (shown in the inset). The various curves correspond to increasing values of the ratio  $k_2/k_1$ .

Similar considerations hold for Type II (Fig. IV.19), where we have varied the parameter  $\alpha$  (see Eq. IV.16) from  $3 \cdot 10^{-11}$  to  $100 \cdot 10^{-11}$  (red circles to green diamonds). The slope is always  $b = 1$ , as expected, with a noticeable increase of nonlinearity when decreasing  $\alpha$ .

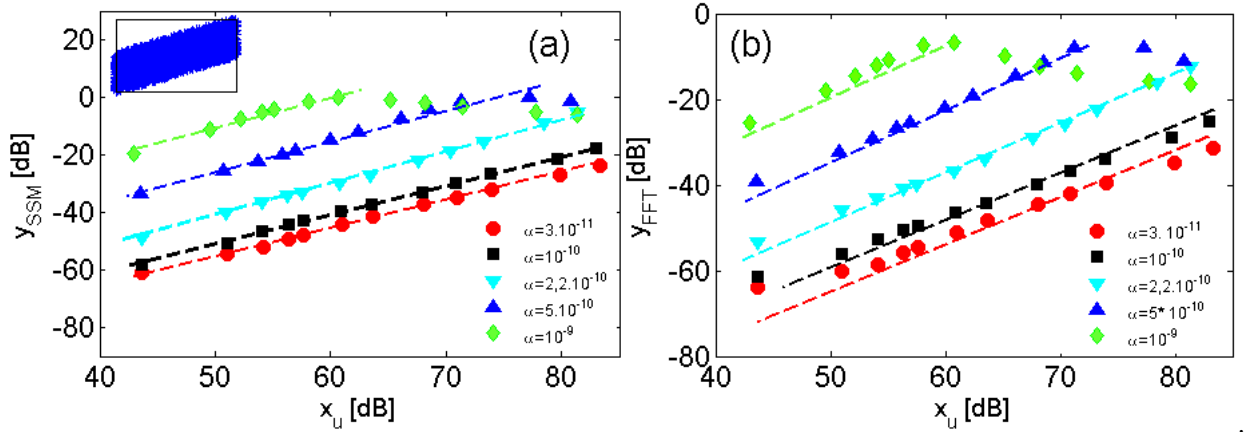


**Figure IV.19** –  $y_{SSM}$  and  $y_{FFT}$  vs.  $x_u$  for constraints of type II. The various curves correspond to increasing values of the parameter  $\alpha$ .

Finally we analyse Type III (see Fig. IV.20). The exponent is  $b = 2$ , for all values of the parameter  $\gamma$  in Eq. IV.17 ( $\gamma$  varies from 1 to 3 for curves from blue triangles to green diamonds).

Again, the limit case  $\gamma = 1$  corresponds to losing one transition point, hence reducing the number of states and increasing  $b$ .

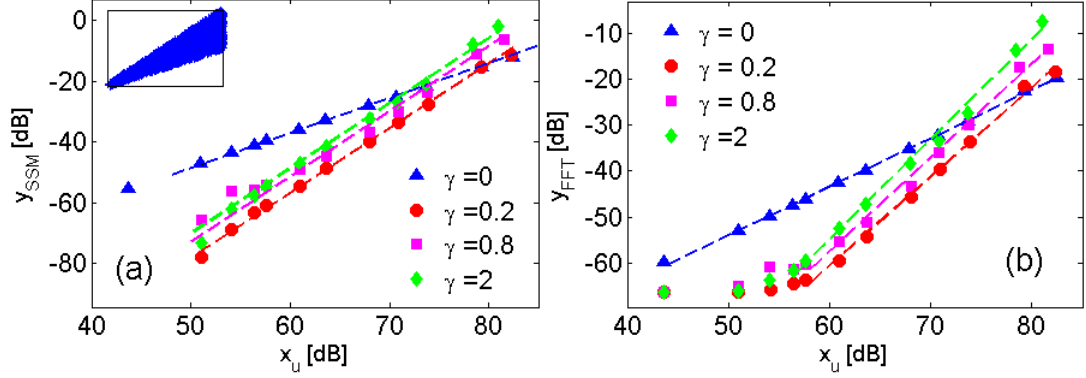


**Figure IV.20** –  $y_{SSM}$  and  $y_{FFT}$  vs.  $x_u$  for constraints of type III. The various curves correspond to increasing values of the parameter  $\gamma$ .

To further confirm the independence of the exponent  $b$  from the model parameters, in Fig. IV.21 we analyse its dependence from the ratio  $k_2/k_1$  for the three types of constraints considered. For both indicators (SSM and FFT), we observe a negligible effect of the choice of the elastic constants ratio. On the contrary, the intensity of nonlinearity described by the coefficient  $a$  of the power law decreases significantly when  $k_2$  increases up to reaching the same value as  $k_1$ .

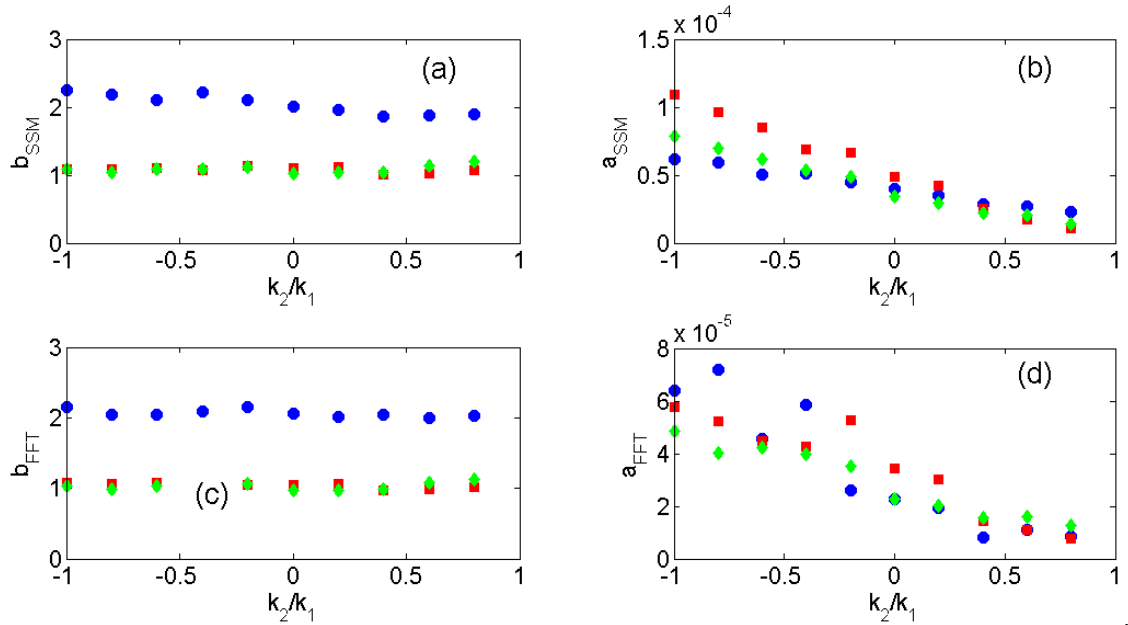


**Figure IV.21** – Exponent  $b$  and coefficient  $a$  for the SSM and FFT nonlinear indicators vs. the ratio  $k_2/k_1$  for the three types of constraints discussed in Fig. IV.17. Green diamonds: type I; Red squares: type II; Blue circles: type III.

Similar considerations hold also when the dependence on the ratio  $k_3/k_1$  is considered. In this case (Fig. IV.22), the exponent  $b$  is constant for the three types of constraints discussed. Also the intensity of nonlinearity (coefficient  $a$ ) is almost independent from the choice of  $k_3$ . A similar behaviour is shown using the FFT indicator.

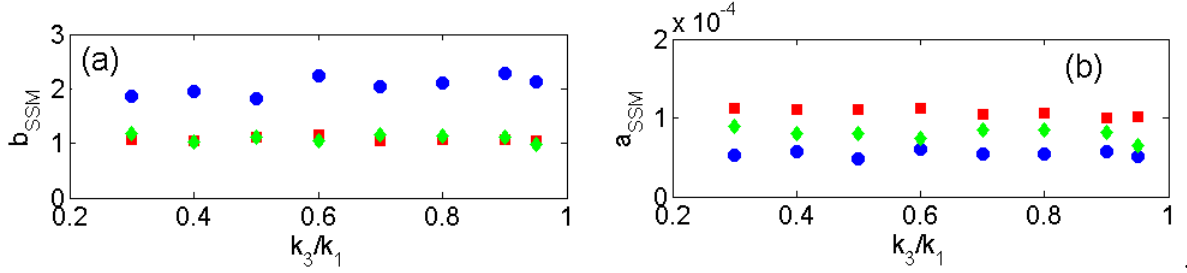


**Figure IV.22** – Exponent  $b$  and coefficient  $a$  for the SSM nonlinear indicator vs. the ratio  $k_3/k_1$  for the three types of constraints discussed in Fig. IV.17. Green diamonds: type I; Red squares: type II; Blue circles: type III.

## 6 Distribution based classification

As previously discussed, the choice of the distribution  $\rho(\vec{Z})$  of the transition parameters in the PM space is also influencing the power law exponent of the nonlinear indicator. We consider again the case of the adhesion microscopic equation of state with geometrical constraints of Type II: see Fig. IV.11 and Eq. IV.16.

### 6.1 The distribution functions

We limit ourselves here to consider power law distributions in the form of Eq. IV.18 and to analyse the dependence of the power law parameters from the exponents  $\beta_0$  and  $\beta_1$

$$\rho[x_0, x_1] \propto x_0^{\beta_0-1} x_1^{\beta_1-1} \quad (\text{IV.18})$$

### 6.2 Results and discussion

In Fig. IV.23, the SSM and FFT nonlinear indicators are reported vs.  $x$  for  $\beta_1 = 1$  and different choices of  $\beta_0$ . The slope is  $b = 2$  only in the case  $\beta_0 = 1$ , i.e. for a uniform distribution. For both nonlinear indicators,  $b$  increases with increasing  $\beta_0$ , but the nonlinear intensity decreases with increasing the exponent.

In Fig. IV.24, the exponent  $b$  and the coefficient  $a$  are plotted for both indicators as a function of  $\beta_0$ , and that in both the two cases  $\beta_1 = 1$  (red diamonds) and  $\beta_1 = \beta_0$  (blue circles).

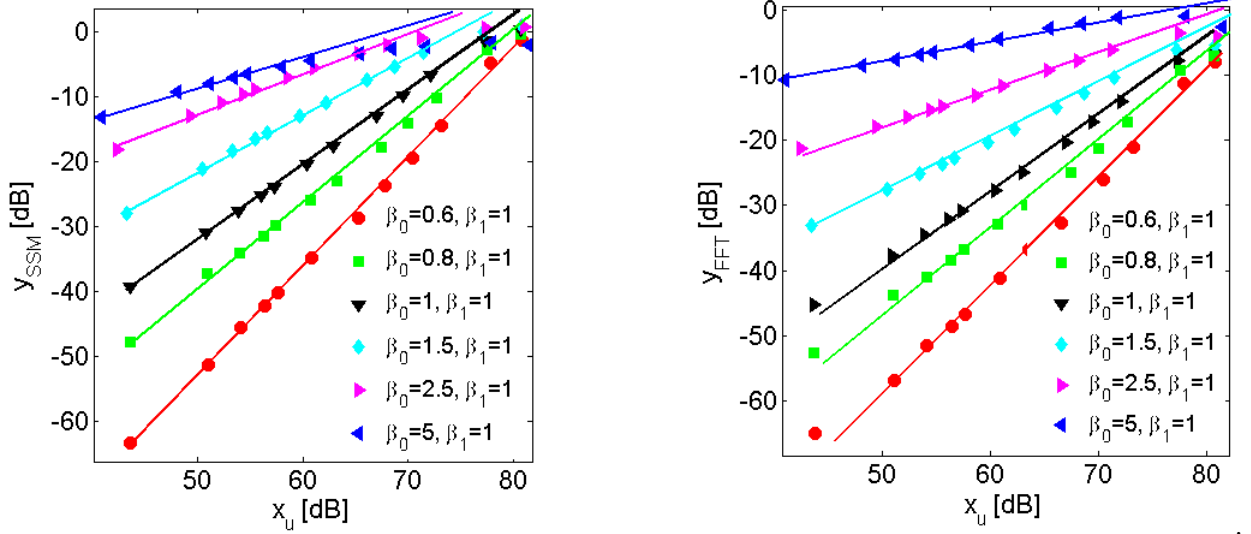


**Figure IV.23** –  $y_{SSM}$  and  $y_{FFT}$  vs.  $x_u$  for the adhesion model and constraints on the values of the transition parameters of type II. We used different nonuniform distributions in the PM space.

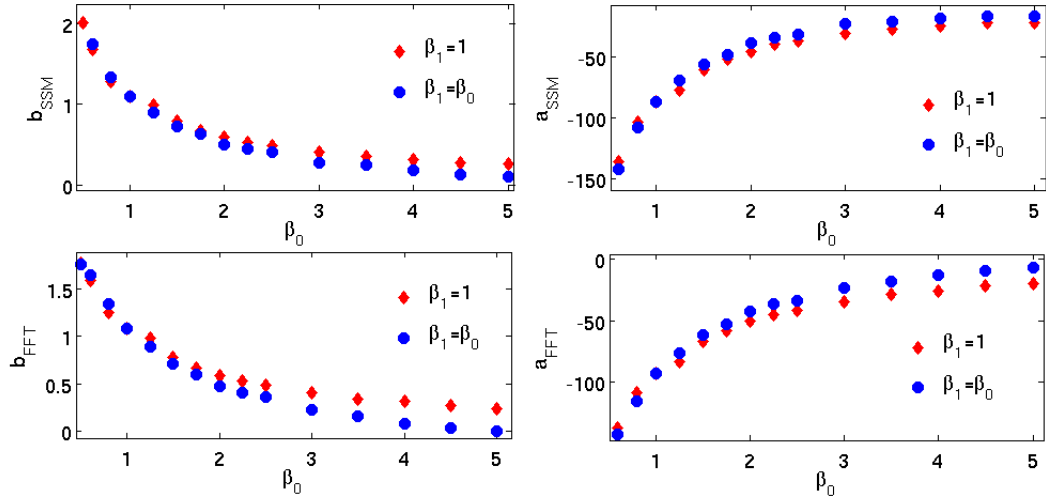


**Figure IV.24** – Exponent  $b$  and coefficient  $a$  for the SSM nonlinear indicator vs. the exponent  $\beta_0$  describing a non uniform power law distribution in the PM space for the adhesion model and constraints on the values of the transition parameters of type II.

We observe that:

- the exponent  $b$  decreases with increasing the exponent  $\beta_0$  of the power law distribution of the transition parameters;

- the coefficient  $a$  increases with increasing the exponent  $\beta_0$ . It should be noted however that in this case the strength of nonlinearity decreases when  $\beta_0$  increases, this is because the increase of  $a$  is not sufficient to compensate for the decrease of  $b$ .

## 7 Application of the classification to experimental damage characterisation

### 7.1 Experimental data for the characterisation of damage evolution

In several cases it has been observed that the evolution of damage is associated to an increase of the exponent  $b$ . This is true when damage is induced mechanically or thermally, while  $b$  is constant when damage is due to chemical reactions in which the expansion induces local stresses causing formation of cracks which are then filled by the residual products of the reaction itself. In this Section we are interested in the former case, i.e. when the effect of local deformations produces open micro-cracks evolving to macro-cracks before the sample failure.

#### 7.1.1 Experimental set up

For our analysis, we will consider in details experimental results obtained on a concrete sample subject to quasi-static loading at increasing levels of the load. We present here some details concerning the experiment we performed. A concrete sample was considered in the shape of a cylinder, 15 cm long and 4 cm diameter. The sample was tested in its intact state and after different levels of mechanical load applied along the longitudinal direction with a Mechanical Testing System (MTS). Loading levels are expressed as a percent of the rupture load.

Ultrasonic measurements were performed using an emitting narrow band PZT transducer connected to a function generator through an amplifier, which generates a continuous sinusoidal wave at the same frequency as the resonance frequency of the transducer (55KHz).

An identical receiving transducer was connected to an oscilloscope. Signals in the time domain are recorded after stationary conditions have been reached. A time window of 3.28 msec was chosen, with sampling rate of 10 MSa/s. Linearity of the generation/acquisition system has been verified. For each loading level, experiments have been conducted as discussed in Chapter III and varying the amplitude of the excitation between 5V and 70V, with a 5 Volts step, corresponding to strain amplitudes between  $10^{-8}$  and  $10^{-7}$ . The signal at the lower voltage level has been assumed to correspond to the linear signal. Signals have been synchronised using the input signal as a time reference frame.

#### 7.1.2 Previous results

Experimental results on similar samples (same cement paste and geometry) have been previously reported in the literature[25]. They show the SSM indicator  $\theta_{SSM}$  (i.e. not normalised), plotted as a function of output energy at different loading levels. The results are reported in Fig. IV.25. The experiment shows an increase in the sample nonlinearity, which was associ-



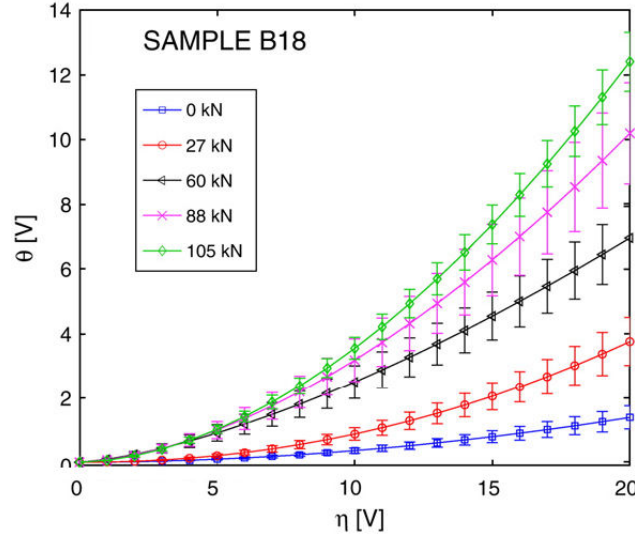


**Figure IV.25** – SSM indicator  $\theta_{SSM}$  plotted as a function of the output signal for a concrete sample under different loading levels.[25]

ated to an increase in damage. If the plots are reformulated in terms of the normalised SSM indicator, the power law fitting will provide an exponent which is increasing continuously with damage.

The results obtained in the experiment performed within the present thesis confirm these observations as it will be presented and discussed in the next Subsection.

## 7.2 Characterisation of damage evolution

Concrete is a consolidated granular medium. It presents the typical brick-mortar structure, i.e. it is composed by hard grains (bricks) separated by soft portions (mortar). These characteristics make concrete hysteretic already in its intact state.

Due to the external loading, the micro-structure of the sample changes. First, micro-cracks are induced when the sample is subject to moderate mechanical loading levels. A further increase in the loading force produce extension of the micro-cracks which will coalesce. Eventually, they may join each other to form larger cracks which will start to have an opening/ closing behaviour under dynamic excitation. When getting close to failure, macro-cracks appear and they behave like strongly clapping systems.

### 7.2.1 Mixed multi-state models

The features described above, suggest that the sample could be composed of microscopic elements with different behaviors. On one side, grain contacts are always present in the material, but gradually, when damage increases, they leave space to cracks which are more and more likely to behave as open cracks. Thus, it comes obvious that models mixing two multi-state microscopic equations are necessary. Furthermore, since excitation amplitudes in experiments

## IV.7 Application of the classification to experimental damage characterisation

---

are very small (strain of the order of  $10^{-8}$  or less), the distribution of elements in the PM space could be considered uniform.

In general, a mixed multistate system is composed of  $\Sigma$  Mesoscopic Elements (ME). Each ME is formed by  $M$  microscopic elements, all described by the same microscopic equation of state (any of those described previously). The mixed model is obtained by changing the ratio  $\Delta$  between the number of MEs described by the various microscopic models. In the case of mixing two microscopic features, we have:

$$\begin{aligned}\Delta &= \frac{\Sigma_{I/II}}{\Sigma} \\ \Sigma &= \Sigma_I + \Sigma_{II}\end{aligned}\tag{IV.19}$$

The Mesoscopic elements MEs are spatially distributed in the sample, i.e. in the macroscopic discretisation grid. They could be homogeneously distributed or spatially or localised in different areas of the sample.

As a consequence of mixing, the exponent  $b$  is no longer an integer value. Given  $b = b_1$  and  $b = b_2$  the exponents provided by two different microscopic models taken separately, the macroscopic  $b$  assumes all the intermediate values, depending on the value of  $\Delta$ .

### 7.2.2 Results and discussion

To model concrete subject to quasi-static compression damage, we use a mixed model composed of  $\Sigma_{hyst}$  hysteretic and  $\Sigma_{clap}$  clapping MEs. Damage evolution is followed with the parameter  $\Delta = \Sigma_{clap} / (\Sigma_{hyst} + \Sigma_{clap})$ .

When  $\Delta = 0$ , the sample is purely hysteretic and  $b = 1$  independently from the other parameters of the model, as shown in Fig. IV.26. (a) where the SSM indicator is plotted vs. the excitation energy for different choices of the hysteretic parameters. Likewise (Fig. IV.26. (b)), when  $\Delta = 1$ , independently from the clapping model parameters we have  $b = 3$ .

On the contrary, when  $\Delta$  assumes intermediate values (Fig. IV.26. (b)), the power law exponent assumes intermediate values as well. In this case, the parameters of the two models are also important in order to calculate the exponent  $b$ . In fact, the average between the two models should also account for the strength of nonlinearity generated by each ME and not only from their number. In principle, a few strong clapping features could be dominant with respect to several hysteretic features exhibiting weak nonlinearity only. In other words, there is not a straight forward relation between  $b$  and  $\Delta$ .

### 7.2.3 Fitting the experimental data

To validate the approach of mixed models, we fit the experimental data collected on a concrete cylinder subject to quasi-static loading. Data were collected using the experimental set-up described at the beginning of the Section. For each loading level, a full SSM experiment was performed and the SSM nonlinear indicator calculated. The use of narrowband transducers did not allow us to calculate the FFT indicator.

#### IV.7 Application of the classification to experimental damage characterisation

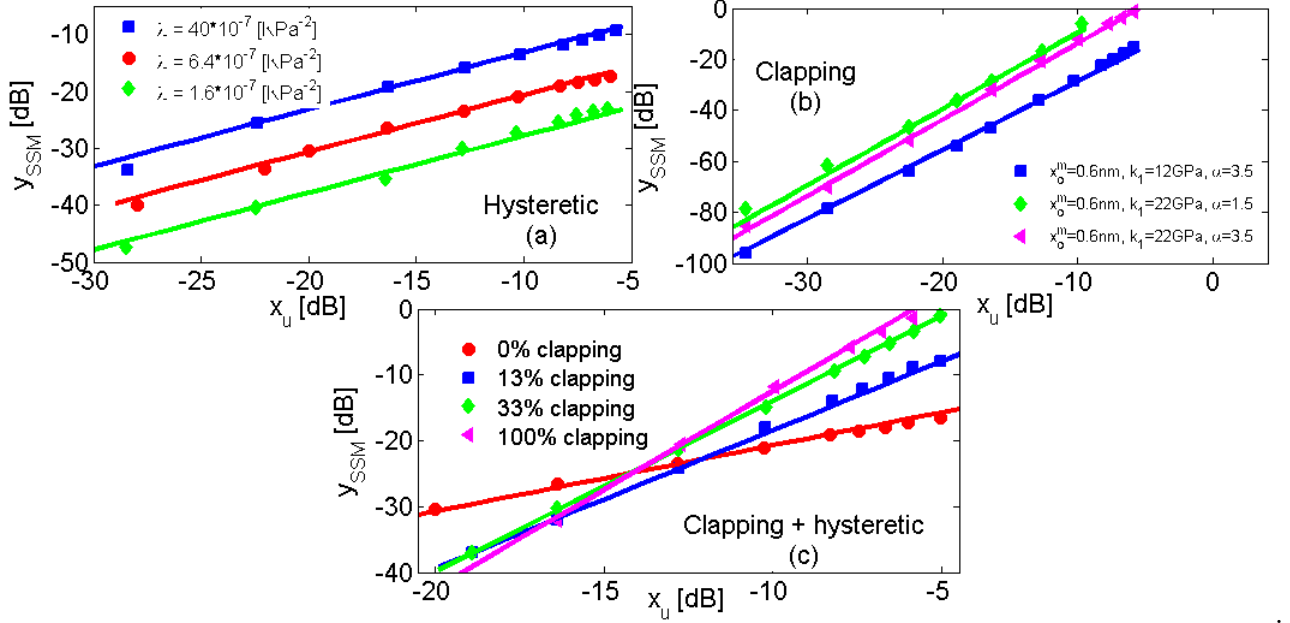


**Figure IV.26** –  $y_{SSM}$  vs.  $x_u$  for (a) The hysteretic; (b) Clapping; (c) Mixed models. The curves in in (a) and (b) refer to different values of the model parameters.

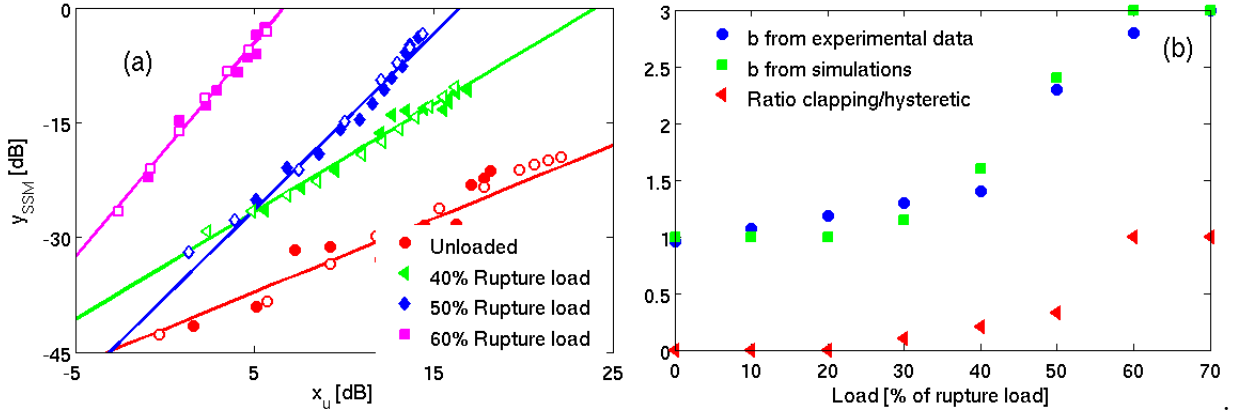


**Figure IV.27** – (a)  $y_{SSM}$  vs.  $x_u$  experimentally measured (solid symbols) and numerically calculated (empty symbols) for a concrete sample subject to increasing mechanical load; (b) Power law exponent determined from experimental and numerical data of subplot (a) (blue circles and green squares) and ratio  $\Delta$  (red triangles) used in the mixed model to fit the experimental data of subplot (a).

Results of the experiment for few different loading levels are shown as solid symbols in Fig. IV.27. (a). As in previous experiments (see e.g. Fig. IV.25), nonlinearity increases with

damage and the same for the exponent  $b$ . The latter is reported in subplot(b) as a function of load for all the different damage levels.

Experimental data have been fitted using a mixed model. At each load, only the ratio  $\Delta$  (see Eq. IV.20) between hysteretic and clapping elements was changed, keeping all other parameters fixed. Results of the simulations are reported as hollow symbols in Fig. IV.27. (a). The calculated exponent  $b$  is compared with the one experimentally measured in subplot(b) and the value of  $\Delta$  used to fit the experimental results is also shown in the same subplot as a function of the load level.

The fit obtained is very satisfactory, despite the complexity of the problem and the fact that only one parameter was used for fitting. Also we can observe that the increase of  $\Delta$  corresponds physically to the increase of the role of open cracks, which could be expected from the considerations reported previously.

Finally it could be noted that open cracks start being significant only once the applied load is about 50% of the rupture load. Increasing further the load, the number of clapping elements increases very rapidly. This rapid growth is in agreement with Acoustic Emission (AE) measurements. These measurements aim to detect the signals emitted by breaking features inside the specimen. One of the major parameters monitored is usually the number of AE events, which is known to have a similar evolution. At low damage, very few events are detected, while, once a threshold is reached, the number of events increases exponentially up to reaching failure. The threshold in AE measurement is in the same range of applied stresses as that observed here, i.e. about 50% of the rupture load.

## 8 Conclusions

In this chapter, a significant number of experimental data, mostly taken from the literature have been analysed. For experiments performed in different conditions, it was found that the nonlinear indicator (either SSM or FFT) has a power law dependence on the excitation energy. Materials could be classified in three main classes: classical nonlinear media ( $b = 2$ ), hysteretic media ( $b = 1$ ) and strongly damaged media ( $b = 3$ ). Also, intermediate values of  $b$  have been found for slightly damaged media.

From the physical point of view,  $b = 1$  is the typical exponent of materials with brick-mortar structure, i.e. hard portions separated by soft portions. They are characterised by the presence of closed microcracks. On the contrary, when  $b = 3$  it seems that open cracks are dominating the elastic behaviour of the system.

From the theoretical point of view, this experimental observation corresponds well to the definition of classes of multi-state multi-scale models. The power law corresponding to a given model has been shown to be dependent of the microscopic equation of state, of the constraints on the transition parameters and of their distribution. On the contrary the power law exponent is roughly independent from the absolute values of the parameters used. Thus, we could conclude

that the power law exponent is an indicator of the physical origin of nonlinearity, both at the microscopic level and in the statistical distribution of the nonlinear features.

The validity of the proposed approach was tested by measuring the evolution of the exponent in a concrete sample subject to damage. Simulations of the process have revealed that good fitting of the experimental data could be obtained assuming a progressive transition from a closed microcrack distribution to a distribution of nonlinear features dominated by the presence of macrocracks.

In conclusion, we claim here that a change in the exponent  $b$  is an indication of a variation of the physical origin of nonlinearity. From the knowledge of the processes responsible of damage formation, a multi-state modelling approach allows to extract quantitative parameters about the role of different mechanisms.

However, when dealing with more complex and/or 'unknown' media, the situation is more complicated. Many equivalent hypotheses could be formulated to explain the origin of variations in the exponent, linked to changes in the microscopic equation of state (e.g. number of states) but also linked to variations in constraints on the values of the transition parameters and, more generally, on the statistical distributions of microscopic nonlinearities.

At the moment it seems difficult to think of experiment allowing to discriminate unambiguously between different causes of the variation of the exponent  $b$ , since only the macroscopic stress-strain equation is available (and not in tension, usually) and different microscopic models with different averaging statistics could provide the same macroscopic constitutive equation. Nevertheless, the approach proposed could still allow to draw plausible conclusions about the evolution of damage, which could be supported by other independent and partial experimental evidences.

---

## References

- [1] H. K. Janssen and O. Stenull. Field theory of directed percolation with long-range spreading. *Phys. Rev. E*, 78:031704, 2008. [82](#)
- [2] S. Ramakrishnan et al. Elasticity and clustering in concentrated depletion gels. *Phys. Rev. E*, 70:040401, 2004. [82](#)
- [3] D. G. Enzer et al. Observation of power-law scaling for phase transitions in linear trapped ion crystals. *Phys. Rev. Lett*, 85:2466, 2000. [82](#)
- [4] J. Barò and E. Vives. Analysis of power-law exponents by maximum-likelihood maps. *Phys. Rev. E*, 85:066121, 2012. [82](#)
- [5] P. A. Johnson and A. Sutin. Hysteresis models from the mathematical and control theory point of view. *J. Acoust. Soc. Am.*, 117:124–130, 2005. [82](#)
- [6] T. J. Ulrich et al. Application of nonlinear dynamics to progressive fatigue damage in human cortical bone. *Appl. Phys. Lett.*, 91:213901., 2007. [xi](#), [83](#), [84](#)
- [7] G. Renaud, P. Y. Le Bas, and P. A. Johnson. Revealing highly complex elastic nonlinear (anelastic) behavior of earth materials applying a new probe: Dynamic acoustoelastic testing. *J. Geoph. Res. -Solid Earth*, 117:B06202, 2012. [83](#)
- [8] K. Van Den Abeele et al. Nonlinear elastic wave spectroscopy (NEWS) techniques to discern material damage, part I: nonlinear wave modulation spectroscopy (NWMS). *Res. Nond. Eval.*, 12:17–30, 2000. [83](#)
- [9] P. Antonaci et al. Effects of corrosion on linear and nonlinear elastic properties of reinforced concrete. *Cem. Concr. Res.*, 51:96–103, 2013. [xi](#), [83](#), [84](#), [85](#)
- [10] X.J. Chen et al. Characterization of progressive microcracking in portland cement mortar using nonlinear ultrasonics. *NDT&E Int.*, 41:112–118, 2008. [xi](#), [83](#), [84](#)

- 
- [11] C. Payan, V. Garnier, and J. Moysan. Effect of water saturation and porosity on the nonlinear elastic response of concrete. *Cem. Concr. Res.*, 40:473–476, 2010. [xi](#), [84](#)
- [12] M. Scalerandi et al. Discriminating closed and open cracks in concrete using nonlinear ultrasounds and power laws. *Submitted to Cem. Concr. Res.*, x, 2013. [xi](#), [84](#)
- [13] P. Antonaci et al. Evolution of damage-induced nonlinearity in proximity of discontinuities in concrete. *Int. J. of Solids and Structures.*, 47:011905, 2010. [xi](#), [84](#), [85](#)
- [14] U. Polimeno and M. Meo. Detecting barely visible impact damage detection on aircraft composites structures. *Cmp.St*, 91:3980402, 2009. [xi](#), [84](#)
- [15] D. Donskoy, A. Sutin, and A. Ekimov. Nonlinear acoustic interaction on contact interfaces and its use for nondestructive testing. *NDT&E Int*, 34:231–238, 2001. [xi](#), [84](#)
- [16] H. E. Engan et al. Nonlinear ultrasound detection of osteoporosis. *IEEE Ultrasonics Symposium*, 34:2096, 2006. [xi](#), [84](#)
- [17] B. Zinszner, P. A. Johnson, and P. N. J. Rasolofosaon. Influence of change in physical state on elastic nonlinear response in rock: Significance of effective pressure and water saturation. *J. Geoph. Res.*, 102:8105–8120, 1997. [xi](#), [84](#)
- [18] B. Zinszner, P. A. Johnson, and P. N. J. Rasolofosaon. Resonance and elastic nonlinear phenomena in rock. *J. Geoph. Res.*, 101:553–564, 1996. [xi](#), [84](#)
- [19] K.E-A. Van Den Abeele et al. Micro-damage diagnostics using nonlinear elastic wave spectroscopy (news). *NDT&E Int.*, 34:239–248, 2001. [xi](#), [84](#)
- [20] M. Scalerandi et al. Nonlinear elastic response of thermally damaged consolidated granular media. *J. Appl. Phys*, in press (2013). [xi](#), [84](#), [85](#)
- [21] M. Scalerandi, A.S. Gliozzi, and D. Olivero. Discrimination between ultrasonic indications in steel using nonlinear techniques. *Submitted to J. NonDestruct. Eval*, 2013. [xi](#), [84](#)
- [22] K. Van Den Abeele et al. Nonlinear Elastic Wave Spectroscopy(NEWS) Techniques to Discern Material Damage, Part II: Single-Mode Nonlinear Resonance Acoustic Spectroscopy. *Res. Nondestr. Eva1*, 12:31–42, 2000. [xi](#), [84](#)
- [23] M. Scalerandi et al. A scaling method to enhance detection of a nonlinear elastic response. *Appl. Phys. Lett.*, 92:101912, 2008. [85](#)
- [24] K.J. Lesnicki et al. [85](#)
- [25] P. Antonaci . et al. Monitoring evolution of compressive damage in concrete with linear and nonlinear ultrasonic methods. *Cem. Concr. Res.*, 40:1106–1113, 2010. [xiii](#), [85](#), [109](#), [110](#)

- [26] G.Shui and Yue-S Wang. Ultrasonic evaluation of early damage of a coating by using second-harmonic generation technique. *J. Appl. Phys.*, 111:124902., 2012. [85](#)
- [27] M. Bentahar . et al. Influence of noise on the threshold for detection of elastic nonlinearity. *J. Appl. Phys.*, 113:043516, 2013. [104](#)



---

---

# Chapter V

---

## Conditioning effects on the power law behavior of NME materials

### 1 Introduction

In the previous Chapter we analysed the microscopic mechanisms which might be behind the anomalous dynamic behavior of NME materials. Be it phenomenological like in the hysteretic model or physical, like adhesion and clapping, these mechanisms provide qualitatively similar macroscopic observations. The dependence of nonlinear indicators as a function of excitation amplitudes is always a power law  $y = ax^b$ . However, the value of the exponent  $b$  is dependent on the physical processes at play. Introducing a multi-state multi-scale approach, from the knowledge of the number of transition parameters, the geometrical constraints and the distribution of microscopic elements, the power law exponent  $b$  could be predicted.

Here we focus on an additional observation typical of NME materials: conditioning and slow dynamics. Resonance experiments have shown that the frequency shift at a given amplitude is associated with variations of the elastic properties of the medium (softening). However, if the excitation persists, the modulus continues to decrease for some period of time until the material reaches a new equilibrium state where no more change takes place [1]. This induced softening does not disappear immediately when the perturbing amplitude is removed, it is conditioning. This observation implies that when the sample is excited by an elastic wave at increasing amplitudes nonlinearity is generated not only as a consequence of the immediate amplitude dependent softening, but also by conditioning at the previous amplitude which contributes to the material softening and thus to the measured nonlinearity [2].

Except in the hysteretic model, contribution of conditioning to nonlinear indicators was not included in the multi-state multi-scale mechanisms as presented in the previous Chapters. This issue is not particularly relevant for the results obtained so far. However, the effects of conditioning on the power law behavior should be included in the analysis, since it might provide further information about the statistical distributions of the properties of the microscopic elements at the basis of the multi-state models proposed to simulate the elastic behavior of NME materials.

The goal is not trivial. Indeed, the hysteretic model proposed in the literature and used in the previous Chapter accounts for softening and relaxation effects in a straightforward way. Nevertheless the feature of nonlinearity activation induced by conditioning and recently ob-

served in damaged concrete [3] is still not well described theoretically. In this Chapter, we first introduce the experimental context, recalling the mentioned results on damaged concrete and showing novel experimental results on damaged metallic composites. Then, we present a numerical study, to show how conditioning could be included in multi-state models and show its effects on the measured nonlinearity.

## 2 Experimental results

Many authors were interested in the separation of conditioning from nonlinearity in the response of NME materials to a dynamic excitation [1, 4]. Despite the numerous studies on the subject and although many experiments confirmed the existence of conditioning, the phenomenon is not yet completely understood. In particular the existence of thresholds for conditioning, its physical origin and the way it affects the measurement of nonlinearity are still to be fully analyzed. Here, we focus our attention on two experimental results showing that the nonlinearity measured after conditioning is much larger than before: mechanism of nonlinearity activation.

The first experiment was performed using flexural waves in a metal based composite sample (stainless steel matrix reinforced with TiC particles) in the shape of a plate (2cm x 10cm x 0.1cm). The sample was excited using PZT transducers glued on the upper surface of the plate and the strain was measured using a laser vibrometer, providing strains in the range  $10^{-9}$  to  $10^{-6}$ . The experiment was performed using sweeps, where the frequency interval is around the fundamental resonance bending mode of the sample. The  $y_{FFT}$  indicator (in this case was chosen the energy of the third harmonic normalized to the fundamental) was measured at increasing amplitudes of excitation. After having reached the highest amplitude of excitation, the sample was excited continuously at 128 Volts during  $\sim 1$  mn. Right after this high drive conditioning, the sample was excited again around its first bending resonance mode ( $\sim 6KHz$ ) where the third harmonic ( $\sim 18KHz$ ) was probed using the same amplitudes as before. The measured indicator was plotted as a function of the driving amplitudes  $x$  before and after conditioning: see Fig. V.1.

The experiment shows that conditioning is activating nonlinearity. Indeed, the coefficient  $a$  of the power law increases by almost 10 dB after conditioning, while the exponent  $b$  is not affected and remains approximately equal to 1. This effect is shown to be completely reversible as shown by green diamonds curve representing the nonlinear indicator measured at the beginning of relaxation. Indeed, if measurements are successively repeated in time without conditioning the sample, we notice the curve to fall back on the original one. Thus the nonlinearity activation mechanism disappears slowly.

Very similar results have been shown in an independent experiment. The nonlinear response of a damaged concrete sample was measured using the SSM technique at increasing amplitudes before and after conditioning. Here the sample was a concrete cylinder (radius of 3 cm and length of 15cm). The source function was a sinusoidal wave and self-conditioning was studied. A first experiment (before conditioning) was performed increasing the amplitude of the source. Then (after conditioning) the experiment is repeated again with the same amplitude range for

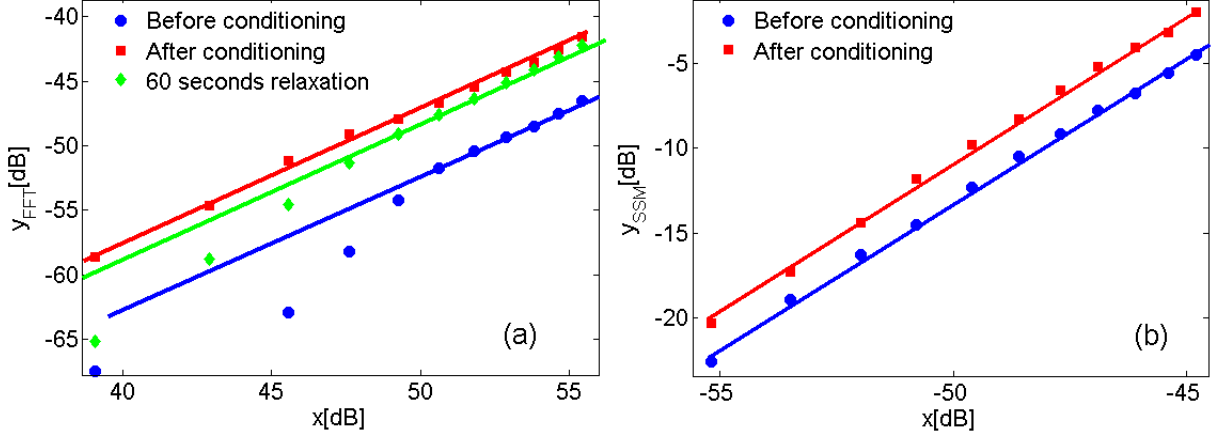


**Figure V.1** – Experimental results obtained exciting: (a) A fatigue damaged metal based composite sample (stainless steel matrix reinforced with TiC particles) with a sweep source at frequencies close to the third flexural mode of the sample; (b) A concrete bar using a sinusoidal wave.  $y_{FFT}$  is plotted as function of the driving  $x$  before (blue) and after (red) conditioning in both experiments and at the beginning of relaxation (green) for the first experiment.

the source. In the second case, conditioning induced by the largest amplitude of the first run is influencing measurements in the repeated experiment.

We should also mention that experiments in rocks using the Dynamic AcoustoElastic method [5] seem to show that in rocks, after conditioning, the nonlinearity of the sample decreases. In this case, we speak of purely hysteretic media without damage. The measurement performed differs significantly from the techniques discussed here. However, even though not yet definitively proved, such a decrease in the nonlinear parameters is of interest for the discussion of the next Section.

### 3 Multi scale multi state models with conditioning

Using the multi-scale multi-state approach, based on the generalized PM space formalism, we will introduce in the next Sections two different microscopic mechanisms presenting both nonlinearity and conditioning in their stress-strain relations. To do this, we need the transition parameters vector  $Z$  to assume values such that, for at least some of the microscopic elements, more than one state are allowed in the initial condition, i.e. where no drive is applied.

From the mathematical point of view, the condition  $z_{ij} \cdot z_{ji} < 0$  should be satisfied for at least one couple  $ij$ . In this case, the state at time  $t = 0$ , i.e. when  $z(t) = 0$  is not uniquely defined. As a consequence, the element can switch between different states during a dynamic excitation and when  $z(t)$  goes back to zero the element is no more in the same initial state.

To be more specific, let us assume a two state system and consider a microscopic element

with  $z_{2,1} < 0$  and  $z_{1,2} > 0$  meaning that for  $z(t = 0) = 0$  the microscopic element can be either in state 1 (assuming an elastic constant value  $k_1$ ) or 2 (state 2 corresponding to an elastic constant  $k_2$  is assumed here to be the initial state). Then we consider an external excitation  $z(t)$  such that  $\max(z(t)) < z_{1,2}$  and  $\min(z(t)) < z_{2,1}$ . It follows that during the excitation elements jump to state 1 as soon as  $z(t) < z_{2,1}$  but since  $z(t) > z_{1,2}$  never occurs, elements never returns to state 1. At the end of the excitation  $z(t) = 0$  again, but the elastic constant of element is  $k_1$ , which is different from the elastic constant at time  $t = 0$ , which was  $k_2$ .

Of course the main question is the definition of the initial state at time  $t = 0$ . However, relaxation processes could be considered (but are not discussed here). That could be done considering that one of the two states allowed at  $z = 0$  is more stable than the other. As a consequence, given a microscopic element which is kept at rest for a long time, state with minimal energy which is the most stable is the initial state. Note that a realistic description of the problem could be more complex than the simplest situation depicted here.

To simulate conditioning, we follow the same approach normally used in experiments. We first apply an excitation of low amplitude  $A_0$ . Then we increase the excitation amplitude up to  $A = A_{max}$ , we measure the nonlinear response and calculate the nonlinear indicator for a non conditioned sample. Afterwards, we condition the sample. To this purpose we first apply an excitation of amplitude  $A_{cond} \geq A_{max}$ . Then, we repeat the first part of the experiment, i.e. we excite at the same low amplitudes  $A_0$  to  $A_{max}$  and measure the corresponding nonlinear responses of the fully conditioned sample. Finally, we compare the two responses before and after conditioning.

To properly simulate such effects, we apply in our simulations an excitation protocol using a sinusoidal wave which does not stop instantaneously but starts decaying exponentially after a certain time due to attenuation in the propagation medium. The excitation is shown in Fig. V.2 where the different phases in one period of the signal are distinguished by the letters  $A, B, C, D$ .

## 4 Hysteretic model

The same hysteretic model with conditioning described in Chapter IV is used. We will limit ourselves here to show again in Fig. V.3 the microscopic and mesoscopic stress-strain equations. Further details have already been discussed in the previous Chapters.

### 4.1 Theory

At the initial time, when no external pressure is applied  $P(t = 0) = 0$ , all microscopic elements with  $P_o > 0$  are in the elastic state (denoted by the letter  $E$  in Fig. V.4) while those satisfying the condition  $P_c < 0$  are rigid( $R$ ). Of course, elements in the configuration  $P_o < 0 < P_c$  might, in principle, be elastic or rigid depending on the stress history at negative times. We assume to start our experiments from a fully relaxed sample and that the rigid state is more stable than the elastic one. It follows that all element with  $P_o < 0 < P_c$  are considered

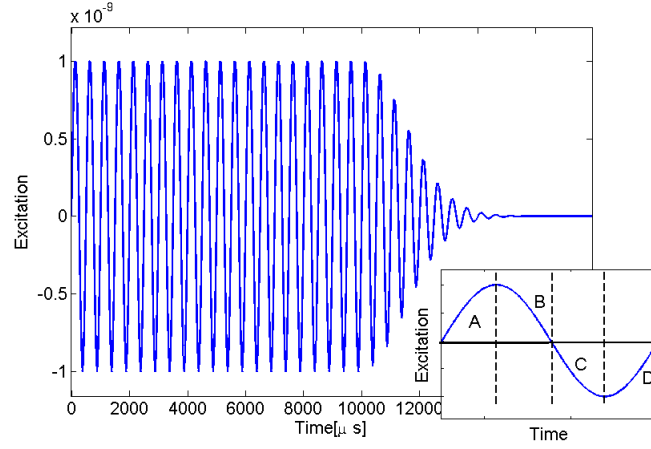


**Figure V.2** – The dynamic excitation protocol used to simulate conditioning effect. The letters ( $A, B, C, D$ ) are attributed to the four phases within one period of the signal: increasing tension( $A$ ), decreasing tension( $B$ ), increasing compression( $C$ ) and decreasing compression( $D$ ). The exponential decay of the source amplitude at late times ensure a correct simulation of attenuation effects in real experiments.

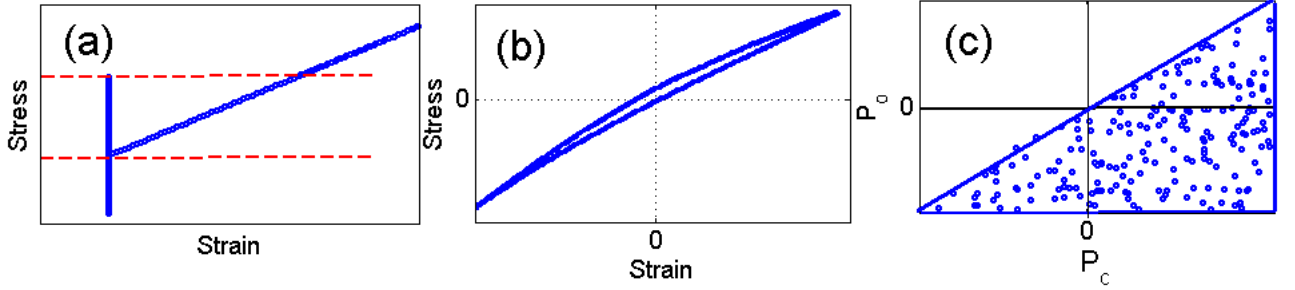


**Figure V.3** – Hysteretic PM model for nonlinearity with conditioning effects. (a) Microscopic stress-strain equation; (b) Macroscopic equation of state derived from averaging; (c) Distribution  $\rho_0$  of microscopic elements in the PM space

to be initially rigid (area  $R$  corresponds to rigid elements). The initial configuration of the hysteretic P-M space is shown in Fig. V.4. (a).

We follow the evolution of the PM space during a strain excitation of amplitude  $A_0$  (see Fig. V.2). In Figs. V.4. (b) and V.4. (c), we show the PM space configurations corresponding to successive phases of the first period of excitation. During phase A, the excitation is increased up to the value shown by the vertical dashed line. During the phase B, the excitation returns to zero. As a result, the final configuration is shown in subplot (b): elements in the triangle denoted with E have switched to rigid (phase A) and back to elastic (phase B), but the final configuration is the same as the initial one (subplot (a)).

During phase C, the pressure becomes negative up to reaching a minimum (dashed red lines) and returns to zero during phase D. As a result, as shown in subplot (c) some elements switched to elastic and back to rigid, except those in the rectangle denoted with the letter R which remains elastic. Thus at the end of one cycle, the configuration is not the same as at the initial time.

After repeating several cycles with the same amplitude, the amplitude of excitation decays exponentially to zero. The final distribution in the PM space is that reported in subplot (d), elements in the dashed area are elastic, while elements in the area denoted by R/E are in a state which strongly depends on the decay process. Roughly the square is divided by its diagonal in a rigid and an elastic part.

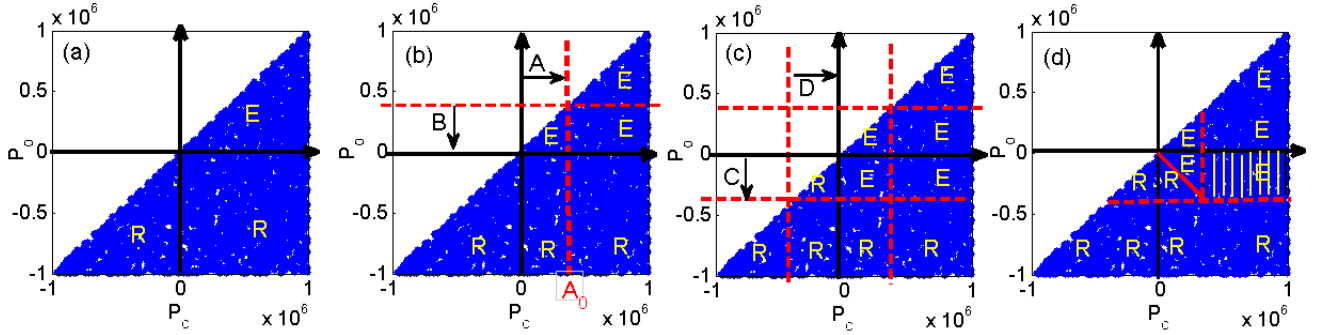


**Figure V.4** – The distribution  $\rho_0$  of microscopic elements in the PM space. The state evolution for each element in the PM space is shown during a strain excitation of amplitude  $A_0$  starting from a relaxed configuration.  $R$  indicate areas where all elements are in the rigid state and  $E$  the areas with elements in the elastic state.

By comparing the first and last configurations, one can notice that the elastic properties of the sample are no more the same as in the original state when the applied pressure goes back to zero. This is an evidence of conditioning in the sample. Furthermore, since we have more elastic elements than in the initial state, softening is expected.

In particular, the dashed rectangle in the PM space contains elements which have switched from the rigid to the elastic state only one time during excitation (i.e. during the first cycle), while all other active elements are switching repeatedly from one state to the other. These elements are responsible of the permanent softening due to conditioning and the area is proportional to  $A_0$ .

In terms of nonlinearity, during the excitation cycles all elements activated contribute to nonlinearity, including those in the dashed rectangle which switch only once. However, if the same excitation is repeated on the conditioned sample, the conditioned elements do not switch any more and thus do not give contributions to the nonlinearity. As a consequence, we expect less nonlinearity generation in the sample.

In particular let us consider the sample to be conditioned at a large amplitude  $A_1$  (dashed red lines) ending up with an initial PM space configuration shown in Fig. V.5. (a). If we repeat

the excitation at the smaller amplitude  $A_0$ , immediately after conditioning we can expect the evolution in the PM space shown in Fig. V.5. (b) to (d). Similar considerations as before apply.

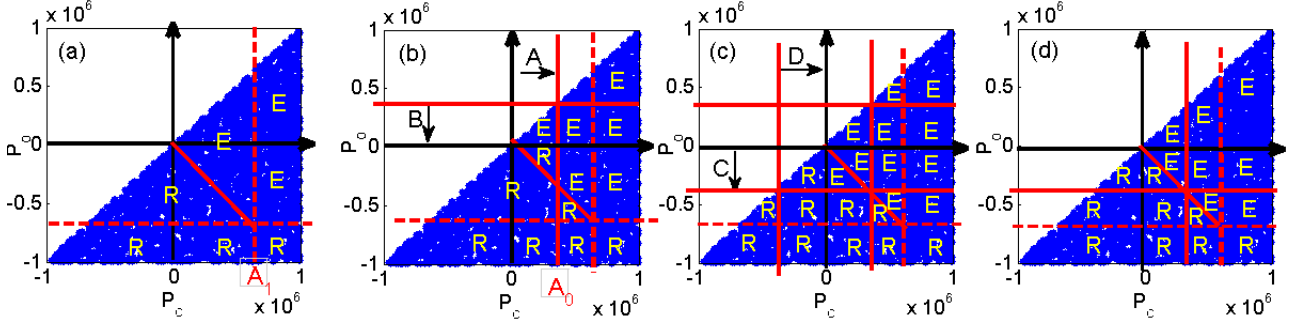


**Figure V.5** – The distribution  $\rho_0$  of microscopic elements in the PM space. The state evolution for each element in the PM space is shown during a strain excitation of amplitude  $A_0$  starting from a conditioned configuration. The letter  $R$  indicates areas occupied by elements in the rigid state, while the letter  $E$  to areas occupied by elastic elements.

We should remark that here, the PM space in its last configuration (subplot (d)) is almost identical to the initial one (subplot (a)). Therefore all elements have returned to their initial states when the drive goes back to zero. Conditioning contribution being eliminated, elements contributing to nonlinearity are those situated inside the triangle of area  $T$ , proportional to  $A^2$ . Thus in this experiment, after conditioning we are measuring pure nonlinearity, having filtered out conditioning effects.

We conclude that, using the hysteretic model, it is expected to measure less nonlinearity after conditioning which corresponds to a smaller value of  $a$  in the power law behavior. Also, we could expect an increase of the exponent from  $b = 1$  before conditioning to  $b = 2$  after, even though the presence of a significant number of elements on the diagonal ( $P_o = P_c$ ) might hide the transition to  $b = 2$ .

## 4.2 Simulation and results

We performed a numerical experiment to confirm the theory we proposed for the hysteretic model with conditioning. All the model parameters are similar to those used in Section 4.2.3 of Chapter IV. For what concerns the conditioning procedure, the sample is first excited at increasing amplitudes  $A_0$  assuming the values in the interval  $[10^{-12}, 10^{-8}]$ . At the end of the experiment the sample is conditioned at the largest amplitude  $A_0 = 10^{-8}$ . Afterwards, the same experiment is repeated a second time.

The SSM nonlinear indicator is then plotted as a function of output energy for each set of data. The two power laws are compared before and after conditioning.

Results are shown in Fig. V.6. The exponent  $b$  increases from  $b = 1$  before conditioning to  $b = 2$  after. Since the two SSM curves have different values of the exponent  $b$ , it is not evident to compare their corresponding values of the coefficient  $a$ . In the specific case of Fig. V.6, it is still evident that the decrease of  $a$  after conditioning is not due to the increase of  $b$ . We stress again that introducing many elements with equal closing and opening pressures the exponent  $b$  is the same before and after conditioning. Still the coefficient  $a$  decreases.

This result could be in agreement with some observations in rocks. In ref. [5], Renaud and coworkers observed a general decrease of the third order nonlinear parameter  $\delta$  after conditioning on rocks. In particular a decrease in  $\delta$  of a factor 10 was roughly observed, which is qualitatively similar to the decrease of about 10 dB observed in our simulations. We should mention that at this stage the comparison with Renaud's data is very preliminary, due to the significant differences in the set-up. Also, the correlation between the way  $\delta$  is defined and our nonlinear indicator is not straightforward. Nevertheless, the apparent agreement in the observations is encouraging.

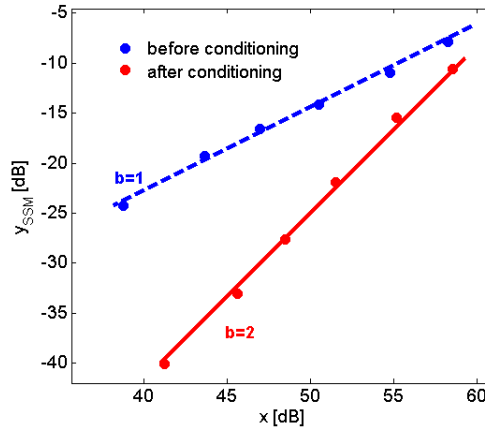


**Figure V.6** – SSM nonlinear indicator plotted as a function of the output energy before and after conditioning. The plot shows a decrease of nonlinearity after conditioning and an increase of the exponent  $b$  at the same time.

## 5 Adhesion hysteretic model with conditioning

In this case we consider a slight modification from the model used in the previous Chapters. The constitutive equation of the microscopic element is shown in Fig. V.7. The reasons for this change are the following:

- The new equation of state does not change substantially the considerations reported before. On the contrary it has the advantage of avoiding the introduction of a discontinuity in the stress when strain is changing (compare with the corresponding figure of the equation of state in Chapter 2: Fig. II.13);



- The same microscopic equation of state was introduced by Granato and Lucke to describe effects due to dislocations (see Fig. II.1). Such equivalence is important from the theoretical point of view, since it could explain, at least partly, why material with very diverse properties, such as rocks or metals, could share the same elastic behavior, even though the physical origin could not be the same.

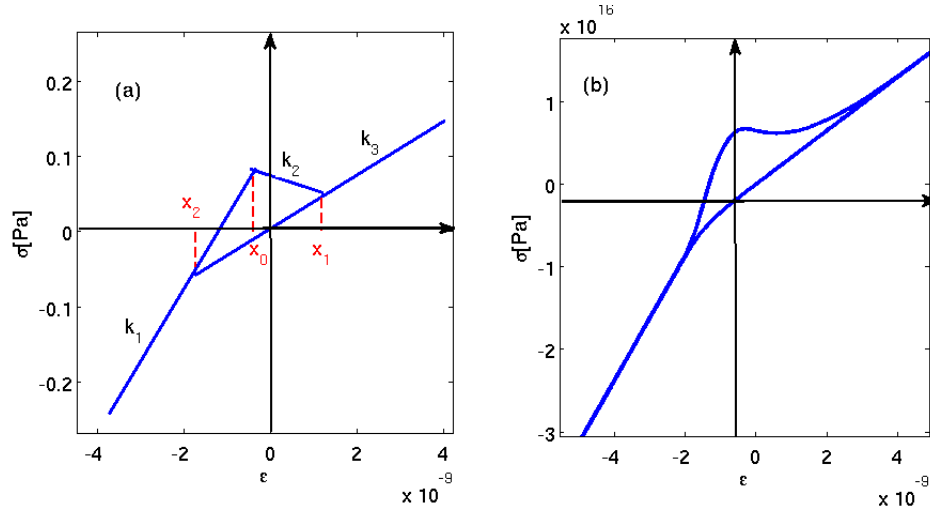


**Figure V.7** – Constitutive equation for the adhesion model with conditioning : (a) Microscopic equation where the transition parameters  $\vec{Z} = (x_0, x_1, x_2)$  and the elastic constants  $E = (k_1, k_2, k_3)$  are reported; (b) Macroscopic stress-strain relation.

## 5.1 The model

We proposed a three state model where each state is defined by a different elastic constant resulting in a vector  $E = (k_1, k_2, k_3)$ . Transition between two successive states  $i$  and  $j$  occurs at the value of the corresponding transition parameter  $z_{ij}$  given by  $\vec{z} = (z_{1,2} = x_0, z_{2,3} = x_1, z_{3,1} = x_2)$ .

The microscopic stress-strain relation (see Fig. V.7) is thus defined by the following set of equations:

$$\begin{aligned}
 \sigma &= k_1(\epsilon - x_{01}) & \text{if } \epsilon < x_2 \\
 \sigma &= \begin{cases} k_1(\epsilon - x_{01}) \\ k_3\epsilon \end{cases} & \text{if } x_2 < \epsilon < x_0 \\
 \sigma &= \begin{cases} k_2(\epsilon - x_{02}) \\ k_3\epsilon \end{cases} & \text{if } x_0 < \epsilon < x_1 \\
 \sigma &= k_3\epsilon & \text{if } \epsilon > x_1
 \end{aligned} \tag{V.1}$$

The elastic constants in the adhesion model are chosen such that  $k_1 > 0, k_2 < 0, k_3 > 0$  and  $k_3 < k_1$ . Both  $k_3$  and  $k_2$  are considered fixed model parameters. Here  $x_{eq} = (x_{01}, x_{02}, x_{03})$  is the equilibrium strain vector, the parameter  $x_{03}$  is fixed to zero and the others are calculated, together with the elastic constant  $k_1$  using the continuity conditions of the force  $\sigma$  at each transition point:

$$\begin{aligned}\sigma(\epsilon = x_2) &= k_1(x_2 - x_{01}) = k_3x_2 \\ \sigma(\epsilon = x_0) &= k_1(x_0 - x_{01}) = k_2(x_0 - x_{02}) \\ \sigma(\epsilon = x_1) &= k_2(x_1 - x_{02}) = k_3x_1\end{aligned}\tag{V.2}$$

Each of the transition parameters  $x_0, x_1$  and  $x_2$  is defined as a random variable uniformly distributed in a proper range as discussed below. Conditioning is introduced considering the transition from state 3 to state 1 occurring only in compression:  $x_2 < 0$ . The transition from state 2 to state 3 occurs only in tension:  $x_1 > 0$ . It follows that at strain equal zero, all three states are allowed and each element could, in principle, be in one of the three states.

However, if we assume state 3 to be the most stable, at the initial time all elements are in state 3. This choice is reasonable since at  $\epsilon = 0$  the stress is zero only if the element is in state 3 (see Fig. V.7).

To optimize the softening property after conditioning, we also consider the transition between states 1 and 2 to occur in compression. It follows  $x_0$  is negative and  $x_2 \leq x_0 \leq 0$ . Note that as a consequence of conditioning, after excitation with a large strain amplitude, an element could end in state 2 when the strain returns to zero. This corresponds to the generation of a residual stress, since  $\sigma \neq 0$  for state 2 when  $\epsilon = 0$ . To avoid a situation where such residual stress in the medium is very large, even larger than the applied dynamic stress, which is physically not acceptable, we add a geometrical constraint on the parameter  $x_1$ :

$$0 \leq x_1 \leq \alpha|x_0|\tag{V.3}$$

The macroscopic constitutive equation resulting after averaging is shown in Fig. V.7.(b),

### 5.1.1 Theory

In the case considered here, we deal with a 3-D PM space since the model have three transition parameters randomly defined. To learn about the way conditioning affects the nonlinear measurements, we follow, as we did for the previous model, the evolution of the elements distribution as a function of a dynamic strain protocol. Instead of considering the distribution in the 3-D space, in the following we will consider the evolution of elements in 2-D plots using the  $(x_0, x_1)$  and  $(x_0, x_2)$  spaces, for sake of clarity.

To do that, let us consider a relaxed medium. As we could see from Fig. V.8. (a), the initial configuration corresponds to a fully relaxed sample, thus all of them are in the state 3, as discussed above.

In tension, during phases A and B of the dynamic strain cycle shown in Fig V.2, the strain is  $\epsilon > 0$  thus the condition  $\epsilon > x_0$  is always satisfied. In the first cycle during phases A and B

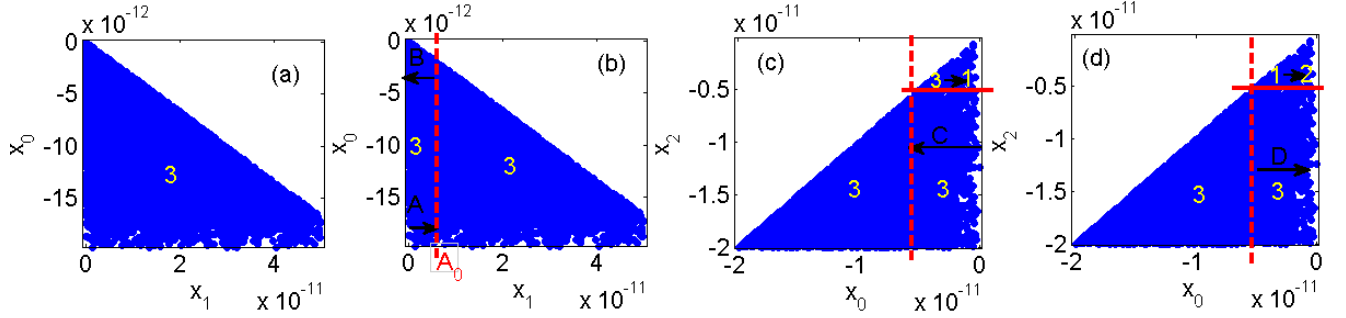


**Figure V.8** – The distribution  $\rho_0$  of microscopic elements in the PM space. The amplitude of the excitation is  $A_0$  shown by red lines. In the first cycle of excitation, during tension no element is changing state, while some elements contribute to nonlinearity and conditioning as a consequence of the compressive part of the excitation.

of the excitation no change in the states of elements occurs. At the end of phase B all elements are in state 3, as in the initial state.

The compressive phase is the most interesting. Here  $\epsilon$  should be compared with  $x_0$  and  $x_2$ . As long as  $\epsilon > x_2$ , the element remains in state 3, thus does not contribute to nonlinearity. During the phase C gradually several elements make a transition to state 1. Releasing the compression state, the same set of elements which changed their state to 1, switch one more time to state 2 before reaching back  $\epsilon = 0$ . It comes out that conditioning takes place during the first cycle of the dynamic excitation, it manifests itself by a change in the elastic properties of the medium. This change could be seen from the last configuration of the PM space of Fig. V.8. (d) where some of the elements are in state 2, while at time  $t = 0$  all elements were in state 3.

Of course, during the successive cycles of excitation, such elements contribute strongly to nonlinearity both in compression and tension, since they could make transitions from state 2 to state 3 or back to state 1 or both. One can conclude that finally only microscopic elements with  $(-A_0 < x_2)$  contribute to nonlinearity.

Now, we condition the sample following the same procedure as before, i.e. apply an excitation of amplitude  $A_1 \gg A_0$ . The initial configuration is more complex in this case because elements at the initial time are partly in state 3 and partly in state 2 as a result of conditioning (see first subplot of Fig. V.9). In particular some of the elements with  $(-A_1 < x_2)$  could be initially in state 2, depending on the relaxation of the excitation and on the values of  $x_1$ .

Let us consider again the excitation of amplitude  $A_0$ . Increasing the strain (tension) during the phase A, some of elements initially in state 2 switch to state 3, thus contributing to nonlinearity. During the phase B, i.e. releasing tension, we do not have any transition (see Fig. V.9. (b)).

Once more, the most significant contribution occurs in compression. At  $\epsilon = 0$  after the first tension cycle, the states of the various elements could be described as follows:

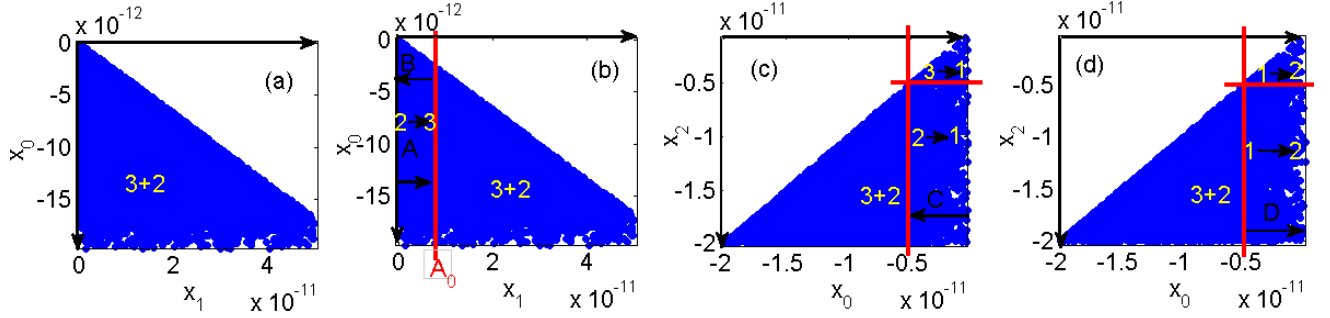


**Figure V.9** – The distribution  $\rho_0$  of microscopic elements in the PM space for an excitation applied after conditioning. The amplitude of the excitation is  $A_0$  shown by red lines. In the first cycle of excitation, both during tension and compression more elements contribute to nonlinearity with respect to the same case for the relaxed sample.

- $(x_2 < -A_1)$ : elements are in state 3, as at time  $t = 0$ . They have not been conditioned.
- $(-A_1 < x_2)$ : elements are partly in state 2 (if they were initially in state 2 and  $A_0 < x_1$ ) and partly in state 3 (all the others).

When the strain further decreases (compression), i.e. during phase C of the excitation, elements in state 3 switch to state 1 as soon as  $(-A_0 < x_2)$  and return to state 2 during the unloading phase (phase D of the excitation). These elements behave as in the relaxed case. In addition, elements in state 2 could switch to state 1, if  $(-A_0 < x_0)$  and back to state 2 during release of compression (phase D of the excitation): see Fig. V.9. (c) and (d). These additional elements were not contributing to nonlinearity in the case of the relaxed sample.

We could notice that when the strain returns to zero we recover the same initial configuration for the conditioned sample, i.e. no further conditioning is induced. For what concerns nonlinearity, for the reasons mentioned above, more elements are contributing to the nonlinear behavior with respect to the case of the relaxed sample. Thus we expect an increase of nonlinearity.

Theoretical prediction of the exponent  $b$  is more complex in this case of adhesion model and we do not discuss them.

## 5.2 Simulation and results

### 5.2.1 Simulation

We performed a numerical simulation using  $N = 10000$  microscopic elements with behavior described by the stress-strain equation of the adhesion hysteretic mechanism with conditioning (Fig. V.7). Elements are arranged in series, thus the strain is the same for each element and it is equal to the global applied strain on the mesoscopic cell. Strain is used as a driving variable with the same form as in Fig. V.2.

Given the strain, the stress is calculated for each element and the sum over all  $N$  microscopic elements provides the global stress on the mesoscopic cell (averaging process). Strain amplitudes are chosen in the range  $[10^{-11} \ 10^{-8}]$ . We use a frequency  $\omega = 25.9kHz$ . For what concerns the model parameters, we have used :  $x_2^{min} = -20.10^{-12}$ ,  $x_1^{max} = 50.10^{-12}$ ,  $E = [k1 \ -25 \ 72]GPa/m$ . The parameter  $\alpha$  in the geometrical constraint on  $x_1$  is  $\alpha = 3$ .

As in the previous section, the sample is excited at increasing amplitudes  $A$ . Both SSM and FFT indicators are calculated at each amplitude. At the end of the experiment, the sample is conditioned at the highest amplitude  $A_{max}$  used. We immediately repeat the same experiment and again calculate the nonlinear indicators for each amplitude of excitation.

### 5.2.2 Results

#### Conditioning induced non linearity activation

In Fig. V.10 below, we follow the variations in time of the number  $N_i$  of elements in each of the three states  $i = 1, 2, 3$  during a dynamic strain excitation of amplitude  $A = 3.5.10^{-9}$ . The result is shown for each state  $i$  separately both during the first experiment, i.e. before conditioning (subplot (a)) and during the second experiment on a conditioned sample (b).

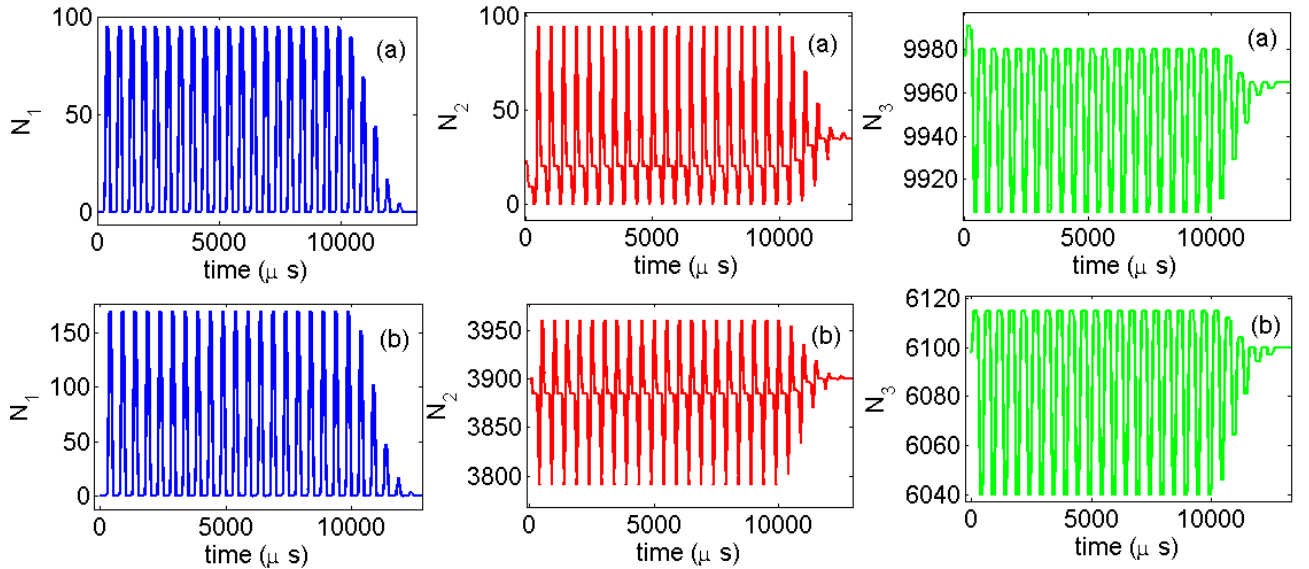


**Figure V.10** – Time Evolution of the number  $N_i$  of elements in each of the three states ( $i = 1, 2, 3$ ) for an excitation amplitude  $A = 0.35.10^{-9}$ : (a) Before conditioning; (b) After conditioning.

We observe that the number of elements switching state is larger after conditioning than before. This result is a confirmation that conditioning is activating nonlinearity in the sample. Comparing the couple of subplots in the first and second rows for both states 1 and 2, we notice a significant increase in the number of elements in the corresponding states. Both follows well the applied excitation.

The conditioning effect could also be seen in the same figure. For the experiment on the relaxed sample (upper row) the number of elements in state 2 at the end of the excitation is larger than the number of elements in state 2 at the beginning. Correspondingly the number of elements in state 3 is smaller. As expected, the number of elements in state 1 is zero at the beginning and at the end of the excitation. On the contrary, the number of elements in each state at the end of the excitation always goes back to its original value when the sample is already conditioned (lower row).

Finally, both SSM and FFT nonlinear indicators are calculated for each amplitude  $A$  of the strain excitation before and after conditioning. In Fig. V.11. (a), we plot the SSM indicator as a function of the output energy before (data are fitted with a dashed blue line) and after conditioning (data are fitted with a solid red line).

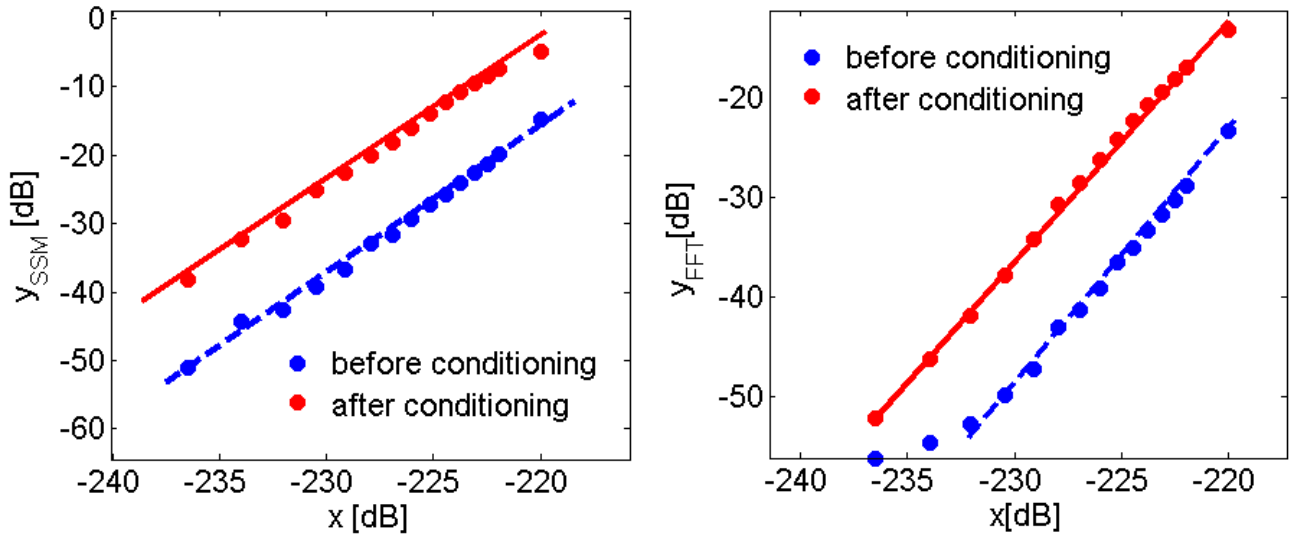


**Figure V.11** – Nonlinear indicator plotted as a function of the output energy before and after conditioning. The plot shows an increase of nonlinearity after conditioning while the exponent  $b$  does not change: (a) SSM indicator; (b) FFT indicator.

In terms of power law parameters, Fig. V.11. (a) shows that the coefficient  $a$  increases after conditioning, which is reasonable since we have seen that conditioning activates nonlinearity. For what concerns  $b$ , it doesn't change.

The same observation holds for the FFT indicator (see Fig. V.11.(b)). Again, the increase of nonlinearity after conditioning is confirmed. Indeed, the coefficient  $a$  of the power law increases while the exponent  $b$  is almost the same as before conditioning.

These results are in agreement with the experimental data for damaged samples discussed in the first Section of this Chapter.

### Conditioning induced softening and residual stress

Another effect which is emerging from the model is discussed in Fig. V.12 to confirm the validity of the proposed theoretical approach. Here, we plot the stress-strain equation of one mesoscopic element (i.e. averaging over many microscopic elements) at a small excitation

amplitude  $A = 0.15 \cdot 10^{-9}$  ( see Fig.V.12. (a)) and at an intermediate amplitude  $A = 0.3 \cdot 10^{-9}$ . We show, in the same plot both results obtained on a sample before conditioning (dashed blue line) and after conditioning (red solid line).

As expected, at small strain amplitudes the stress-strain dependence is almost linear, both before and after conditioning. However, the Young modulus of the sample decreases as a consequence of conditioning. This softening could be seen from the decrease in slope of the curve. One can also see that conditioning induces residual stress in the sample manifested by a given value  $\sigma_r \neq 0$  of the stress at zero strain.

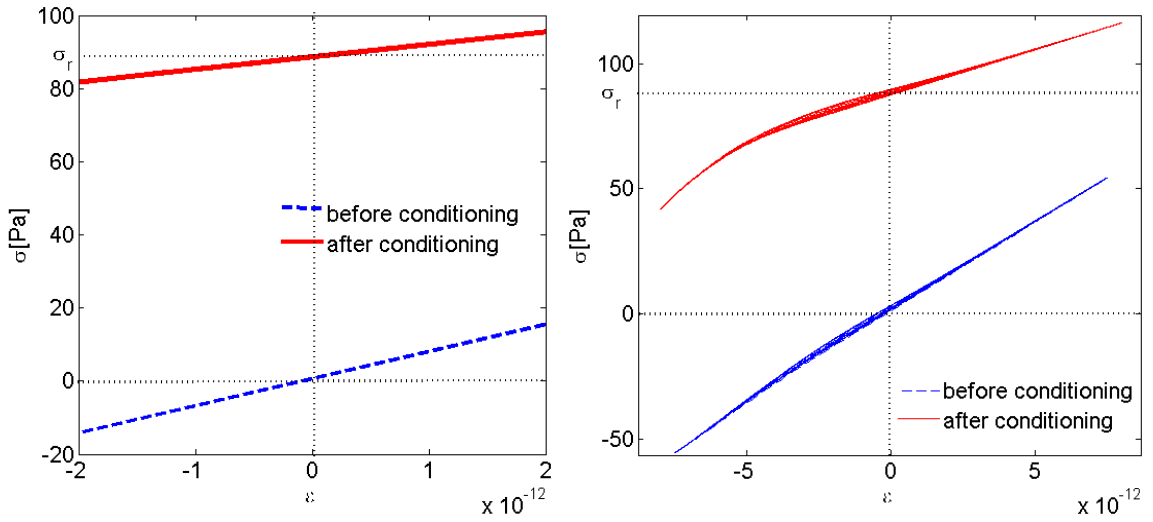


**Figure V.12** – The mesoscopic stress-strain equation at (a) small strain amplitude  $A = 0.15 \cdot 10^{-9}$ ; (b) at an intermediate strain amplitude  $A = 0.3 \cdot 10^{-9}$ . The curves are plotted for the relaxed(blue) and conditioned(red) samples

The residual stress can also be seen in Fig. V.12. (b) when the excitation amplitude is larger, but still much smaller than the one corresponding to conditioning. Here, the strain amplitude is large enough to appreciate nonlinearity in the stress-strain relation. In agreement with the observations reported previously, also in the constitutive equation it could be appreciated the increase of bending and the widening of the hysteretic loop for the conditioned sample. Both are indication of an increase in nonlinearity, which is confirming the results reported previously.

## 6 Conclusions

Analyzing experimental data collected from literature, we have found that conditioning seems to affect the nonlinearity measurements in two different ways depending on the medium. Data on rocks obtained with the Dynamic AcoustoElastic testing method seems, albeit not conclusively, to indicate a decrease in nonlinearity after conditioning. The second kind of behavior is characterized by nonlinearity activation after conditioning as shown for damaged concrete using the SSM indicator [3] and for fatigues metal based composites using FFT.

We have shown in this Chapter how such effects could be described in the framework of multi-state models, introducing a proper hysteretic microscopic stress-strain equation with conditioning in the multi-state multi-scale approach. We have performed numerical simulations to analyse the effects of conditioning on the exponent  $b$  and the coefficient  $a$  of the power law dependence of the nonlinear indicators on the excitation energy. A good qualitative agreement with experimental data has been obtained.

Results and models presented here represent a preliminary attempt to investigate the subject. Even though results are encouraging, a more accurate analysis will be performed in the future. In this context, we have optimized the model parameters, particularly the distributions in the PM space of the values of the transition parameters, in order to maximize the observed effects. Further work will be performed to better motivate the choices used here.

As a final remark, the work done allowed to make useful considerations related to Physical mechanisms which are at the origin of conditioning in NME materials. Indeed, the nonclassical elastic behavior was observed in materials whose micro-structure is extremely diverse. In this Chapter, we have shown results obtained from measurements on concrete and metal based composites. Dislocations and Stick-slip or adhesion could be the common physical features, in both consolidated granular media and metals, which are at the origin of the observed conditioning effects.

In the model proposed in the last Section of this Chapter, we have used a microscopic constitutive equation which was derived in 1956 for dislocations in metals. But we have also shown that the same microscopic equation of state holds also when we consider adhesion mechanisms, as used in the literature more recently by Gusev and coworkers[6] (even though modifications to introduce hysteresis are considered here). Thus, it seems that different physical mechanisms could share the same microscopic behavior, perhaps differing in the statistical distribution of the parameters.

In this direction, the work performed in the thesis provides suggestions for future work. However, it could be of great importance to develop the issue further, in view of explaining why nonclassical elasticity seems to be a 'universal' behavior shared by a huge class of extremely diverse materials.



---

## References

- [1] M. Bentahar, H. El Aqra, R. El Guerjouma, M. Griffa, and M. Scalerandi. Hysteretic elasticity in damaged concrete: Quantitative analysis of slow and fast dynamics. *Phys.Rev.B*, 73:104114, 2006. [118](#), [119](#)
- [2] M. Scalerandi. A preisach-mayergoyz approach to fatigue induced irreversibility. *Phys. Rev. B*, 73:092103, 2006. [118](#)
- [3] M. Scalerandi. Detection and localisation of cracks using loss of reciprocity in ultrasonic waves propagation. *J. Acoust. Soc. Am*, 131:EL81–EL85., 2012. [119](#), [132](#)
- [4] P. P. Delsanto and M. Scalerandi. Modeling nonclassical nonlinearity, conditioning and slow dynamics effects in mesoscopic elastic materials. *Phys. Rev. B*, 68:064107(1–9), 2003. [119](#)
- [5] G.Renaud et al. Remote dynamic acoustoelastic testing: Elastic and dissipative acoustic nonlinearities measured under hydrostatic tension and compression. *Appl.Phys.Lett.*, 94:011905, 2009. [120](#), [125](#)
- [6] N. Chigarev and V. Gusev. *IEEE Trans. On Ultras. Ferr. and Freq. Control*, 57:1426–1433, 2010. [133](#)

---

## Conclusion and Perspectives

My PhD thesis has been concerned with the investigation of the power law behavior of the nonlinear indicator in Nonlinear Mesoscopic Elastic (NME) materials, with the goal to improve our understanding of the emergent phenomena of Non Classical Non Linear elasticity. Mainly theoretical work (numerical studies) are proposed in this thesis. Nevertheless a few simple experiments have also been performed, mostly to confirm the observations theoretically predicted.

As a first preliminary step, in Chapter III, I have analysed the problem of the determination of the amplitudes range in which the power law dependence  $y = ax^b$  of nonlinear indicators on the driving amplitudes is meaningful. This is crucial for the correct estimation of the power law exponent. We have shown that both *SSM* and *FFT* indicators fit a power law only in an intermediate amplitude range: at low/high amplitudes noise/saturation effects are dominant. We have shown that nonlinearity starts to be measurable at a threshold value which we can determine, in log-log scale, from the intersection of two fitting lines: one representing nonlinearity and the other, with slope 0, due to noise effects. We studied numerically the effects of experimental noises on the detection threshold of nonlinearity.

Our findings indicate that:

- for both SSM and FFT methods, the threshold increases when equipment noise increases. SSM method remains sensitive up to a larger value of the equipment noise;
- an ambient noise in the SSM signal is equivalent to an equipment noise whose amplitude is inversely proportional to the lowest excitation amplitude  $A_0$  used to build the SSM signal. Thus, in experiments a compromise is necessary for the choice of  $A_0$ , which should be as high as possible to enhance the SNR but small enough to provide a quasi-linear response;
- effects of ambient noise on FFT signal decreases with amplitude. As a consequence it is generally not significant compared to equipment noise when harmonics are considered.

In the same Chapter, we also addressed the problem of the dependence of nonlinear measurements on the experimental configuration. We have focused our work mostly on determining the influence of the relative distance between receivers and the nonlinear scatterer on the quantitative estimation of nonlinearity. As a consequence of attenuation and geometrical dispersion in the medium, it is not easy to assign an absolute value to the coefficient  $a$  of the power law

dependence, which makes difficult to compare nonlinearity of different samples, unless care is taken to reproduce equivalent experimental configurations.

Our main results show that a possible solution to the problem is to plot *SSM* and *FFT* nonlinear indicators as a function of the input energy, rather than of the energy estimated from the output signal. However, this solution presents limitations in several experimental situations, as in the case of continuous waves where the resonance structure of the system affects the wave propagation. *SSM* methods, being based on the determination of the nonlinearity present at the fundamental frequency, have the advantage of cancelling effects due to the resonance structure. In fact the nonlinear indicator is introduced as the ratio between energies of signals at the same frequency.

The main part of my research work, reported in Chapter IV, was devoted to link the macroscopic measurements to the microscopic mechanisms responsible of nonlinearity generation through the exponent  $b$  of the power laws. Indeed, by collecting a large number of experimental results we have shown that, while similarities in the elastic behavior of many materials can be individuated, a careful analysis of the exponent  $b$  allows to classify materials in different classes. There seems to be a link between the value of  $b$  (ranging from 1 to 3 in the experiments at low strain amplitudes) and the microstructure of the medium. In particular, the presence of partially open or closed cracks seems to be determinant for the prediction of the exponent value.

Using a multi-state multi-scale approach based on a generalised PM space description to define microscopic constitutive equations, we have found that:

- the exponent  $b$  is related to the physical origin of nonlinearity, both at the microscopic level, through the number of transition parameters and their constraints in the model, and in the physics behind the statistical distribution of the nonlinear features;
- useful quantitative information about the microstructure evolution could be extracted if we know the processes responsible of damage. For instance, a quasi-static loading is likely to induce increase in the cracks size, thus producing a transition from closed to open cracks;
- we have been able to fit experimental data obtained on concrete samples with increasing damage considering hysteretic and clapping physical mechanisms as responsible of nonlinearity.

Finally, in Chapter V, conditioning effects on nonlinear measurements have been analysed. Experimental observations reported in the literature indicate that in some cases nonlinearity measured after having conditioned the sample is larger than the one measured with identical experimental configuration on a completely relaxed sample.

Such nonlinearity activation was not described by any existing model. Here I have shown that multi-state models could be proposed to simulate either an increase or a decrease of nonlinearity after conditioning. As a particular case, I have studied the nonlinearity activation

in fatigued metallic composite plates. I proposed a multi-state dislocation model, based on the Granato Lucke model. The obtained results show that, in agreement with experiments, the exponent  $b$  is not sensitive to conditioning, while the coefficient  $a$  is larger for the conditioned sample.

The work performed in this thesis, which was aiming to link the nonlinearity observed in NME materials to physical processes, is of course not yet conclusive. The following research perspectives are envisaged, some of them being determinant in order to lead the preliminary work performed here to possible applications.

In particular, I plan to continue the research in the field of Nonlinear Acoustics along some of the following directions:

**Nonlinearity mechanisms** Several steps are necessary in order to identify in a unique way the mechanisms responsible for nonlinearity. It is indeed to be considered that, while the nonlinear elastic behavior is common to several materials, the physical origin should be different. Therefore we need:

- to collect experimental data on materials with possibly different physical sources of nonlinearity (e.g. metals with dislocations and rocks with fluids residing in the area at the interface between grains) to highlight differences and similarities in their macroscopic response. This issue was partially addressed here, but it should be focused on determining also the behavior varying some material parameters such as humidity, temperature, grain sizes, etc.;
- to analyse the theoretical predictions of models based on different physical mechanisms and determine their similarities and differences, in order to compare them with experimental observations. Again, this was partially addressed here, but still the quantitative link between the multistate parameters and the physical parameters in existing continuous models should be better investigated;
- to provide a physical interpretation for the statistical distribution chosen. We recall that the choice of the properties corresponding to the statistical distribution is relevant for the prediction of the exponent  $b$ . Decoupling its effects from those of the choice of the physical mechanisms is not easy and was not addressed here;
- validate the choice of the model parameters in the equation of state by fitting quasi-static measurements. From the experimental point of view, quasi-static measurements in the strain range useful for dynamic experiments (i.e.  $10^{-9}$  to  $10^{-6}$ ) is not feasible, especially in tension. As an alternative, we could expect to use results from an emerging technique, called Dynamic AcoustoElastic testing, which seems to be very efficient in providing experimental stress-strain relations equivalent to quasi-static measurements.

**Conditioning mechanisms** Decoupling conditioning from nonlinearity is not correct, since the influence of conditioning on measurements of nonlinearity is large (and may be dominant, at least in some cases). Here, in Chapter V, we have presented a very preliminary attempt to include the interaction of conditioning and nonlinear features in a dislocation model. However, the one proposed here is not yet definitive. More experimental observations and theoretical

studies are needed. We expect however, the behavior induced by conditioning to be very important for discriminating correctly the different nonlinearity sources.

**Absolute measurements of nonlinearity** In applications, it is of obvious relevance to allow the possibility of quantitatively comparing measurements on different samples and in different experimental/environmental conditions. As we have shown here this is not easy, due to the difficulty of controlling the energy which is really exciting the nonlinearity, being measurements performed only at the source and detector position. Considering pulses propagation, correction for attenuation should be defined and used to 'normalise' data. The SSM could provide a solution to the problem, since it allows to isolate effects due to attenuation, calculate and perhaps compensate them. Again, this issue was addressed here only marginally, but it is worth to developing in future studies .